Direct Top Quark Decay Width Measurement in the $t\bar{t}$ Lepton+Jets Channel at $\sqrt{s} = 8$ TeV with the ATLAS Experiment

Dissertation

zur Erlangung des mathematisch-naturwissenschaftlichen Doktorgrades
„Doctor rerum naturalium“
der Georg-August-Universität Göttingen

im Promotionsprogramm ProPhys
der Georg-August University School of Science (GAUSS)

vorgelegt von

Philipp Stolte-Cord to Krax

aus Göttingen

Göttingen, 2017

Betreuungsausschuss

Prof. Dr. Arnulf Quadt
II. Physikalisches Institut, Georg-August-Universität Göttingen

Prof. Dr. Ariane Frey
II. Physikalisches Institut, Georg-August-Universität Göttingen

Prof. Dr. Kevin Kröninger
Lehrstuhl für Experimentelle Physik IV, Technische Universität Dortmund

Mitglieder der Prüfungskommission:

Referent:	Prof. Dr. Arnulf Quadt II. Physikalisches Institut, Georg-August-Universität Göttingen
Koreferent:	Prof. Dr. Stan Lai II. Physikalisches Institut, Georg-August-Universität Göttingen

Weitere Mitglieder der Prüfungskommission:

Prof. Dr. Ariane Frey
II. Physikalisches Institut, Georg-August-Universität Göttingen

Prof. Dr. Wolfram Kollatschny
Institut für Astrophysik, Georg-August-Universität Göttingen

Prof. Dr. Ulrich Parlitz
Max-Planck-Institut für Dynamik und Selbstorganisation, Göttingen

Prof. Dr. Steffen Schumann
II. Physikalisches Institut, Georg-August-Universität Göttingen

Tag der mündlichen Prüfung: 24.10.2017

GEORG-AUGUST-UNIVERSITÄT
GÖTTINGEN

Direct Top Quark Decay Width Measurement in the $t\bar{t}$ Lepton+Jets Channel at $\sqrt{s} = 8$ TeV with the ATLAS Experiment

Philipp Stolte-Cord to Krax

Abstract

The top quark t plays an essential role in the field of elementary particle physics - in particular due to its exceptional properties comprising a large mass, which approximately equals the mass of a tungsten atom, and an enormously short lifetime. This thesis is devoted to the study of a fundamental property of the top quark - its decay width. Its value is predicted by the established Standard Model of particle physics and deviations may hint at yet unknown physics beyond this model.
A direct measurement of the decay width of the top quark is presented. The analysis is based on $t\bar{t}$ events in the lepton+jets decay channel using data taken in proton-proton collisions at a centre-of-mass energy of $\sqrt{s} = 8$ TeV. The dataset was recorded in 2012 with the ATLAS detector at the Large Hadron Collider at CERN and corresponds to an integrated luminosity of 20.2 fb^{-1}. The decay width of the top quark is extracted by utilising a template fit to one-dimensional distributions of kinematic quantities, performed simultaneously in the hadronic and the leptonic decay branch of $t\bar{t}$ events. Since the measurement is a direct measurement of the top quark decay width, it is less model-dependent in comparison to indirect approaches. This enables the measurement to probe a broad class of Standard Model extensions.

II.Physik-UniGö-Diss-2017/03
II. Physikalisches Institut
Georg-August-Universität Göttingen

GEORG-AUGUST-UNIVERSITÄT
GÖTTINGEN

Direkte Zerfallsbreitenmessung des Top-Quarks im $t\bar{t}$-Lepton+Jets-Zerfallskanal bei $\sqrt{s} = 8$ TeV mit dem ATLAS-Experiment

Philipp Stolte-Cord to Krax

Zusammenfassung

Das Top-Quark t spielt eine wesentliche Rolle im Bereich der Elementarteilchenphysik - insbesondere aufgrund seiner bemerkenswerten Eigenschaften, die eine sehr große Masse, die in etwa mit der eines Wolframatoms vergleichbar ist, sowie eine enorm kurze Lebensdauer umfassen. Ziel dieser Arbeit ist die Untersuchung einer fundamentalen Größe des Top-Quarks - der Zerfallsbreite. Der Wert der Zerfallsbreite wird vom etablierten Standardmodell der Teilchenphysik vorhergesagt, und Abweichungen können auf Physik jenseits dieses Modells hinweisen.
Diese Dissertation stellt eine direkte Messung der Zerfallsbreite des Top-Quarks vor. Die Analyse basiert auf $t\bar{t}$-Ereignissen im Lepton+Jets Zerfallskanal und nutzt Analysedaten, die in Proton-Proton-Kollisionen bei einer Schwerpunktsenergie von $\sqrt{s} = 8$ TeV genommen wurden. Der Datensatz wurde im Jahr 2012 mit dem ATLAS-Detektor am Large Hadron Collider am CERN aufgezeichnet und entspricht einer integrierten Luminosität von 20.2 fb^{-1}. Die Zerfallsbreite des Top-Quarks ergibt sich mittels eines sogenannten Template-Fits an eindimensionale Verteilungen verschiedener kinematischer Größen. Jener Fit ist simultan im hadronischen und leptonischen Zerfallszweig der $t\bar{t}$-Ereignisse realisiert. Da die Messung auf direkte Weise durchgeführt wird, ist sie modellunabhängiger als indirekte Methoden, was die Prüfung einer breiten Klasse von Standardmodellerweiterungen erlaubt.

II.Physik-UniGö-Diss-2017/03
II. Physikalisches Institut
Georg-August-Universität Göttingen

Contents

1 Introduction **1**

2 The Standard Model and the Role of the Top Quark Therein **5**

2.1 The Standard Model of Particle Physics 5

2.1.1 Quarks, Leptons and Mediators 6

2.1.2 Interactions and the Higgs Mechanism 8

2.2 The Top Quark 14

2.2.1 Top Quark Production 15

2.2.2 Top Quark Decay 22

2.2.3 Top Quark Properties 25

2.3 Top Quark Decay Width 27

2.3.1 Theoretical Aspects 27

2.3.2 Measurements of the Top Quark Decay Width 31

2.3.3 Predictions for the Top Quark Decay Width in BSM Models 34

3 The ATLAS Experiment **39**

3.1 The Large Hadron Collider 39

3.2 Detector Observables and Coordinates 42

3.3 The ATLAS Detector 44

3.3.1 Inner Detector 45

3.3.2 Calorimeter System 47

3.3.3 Muon System 49

3.3.4 Forward Detectors 50

3.3.5 Magnet System 51

3.3.6 Trigger System 51

4 Object Definition **53**

4.1 Fundamentals of the Object Reconstruction 53

4.2 Muons 55

4.3 Electrons 57

4.4 Jets 59

4.5 b-Tagging 62

4.6 Missing Transverse Momentum 64

5 Signal and Background Modelling **67**

5.1 Fundamentals of the Event Simulation 67

5.1.1 Stages of the Event Simulation 67

5.1.2 Monte Carlo Event Generators and Detector Simulation 70

5.2 Signal Monte Carlo Samples 71

5.3 Background Monte Carlo Samples 71

5.3.1 Single Top Background 71

5.3.2 W and Z Boson Background 72

5.3.3 Diboson Background 73

5.3.4 Multijet Background 73

5.4 Summary of Signal and Background Generators 74

6 Dataset, Event Selection and Reconstruction **75**

6.1 Dataset 75

6.2 Event Selection 77

6.3 Event Reconstruction 88

6.3.1 Kinematic Likelihood Fit 88

6.3.2 Transfer Functions 93

6.3.3 Extensions of the Likelihood 95

6.3.4 Further KLFitter Configurations 96

7 Analysis Strategy **103**

7.1 Observables Sensitive to the Top Quark Decay Width 103

7.2 Template Reweighting 105

7.3 Definition of the Likelihood 112

7.4 Evaluation of Systematic and Expected Statistical Uncertainties 115

7.5 Validation of the Fit Method 116

7.6 Correlations Between the Observables 119

7.7 Fit Configurations 121

8 Systematic Uncertainties **123**

8.1 Evaluation of Systematic Uncertainties 123

8.2 Uncertainties in Detector Modelling 125
8.2.1 Charged Lepton Uncertainties 125
8.2.2 Missing Transverse Momentum Uncertainty 125
8.2.3 Jet Reconstruction Efficiency 126
8.2.4 Jet Vertex Fraction 126
8.2.5 Jet Energy Scale 126
8.2.6 Jet Energy Resolution 128
8.2.7 Heavy and Light Flavour Tagging 129
8.3 Uncertainties in Background Modelling 130
8.3.1 Normalisation Uncertainties 130
8.3.2 W+Jets Shape Uncertainty 130
8.3.3 Single Top Shape Uncertainty 130
8.3.4 Multijet Shape Uncertainty 130
8.4 Uncertainties in Signal Modelling 131
8.4.1 Radiation Uncertainty 131
8.4.2 Matrix Element Generator Uncertainty 135
8.4.3 Parton Shower and Fragmentation Uncertainty 135
8.4.4 Colour Reconnection Uncertainty 136
8.4.5 Underlying Event Uncertainty 136
8.4.6 PDF Set Uncertainty 136
8.5 NLO and Off-Shell Effects in the Top Quark Decay 137
8.6 Impact of the Top Quark Mass 142
8.7 Other Systematic Uncertainties 150
8.7.1 Luminosity Uncertainty 150
8.7.2 Template Statistical Uncertainty 150
8.8 Total Systematic Uncertainty 150
9 Comparison of Fit Configurations and Observables **153**
9.1 Comparison of Fits with One Observable 153
9.2 Comparison of Fits with Two Observables 155
9.3 Modelling of the Observables 160
9.4 Comparison of Results Using Events with at Least 2 b-Tags 161
10 Results **163**
10.1 Results of the Fit to Data 163
10.2 Impact of the W+Jets Background 169
10.3 Statistical Significance 171

11 Summary and Conclusion **173**

11.1 Summary of the Obtained Results 173

11.2 Outlook 175

A Monte Carlo Samples **177**

B Additional Event Yield Tables **183**

C Additional Control Plots **185**

D Additional Correlation Plots **191**

E Systematic Uncertainties with Effective Components **199**

F Additional Plots for the Estimation of the Impact of the Top Quark Mass **203**

G Pre-Fit Plots to Test the Observable Modelling **207**

H Post-Fit Plots in Individual Analysis Regions **211**

I Two-Dimensional Template Fit **215**

List of Figures **219**

List of Tables **223**

Bibliography **225**

Acknowledgements & Danksagung **245**

1 Introduction

One of the most fundamental questions which has bothered scientists for generations is concerned with the basic or *elementary* constituents of matter, examined at the smallest possible scale. Consequently, these constituents are referred to as particles or *elementary particles*. But what does elementary or, generally speaking, *elementary particle physics* mean?
The underlying definition of the term “elementary” has evolved significantly over time - although the aim of this field of physics is still the same: the hunt for those fundamental constituents and their possible interactions, which gained pace remarkably over the last decades. Chemists in the 19th century can perhaps be regarded as the first researchers in the field of particle physics since they discovered distinct elements postulated to be composed of atoms, whose name originates from *átomos*, the Greek word for “uncuttable”. These discoveries resulted in the periodic table of chemical elements, first published by the Russian chemist D. Mendeleev in 1869. The discovery of the electron by J. J. Thomson in 1897 marks the starting point of subatomic particle physics followed by the gold foil experiments, the first fixed target experiments, performed by H. Geiger, E. Marsden and E. Rutherford between 1908 and 1913, leading to Rutherford’s proposal of a model where the atom is mostly empty, and the positive charge inside atoms is concentrated in a point-like and massive centre, the atomic nucleus, which is surrounded by a cloud of electrons.
Due to technological improvements in the 1950s and later decades allowing for the development of more advanced particle accelerators and detectors, more and more subatomic particles could be discovered; in addition to the positively charged proton and the electrically neutral neutron, being the constituents of the atomic nuclei. Many of these newly discovered particles were included in the “eightfold way”, introduced by M. Gell-Mann. Later, based on deep-inelastic scattering, it was experimentally verified that also protons and neutrons are not elementary but compound particles composed of quarks. Further developments and in particular the electroweak theory by S. Glashow resulted in the formulation of the Standard Model of Elementary Particle Physics which describes all elementary particles and their interactions while the particle masses are explained by the Higgs mechanism. Today’s experiments in the field of particle physics, around 120 years after the discovery of the electron, are based on collisions of particles obtaining their high energy from accelerators which is why the expression *high energy physics* is commonly used to characterise those experiments. After the acceleration and collision of particles, the resulting decay products need to be measured with precise particle detectors to draw inferences about the underlying processes and the involved particles, which comprises, for example, a measurement of their properties.
Caused by a decreasing distance scale of the observed processes, higher energies and, as a result, larger machines are essential to accelerate particles before colliding. Nowadays, the *Large Hadron*

Collider (LHC) at CERN, the European Organisation for Nuclear Research, is the world's most powerful particle accelerator which started operating with beam energies of 3.5 TeV in 2010, and is designed to reach beam energies of up to 7 TeV. These high energies, in combination with a high luminosity, which can be described as the number of occurring events per time and area, allowed for the discovery of a new boson at the LHC. The observation was announced in July 2012 [1, 2], observed by the two LHC multipurpose experiments ATLAS (A Toroidal LHC ApparatuS) and CMS (Compact Muon Solenoid). Further measurements in the past years confirmed that this new particle is indeed the Standard Model Higgs boson, which has been searched for since its prediction in the 1960s [3–13]. Additionally, this high energy regime enables particle physicists to test the Standard Model in more detail, and it may unveil something unsuspected, commonly classified as physics beyond the Standard Model.

The Standard Model fermion with the strongest coupling to the Higgs boson is the top quark due to its relatively large mass, which is of the order of the tungsten atom mass. Hence, the lifetime of the top quark is expected to be rather small and, consequently, the decay width of this heaviest quark very large. Measuring the top quark decay width is of strong interest since deviations from the Standard Model decay width expectation would be an indication of new and yet unknown physics. For example, such deviations may hint at currently unknown top quark decay channels - such as decays through a charged and yet undetected Higgs boson, decays through the supersymmetric partner of the top quark or a flavour changing neutral current decay of the top quark.

This thesis intends to present a direct measurement of the top quark decay width. The most conspicuous characteristic of such a direct measurement is its model-independence as fewer Standard Model assumptions need to be made - in comparison to an indirect measurement, which is defined in the following chapters. Thus, a direct measurement serves to probe a potentially broader class of models involving Standard Model extensions.
The most recent direct measurements of the top quark decay width were performed at the Tevatron by the CDF collaboration [14] and at the LHC by the CMS collaboration [15]. The CDF measurement is based on the Tevatron dataset of $\sqrt{s} = 1.96$ TeV proton-antiproton collision data which corresponds to an integrated luminosity of 8.7 fb^{-1}. A decay width of $1.10 < \Gamma_t < 4.05$ GeV for a top quark mass of 172.5 GeV was extracted at the 68% confidence level. The preliminary CMS result was obtained using 12.9 fb^{-1} of proton-proton collision data taken at the LHC in 2015 and 2016 at a centre-of-mass energy of $\sqrt{s} = 13$ TeV yielding a range of $0.6 < \Gamma_t < 2.5$ GeV for the decay width at the 95% confidence level.

Performing a direct measurement is very challenging because of the limited detector resolution for objects used to define observables needed to extract the top quark decay width. This resolution, provided by large multipurpose detectors like ATLAS and CMS, translates into smeared and broadened observable distributions with resolutions which are around one order of magnitude larger than the expected underlying decay width itself. As a result, extensive optimisation studies need to be carried out to find a well-suited and sophisticated analysis setup to extract the decay width

out of the given dataset and ease the effort of such a demanding measurement, which was one of the most relevant aspects of the analysis presented in this thesis.

The measurement is based on data which was recorded with the ATLAS detector at a centre-of-mass energy of $\sqrt{s} = 8$ TeV at the LHC in 2012 using proton-proton collision data. It is performed in the lepton+jets decay channel of $t\bar{t}$ events with one of the two top quarks decaying into a b quark and a W boson that decays further into two quarks, denoted as the hadronic decay branch, while the other top quark decays into a b quark and a W boson decaying further into a charged lepton, namely an electron or a muon, and the corresponding neutrino, representing the leptonic decay branch.
The decay width is determined using a template method. The required templates are generated with Monte Carlo simulations for signal and all background contributions except for multijet processes with misidentified leptons for which a data-driven method is exploited. In order to generate signal templates for different values of the top quark decay width, a reweighting method is applied. These templates enter a binned likelihood fit to data to measure the decay width. The fit is performed using templates of two different observables sensitive to the top quark decay width simultaneously. One observable is defined using the hadronically decaying top quark whereas the other depends on the leptonically decaying top quark kinematics to take advantage of the full information of $t\bar{t}$ events. The latter observable is the reconstructed invariant mass of the system formed by the b jet and the charged lepton ℓ from the leptonic top quark decay, $m_{\ell b}$. The other observable is the angular distance between the b jet j_b associated with the hadronic top quark and the closest light jet j_l from the hadronically decaying W boson, $\Delta R_{\text{min}}(j_b, j_l)$. These observables and the underlying quantities and angles are defined in detail in the upcoming chapters.
The input distributions used in the fit are split into two pseudorapidity regions to isolate a region which suffers less from detector resolution and pile-up effects. Pile-up effects refer to the effect of multiple pp interactions from the same or previous bunch crossings in the detector. The events are also split according to the charged lepton flavour (electron or muon) and, finally, split into events where exactly one or at least two jets are tagged as originating from a b quark. Thus, concatenated distributions composed of eight individual channels constitute the templates utilised in the binned likelihood fit. The fit and the entire analysis strategy are explained in the following chapters in more detail.

Before the main topic of this thesis can be thoroughly discussed, more fundamental aspects need to be delineated first. Chapter 2 contains an introduction into the Standard Model of Particle Physics followed by the presentation of some detailed information about top quarks and their properties with a particular focus on the decay width of the top quark. The LHC and the ATLAS detector including the most significant features of its subsystems are depicted in Chapter 3.
Chapter 4 serves to outline the reconstruction of physics objects used in the analysis whereas the dataset and the Monte Carlo generators employed to simulate signal and all background events are introduced in Chapter 5. In Chapter 6, fundamentals of the event selection and reconstruction, also covering studies on the agreement between data and prediction, are described. Special emphasis is

placed on different options and extensions of the tool used to reconstruct $t\bar{t}$ signal events. Chapter 7 gives a detailed description of the likelihood fit and the underlying machinery. This includes the definition of the observables sensitive to the top quark decay width, the template reweighting, the fit method validation and studies of fit configurations. Chapter 8 is devoted to the definition and evaluation of systematic uncertainties including studies which aimed at reducing dominant systematic uncertainties affecting the measurement. A dedicated observable comparison based on leading systematic effects is delineated in Chapter 9. The subsequent Chapter 10 contains the results of the analysis. Eventually, a summary of the performed measurement and a brief outlook are presented in Chapter 11.

Feynman diagrams used to illustrate various processes, especially in the following chapter, are drawn with the `tikzfeynman` package [16].

The following unit systems are used throughout the thesis: The familiar SI unit system with metres, kilograms and seconds is mainly employed in Chapter 3 to express various dimensions of the detector. Most other sections bear on the use of natural units according to $\hbar = c = 1$, with $\hbar$ as the reduced Planck constant and c as the speed of light. This implies that energies, masses and momenta are usually written in the unit of electron volt, eV, while time and length are given as 1/eV. Thus, also decay widths, which correspond to the inverse of the decay time in natural units, are expressed in units of eV.

2 The Standard Model and the Role of the Top Quark Therein

The Standard Model of Particle Physics, usually denoted as the Standard Model or abbreviated as SM, involves the top quark and predicts properties of this quark as they are presented in the context of this thesis. Hence, the fundamental principles and the theoretical framework of this model are outlined in the first part of this chapter. The top quark production channels, decay modes as well as properties of this quark are discussed in detail in the second part. Special emphasis is placed on the decay width of the top quark Γ_t as a direct measurement of this quantity is presented in this thesis. The corresponding sections also cover recent measurements of Γ_t as well as physics models beyond the SM (BSM) which predict deviations from the decay width value calculated within the Standard Model.

2.1 The Standard Model of Particle Physics

The Standard Model emerged from the 1960s and 1970s and characterises all known elementary particle interactions excluding gravity. Nowadays, no other theoretical framework allows for a more precise description of elementary particles, their interactions and properties which are measured to a high accuracy in a variety of experiments. The SM serves to describe two types of elementary particles, namely fermions (comprising the so-called quarks and leptons) and bosons including the so-called mediators or force carriers, referred to as gauge bosons. The following theories are incorporated in the SM: quantum electrodynamics (QED), the Glashow-Weinberg-Salam theory of electroweak (EW) processes [17–19] and quantum chromodynamics (QCD) [20–22].
All the different interactions between the initially massless quarks and leptons, whose masses are generated by the so-called Higgs mechanism [23, 24] complying with the laws of EW theory, are mediated by the gauge bosons. The relationship between this mechanism and another massive scalar elementary particle included in the SM, which is correspondingly called Higgs boson, is part of Sec. 2.1.2. Quantum mechanics and special relativity are incorporated into a quantum field theory based on the concept of gauge symmetry in order to describe the interactions between the SM particles. In this connection, the generalised formalism of Lagrangian mechanics is adapted to SM fields and particles, mathematically expressed by operators that are subject to a certain space-time point, while the Lagrangian density is a function of these fields and their space-time derivatives. As the SM rests on a combination of local gauge symmetries, it gives rise to conservation laws in compliance with Noether's theorem. These SM concepts are delineated in the following sections.

2.1.1 Quarks, Leptons and Mediators

Three kinds of elementary particles are differentiated by the Standard Model, as introduced in the last paragraph: *leptons*, *quarks* and *bosons*. The first two categories constitute spin-1/2-particles, the *fermions*, while the SM bosons, which carry integer spin, include the Higgs boson and gauge bosons, the latter also referred to as *mediators*.
Quarks and leptons are grouped into three *generations* having increasing masses. Each generation is composed of two out of the six existing lepton or quark "flavours", respectively. This scheme also describes antifermions with opposite quantum numbers, such as electric charge, but same mass as the corresponding fermion - on the assumption of *CPT* (*charge parity time*) conservation. The definition of leptons is based on the quantities: charge Q, electron number L_e, muon number L_μ and tau number L_τ. The six quark flavours are specified by charge, upness U, downness D, strangeness S, charmness C, bottomness B and topness T, related to the name of the quarks [25, 26].
All quarks and leptons form left-handed *doublets* but right-handed *singlets*, deduced by taking the concepts of chirality and handedness into account, resulting in three generations of left-handed leptons arranged as:

$$\begin{pmatrix} \nu_e \\ e \end{pmatrix}_L, \qquad \begin{pmatrix} \nu_\mu \\ \mu \end{pmatrix}_L, \qquad \begin{pmatrix} \nu_\tau \\ \tau \end{pmatrix}_L.$$

Hence, the lepton generations consist of an electrically neutral neutrino ν_i and a negatively charged lepton $\ell = e, \mu, \tau$ with $Q = -e$. The left-handed up-type quarks (u, c, t) with charge $Q = 2/3 \cdot e$ and the left-handed down-type quarks (d, s, b) with negative charge $Q = -1/3 \cdot e$ are written as:

$$\begin{pmatrix} u \\ d' \end{pmatrix}_L, \qquad \begin{pmatrix} c \\ s' \end{pmatrix}_L, \qquad \begin{pmatrix} t \\ b' \end{pmatrix}_L.$$

The (d', s', b') cited in the left-handed doublets constitute the weak eigenstates being different from the mass eigenstates which represent the quarks d, s and b. As these weak eigenstates are linear combinations of the mass eigenstates, the mixing of the three quark generations can be described by a 3×3 matrix, the Cabibbo-Kobayashi-Maskawa (CKM) matrix, denoted as V [27]:

$$\begin{pmatrix} d' \\ s' \\ b' \end{pmatrix} = V \cdot \begin{pmatrix} d \\ s \\ b \end{pmatrix} = \begin{pmatrix} V_{ud} & V_{us} & V_{ub} \\ V_{cd} & V_{cs} & V_{cb} \\ V_{td} & V_{ts} & V_{tb} \end{pmatrix} \cdot \begin{pmatrix} d \\ s \\ b \end{pmatrix}.$$

Given the unitarity of V, four parameters are sufficient to characterise this matrix, three real parameters, the mixing angles, and one imaginary phase factor, responsible for CP (*charge parity*) violation [28, 29]. Analogously, the Pontecorvo–Maki–Nakagawa–Sakata (PMNS) matrix [30, 31] is formulated for the lepton sector serving to mathematically describe neutrino oscillations.

The SM particles and their properties are listed in Table 2.1 [25, 28]. The *weak hypercharge* Y, defined as $Y = 2(Q - T_3)$, is also given. The values of the third component of the weak isospin T_3

explain the order of fermions in the doublets shown above.

Particles				Q [e]	C	s	T_3	Y
Leptons	$\begin{pmatrix} \nu_e \\ e \end{pmatrix}_L$	$\begin{pmatrix} \nu_\mu \\ \mu \end{pmatrix}_L$	$\begin{pmatrix} \nu_\tau \\ \tau \end{pmatrix}_L$	$\begin{pmatrix} 0 \\ -1 \end{pmatrix}$	-	$\frac{1}{2}$	$\begin{pmatrix} +\frac{1}{2} \\ -\frac{1}{2} \end{pmatrix}$	-1
	e_R	μ_R	τ_R	-1	-	$\frac{1}{2}$	0	-2
Quarks	$\begin{pmatrix} u \\ d' \end{pmatrix}_L$	$\begin{pmatrix} c \\ s' \end{pmatrix}_L$	$\begin{pmatrix} t \\ b' \end{pmatrix}_L$	$\begin{pmatrix} +\frac{2}{3} \\ -\frac{1}{3} \end{pmatrix}$	r,g,b	$\frac{1}{2}$	$\begin{pmatrix} +\frac{1}{2} \\ -\frac{1}{2} \end{pmatrix}$	$+\frac{1}{3}$
	u_R	c_R	t_R	$+\frac{2}{3}$	r,g,b	$\frac{1}{2}$	0	$+\frac{4}{3}$
	d_R	s_R	b_R	$-\frac{1}{3}$	r,g,b	$\frac{1}{2}$	0	$-\frac{2}{3}$
Gauge bosons	Photon γ			0	-	1	0	0
	Z^0			0	-	1	0	0
	$W^\pm$			± 1	-	1	± 1	0
	8 Gluons g			0	r,g,b	1	0	0
Higgs boson				0	-	0	$-\frac{1}{2}$	$+1$

Table 2.1: Particles and mediators in the Standard Model. Given are the particle properties electric charge Q, colour C, spin s, the third component T_3 of the weak isospin T as well as weak hypercharge Y [25, 28].

The quarks and their antiparticles, except for top quarks, as discussed in Chapter 2.2.3, form *hadrons* which are categorised into *mesons* carrying integer spin and *baryons* with an odd half-integral spin. *Confinement*, introduced in Section 2.1.2, causing the coupling strength to increase with distance, explains why quarks cannot act as free particles. Furthermore, quarks denote the only elementary particles that are able to interact via all fundamental forces of the Standard Model [25, 26].

The fermions cover a broad range of masses, shown in Table 2.2. The top quark mass is by far the largest, hinting at a possible special role in the framework of the Standard Model, which will be described more thoroughly in Section 2.2.

Lepton	Mass m in [MeV]	Quark	Mass m in [MeV]
e [32]	0.5109989461(31)	u [38, 39]	$2.2^{+0.6}_{-0.4}$
μ [33]	105.6583745(24)	c [40, 41]	1280 ± 30
τ [34]	1776.86(12)	t [42, 43]	173100 ± 600
ν_e [35]	$< 2 \cdot 10^{-6}$	d [38, 39]	$4.7^{+0.5}_{-0.4}$
ν_μ [36]	< 0.19	s [38, 39]	96^{+8}_{-4}
ν_τ [37]	< 18.2	b [44]	4180^{+40}_{-30}

Table 2.2: Masses of fermions according to [28]. More information concerning the top quark mass is given in Section 2.2.3. The values given for the neutrinos are not mass eigenstates. The listed references cite the discovery of the corresponding particle.

2.1.2 Interactions and the Higgs Mechanism

The mathematical foundations of the Standard Model regarding the three elementary particle interactions contained in the model, i.e. electromagnetic, weak and strong ones, is outlined in this subsection. Since the SM is a gauge theory, these interactions are characterised by local gauge symmetries implying that the Lagrangian is locally invariant under a transformation of a specific gauge group, denoted as *Lie group*. Two types of Lie groups are relevant for a description of the SM: unitary and special unitary Lie groups, abbreviated as U and SU. The number of generators of a group from the mathematical point of view conforms with the number of gauge fields associated with a certain interaction and amounts to n^2 (in case of a $U(n)$ group) or n^2-1 ($SU(n)$ group). The value of n^2-1 is consistent with the dimension of a group with order n.

Electroweak Theory

As the name indicates, the electroweak theory comprises a description of electromagnetic and weak processes. The former interactions are characterised by the unitary Abelian Lie group $U(1)_{\text{em}}$ with the phase transformation $\phi \rightarrow \phi' = e^{i\theta}\phi$ with a spinor field ϕ and a real number $\theta \in \mathbb{R}$. Weak interactions, on the contrary, are described by a $SU(2)$ group which is generated by the three *Pauli matrices* σ_i with $i = 1,2,3$. The underlying phase transformation for this interaction with the Pauli matrices is $\phi \rightarrow \phi' = e^{i\vec{\sigma}\cdot\vec{\alpha}}\phi$ with $\vec{\alpha} = (\alpha_1, \alpha_2, \alpha_3)$ where $\alpha_1, \alpha_2, \alpha_3 \in \mathbb{R}$. These two interactions are both combined to the symmetry group $SU(2)_L \otimes U(1)_Y$ by the electroweak theory, introduced by S. Glashow, A. Salam and S. Weinberg in the 1960s [17–19], due to their surnames also abbreviated as GSW or GWS theory. The above given indices are chosen because L implies that the weak isospin current couples only to left-handed fermions while Y represents the weak hypercharge, which is the generator of the group $U(1)_Y$, including the electromagnetic processes.
The following massless gauge fields are associated with $SU(2)_L \otimes U(1)_Y$: a single vector field B_μ (for $U(1)_Y$) which couples to the weak hypercharge current j^Y_μ with a strength commonly denoted as $\frac{g'}{2}$ and an isotriplet of vector fields W^i_μ (for $SU(2)_L$, indices $i = 1,2,3$ as above) with a coupling strength g and a weak isospin current J^i_μ. This results in the following expression for the basic EW interaction:

$$-i \cdot g(J^i)^\mu W^i_\mu - i \cdot \frac{g'}{2}(j^Y)^\mu B_\mu \,.$$

The mixing between the two groups $SU(2)_L$ and $U(1)_Y$ is described by an angle denoted as the *Weinberg angle* or *weak mixing angle* θ_W. The relationship between this angle and the coupling strengths can be expressed by either:

$$\sin\theta_W = \frac{g'}{\sqrt{g^2+g'^2}} \qquad \text{and} \qquad \tan\theta_W = \frac{g'}{g}\,.$$

The measured value amounts to $\sin^2\theta_W = 0.23129 \pm 0.00005$ [28] and relates the electromagnetic charge with the given coupling constants g and g': $e = g \cdot \sin\theta_W = g' \cdot \cos\theta_W$. Linear combinations

of the gauge fields lead to equations for the associated gauge bosons. Using the neutral fields W_μ^3 and B_μ, the following definitions for the neutral gauge bosons, γ and Z^0, as the mediators of the neutral currents of electromagnetism and weak interactions, respectively, can be obtained using a matrix containing solely the mixing angles:

$$\begin{pmatrix} A_\mu \\ Z_\mu \end{pmatrix} = \begin{pmatrix} \cos\theta_W & \sin\theta_W \\ -\sin\theta_W & \cos\theta_W \end{pmatrix} \begin{pmatrix} B_\mu \\ W_\mu^3 \end{pmatrix},$$

which leads to the two separate equations:

$$\begin{aligned} A_\mu &= \quad B_\mu \cos\theta_W + W_\mu^3 \sin\theta_W \qquad (\text{boson } \gamma), \\ Z_\mu &= -B_\mu \sin\theta_W + W_\mu^3 \cos\theta_W \qquad (\text{boson } Z^0). \end{aligned}$$

The two remaining fields W_μ^1 and W_μ^2 are used to define the two charged bosons as:

$$W_\mu^\pm = \sqrt{\frac{1}{2}}(W_\mu^1 \mp i \cdot W_\mu^2) \qquad (\text{charged bosons } W^\pm).$$

The full Lagrangian of the electroweak theory has the following form:

$$\begin{aligned} \mathscr{L}_{\text{EW}} = &-\frac{1}{4} W_{\mu\nu}^i W_i^{\mu\nu} - \frac{1}{4} B_{\mu\nu} B^{\mu\nu} \\ &+ \overline{L}\gamma^\mu (i\partial_\mu - g\frac{\sigma_i}{2} W_\mu^i - \frac{g'}{2} Y B_\mu) L + \overline{R}\gamma^\mu (i\partial_\mu - \frac{g'}{2} Y B_\mu) R. \end{aligned}$$

The interactions between the gauge fields themselves are described by the first two terms, the two remaining terms characterise the interactions between the particles that are mediated by the corresponding gauge bosons. According to their abbreviation, L and R as wave functions signify a left-handed fermion doublet and a right-handed fermion singlet of fermion spinors.
The vertex for the weak interaction has a vector-axial vector (V-A) structure which mathematically expresses the parity violation of the weak interaction.
All four gauge bosons described by the electroweak theory are obtained from linear combinations of massless gauge fields. Hence, the gauge bosons are massless in this model which is in contradiction to experiments which have proven the massiveness of the three bosons $W^\pm$ and Z^0 (commonly the simpler notation W and Z is used). These massive gauge bosons indicate the symmetry breaking of the $SU(2)_L \otimes U(1)_Y$ group, and thus the electroweak model needs to be extended.

Higgs Mechanism

This extension is realised by the Higgs mechanism with the so-called Higgs boson. This mechanism explains how particle masses are generated in a gauge invariant way [23, 24].
A first naive approach based on adding explicit mass terms for the massive gauge bosons W and Z to the Lagrangian would violate gauge invariance and lead to unrenormalisable divergences. The massive gauge boson masses, however, can be incorporated by spontaneous symmetry breaking

of the vacuum ground state which keeps the Lagrangian gauge invariant. For this purpose, four real scalar fields ϕ_k are defined which are elements of $SU(2) \otimes U(1)$ and integrated into an isospin doublet with weak hypercharge $Y = 1$ as follows:

$$\phi = \begin{pmatrix} \phi^+ \\ \phi^0 \end{pmatrix} \qquad \text{with} \qquad \begin{aligned} \phi^+ &= (\phi_1 + i\phi_2)/\sqrt{2}, \\ \phi^0 &= (\phi_3 + i\phi_4)/\sqrt{2}. \end{aligned}$$

A coupling of this complex scalar doublet to the gauge bosons, which is responsible for the symmetry breaking as shown later, results in an additional gauge invariant Lagrangian:

$$\mathscr{L}_{\text{Higgs}} = (D_\mu \phi)^\dagger (D^\mu \phi) - V(\phi^\dagger \phi),$$

with a covariant derivative D_μ. The term $V(\phi^\dagger \phi)$ constitutes the most general renormalisable potential, the Higgs potential, depending only on the combination $\phi^\dagger \phi$ and defined by the choice of the parameters μ and λ:

$$V(\phi^\dagger \phi) = \mu^2 \phi^\dagger \phi + \lambda (\phi^\dagger \phi)^2 .$$

The parameter v represents the vacuum expectation value and is, in case of $\mu^2 < 0$ and $\lambda > 0$, given by $v^2 = -\mu^2/\lambda$. The choice of the ground state $\phi_0(v)$, depending on v, is arbitrary. An appropriate option with $\phi_1 = \phi_2 = \phi_4 = 0$ and $\phi_3 = v$ yields:

$$\phi_0(v) = \frac{1}{\sqrt{2}} \begin{pmatrix} 0 \\ v \end{pmatrix}, \tag{2.1}$$

which is invariant with respect to the underlying $U(1)_{\text{em}}$ symmetry. For the scalar Higgs $SU(2)$ doublet, an expansion around the ground state yields:

$$\phi(x) = \frac{1}{\sqrt{2}} \begin{pmatrix} 0 \\ v + H(x) \end{pmatrix}.$$

The $SU(2)_L \otimes U(1)_Y$ symmetry is spontaneously broken by using the vacuum state defined in Eq. (2.1) if $v \neq 0$. As the $U(1)_{\text{em}}$ symmetry is still kept, the photon remains massless as desired. This spontaneous symmetry breaking gives rise to the creation of a real massive boson, identified with the Higgs boson, having spin 0 and a mass of $m_H^2 = 2v^2\lambda$. Based on the mathematical terms and assumptions shown above, the final Lagrangian of the Higgs fields contains, apart from a kinetic part, mass terms for the bosons including the Higgs, terms for trilinear (HW^+W^- and HZZ) and quartic (HHW^+W^- and $HHZZ$) couplings, as well as terms for the Higgs self-coupling.
The masses which the gauge bosons acquired by the Higgs mechanism are:

$$m_W = \frac{1}{2} v g \qquad \text{and} \qquad m_Z = \frac{1}{2} v \sqrt{g^2 + g'^2},$$

in terms of the vacuum expectation value v. The photon mass is zero, $m_\gamma = 0$, as described

above. The vacuum expectation value is related to the Fermi coupling constant G_F via $v = 1/\sqrt{\sqrt{2}G_F} \approx 246.2$ GeV. The current world average of the Higgs boson mass amounts to $m_H = 125.09 \pm 0.21\,(\text{stat.}) \pm 0.11\,(\text{syst.})$ GeV [28]. The value of the Higgs mass is not predicted by this theory before due to the fact that the parameters μ and λ were unknown.
The Higgs mechanism also generates the masses of fermions whose couplings to the Higgs field are described by the Yukawa coupling y_f. The mathematical expression is obtained after adding the required corresponding term to the Standard Model Lagrangian, resulting in the relationship:

$$m_f = \frac{1}{\sqrt{2}} v y_f \,,$$

indicating a direct proportionality between fermion mass and Yukawa coupling since v is a constant. Hence, the top quark as the fermion with the highest mass, see Table 2.2, has the largest coupling to the Higgs field compared to all other fermions: $y_t \approx 1$.

Quantum Chromodynamics

The third interaction, the strong one, is described by quantum chromodynamics using the non-Abelian symmetry group $SU(3)_C$. The matrices $T_a = \lambda_a/2$ based on the eight *Gell-Mann matrices* λ_a, with $a = 1, 2, ..., 8$, serve as generators of this group. The phase transformation is $q \rightarrow q' = \mathrm{e}^{\mathrm{i}\alpha_a T_a} q$ with the group parameters α_a and the quark field q. Eight gluon fields G^a_μ for the eight massless gluons as mediators of the strong interaction need to be distinguished. They carry colour charge themselves, the quantum number of the strong interaction, which is labelled as C, being the index of the group definition. The colour states red, blue and green with corresponding anticolours exist. Merely colourless bound states are invariant under $SU(3)_C$ transformations. The full QCD Lagrangian containing the gluon fields, the mass m for a quark, the coupling constant $g_s = \sqrt{4\pi\alpha_s}$ and the quark field can be written in the following form:

$$\mathscr{L}_{\text{QCD}} = \bar{q}(i\gamma^\mu \partial_\mu - m)q - g_s \bar{q}\gamma^\mu T_a q G^a_\mu - \frac{1}{4} G^a_{\mu\nu} G^{\mu\nu}_a \,.$$

The given $G^a_{\mu\nu}$ constitute field strength tensors including a term for the self-interaction between the gauge bosons as carriers of the colour charge:

$$G^a_{\mu\nu} = \partial_\mu G^a_\nu - \partial_\nu G^a_\mu - g_s f_{abc} G^b_\mu G^c_\nu \,,$$

with the structure constant f_{abc} providing a relationship between the generator matrices: $[T_a, T_b] = i f_{abc} T_c$.

In contrast to all other fundamental forces, the strong force increases with distance and decreases with smaller scales and higher energies, respectively. Thus, α_s as a measure of the coupling strength cannot be regarded as a constant. It depends on the energy scale of the physical process, as additional internal loops affect its value. Consequently, to take these higher order corrections into account, α_s is defined at a certain energy scale, a *renormalisation scale* μ_R, resulting in an effective

coupling. The following relationship between α_s and an energy scale Q^2 using the renormalisation scale μ_R^2 holds:

$$\alpha_s(Q^2, \mu_R^2) = \frac{\alpha_s(\mu_R^2)}{1 + \alpha_s(\mu_R^2)\frac{11n_C - 2n_f}{12\pi}\ln(\frac{Q^2}{\mu_R^2})} .$$

The parameter n_f defines the number of active quark flavours f and n_C the number of colours C. This formula describes the behaviour of the strong interaction at small and large scales, as depicted above.

For smaller energies $Q^2 \to 0$ which corresponds to increasing distances, α_s increases as well. Due to this effect, called *quark confinement*, free quarks, i.e. those outside of bound states, are not observed in nature. As a result, the creation of a quark pair having opposite colour charge is energetically preferred at high energies, in contrast to a separation of quarks. Thus, new bound states arise containing the original two quarks. Quark confinement is therefore the explanation for the formation of jets of hadrons diverging from the collision point when quarks are produced in such high energy collisions. As already mentioned, top quarks play a special role and cannot be observed in bound states, which is delineated in more detail in the next subsection.
On the other hand, for larger energies $Q^2 \to \infty$, i.e. smaller distances close to zero, α_s decreases and reaches zero asymptotically. Consequently, quarks in these extreme cases can be regarded as free quarks which is why QCD in the Standard Model is described as *asymptotically free* [25, 45].

Summary of Standard Model Interactions

In summary, the electroweak as well as the strong interactions can be joined together to form the *Standard Model Symmetry Group*:

$$SU(3)_C \otimes SU(2)_L \otimes U(1)_Y .$$

The different mediators of these interactions and their properties with additional information about the type of interaction are summarised in Table 2.3.

The Standard Model incorporates in total 18 different parameters whose values cannot be predicted by theory but have to be measured by experiments: the six masses of the quarks and the three masses of the charged leptons, the three mixing angles and the complex phase of the CKM matrix, the three couplings for the three SM gauge groups $U(1)_Y$, $SU(2)_L$ and $SU(3)_C$, the Higgs boson mass and the vacuum expectation value v.

Force	Strong	Electromagnetic	Weak
Theory	Chromodynamics	Electrodynamics	Flavourdynamics
Mediator	Gluon [46, 47]	Photon [48, 49]	W,Z [50–53]
Electric charge [e]	0	0	$Q_W = \pm 1$ $Q_Z = 0$
Colour	8 combinations	-	-
Coupling constant	$\alpha_s(m_Z) \approx 0.1181$	$\alpha_{\text{em}} \approx 0.0073$	$\alpha_w \approx 0.0316$
Mass [GeV] of mediators	0	0	$m_W = 80.385 \pm 0.015$ $m_Z = 91.1876 \pm 0.0021$

Table 2.3: The three fundamental forces incorporated in the Standard Model and their properties [25, 28]. The variables Q_W and Q_Z refer to the electric charge and m_W and m_Z to the masses of the massive bosons. The coupling constants α_i and g_i for the forces i are related to each other [45]. The given references cite the discovery of the corresponding particle.

All these predictions of the Standard Model have been tested to a very good level of accuracy over the last years, and the SM could meet every experimental observation in the past decades making it to one of the most successful theories in history. Nevertheless, despite the successful validation so far, the SM cannot be regarded as a complete theory, and a number of shortcomings need to be understood.

Gravity as the fourth fundamental force is not included in the SM and is solely described by the theory of general relativity developed by A. Einstein. The SM does not consider non-zero neutrino masses whereas these masses are implied by the existence of neutrino flavour oscillations [54–56]. Furthermore, the SM does not contain dark matter or dark energy, which form around 95% of the mass of the entire universe. In other words, merely 5% of the known amount of mass are made of matter described by the Standard Model.
Apart from that, the relatively large amount of free SM parameters listed above may hint at the existence of a more fundamental theory which contains the SM as an effective low-energy approximation. The SM is furthermore not able to explain the baryon-antibaryon asymmetry, i.e. the imbalance between the baryonic and the antibaryonic matter observable in our universe.

In the past years, various theories emerged which aim at resolving these problems of the Standard Model, predicting new particles or new types of interactions. Those theories involve supersymmetry, further dimensions or, for example, technicolor models. Some of these theories provide predictions for the effect on SM parameters and values like the top quark decay width, which is further discussed in Ch 2.3.3.

2.2 The Top Quark

The existence of the top quark was proposed more than two decades before its experimental discovery. In order to explain the observation of CP violation [57] in 1964, Kobayashi and Maskawa proposed a third quark generation [27] which resulted in their formulation of a three-dimensional quark mixing matrix, the CKM matrix, as introduced in Sec. 2.1.1, in 1973. Four years later, the existence of the b quark as the first third generation quark was experimentally confirmed by the E288 experiment at Fermilab [44] with the discovery of the Υ meson, a meson which is composed of a b and a $\bar{b}$ quark. Hence, a weak isospin partner of the bottom quark to form the third quark generation was required and an almost two-decade period of searches began to find this quark, the so-called top quark. The search finally succeeded at the Tevatron collider in 1995. Since the top quark is not only the heaviest quark but even the heaviest SM particle ($m_t > m_H > m_Z > m_W$), the top quark could only be observed with the high collision energies reached at the Tevatron.

The top quark was discovered in $t\bar{t}$ production by both the CDF and DØ experiment at Tevatron Run I, which operated at a centre-of-mass energy of $\sqrt{s} = 1.8$ TeV at the time using proton-antiproton $p\bar{p}$ collisions [42, 43]. Another 14 years later, the observation of electroweak production of single top quarks was confirmed by the CDF and DØ collaborations based on data taken at the Tevatron in Run II at $\sqrt{s} = 1.96$ TeV [58, 59]. The start of the LHC in 2008 marked the beginning of a new era of experimental top quark physics as top quarks are produced abundantly at the high centre-of-mass energies of the LHC. During Run I of the LHC, which includes the data-taking periods at $\sqrt{s} = 7$ TeV and $\sqrt{s} = 8$ TeV, more than ten million top quark events were produced at the two multipurpose detectors of the LHC, ATLAS and CMS, together. Such large amounts of data allowed for the realisation of many precision measurements in the field of top quark physics and the improvement of the Tevatron results. Efforts for measuring top quark properties in more detail are still very important since the heaviest quark, due to its large mass, is expected to play a distinct role in electroweak symmetry breaking mechanisms, as described in Sec. 2.1.2, and to provide a sign of new physics beyond the SM.

Before the top quark properties are presented in more detail, production mechanisms and decay modes of the top quark are described in the next subsections. Theoretical concepts like the QCD factorisation theorem or parton distribution functions are discussed as well. The chapter concludes with a section about the top quark decay width, the property of the top quark which is measured in the context of this thesis. Emphasis is placed on theoretical aspects of the decay width, recently published top quark decay width measurements and BSM theories which predict decay width values that differ from Standard Model expectations.

2.2.1 Top Quark Production

Two production mechanisms of top quarks exist at hadron colliders like the Tevatron and the LHC: electroweak production of single top quarks or top quark pair ($t\bar{t}$) production via the strong interaction - whereby the latter process occurs much more frequently. Electroweak production of $t\bar{t}$ pairs is negligible at hadron colliders and thus not considered here. Before these mechanisms are discussed, the QCD factorisation theorem is introduced in the following.

Top Quark Production: The QCD Factorisation Theorem

Top quark pair production at high energies via proton-antiproton $p\bar{p}$ (at the Tevatron) or proton-proton pp (at the LHC) collisions can be described by perturbative quantum chromodynamics (pQCD). Such hard scattering processes originate from the interactions between the constitutents of the two colliding hadrons, namely quarks and gluons, which are summarised by the term parton in the following. The subsequent paragraph describes the determination of the $t\bar{t}$ cross-section. The probability density to observe a parton i having a momentum fraction x_i at momentum transfer Q^2 within a hadron is mathematically expressed by parton distribution functions, abbreviated as PDFs, $f_i(x_i, Q^2)$ [60–62]. Such a ratio x of the parton momentum to the total momentum is often also referred to as Bjorken-x. Quark and gluon PDFs, however, cannot be directly predicted a-priori by means of QCD. So-called DGLAP equations [60–62], short for Dokshitzer-Gribov-Lipatov-Altarelli-Parisi, fulfil the purpose of describing the evolution of the PDF $f_i(x_i, Q^2)$ for a fixed value of x_i. These PDFs serve to calculate the cross-section of top quark events, here shown as an example for $t\bar{t}$ pairs. In the next step, the cross-section of two incoming and colliding partons i and j, denoted as $\hat{\sigma}^{ij\to t\bar{t}}$, is convolved with the PDFs f_i and f_j, evaluated at an energy scale, called factorisation scale $Q^2 = \mu_F^2$. This scale μ_F and the renormalisation scale, as introduced in Sec. 2.1.2, are set to a value that reflects the energy scale of the analysed process; in case of top quark events, the top quark mass is a common and reasonable choice: $m_t = \mu_F = \mu_R$. Therefore, one can derive the $t\bar{t}$ cross-section for proton-proton collisions at the LHC given the centre-of-mass energies of the pp collision $\sqrt{s}$ and of the parton-parton collision $\sqrt{\hat{s}}$ [63]:

$$\sigma^{pp\to t\bar{t}}(\sqrt{s}, m_t) = \sum_{i,j=g,q,\bar{q}} \int \mathrm{d}x_i \mathrm{d}x_j f_i(x_i, \mu_F^2) f_j(x_j, \mu_F^2) \cdot \hat{\sigma}^{ij\to t\bar{t}}(m_t, \sqrt{\hat{s}}, x_i, x_j, \alpha_s(\mu_R^2), \mu_R^2)\,.$$

A general expression of this term is *QCD factorisation theorem* as already indicated by the title of this paragraph. The name originates from the *factorisation* of the production process ($pp \to t\bar{t}$ here) into two components: The cross section of the hard interaction process ($ij \to t\bar{t}$) and the PDFs of the two participating partons in the initial state i and j. It is the theoretical basis for cross-section calculations and cross-section measurements of top quarks as described in the next subsections.

Top-Antitop Quark Pairs

Pairs of top-antitop quarks are produced via the strong interaction by two different processes, either $q\bar{q}$ annihilation with a quark q and an antiquark $\bar{q}$ or gg fusion. For the latter process, $gg \to t\bar{t}$, three leading order (LO) Feynman diagrams exist whereas one Feynman diagram visualises the reaction $q\bar{q} \to t\bar{t}$, as illustrated in Fig. 2.1.

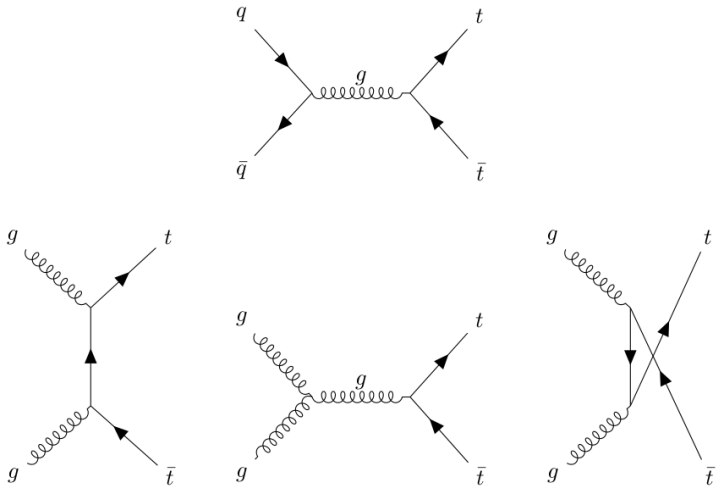

Figure 2.1: Feynman diagrams for $t\bar{t}$ production via the strong interaction at lowest order. Depicted are the diagrams of both $q\bar{q}$ annihilation (top) and gluon fusion (bottom).

With a rising energy of the colliding particles, i.e. the centre-of-mass energy of the corresponding hadron collider, the cross-section of top quark production processes increases. This dependence of the cross-section for various important physics processes as a function of the centre-of-mass energy is visualised in Fig. 2.2. The cross-section for top quarks given in that figure contains not only $t\bar{t}$ production but also single top production. The curve indicates that the production cross-section at the design centre-of-mass energy of the LHC exceeds the value corresponding to the Tevatron collider significantly by around two orders of magnitude. This results in a huge amount of events involving top quarks which can be acquired by the LHC experiments. The cross-sections of other Standard Model processes increase with higher energies as well, though, these are considerably larger than the one of top quarks. Some of those events constitute important backgrounds of processes comprising top quarks, as described later in Sec. 2.2.2. The $t\bar{t}$ production also increases at the LHC, which is a pp accelerator in contrast to the Tevatron that collided p with $\bar{p}$.
Theoretical calculations of the total production cross-section $\sigma_{t\bar{t}}$ of top quark pairs at the precision of full next-to-next-to-leading order (NNLO) which include soft gluon resummation at next-to-next-to-leading logarithmic (NNLL) order are available [64–68]. The latest calculations rely on a top quark mass of $m_t = 172.5$ GeV and the MSTW2008 68% CL NNLO PDF set [69, 70], using the `top++ 2.0` programme [71] for the evaluation. The following results are obtained for various centre-of-mass energies: The full NNLO calculation for $t\bar{t}$ production at the Tevatron at $\sqrt{s} = 1.96$ TeV assuming a top quark mass of $m_t = 173.3$ GeV is $7.16^{+0.20}_{-0.23}$ pb. The measured result for the LHC at $\sqrt{s} = 8$ TeV,

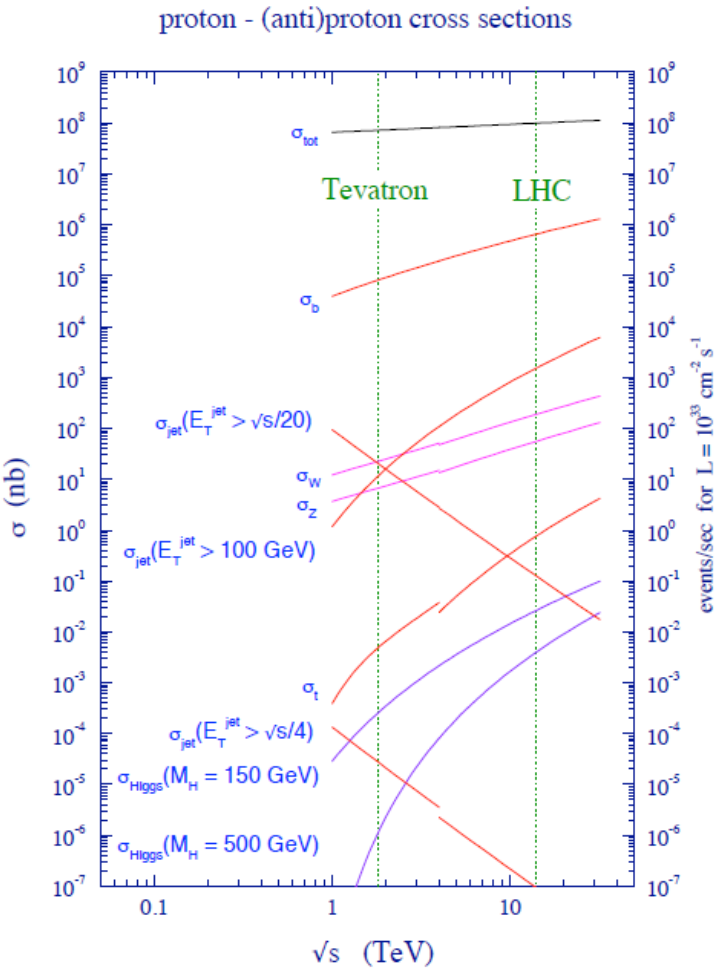

Figure 2.2: Cross-sections (left axis) as well as events per second (right axis) of different important physics processes in $p\bar{p}$ and pp collisions at the Tevatron and the LHC. The additional two vertical lines correspond to the Run II centre-of-mass energy at the Tevatron collider and to the design centre-of-mass energy of $\sqrt{s} = 14$ TeV at the LHC, respectively. The given curve for top quark production labelled as σ_t comprises $t\bar{t}$ as well as single top quark production. According to the colliding particles used at the Tevatron and the LHC, the cross-sections shown at lower energies refer to $p\bar{p}$ collisions while the ones at higher energies are based on pp collisions. The curve for top quark production reveals a step exactly at the transition between the two regions for $p\bar{p}$ and pp collisions at $\sqrt{s} = 4$ TeV which arises because valence quarks instead of sea quarks - which are less likely to occur - contribute to $q\bar{q}$ annihilation in $p\bar{p}$ collisions leading to the small dip at $\sqrt{s} = 4$ TeV when switching to a pp collider [72].

the centre-of-mass energy on which the measurement presented in this thesis is based, amounts to 253^{+15}_{-16} pb. A calculation at $\sqrt{s} = 13$ TeV, at which the LHC currently operates in Run II, yields 832^{+40}_{-46} pb, both evaluated for a top quark mass of $m_t = 172.5$ GeV according to [64–68].

The two different production mechanisms of $t\bar{t}$ pairs, $q\bar{q}$ annihilation and gluon fusion, have different contributions to the full production cross-section for different collider types ($p\bar{p}$ or pp) and varying centre-of-mass energies, discussed here in more detail. At a fixed value of $\sqrt{s}$, a certain parton momentum fraction x as defined at the beginning of Sec. 2.2.1, is required to produce a $t\bar{t}$ pair. The values of the parton density distributions f of quarks as well as gluons rise with smaller and smaller fractions x where the parton densities for gluons grow faster than the ones of quarks. Hence, not only the entire production cross-section of $t\bar{t}$ pairs increases but also the PDF values for quarks are dominated by those for gluons with larger centre-of-mass energies. This explains the main $t\bar{t}$ production differences between the Tevatron and the LHC. While $q\bar{q}$ annihilation predominates at the Tevatron, gg fusion is the dominant production process of top quark pairs at the LHC with its larger centre-of-mass energy. In addition to that, the antiquark $\bar{q}$ required in the initial state of $q\bar{q}$ annihilation may be a valence quark of the antiproton as part of a $p\bar{p}$ collision whereas it must be a sea quark at the pp collider LHC. Independent of the centre-of-mass energy, valence quarks occur much more frequently than sea quarks, leading to a further suppression of $q\bar{q}$ annihilation at a pp collider in comparison to a $p\bar{p}$ collider like the Tevatron [73, 74]. These PDFs are shown in Fig. 2.3 as a function of the momentum fraction x. They reflect the behaviour of the gluon functions exceeding the different quark PDFs at small x whereas at very large momentum fractions the shown up and down quark functions from the proton are larger than the gluon one.
At Run II of the Tevatron at $\sqrt{s} = 1.96$ TeV, 86.3% of all top quark pairs were produced via $q\bar{q}$ annihilation and 13.7% via gluon fusion. On the contrary, at the LHC design centre-of-mass energy of $\sqrt{s} = 14$ TeV, about 90.7% of all $t\bar{t}$ pairs are expected to originate from gluon fusion and merely 9.3% from quark-antiquark annihilation. Gluon fusion dominates over the $q\bar{q}$ annihilation with a ratio amounting to around 85.1% to 14.9% [75] at a centre-of-mass energy of $\sqrt{s} = 8$ TeV.

Various measurements of the $t\bar{t}$ production cross-section with the ATLAS detector at $\sqrt{s} = 8$ TeV were performed in the last few years. A measurement in the dilepton channel resulted in $\sigma_{t\bar{t}} = 242.4 \pm 1.7\,(\text{stat.}) \pm 5.5\,(\text{syst.}) \pm 7.5\,(\text{lumi.})$ pb [76], one using the lepton+jets decay channel in: $\sigma_{t\bar{t}} = 260 \pm 1\,(\text{stat.})^{+22}_{-23}\,(\text{syst.}) \pm 4\,(\text{lumi.})$ pb [77]. The recently published measurement on τ+jets final states yielded $\sigma_{t\bar{t}} = 239 \pm 4\,(\text{stat.}) \pm 28\,(\text{syst.}) \pm 5\,(\text{lumi.})$ pb [78].
A combination of ATLAS and CMS $t\bar{t}$ cross-section measurements using the dilepton decay channel led to: $\sigma_{t\bar{t}} = 241.5 \pm 1.4\,(\text{stat.}) \pm 5.7\,(\text{syst.}) \pm 6.2\,(\text{lumi.})$ pb [79], at the same centre-of-mass energy. All the shown results are fully consistent with the SM prediction.
Since 2015, the LHC runs at a centre-of-mass energy of $\sqrt{s} = 13$ TeV revealing much larger cross-section values. The most precise measurement performed by the ATLAS experiment focussing on dileptonic $e\mu$ events yielded: $\sigma_{t\bar{t}} = 818 \pm 8\,(\text{stat.}) \pm 27\,(\text{syst.}) \pm 19\,(\text{lumi.})$ pb [80].
These measurements along with other $t\bar{t}$ production cross-section measurements are visualised in Fig. 2.4 and compared to theory predictions. The plot shows that the measured values are in good

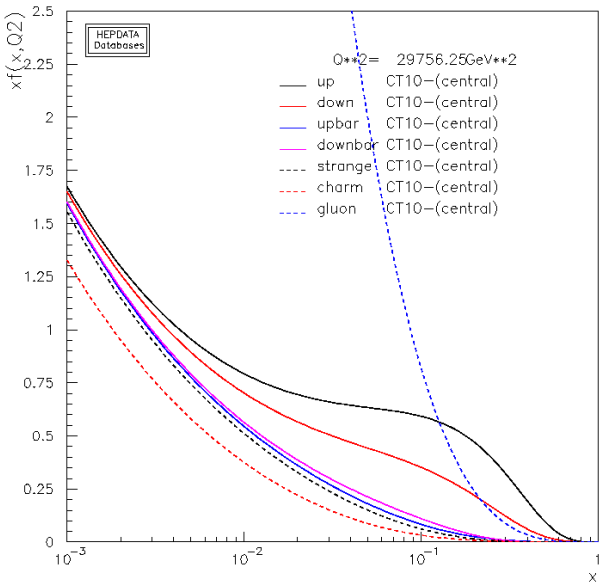

Figure 2.3: Different parton distribution functions (PDFs) for protons at the scale $Q^2 = m_t^2$ with a top quark mass of $m_t = 172.5$ GeV based on the CT10 PDF set [81], complying with the set employed for the generation of the Monte Carlo signal sample used in this measurement. The plot is produced with a tool available at [82].

agreement with the curve obtained from theory [68].

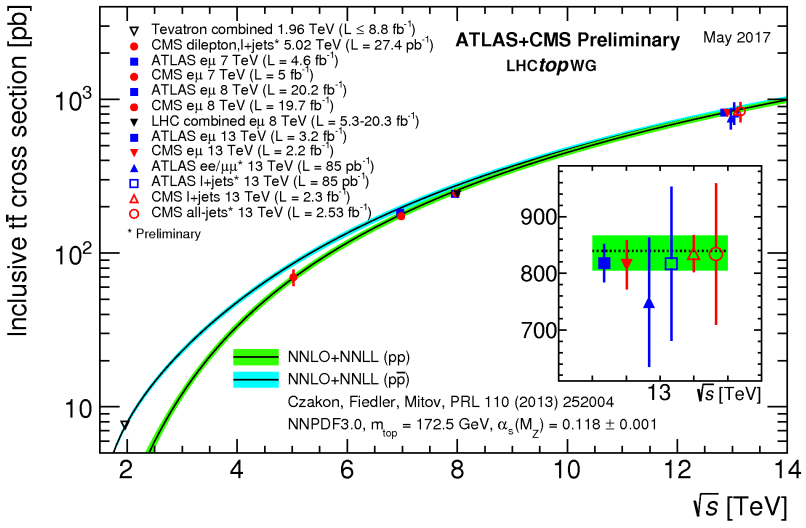

Figure 2.4: Summary of $t\bar{t}$ production cross-section measurements [76, 79, 80, 83–89] performed at the Tevatron and the LHC at different centre-of-mass energies [90]. The theory curve is based on [68].

Single Top Quarks

Single top quarks are produced through the weak interaction. Due to the virtuality of the exchanged boson, three instead of two production processes for single top quarks can be distinguished, whose fundamental leading order Feynman diagrams are displayed in Fig. 2.5. The W boson acts as mediator in the t- and s-channel where thus a virtual W boson is exchanged, shown in Fig. 2.5a and Fig. 2.5b, respectively, while the Wt production channel describes the associated production of an on-shell W boson and a single top quark, as visualised in Fig. 2.5c. The t-channel process constitutes the predominant production mechanism of single top quarks, followed by the Wt production. The s-channel Drell-Yan type production, on the contrary, contributes only to a small extent to the entire single top cross-section.

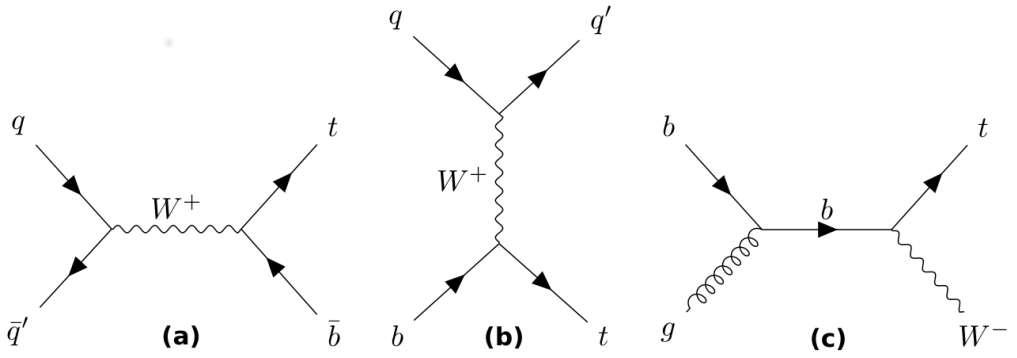

Figure 2.5: Single top quark production via the weak interaction. The LO Feynman diagrams of (a) s-channel production, (b) t-channel production and (c) associated Wt production are presented.

Calculations at next-to-leading order (NLO) QCD with NNLL soft gluon corrections are exploited to estimate the production cross-sections of the three processes drawn in Fig. 2.5 depending on the assumed top quark mass [91–96]. Results for all three production processes are listed in Table 2.4 for different centre-of-mass energies in accordance with former and current accelerator setups.

The tabulated values reveal that the sum of all three individual production mechanisms of single top quarks leads to total cross-section values which reach, depending on the centre-of-mass energy, up to approximately one third or even one half of the theory prediction of the total $t\bar{t}$ cross-section, as given in the last subsection. Both single top and $t\bar{t}$ production are of the same order of magnitude. But single top quarks were only observed several years after the discovery of the top quark in $t\bar{t}$ production because isolating a single top event from background processes is more demanding than for $t\bar{t}$ events as fewer jets occur in those events. The values for the s- and t-channel production processes listed in Table 2.4 underline furthermore that more top quarks than antitop quarks are produced at the LHC as it is a proton-proton collider meaning that antitop quarks solely originate from sea quarks.

Production process:		t-channel		Wt		s-channel	
$\sqrt{s}$ [TeV]	Collider	σ_t [pb]	$\sigma_{\bar{t}}$ [pb]	σ_t [pb]	$\sigma_{\bar{t}}$ [pb]	σ_t [pb]	$\sigma_{\bar{t}}$ [pb]
1.96	Tevatron	$1.04^{+0.06}_{-0.07}$		-		$0.52^{+0.03}_{-0.03}$	
8	LHC	$54.9^{+2.3}_{-1.9}$	$29.7^{+1.7}_{-1.5}$	22.4 ± 1.5		3.75 ± 0.15	1.90 ± 0.08
13	LHC	$136.0^{+5.4}_{-4.6}$	$81.0^{+4.1}_{-3.6}$	71.7 ± 3.9		$7.07^{+0.27}_{-0.26}$	$4.10^{+0.15}_{-0.17}$

Table 2.4: Predictions for single top quark production cross-sections σ for different centre-of-mass energies and corresponding colliders obtained from [91–96]. Values for all three production mechanisms, as shown in Fig. 2.5, are presented. In particular older Tevatron predictions are based on a top quark mass of $m_t = 173.3$ GeV while LHC predictions which are compared to recent ATLAS and CMS measurements in the following assume a top quark mass of $m_t = 172.5$ GeV. The t- and s-channel production cross-sections are symmetric for top and antitop quarks at the $p\bar{p}$ collider Tevatron. The Wt cross-section at the LHC is symmetric as well because this process does not depend on the type (particle or antiparticle) of the underlying proton.

The t-channel production rate was determined by the Tevatron soon after the observation of single top quark processes [97, 98], the s-channel production process was measured at the Tevatron a few years later [99] whereas Wt production was first observed at the LHC [100, 101].
All three single top production processes were measured with the ATLAS detector at $\sqrt{s} = 8$ TeV in the past. The resulting numbers are summarised in Table 2.5.

ATLAS, $\sqrt{s} = 8$ TeV	Cross-section σ [pb]
t-channel, σ_t	$56.7 \pm 0.9\,(\text{stat.})^{+4.1}_{-3.5}\,(\text{syst.}) \pm 1.1\,(\text{lumi.})$ [102]
t-channel, $\sigma_{\bar{t}}$	$32.9 \pm 0.8\,(\text{stat.})^{+2.9}_{-2.6}\,(\text{syst.}) \pm 0.6\,(\text{lumi.})$ [102]
Wt	$23.0 \pm 1.3\,(\text{stat.})^{+3.2}_{-3.5}\,(\text{syst.}) \pm 1.0\,(\text{lumi.})$ [103]
s-channel	$4.8 \pm 0.8\,(\text{stat.})^{+1.6}_{-1.3}\,(\text{syst.})$ [104]

Table 2.5: Measurements of single top quark production cross-sections σ performed with the ATLAS detector at a centre-of-mass energy of $\sqrt{s} = 8$ TeV, which is also used in the analysis presented in this thesis. References to corresponding publications are given as well.

For this centre-of-mass energy, also combinations of ATLAS and CMS results exist in the Wt- and t-channel. The combined measurement yielded $\sigma_{t-\text{ch.}} = 85 \pm 4\,(\text{stat.}) \pm 11\,(\text{syst.}) \pm 3\,(\text{lumi.})$ pb [105] for t-channel production (including top and antitop quark events) and $\sigma_{Wt} = 23.1 \pm 1.1\,(\text{stat.}) \pm 3.3\,(\text{syst.}) \pm 0.8\,(\text{lumi.})$ pb [106] for Wt production. These two production processes were also recently measured by the ATLAS collaboration at $\sqrt{s} = 13$ TeV resulting in a t-channel production cross-section for top quarks of $\sigma_{t-\text{ch.},t} = 156 \pm 5\,(\text{stat.}) \pm 27\,(\text{syst.}) \pm 3\,(\text{lumi.})$ pb, for antitop quarks of $\sigma_{t-\text{ch.},\bar{t}} = 91 \pm 4\,(\text{stat.}) \pm 18\,(\text{syst.}) \pm 2\,(\text{lumi.})$ pb [107] and in a Wt production cross-section of $\sigma_{Wt} = 94 \pm 10\,(\text{stat.})^{+28}_{-22}\,(\text{syst.}) \pm 2\,(\text{lumi.})$ pb [108]. All the listed results are in good agreement with the predictions from theory listed in Table 2.4.

2.2.2 Top Quark Decay

After the description of possible production mechanisms of top quarks, the decay of the heaviest SM elementary particle, which is less diverse than top quark production, is outlined in this section. In the SM, top quarks decay via the weak interaction into a W boson and a down-type quark. The probability of how often which down-type quark acts as decay product is expressed by the CKM matrix elements that contain top quarks, namely $|V_{td}|$, $|V_{ts}|$ and $|V_{tb}|$. According to the measured value of $|V_{tb}| = 0.99915 \pm 0.00005$ [28], extracted on the assumption of CKM unitarity (see also Sec. 2.3), top quarks decay almost exclusively into a W^+ boson and a bottom quark, the antitop quark correspondingly into a W^- boson and an antibottom quark. This relationship can also be written in terms of branching ratios $\mathscr{B}$ which are defined as $\mathscr{B}_i = \Gamma_i/\Gamma$ with the total decay width Γ and the partial decay width Γ_i that is associated with a certain decay mode i. Thus, $\mathscr{B}_i$ describes the fraction of particles which decay via the mode i with respect to the total number of decaying particles. Considering again the unitarity of the CKM matrix, the following ratio of branching ratios can be defined for top quark decays with the three quark generations where q refers to all three possible down-type quarks d, s and b:

$$\frac{\mathscr{B}(t \to Wb)}{\mathscr{B}(t \to Wq)} = \frac{|V_{tb}|^2}{|V_{td}|^2 + |V_{ts}|^2 + |V_{tb}|^2} = |V_{tb}|^2 \approx 1\,.$$

Compliant with this definition of the ratio of branching fractions, such a ratio can also be written in terms of decay widths and partial decay widths. Direct measurements of this quantity were performed in the past resulting in $\Gamma_{Wb}/\Gamma_{Wq} = 0.957 \pm 0.034$ [28] where q contains the sum of three down-type quark contributions. This value, obtained assuming the unitarity of the CKM matrix, is close to the above stated values and underlines once more the rarity of top quark decays into the lighter quarks d and s.

The fact that top quarks decay to bottom quarks in almost all cases can be exploited for the identification of top quark decays in collider experiments. The b quarks from the top quark decays hadronise to form jets which include B hadrons. These hadrons, like the B mesons, can possess a relatively long lifetime of about 1.5 ps leading to a flight length path exceeding 1 mm. This may result in a decay vertex of b jets that is displaced from the primary vertex as the initial interaction point where the top quark decayed. Such a secondary vertex allows for the differentiation between b jets and jets originating from lighter quarks.

The W boson as the second decay product of the top quark decays either into two light quarks q_1 and $\overline{q_2}$ which then hadronise to light jets, called hadronic decay, or, alternatively, into a charged lepton ℓ and the corresponding antineutrino where ℓ comprises electrons e, muons μ and tau leptons τ, called leptonic decay. Approximate branching fractions $\mathscr{B}$ in the different decay channels of W bosons are presented in Table 2.6. There, n_C denotes a colour factor, as already introduced in Sec. 2.1.2, which is essential for a correct estimate and set to $n_C^{\text{lep}} = 1$ and $n_C^{\text{had}} = 3$.

Final states	$e\nu_e$	$\mu\nu_\mu$	$\tau\nu_\tau$	$u\bar{d}/d\bar{u}$	$c\bar{s}/s\bar{c}$
n_C	1	1	1	3	3
$\mathscr{B}$	$\frac{1}{9}$	$\frac{1}{9}$	$\frac{1}{9}$	$\frac{1}{3}$	$\frac{1}{3}$

Table 2.6: Final states of W boson decays and their roughly estimated branching ratios. The most probable final states according to the CKM matrix are given for the hadronic decays. Possible combinations are specified in the latter case, depending on the charge of the related initial W boson.

Decay Channels of Top Quark Pairs

The two W bosons from a $t\bar{t}$ pair decay independently, leading to three different combinations of the two W boson decays for the $t\bar{t}$ pair: *all-jets*, *dileptonic* and *lepton+jets*, where the latter specifies a channel with one W boson decaying leptonically while the other decays into two jets. The following description of these three $t\bar{t}$ decay channels ignores the contribution from tau leptons as those are difficult to identify because of the different decays of tau leptons in either two lighter leptons or quarks. Thus, the decay probabilities of W bosons decaying leptonically or hadronically are $P_{\text{lep}} = 2/9$ and $P_{\text{had}} = 2/3$, based on the numbers in Table 2.6. These probabilities allow for an estimate of the branching ratios of $t\bar{t}$ pair decays.

The *all-jets decay channel* with both W bosons decaying hadronically has a large branching ratio of $\mathscr{B} \simeq 2/3 \cdot 2/3 = 4/9$. But the six jet signature with two b jets resembles that of QCD multijet background impeding the clean separation of signal and background. Furthermore, the event reconstruction is difficult in this channel. The correct assignment of all jets is hard to achieve, leading to larger combinatorial background, apart from the fact that the energy and angular resolution of leptons is better than the one of jets. In contrast to the other channels, however, no missing transverse momentum needs to be taken into account.

The *dileptonic decay channel*, where both participating W bosons decay leptonically into either electrons or muons, has a low branching ratio of $\mathscr{B} \simeq 2/9 \cdot 2/9 = 4/81$. The signature is composed of two oppositely charged leptons having high transverse momenta, two b jets and missing transverse momentum $E_{\text{T}}^{\text{miss}}$. Energy and momentum conservation enable the reconstruction of the momentum sum of the involved neutrinos based on the contribution of missing transverse momentum, delineated in Chapter 4.6. The signature is the cleanest of all possible $t\bar{t}$ decays as the multijet background is negligible. But, at the same time, the full event reconstruction is challenging because of the two undetectable neutrinos. In latest analyses at $\sqrt{s} = 13$ TeV, however, the dilepton channel yields most precise results despite these challenges.

The *lepton+jets decay channel* with one hadronically and one leptonically decaying W boson is characterised by the following signature: four jets, out of which two are b jets, one isolated lepton $\ell = e, \mu$ and, due to the neutrino emerging from the W decay, missing transverse momentum. The resulting branching ratio amounts to $\mathscr{B} \simeq 2 \cdot 2/9 \cdot 2/3 = 8/27$.

This channel constitutes a compromise between the other channels; it has an adequate branching ratio and a reduced amount of background events. It benefits from a sufficient rejection of multijet background and from the possibility to fully reconstruct these events since only one neutrino contributes so that no quantity remains underconstrained [74, 109]. This is why this final state, visualised in Fig. 2.6, is chosen for the measurement of the top quark decay width in this thesis.
The discussion of the three $t\bar{t}$ decay channels is facilitated by explicitly not considering tau leptons. In fact, they contribute to the measured signal as lepton+jets events may contain a tau lepton subsequently decaying leptonically. Further potential migration effects are caused by dileptonic $t\bar{t}$ events with one top quark decaying into a tau lepton which decays into hadrons (migration to the lepton+jets channel) or caused by lepton+jets events where the lepton is a hadronically decaying tau lepton (migration to the all-jets channel).

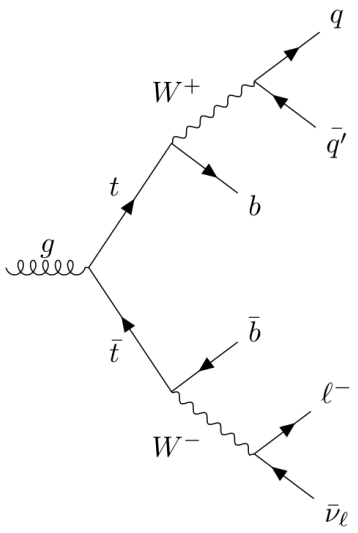

Figure 2.6: Feynman diagram for the decay of a $t\bar{t}$ pair in the lepton+jets decay channel.

Background Contributions

Several backgrounds contribute to the lepton+jets decay channel. One contribution arises from W+jets events caused by light jets misidentified as b jets or by W production in association with heavy flavour jets. Two LO Feynman diagrams for the W+jets production with one jet in the final state are shown by way of example in Fig. 2.7. Single top events constitute another relevant background. Those events including Feynman diagrams are discussed thoroughly in Sec. 2.2.1. Diboson (WW, WZ, ZZ) and Z+jets events are smaller background sources which are taken into consideration as well. Details are given in Ch. 5.3.
Generic QCD multijet production is an important instrumental background originating from a high-p_T lepton within a jet emerging from the decay of a heavy flavour hadron in a jet or from a jet misidentified as a lepton.

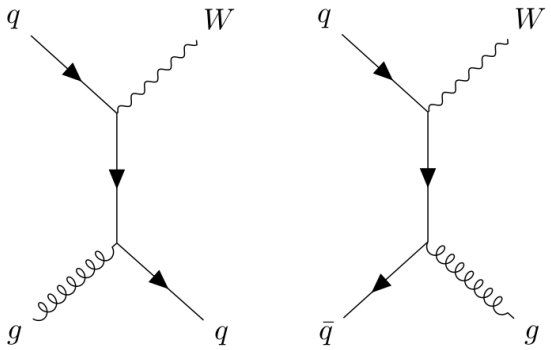

Figure 2.7: W+1 jet production: QCD Compton process (left) and $q\bar{q}$ annihilation (right).

2.2.3 Top Quark Properties

As this thesis covers a measurement of the decay width of the top quark Γ_t, this quantity is discussed in a separate section, see Sec. 2.3. Other properties of the top quark including latest measurements are described briefly in the following. Since Γ_t depends in particular on the top quark mass, the latter quantity is addressed first. The current world average is [28]:

$$m_t^{\mathrm{PDG}} = 173.1 \pm 0.6 \text{ GeV}.$$

This value is approximately two orders of magnitude larger than the mass of the bottom quark, the weak isospin partner of the top quark. The total uncertainty of this average mass value corresponds to the relative precision of the top quark mass measurement of $\sigma_{\mathrm{rel}} = \sigma_{\mathrm{tot}}/m_t \approx 0.35\%$. This underlines a high accuracy that outvalues the precision of all other five measured quark masses. Although the top quark mass can be constrained using loop corrections of the W and Z boson mass, direct measurements of the largest SM fermion mass are crucial as they provide essential information for global fits of electroweak parameters [28, 110] and have much smaller uncertainties. Hence, precision measurements of m_t enable tests of the internal consistency of the SM and probing related extensions, apart from the fact that the top quark mass affects the stability of the SM Higgs potential. The latest ATLAS combination of several direct mass measurements yielded [111]:

$$m_t^{\mathrm{ATLAS}} = 172.84 \pm 0.34\,(\mathrm{stat.}) \pm 0.61\,(\mathrm{syst.}) \text{ GeV}.$$

A variety of mass measurements performed using the ATLAS and CMS experiments including also Tevatron results are listed in Fig. 2.8.

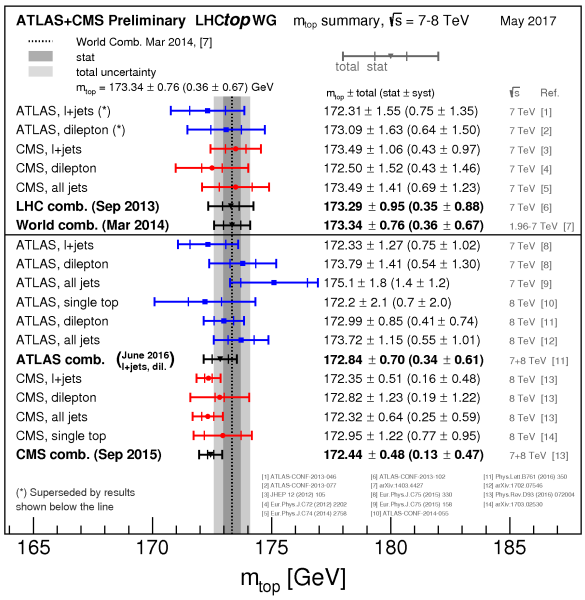

Figure 2.8: Summary of different direct m_t measurements [111–123] by the ATLAS and the CMS detector and their combinations [90]. The world combination also contains Tevatron results [124]. Measurements performed at $\sqrt{s} = 13$ TeV are not published yet.

Other important characteristics of the top quark are charge and spin. The top quark is presumed to carry charge $Q = +2/3 \cdot e$ and to have spin $s = 1/2$. Measurements of the top quark charge were performed at a centre-of-mass energy of 7 TeV with the ATLAS [125] and the CMS [126] detector. The ATLAS measurement quoted a result of $Q = 0.64 \pm 0.02\,(\text{stat.}) \pm 0.08\,(\text{syst.})$ which exclude models that propose an electric top quark charge of -4/3 with a significance of more than 8σ. This alternative charge value has already been excluded at the Tevatron [127, 128]. As the top quark decays before hadronisation, the spin of the two quarks from a $t\bar{t}$ pair is transferred to the decay products. The correlation between the top quark spins was measured by the ATLAS [129–132] and CMS [133–135] experiments. All these measurements agree well with the SM predictions.
Another feature of top quark decays which was studied in the past is the helicity of the W bosons from the $t\bar{t}$ decay, defined as the projection of the spin onto the direction of momentum, since the W boson polarisation allows to test the Wtb vertex Lorentz structure as well as to look for BSM physics. The measurements realised with the ATLAS [136, 137] and CMS [138–140] detectors revealed helicity fractions which are in good agreement with SM expectations.
Studies of the structure of the Wtb vertex and the strength of the coupling were also performed in the single top t-channel using both ATLAS [141–143] and CMS [144] data. No deviation from the Standard Model prediction was observed.
The $t\bar{t}$ production process can be tested by measuring its charge asymmetry. This asymmetry is due to interference effects at NLO QCD between gluon radiation in the initial and final state and interferences between LO and box diagrams, causing differences in the rapidity y (see Sec. 3.2) of top and antitop quarks. At the Tevatron, as a $p\bar{p}$ collider with a high rate of $t\bar{t}$ production via $q\bar{q}$ annihilation, a forward-backward asymmetry A_{FB} could be accessed. The DØ results [145, 146] are close to the SM expectation while discrepancies of around 2σ with the SM values were observed by the CDF collaboration [147, 148]. At the symmetric pp collider LHC, a charge asymmetry A_{C} can be measured solely by exploiting momentum differences between valence quarks and sea antiquarks. The ATLAS [149–153] and CMS [154–157] results are consistent with the SM predictions.
Furthermore, electromagnetic and weak couplings of the top quark can be probed exploiting processes with an additional photon or a W or Z boson. Those processes are referred to as $t\bar{t}V$ with $V = \gamma, W, Z$. Measurements of the cross-sections of $t\bar{t}W$ and $t\bar{t}Z$ at different centre-of-mass energies published by the ATLAS [158, 159] and CMS [160–162] experiments are consistent with NLO calculations for these processes. Also, the results for the $t\bar{t}\gamma$ production are in good agreement with the predictions from the Standard Model using ATLAS [163, 164] and CMS [165, 166] data.
A variety of other measurements of the different properties of the top quark, processes with top quarks and its decay were published in the last years. A detailed description of all those analyses would go beyond the scope of this thesis and could thus not be covered. A complete overview is given in [28], which also comprises measurements performed at the CDF and DØ experiments at the Tevatron.

2.3 Top Quark Decay Width

2.3.1 Theoretical Aspects

Due to its large mass, top quarks have a very short lifetime of about $\tau_t \approx 5 \cdot 10^{-25}$ s [167]. The lifetime is related to the decay width according to:

$$\Gamma_t = \frac{\hbar}{\tau_t}, \qquad \text{or in natural units :} \qquad \Gamma_t = \frac{1}{\tau_t},$$

with the reduced Planck constant $\hbar = h/2\pi = 6.582119514(40) \cdot 10^{-16}$ eV $\cdot$ s [28]. This notation of $\hbar$ illustrates why the decay width is usually given in units of electron volts. This short lifetime of the top quark has different implications. Pursuant to the above definition, the decay width of the top quark is the largest of all SM fermions. Furthermore, as it takes $\tau_{\text{had}} \approx 3 \cdot 10^{-24}$ s to form bound state hadrons, top quarks decay before hadronisation. This hadronisation time results from the formula $\tau_{\text{had}} = \hbar/\Lambda_{\text{QCD}}$ and thus relies on the actual value of the cutoff parameter Λ_{QCD} [168]. As a consequence, bound states which comprise top quarks do not exist in nature. This is the reason why, as already mentioned in the last sections, properties of the bare top quark are experimentally accessible through the decay products of the top quark. Any hadronisation would lead to a loss of information about the underlying decay process.

The decay width of a particle can also be visualised using its mass distribution. This is highlighted in Fig. 2.9 where a Breit-Wigner function f serves to describe an idealised mass distribution of the top quark.

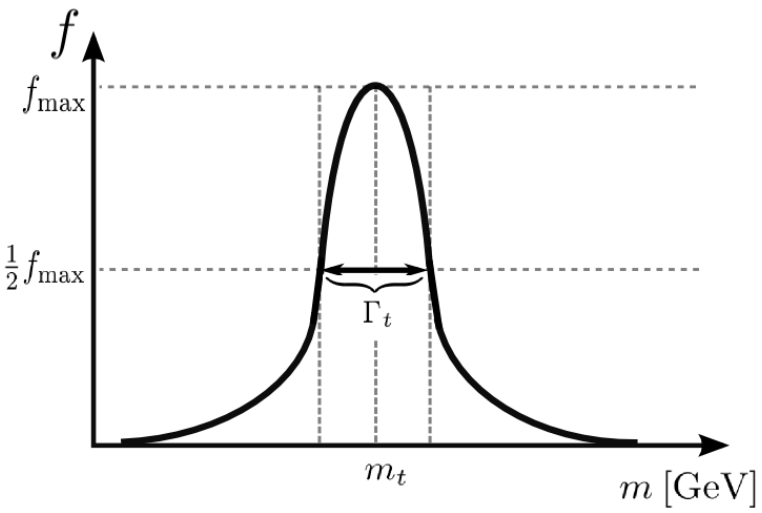

Figure 2.9: Illustration of the relationship between the top quark decay width Γ_t within a top quark mass distribution represented by an idealised Breit-Wigner function.

The top quark mass in this idealised curve is consistent with the peak position, and its decay width can be extracted from this curve: Γ_t corresponds to the width of the curve at half maximum. That is why this quantity is often abbreviated as FWHM standing for “full width half maximum”, as

indicated in Fig. 2.9.
In a real measurement, the top quark decay width cannot be extracted easily from such a curve directly since the detector resolution of objects used to define corresponding observables like the mass needs to be taken into account. The resulting resolution of corresponding observable distributions is about one order of magnitude larger than the underlying Γ_t, making a direct measurement of this quantity so challenging. This is further explained in the next subsections. Before, theoretical calculations of Γ_t are presented.

The top quark decay width is in good approximation proportional to the third power of the top quark mass and proportional to $|V_{tb}|^2$ with the CKM matrix element V_{tb}. The calculations are usually performed for the process $t \to Wb$ and thus the decay width $\Gamma(t \to Wb)$ is calculated, which can be equated with the full Γ_t according to the value of $|V_{tb}|$. V_{tb} determines the coupling strength at the Wtb vertex in combination with the universal electroweak coupling constant. The absolute value of V_{tb} can be evaluated using a measurement of the single top quark production cross-section since it scales with $|V_{tb}|^2$ [141, 142, 144]. By the application of unitarity constraints, CKM matrix elements except for V_{tb} are used to indirectly calculate $|V_{tb}|$ more accurately resulting in $|V_{tb}|$ values close to one. The current measured number amounts to $|V_{tb}| = 0.99915 \pm 0.00005$ [28].

At leading order, the decay width $\Gamma(t \to Wb)$ can be calculated from the corresponding Feynman diagram, drawn in Fig. 2.10, exploiting the fact that the W boson from the top quark decay is on shell. The following assumptions need to be made to facilitate the calculation: $|V_{tb}| = 1$, the W boson is treated as a real on-shell particle and the mass of the b quark is neglected, i.e. $m_b = 0$. This results in the following four-momenta of the three participating particles: $p_t = (m_t, 0, 0, 0)$, $p_b = (P_M, 0, 0, P_M)$ and $p_W = (E_M, 0, 0, -P_M)$ with the magnitude of the momentum in the centre-of-mass frame P_M and the energy of the W boson $E_M^2 = P_M^2 + m_W^2$ with the W boson mass m_W. The calculation based on these three four-momenta leads to the squared spin-average matrix element:

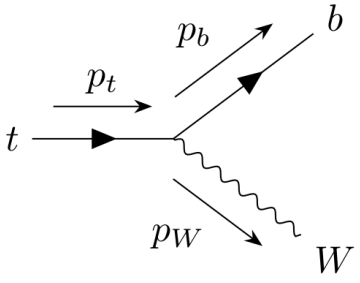

Figure 2.10: Feynman diagram for the decay of a top quark into a W boson and a b quark including arrows representing the four-momenta.

$$\langle|\mathscr{M}^2|\rangle = \frac{1}{2} g_w^2 m_t P_M \left(2 + \frac{m_t^2}{m_W^2}\right),$$

where g_w denotes the weak coupling constant $g_w = \sqrt{4\pi\alpha_w}$. Taking into account the relationship between this matrix element and the decay width for a standard decay of particle a in the products b and c, one obtains, after integrating over the full 4π solid angle:

$$\Gamma(t \to Wb) = \frac{P_M}{8\pi m_t^2} \cdot \langle|\mathscr{M}^2|\rangle = \frac{g_w^2 P_M^2}{16\pi m_t} \left(2 + \frac{m_t^2}{m_W^2}\right).$$

Replacing the momentum component P_M in this expression results in:

$$\Gamma(t \to Wb) = \frac{G_F}{8\pi\sqrt{2}} \cdot m_t^3 \left(1 - \frac{m_W^2}{m_t^2}\right)^2 \left(1 + 2\frac{m_W^2}{m_t^2}\right),$$

where g_w is expressed in terms of the Fermi coupling constant $G_F = \sqrt{2}g_w^2/(8m_W^2)$. This equation can also be written using $|V_{tb}|$ as [167]:

$$\Gamma(t \to Wb) = \frac{G_F}{8\pi\sqrt{2}} \cdot m_t^3 |V_{tb}|^2 \left(1 - 3\left(\frac{m_W}{m_t}\right)^4 + 2\left(\frac{m_W}{m_t}\right)^6\right). \tag{2.2}$$

Such a leading order approach constitutes only an approximate computation of the top quark decay width. In the following, first and second order QCD corrections are introduced, which have a large impact on the calculated value of Γ_t. As the top quark can be treated as an almost free particle, perturbative methods are applicable to estimate those quantum corrections. The full decay width for a top quark decaying into a W boson and a b quark can then be written as [169, 170]:

$$\Gamma(t \to Wb) = \Gamma_0 \left(A^{(0)} + \frac{\alpha_s}{\pi} C_F A^{(1)} + \left(\frac{\alpha_s}{\pi}\right)^2 A^{(2)} + \ldots\right), \tag{2.3}$$

which includes first and second order QCD corrections described by the terms $A^{(1)}$ and $A^{(2)}$, respectively. The first term, $\Gamma_0 A^{(0)}$, refers to the leading order calculation according to Eq. (2.2) with $\Gamma_0 = G_F m_t^3 |V_{tb}|^2/(8\pi\sqrt{2})$ and $A^{(0)} = 1 - 3m_W^4/m_t^4 + 2m_W^6/m_t^6$. The additional factor C_F is set to 4/3. The one-loop $\mathcal{O}(\alpha_s)$ correction is known in analytical form [167] and can be written using terms of m_W/m_t as:

$$A^{(1)} = \frac{5}{4} - \frac{\pi^2}{3} + \frac{3}{2}\frac{m_W^2}{m_t^2} + \frac{m_W^4}{m_t^4}\left(-6 + \pi^2 - \frac{3}{2}\ln\frac{m_t^2}{m_W^2}\right) + \frac{m_W^6}{m_t^6}\left(\frac{46}{9} - \frac{2}{3}\pi^2 + \frac{2}{3}\ln\frac{m_t^2}{m_W^2}\right) + \mathcal{O}\left(\frac{m_W^8}{m_t^8}\right). \tag{2.4}$$

This first order correction reduces the top quark decay width by about 10%. An approximation with $m_W = 0$ so that only the first mass-independent terms remain, results in an error in $A^{(1)}$ of 22%. Including only the quadratic mass terms yields an error of 4% while the first order correction with all terms in Eq. (2.4) leads to an almost negligible error.

In order to estimate predictions for the decay width at order $\mathcal{O}(\alpha_s^2)$, the factor $A^{(2)}$ is decomposed into terms reflecting the underlying colour structure:

$$A^{(2)} = C_F^2 A_A^{(2)} + C_A C_F A_{NA}^{(2)} + C_F T n_l A_l^{(2)} + C_F T A_F^{(2)}.$$

These colour factors are defined as $C_F = 4/3$, $C_A = 3$ and $T = 1/2$. The number of quark flavours is set to $n_l = 5$ and thus includes all SM quarks except top quarks. $A_A^{(2)}$ denotes the Abelian contribution already present in QED and $A_{NA}^{(2)}$ the non-Abelian. $A_l^{(2)}$ and $A_F^{(2)}$ are corrections comprising a second fermion loop with either massless or massive quarks. The individual contributions of the

$A_i^{(2)},\ i = A, NA, l, F$, can be split into different components in terms of m_W^2/m_t^2 according to:

$$A_i^{(2)} = A_i^{(2)}|_{m_W=0} + \frac{m_W^2}{m_t^2} A_i^{(2)}|_{m_W^2} + \frac{m_W^4}{m_t^4} A_i^{(2)}|_{m_W^4} + \dots . \tag{2.5}$$

The contribution $A_l^{(2)}|_{m_W=0}$ is known analytically and amounts to about 2.859 [171]. All other factors are evaluated based on the calculation of propagator-type diagrams which contribute to the self-energy of the top quarks in terms of an expansion around $q^2/m_t^2 = 0$ where q defines an external momentum. The limit $q^2 \to m_t^2$ is considered by performing a Padé approximation where the resulting polynomial is written as a rational function:

$$[m/n](z) = \frac{a_0 + a_1 z + \dots + a_m z^m}{1 + b_1 z + \dots + b_n z^n} .$$

Applying this procedure to determine all terms present in Eq (2.5) results in the following solution for $A^{(2)}$:

$$A^{(2)} = -16.7(8) + 5.4(4)\frac{m_W^2}{m_t^2} + \frac{m_W^4}{m_t^4}\left(11.4(5.0) - 7.3(1)\ln\frac{m_t^2}{m_W^2}\right).$$

Taking this equation for $A^{(2)}$ and the analytical solutions for $A^{(0)}$ and $A^{(1)}$ conforming with Eq. (2.2) and Eq. (2.4), the total top quark decay width can be evaluated using Eq. (2.3). This leads to a value of $\Gamma_t = 1.33$ GeV for a top quark mass of $m_t = 172.5$ GeV with an approximate precision of 1% [169, 170]. These values of the decay width and the mass of the top quark are exploited to generate the Monte Carlo (MC) events used in this measurement as described in Ch. 5.

In the last few years, further effort was spent on increasing the precision of the theoretical value for Γ_t. One of the recent calculations [172] does not only contain the dominant next-to-leading order and next-to-next-to-leading order QCD corrections, $\delta_{\text{QCD}}^{(1)}$ and $\delta_{\text{QCD}}^{(2)}$, but also smaller NLO electroweak corrections δ_{EW} as well as finite b quark mass and W boson width effects δ_f^b and δ_f^W. Hence, the corrections to the leading order approximation $\Gamma_t^{(0)}$, calculated using again Eq. (2.2), can be written as:

$$\Gamma_t = \Gamma_t^{(0)} \cdot (1 + \delta_f^b + \delta_f^W + \delta_{\text{EW}} + \delta_{\text{QCD}}^{(1)} + \delta_{\text{QCD}}^{(2)}).$$

Decay width values $\Gamma_t^{(0)}$ and Γ_t are listed for different underlying top quark masses in Table 2.7. For a top quark mass of $m_t = 172.5$ GeV, one obtains a leading order width of $\Gamma_t^{(0)} \approx 1.481$ GeV and, utilising the above listed corrections, a total decay width of $\Gamma_t \approx 1.322$ GeV [172] which is in good agreement with the prediction used in the baseline MC samples employed in this analysis. The quoted uncertainty of this second estimate amounts to about 0.8% and is derived from a variation of the renormalisation scale. Considering experimental uncertainties on the parameters which enter the formula for Γ_t increases the uncertainty on this evaluation up to 6%. The dominant contribution originates from the relatively large uncertainty on the CKM matrix element $|V_{tb}|$, using

m_t [GeV]	δ_f^b [%]	δ_f^W [%]	δ_{EW} [%]	$\delta_{\text{QCD}}^{(1)}$ [%]	$\delta_{\text{QCD}}^{(2)}$ [%]	$\Gamma_t^{(0)}$ [GeV]	Γ_t [GeV]
172.5	-0.26	-1.49	1.68	-8.58	-2.09	1.4806	1.3216
173.5	-0.26	-1.49	1.69	-8.58	-2.09	1.5109	1.3488
174.5	-0.25	-1.48	1.69	-8.58	-2.09	1.5415	1.3764

Table 2.7: Total decay width of the top quark at leading order ($\Gamma_t^{(0)}$) and with corrections (Γ_t) for different top quark masses m_t. Decay width values and masses are given in GeV, the different corrections due to a finite b quark mass, a finite W boson width and higher orders comprising NLO EW corrections as well as NLO and NNLO QCD corrections are given in percentages [172].

a conservative approach for the $|V_{tb}|$ measurement without the CKM unitarity assumption which results in $|V_{tb}| = 1.021 \pm 0.032$ [28].

2.3.2 Measurements of the Top Quark Decay Width

In the past years, measurements of the top quark decay width were performed at the Tevatron and the LHC. Such measurements are either direct or indirect. The latter term refers to the fact that indirect measurements rely on certain SM assumptions as it will be explained in more detail in the following. This section presents those recent measurements of Γ_t to allow for a comparison with the result obtained in this analysis.

The latest direct measurement at the Tevatron was published by the CDF collaboration [14]. This analysis uses the full Tevatron Run II dataset of $\sqrt{s} = 1.96$ TeV proton-antiproton collision data and concentrates on decays in the lepton+jets decay channel of $t\bar{t}$ pairs. The dataset recorded by the CDF II detector corresponds to an integrated luminosity of 8.7 fb^{-1}. The mass of the top quark and of the hadronically decaying W boson are reconstructed for all events and compared with distributions from Monte Carlo signal and background samples to evaluate Γ_t. The reconstructed top quark mass distribution measured in data is compared to templates from generated $t\bar{t}$ signal samples based on decay width values in the range from 0.1 to 30 GeV, assuming a fixed top quark mass of 172.5 GeV, in order to distinguish between different Γ_t values in this measurement. Furthermore, a set of samples is generated where the jet energy scale (JES), as one of the dominant systematic uncertainties, is varied independently. The jet energies are modified in data by a factor of $1 + \Delta_{\text{JES}}$ to take the energy scale uncertainty of the measurement into account while in the simulated samples Δ_{JES} is varied from $-3\sigma_c$ to $+3\sigma_c$. The latter factor denotes the CDF fractional uncertainty of the JES.
The main analysis steps are thus the following: After the event selection according to the requirements of the lepton+jets decay channel, the top quark mass m_t and the hadronically decaying W boson mass m_{jj} are reconstructed for all events. The former is the observable sensitive to the decay width Γ_t whereas the latter is used for the in-situ calibration of the JES. This analysis step is followed by a template likelihood fit of both m_t and m_{jj} using simulated signal and background events. Example templates for these two mass observables are shown in Fig. 2.11.
The result of the template fit is utilised to extract 68% confidence level (CL) limits of Γ_t based on

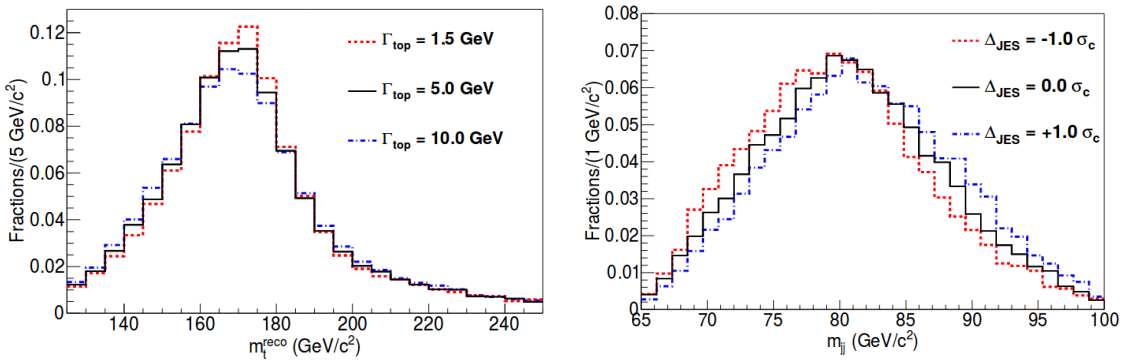

Figure 2.11: (a) m_t templates for three different values of Γ_t with the nominal setting $\Delta_{\text{JES}} = 0$ and (b) m_{jj} templates for three values of Δ_{JES} based on $\Gamma_t = 1.5$ GeV as used in the direct decay width measurement performed by CDF [14].

a likelihood ratio ordering. A central value of $\Gamma_t = 1.63$ GeV is retrieved from data leading to a two-sided limit of $1.10 < \Gamma_t < 4.05$ GeV at the 68% CL for a fixed top quark mass of 172.5 GeV. This measured range is equivalent to a lifetime of $1.6 \cdot 10^{-25} < \tau_t < 6.0 \cdot 10^{-25}$ s.

A direct measurement was also performed by the CMS Collaboration recently using 12.9 fb^{-1} of proton-proton collision data collected at $\sqrt{s} = 13$ TeV [15]. To obtain this preliminary result, the measurement is realised in the dilepton channel of $t\bar{t}$ decays, i.e. events are selected that contain at least two charged leptons (electrons or muons) and at least two jets with at least one jet identified as a b jet. Signal samples include $t\bar{t}$ events and also the single top Wt contribution. The utilised signal MC samples have next-to-leading order precision in production but only leading order accuracy in decay. As a consequence, this measurement is assumed to be sensitive to missing orders in the MC precision.
The observable used for the decay width measurement is the invariant mass of the lepton and the b-tagged jet, $m_{\ell b}$. As two masses can be reconstructed per event, $m_{\ell b}$ is derived from a pairing of the two leading-p_{T} charged leptons with two leading-p_{T} b-tagged jets. The resulting distribution is compared to simulated expectations corresponding to different underlying decay width values employing a likelihood technique. Likelihood ratios obtained from pairs of shape hypotheses are analysed to test different hypotheses of alternative values of Γ_t. The null hypothesis corresponds to the SM prediction of Γ_t. Using ratios of relativistic Breit-Wigner distributions, the alternative hypotheses are created by reweighting the parton level top quark mass distributions. For the validation of this reweighting method, a sample based on a width of four times the SM value is employed. The hypotheses tests yield a result of $0.6 < \Gamma_t < 2.5$ GeV at the 95% CL assuming a top quark mass of 172.5 GeV. The evolution of the corresponding CL_S curve used to evaluate the Γ_t range is shown in Fig. 2.12.

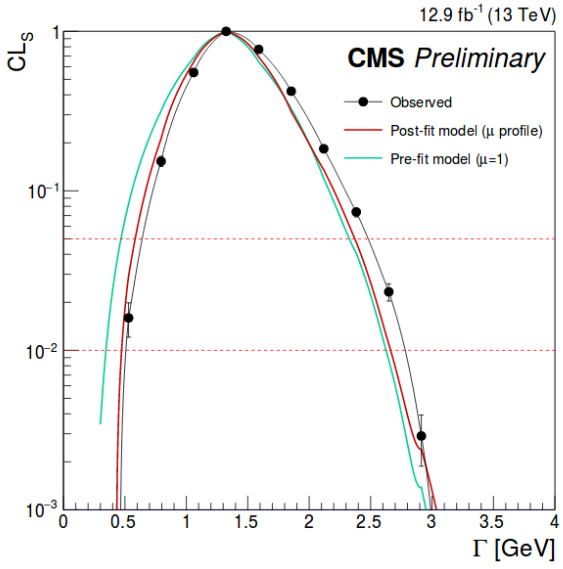

Figure 2.12: Evolution of CL_S as a function of Γ_t used to compute 95% confidence level limits. Pre- and post-fit model expectations as well as the measured curve are shown. μ denotes the signal strength [15].

The top quark decay width was also measured indirectly, i.e. these measurements are based on certain Standard Model assumptions as outlined in the following and thus not as sensitive to BSM physics as direct measurements are.
A very recent indirect measurement of Γ_t was conducted by the CMS experiment using $t\bar{t}$ decays in the dilepton channel collected in proton-proton collision data recorded at $\sqrt{s} = 8$ TeV with an integrated luminosity of 19.7 fb^{-1} [173]. This measurement is based on the extraction of the ratio of branching fractions $\mathcal{R} = \mathcal{B}(t \to Wb)/\mathcal{B}(t \to Wq)$. The value of $\mathcal{R}$ is obtained from a fit using the observed b-tagged jet distributions with a parametric model which relies on the measured cross-section and corrects for the fraction of jets in the events that cannot be associated with a single top quark decay ($t \to Wq$). The resulting value of $\mathcal{R}$ from the fit is combined with a CMS measurement of the single top t-channel cross-section [174] to obtain the indirect estimate of Γ_t. Using the assumption that $\sum_q = \mathcal{B}(t \to Wq) = 1$, the ratio reduces to $\mathcal{R} = \mathcal{B}(t \to Wb)$ and the decay width can be determined via:

$$\Gamma_t = \frac{\sigma_{t-\text{channel}}}{\mathcal{B}(t \to Wb)} \cdot \frac{\Gamma(t \to Wb)}{\sigma^{\text{theory}}_{t-\text{channel}}} = \mathcal{R}^{-1} \cdot \frac{\sigma_{t-\text{channel}}}{\sigma^{\text{theory}}_{t-\text{channel}}} \Gamma(t \to Wb).$$

The term $\Gamma(t \to Wb)$ denotes the partial decay width of the top quark to decay into a W boson and a b quark, $\sigma_{t-\text{channel}}$ and $\sigma^{\text{theory}}_{t-\text{channel}}$ are the measured and the theoretical t-channel single top quark cross-sections, respectively. The value for the measured single top cross-section is taken from [174] where the theoretical calculation originates from [94]. The partial decay width is computed for a top quark mass of $m_t = 172.5$ GeV and amounts to $\Gamma(t \to Wb) = 1.329$ GeV [28] with a theoretical uncertainty of less than 1%. The only quantity remaining is $\mathcal{R}$ and, hence, the

decay width Γ_t is extracted using a maximum-likelihood fit similar to the determination of the value of $\mathscr{R}$ [173] leaving Γ_t as a free parameter. The uncertainties on the predicted and measured cross-sections are considered via additional nuisance parameters in the fit. The result is found to be $\Gamma_t = 1.36 \pm 0.02\,(\text{stat.})^{+0.14}_{-0.11}\,(\text{syst.})$ GeV, which is in good agreement with the SM expectation. The dominant source of systematic uncertainty is due to the value of the measured t-channel cross-section.

Another indirect measurement of Γ_t using the same analysis strategy was performed by the DØ experiment at the Tevatron collider at $\sqrt{s} = 1.96$ TeV and yielded $\Gamma_t = 2.00^{+0.47}_{-0.43}$ [175].

2.3.3 Predictions for the Top Quark Decay Width in BSM Models

Various models based on BSM physics exist which predict top quark decay width values significantly larger or smaller than the results from SM computations as presented before. The following section introduces some of these alternative models, which predict a different decay width Γ_t and which have become very popular over the last decades.
This section intends to give an overview of those alternative models although the latest LHC results are in tension with some of them. The focus is laid on a brief introduction of these BSM models and a presentation of their possible impact on Γ_t to motivate the direct measurement of the top quark decay width. A detailed discussion on how probable individual models are, based on current exclusion limits, cannot be covered in this thesis.

Supersymmetric Models

One of the most famous extensions of the Standard Model is supersymmetry (SUSY). In particular, effects of the R parity conserving Minimal Supersymmetric Standard Model (MSSM) on the top quark decay width have been discussed in the past [176, 177]. However, the theoretical models presented in the following could not be experimentally verified in the past despite intensive searches at the Tevatron or the LHC, making the existence of supersymmetric particles more and more improbable. According to SUSY, all SM particles possess a super-partner called “sparticle” which differs by half a unit of spin. This means that sfermions as spin-0 scalars are the super-partners of the SM fermions while spin-1 gauge bosons have spin-1/2 gauginos as super-partners. In the MSSM, two complex weak isospin Higgs doublets:

$$\begin{pmatrix} H_2^+ \\ H_2^0 \end{pmatrix} \quad \text{and} \quad \begin{pmatrix} H_1^0 \\ H_1^- \end{pmatrix}$$

denote the partners of the SM spin-0 Higgs field having opposite hypercharge, $Y = +1$ and $Y = -1$, respectively, to ensure anomaly cancellation between fermionic particles. The physical chargino and neutralino states originate, in general, from mixtures of the Higgsinos $\tilde{H}$ and gauginos, namely the two charged Higgsinos mix with the winos $\tilde{W}^{\pm}$ to charginos whereas the neutral Higgsinos mix with the neutral gauginos $\tilde{Z}$ and $\tilde{\gamma}$ to be the neutralinos. The lightest neutralino is in many SUSY

models a weakly interacting stable particle and may thus offer an explanation of the dark matter in the universe, as described in Sec. 2.1.2, leading to its popularity [25, 26].
The two Higgs doublets are associated with eight degrees of freedom - out of which three are absorbed to give mass to the three massive SM bosons $W^{\pm}$ and Z. Five physical states remain for five different types of Higgs bosons: two neutral scalars h^0 and H^0, a pseudoscalar A^0 and two charged Higgs bosons $H^{\pm}$. The decay of the top quark into those particles will be discussed later in this subsection.
The existence of SUSY may have an impact on the top quark decay width in two ways: Firstly, unexpected radiative corrections to the dominant SM decay process $t \to Wb$ may affect Γ_t and, secondly, some of the SUSY particles introduced above may have smaller masses than the top quark leading to possible new decay channels of this quark directly modifying its decay width.

Standard Model corrections of Γ_t are shown in Table 2.7. The MSSM, if it exists, may impose further (perturbative) quantum effects on Γ_t caused by one-loop corrections mediated by SUSY particles [178, 179]. Those corrections often depend on $\tan\beta$, which is defined as the ratio of the two vacuum expectation values corresponding to the expectation values v_1 and v_2 of the two neutral Higgs doublets so that $\tan\beta = v_1/v_2$. These values are related to the SM vacuum expectation value via $v^2 = v_1^2 + v_2^2$.
SUSY EW quantum corrections can reduce the top quark decay width by about 1-10% (negative corrections), depending on the choice of several SUSY parameters and in particular on $\tan\beta$. SUSY QCD corrections are also negative but smaller than the SUSY EW corrections and can reach a few percent. These SUSY corrections to $\Gamma(t \to Wb)$ have the same sign as the SM QCD ones and can reach half the size of these SM corrections for large $\tan\beta$ values [176, 178, 179].

In case of the existence of a light charged Higgs boson, the top quark will also decay via $t \to H^+ b$. The partial decay width for this process $\Gamma(t \to H^+ b)$ depends strongly on $\tan\beta$. If this parameter is small or large enough, this partial width is comparable to the SM decay width of the top quark when it reaches a minimum at around $\tan\beta \approx 6$. This MSSM decay process of the top quark is very sensitive to radiative corrections of different types. Partial decay widths of the top quark as well as such radiative corrections for a large range of possible $\tan\beta$ values are visualised in Fig. 2.13.
Fig. 2.13a shows a summary of different scenarios leading to alternative values of $\Gamma(t \to H^+ b)$ compared to the SM decay width which is naturally independent of $\tan\beta$. In a scenario where the Higgsino mass parameter μ is negative, the SUSY QCD corrections are opposite in sign to the SM QCD corrections, thus cancelling the strong SM QCD corrections for increasing $\tan\beta$ whereas for positive parameter values of μ both SUSY and SM QCD corrections possess the same sign. This results in the large negative corrections.
Fig. 2.13b illustrates the relative radiative corrections to $\Gamma(t \to H^+ b)$, revealing an almost linear behaviour of the dominant SUSY contributions. In contrast to the SM EW contribution, which is close to being negligible, the SM QCD contribution to this process reaches a maximum at around $\tan\beta \approx 10$. For $\tan\beta \approx 35$, the SUSY QCD corrections cancel out the SM ones. Hence, for certain values of $\tan\beta$, the partial decay width for a top quark decay into charged Higgs bosons will

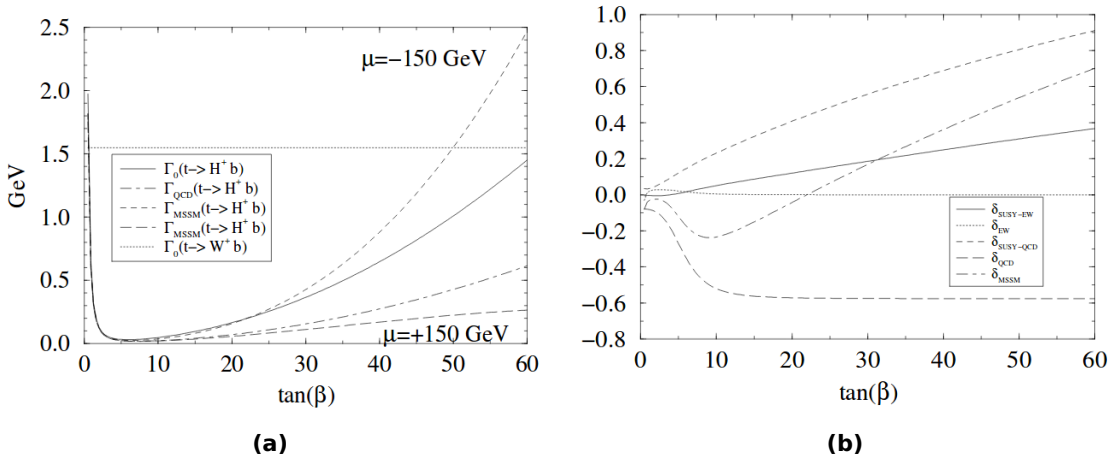

Figure 2.13: (a) The partial decay width $\Gamma(t \to H^+ b)$ compared to the SM top quark decay width as a function of $\tan\beta$ for $m_{H^\pm} = 120$ GeV. Shown are curves for different scenarios of SUSY parameters as the Higgsino mass parameter μ which is set to ±150 GeV. (b) Relative SUSY and SM radiative corrections to the process $\Gamma(t \to H^+ b)$ [176].

drastically modify the total decay width Γ_t. Such a large impact improves the experimental discovery reach of such processes with a direct measurement of Γ_t significantly [176]. The corresponding calculations are, for example, also described in [180–182].

In addition, there may also be top quark decays into supersymmetric particles predicted by certain SUSY models. In such cases, the top quark decays, for example, into a sbottom quark and a chargino, into a stop quark and a gluino or into a stop quark and a neutralino. In particular the latter process changes Γ_t significantly. Depending on the gluino mass, the corresponding radiative corrections may decrease Γ_t by up to 20% [183]. Also the decays of top quarks into more than two particles can be studied which may modify the top quark decay width by a few percent [176].

FCNC Processes

The existence of flavour changing neutral current (FCNC) decays of the top quark in BSM models can also affect the top quark decay width [184]. FCNC processes where a Z boson, a photon or a gluon act as a mediator do not exist at tree level in the Standard Model. They occur solely via loop induced processes which are highly suppressed in the SM and reach branching ratios of about $10^{-10} - 10^{-15}$ [185].
Alternative models as, e.g., some SUSY models predict significantly larger branching ratios for FCNC decays of the top quark. For instance, SUSY EW charged current interactions can induce FCNC processes. Depending on the decay channel, branching ratios of FCNC top quark decays can reach up to $10^{-4} - 10^{-5}$ (for decays of the top quark into a c quark and a gluon or a neutral Higgs boson). This contribution is still relatively small but at least more than five orders of magnitude larger than the corresponding SM processes [176, 186] and thus much closer to the precision that can be achieved with today's particle physics experiments [187–189].

Vector-Like Top Quarks or a Fourth Quark Generation

The CKM matrix element V_{tb} is presumed to be close to one due to unitarity constraints from the 3×3 CKM matrix. Once the unitarity requirement is relaxed, V_{tb} may have a measurable value different from one. Two minimal extensions of the SM that permit such a difference by introducing new quarks directly affecting the decay width of the third generation top quark are described in this paragraph.

The first model [190] introduces a vector-like top singlet which causes a global rescaling of V_{td}, V_{ts} and V_{tb}. The latter may differ from one even if the ratio $R = |V_{tb}|^2/(|V_{td}|^2+|V_{ts}|^2+|V_{tb}|^2)$ is close to one. R is invariant under a rescaling of the V_{ti} entries satisfying $V_{ti}^{(1)} = V_{ti}\cos\theta$ with $i = d, s, b$. This rescaling can be implemented with an additional vector-like quark having $Q = +2/3$. In case such a hypothetical quark has a mass around the electroweak scale, it mixes with its direct neighbour, the SM top quark, which extends the known CKM matrix as follows:

$$V_{4\times3} = \begin{pmatrix} \mathbb{1}_{2\times2} & 0 \\ 0 & U_{2\times2} \end{pmatrix} \begin{pmatrix} V_{3\times3} \\ 0 \end{pmatrix} \qquad \text{with} \qquad V_{4\times3}V_{4\times3}^{\dagger} \neq \mathbb{1}_{4\times4}\,.$$

On the assumption that the mass of the additional top quark t' is not dominated by the vacuum expectation value of the SM Higgs doublet, the mixing angle is required to be less than $\pi/4$. A criterion on V_{tb} can thus be defined as a lower bound: $|V_{tb}| \approx |\cos\theta| > 1/\sqrt{2} \approx 0.71$. The t' quark has three decay modes at leading order: $t' \to Wb$, as the third generation top quark, as well as the modes $t' \to Zt$ and $t' \to Ht$. The total decay width of t' depending on the t' mass is shown in Fig. 2.14a while Fig. 2.14b contains the branching fractions of the three decay modes of t', again depending on the t' mass for a set of the underlying parameters m_H, m_t and $\cos\theta$. The shown mass range is almost excluded by many recent searches for a t' quark. Nevertheless, the motivation of such a model and the trend towards larger masses becomes visible.

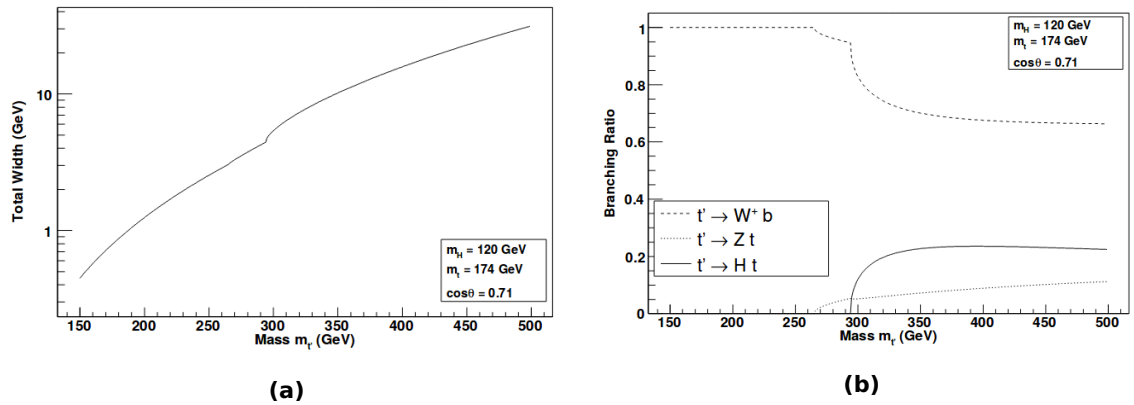

Figure 2.14: (a) The total decay width of the t' quark and (b) the corresponding branching ratios of the contributing decay modes of t' at leading order as a function of its mass. The underlying parameters are chosen to be $m_H = 120$ GeV, $m_t = 174$ GeV and $\cos\theta = 0.71$ [190].

The number of decay modes depend on the t' mass. With larger masses more decay modes contribute; for masses above around 300 GeV all listed LO decay modes need to be considered. Also the parameter choice is relevant for the calculated branching ratios; the branching ratio of $t' \to W\,b$ is reduced with increasing $\cos\theta$.

The second model [190–193] adds a complete fourth generation of quarks to the known 3×3 CKM matrix. This implies the existence of another unitary $V_{4\times4}$ mixing matrix which does not allow FCNC decays with Z bosons at leading order, as they need to be considered for the above vector-like t' quark model. If CP-violating phases beyond the CKM matrix are neglected, the new 4×4 matrix includes three further mixings which can be parametrised by [194]:

$$V_{4\times4} = R_{34}(\theta_u)R_{24}(\theta_v)R_{14}(\theta_w) \cdot \begin{pmatrix} V_{3\times3} & 0_{3\times1} \\ 0_{3\times1} & 1 \end{pmatrix}.$$

The rotation in the flavour plane ij is given by the R_{ij} with the mixing angles θ_u, θ_v and θ_w. In this case, the dominant decay channel is expected to be $t' \to W\,b'$. Also decays of t' into a W boson and lighter quarks like the top quark can contribute although these decays may be suppressed. Latest measurement excluded t' quarks with masses below around 500-700 GeV, depending on the analysed decay channel [28].

Depending on the corresponding t' masses, decays of such vector-like top quarks may contribute to the SM signal of top quark decays and thus directly modify the decay width Γ_t.

These days, limits on those BSM models presented in this section are mainly set by the LHC experiments. For reasons of simplicity, particularly basic models like the MSSM model are delineated here as an example of such alternative models which can affect the measured value of the decay width Γ_t. There are many other more complex models which are not excluded by the LHC yet, starting with N-MSSM (next-to-MSSM) models, which may contain, e.g., an additional singlet state leading to seven instead of five Higgs bosons. A detailed introduction of those models is beyond the scope of this thesis.

3 The ATLAS Experiment

Nowadays, most experiments in the field of particle physics are based on collisions of particles which obtain their high energies from accelerators. In order to measure the properties of nature at smaller and smaller scales, higher energies and thus larger colliders are needed. The size of the structure which is investigated, here given by the wavelength λ, as it can be associated with any object, depends on the probe energy according to the de Broglie equation $\lambda \propto 1/p$.
The analysis presented in this thesis is based on data recorded by the ATLAS detector, a multipurpose detector which is located at the currently most powerful particle accelerator worldwide, the Large Hadron Collider at CERN[1] in Geneva. This chapter introduces the LHC and provides a more detailed description of the ATLAS detector and its different components essential for detecting the decay products of the initial LHC collisions. In addition, useful detector observables are defined, and the used dataset is briefly addressed.

3.1 The Large Hadron Collider

The Large Hadron Collider (LHC) [195–197] began operating at the end of 2009. It is a two-ring superconducting accelerator which is able to accelerate protons or heavy ions. As it is focussed on proton-proton (pp) collisions in this thesis, the experimental setup of the LHC is described based on the acceleration and collision of protons. The choice of protons is motivated by the fact that these baryons form a stable beam, that they can be produced in large numbers and - in comparison to, for example, electrons - that the energy loss due to synchrotron radiation is small. The latter argument is particularly important when a higher energy reach is the experiment's main motivation. Also based on this argument, the LHC superseded the Large Electron Positron Collider (LEP) [198] at CERN, which had been built in the same tunnel that hosts the LHC today, lying approximately 100 m under ground. In 2010 and 2011, the centre-of-mass energy of the LHC pp collisions was $\sqrt{s} = 7$ TeV. One year later, in 2012, the LHC collided protons at $\sqrt{s} = 8$ TeV. The analysis presented in this thesis uses data which was collected by the ATLAS detector [199–201] at the latter centre-of-mass energy which is why the following description of the LHC is based on this data-taking period. Since 2015, after a shutdown period of two years, the LHC is operating at a centre-of-mass energy of $\sqrt{s} = 13$ TeV while the design energy of the LHC is $\sqrt{s} = 14$ TeV at a luminosity of 10^{34} cm^{-2}s^{-1}.

[1] European Organisation for Nuclear Research, name originating from: Conseil Européen pour la Recherche Nucléaire.

The LHC, with a circumference of 27 km, is not built as a perfect circle but is composed of eight arcs and eight straight sections, so called “insertions”. The former contain the dipole bending magnets, the insertions consist of a long straight section with two transition regions at both ends, and two “dispersion suppressors”. Four of these insertions host different LHC detectors while the others also fulfil purposes of injection, beam dumping or beam cleaning, for instance.
Four main detector experiments located at the straight sections record the resulting LHC particle collisions: ATLAS and CMS [202] as the so-called multipurpose high-luminosity detectors, LHCb (Large Hadron Collider beauty) [203], an asymmetric detector with a main focus on B-physics, and ALICE (A Large Ion Collider Experiment) [204] which concentrates on analysing the quark-gluon plasma in heavy ion collisions in order to study conditions comparable to those shortly after the Big Bang. A further small angle scattering experiment is TOTEM (TOTal Elastic and diffractive cross-section Measurement) [205]. Two additional experiments located at the LHC are LHCf (Large Hadron Collider forward) [206] and MoEDAL (Monopole and Exotics Detector at the LHC) [207].

The proton beams which enter the LHC are preaccelerated in a long injection chain of older, already existing and smaller rings or linear accelerators located at CERN. These were upgraded to fulfil all LHC requirements. The LHC as well as this chain of preaccelerators including the four main experiments are sketched in Fig. 3.1.

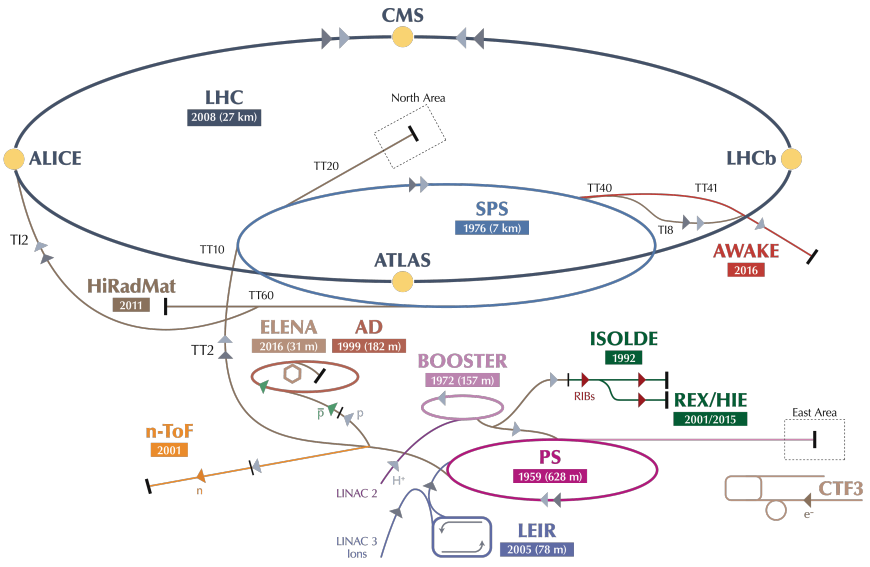

Figure 3.1: The LHC and its accelerator chain with the four main detector experiments at their interaction points within the framework of the entire CERN accelerator complex [208].

The protons of the LHC beam originate from the ionisation of hydrogen atoms and are initially accelerated to 50 MeV in a linear collider called LINAC2. During the first acceleration, radio frequency cavities are used to split the protons into bunches. These protons are then transferred to the Proton Synchrotron Booster where they reach an energy of 1.4 GeV. The Proton Synchrotron (PS), which is the oldest accelerator of the complex and put into operation almost 60 years ago, accelerates

the protons further to an energy of 25 GeV after leaving the booster. The PS was also used in the past to provide beams to other experiments such as a neutrino beam to the bubble chamber Gargamelle which led to the discovery of weak neutral currents in 1974. Following the PS, in the Super Proton Synchrotron (SPS) with a circumference of 7 km the protons gain an energy of 450 GeV, which is the injection energy of the LHC. The SPS on its own was also used for important particle physics experiments - the experiments UA1 and UA2, which ran at the SPS, discovered the W and Z bosons in 1983. Bunches of protons from the SPS enter the separate beam pipes in both opposite directions around the LHC ring. With the help of radio frequency cavities situated inside the beam pipe and providing an ultrahigh vacuum of 10^{-10} mbar, these bunches are accelerated simultaneously. Once the protons reached their final energy of 4 TeV (equivalent to $\sqrt{s} = 8$ TeV) in 2012 and of 6.5 TeV since 2015, they collide at the different interaction points of the LHC where the beam pipes cross. These are directly located at the centre of the main detectors introduced above.
The proton bunches consist of about 10^{11} particles each. The design luminosity value that amounts to 10^{34} cm^{-2}s^{-1} is reached by up to 2,808 bunches with a bunch crossing every 25 ns. This number corresponds to at least 20 inelastic collisions per bunch crossing on average, depending on how the beam is focussed. In 2012, the bunch spacing was mainly 50 ns while 25 ns was reached recently at $\sqrt{s} = 13$ TeV.
In order to keep the beams on their path within the LHC rings, 1,232 superconducting dipole magnets with a magnetic field of up to 8.6 T were installed. In total, 392 quadrupole magnets are responsible for correcting the position of the beams and their focusing. These guidance magnets as well as the acceleration cavities both rely on superconducting technologies. The temperature to which the dipole magnets are cooled down amounts to about 1.9 K. The high central field strengths are realised by the usage of superfluid helium.
In 2012, the LHC delivered pp collision data corresponding to an integrated luminosity of about 22.8 fb^{-1} [209], out of which 21.3 fb^{-1} were recorded by the ATLAS detector. The integrated luminosity in pp collisions in 2012 as a function of time is plotted in Fig. 3.2. The uncertainty in this luminosity was determined to be $\delta\mathcal{L}/\mathcal{L} = \pm 1.9$ % [210]. The recorded dataset is discussed more thoroughly in Sec. 6.1.

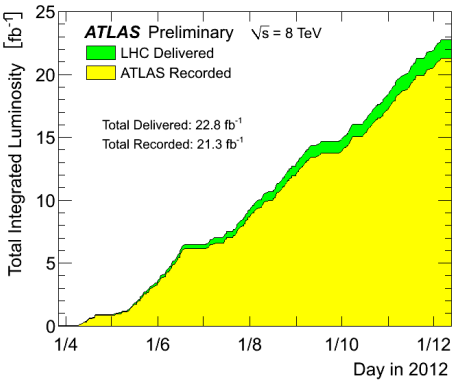

Figure 3.2: The total integrated luminosity in 2012 versus days in pp collisions delivered by the LHC (green) and recorded by the ATLAS detector (yellow) [209].

3.2 Detector Observables and Coordinates

Throughout the analysis and also in the next paragraphs, which describe the ATLAS detector with its components more in-depth, several detector-related quantities are used and thus specified in the following.

The integrated luminosity $\int \mathscr{L}\,\mathrm{d}t$ is a measure of the number of collisions occurring within a particular time interval and constitutes, according to its definition, an integral of the instantaneous luminosity $\mathscr{L}$ that helps to determine the event rates, measured per second and unit area [$\mathrm{cm}^{-2}\mathrm{s}^{-1}$]. The latter luminosity can be calculated for a collider like the LHC in terms of the numbers of particles in the colliding bunches, n_1 and n_2, the collision frequency f of the two bunches and the root-mean-square of the horizontal and vertical beam sizes σ_x and σ_y according to:

$$\mathscr{L} = \frac{f n_1 n_2}{4\pi\sigma_x\sigma_y},$$

based on the assumption that the beams have a Gaussian profile and collide head-on. Geometric luminosity reduction factors correct for effects depending on the corresponding collider setup and geometry. A further focussing of the beam in both directions x and y reduces σ_x and σ_y and can, correspondingly, lead to increased instantaneous luminosities.
The integrated luminosity as an integral over time is usually measured in inverse barns b^{-1} (picobarns and femtobarns are realistic scales) where $1\mathrm{b} = 10^{-28}\,\mathrm{m}^2$. The luminosity $\int \mathscr{L}\,\mathrm{d}t$ can be used to calculate a number of events N measured using a detector like ATLAS for a specific physics process if the cross-section σ of this underlying process is known, following the relation: $N = \sigma \int \mathscr{L}\,\mathrm{d}t$.

A detector coordinate system can be defined using several types of coordinates. A common choice are cylindrical coordinates (r, θ, ϕ) where r represents the radial distance from the beam axis and ϕ the azimuthal angle, which defines the direction vertical to the beam axis, while θ specifies the polar angle as the angle between the beam axis and the particle's flight direction. In addition, a Cartesian coordinate system (x, y, z) can be used to describe positions within the ATLAS detector. The origin is set to the nominal beam interaction point at the centre of the detector. The third coordinate z is equivalent to the beam axis and points anticlockwise so that x and y span the transverse plane, i.e. the plane perpendicular to the beam axis. The x axis is defined in a way that it matches with the local horizon and points to the accelerator's central position while the y axis points upwards.
Based on this definition of the transverse plane, momenta and energies are often given as transverse quantities written in the following form:

$$p_\mathrm{T} = \sqrt{p_x^2 + p_y^2} = |p| \sin\theta \qquad \text{and} \qquad E_\mathrm{T} = E \sin\theta\,,$$

with the above defined polar angle θ. Instead of this angle, the pseudorapidity η is normally used

to characterise positions inside a detector. A related quantity is the rapidity y:

$$y = \frac{1}{2}\ln\left(\frac{E+p_z}{E-p_z}\right).$$

For particles with high energies that are highly relativistic ($m \ll E$), the transverse momentum is approximately $p_z = |p|\cos\theta \approx E\cos\theta$ which leads to the definition of the pseudorapidity:

$$\eta = \frac{1}{2}\ln\left(\frac{1+\cos\theta}{1-\cos\theta}\right) = -\ln\tan\frac{\theta}{2}.$$

The usage of this quantity is mainly based on the fact that differences measured in η are invariant under Lorentz boosts in z direction. Besides, the differential cross-section as a function of the pseudorapidity is approximately flat in the detector region close to the beam axis as an area with a rather high particle density. This also motivates the choice of the coordinate system: (ϕ, η, z).
Distances in the detector and between particles are given in the η-ϕ-plane pursuant to:

$$\Delta R = \sqrt{\Delta\phi^2 + \Delta\eta^2}.$$

Detectors are designed to measure and identify particles originating from high energy collisions. There are different ways to detect these particles and measure their properties depending on the nature of their interactions with matter: One can observe charged particles or the production of secondary charged particles and their paths without affecting the trajectory of the underlying primary particle using their interactions, or one detects particles by stopping them and measures their energy deposit in the detector material, which is done in a calorimeter.
Charged particles can interact electromagnetically with a detector without losing a large portion of their energy. Usually, series of those measurements are made within a large detector following the trajectory of the particle to reconstruct its track with a high precision. Secondary particle trajectories contain information about the momentum and type of the underlying primary particle. Such measurements exploit the curvature of a particle's trajectory in a magnetic field which is related to the transverse momentum p_T of the particle given in GeV according to:

$$p_\mathrm{T}\,[\mathrm{GeV}]\cos\lambda = 0.3B\,[\mathrm{T}]R\,[\mathrm{m}].$$

The variable R denotes the radius of the curvature measured in metres, B is the magnetic flux density in tesla and λ is the pitch angle between the flight direction and the transverse plane perpendicular to the magnetic field. The charge of the particle can be accessed by the bending direction.
There are two types of calorimeters to measure the energy of the particles. One stops electromagnetically interacting particles - electrons and photons - and the other strongly interacting charged and neutral hadrons (that are not fully stopped in the first one), called electromagnetic and hadronic calorimeter, respectively. The location of the energy deposit in the calorimeter provides information about the momentum direction of the particle. The various techniques are exploited by the ATLAS detector and its different components, described more thoroughly on the following pages.

3.3 The ATLAS Detector

ATLAS (A Toroidal LHC ApparatuS) is one of the two multipurpose detectors built around the beam line of the LHC and composed of different subdetectors. Its name originates from the largest magnet system incorporated in the detector, a toroid magnet. ATLAS consists of four main parts: an inner detector, a calorimeter system, a muon spectrometer and a magnet system, made up of a solenoid and a toroidal system. An overview of the entire detector and its subsystems is sketched in Fig. 3.3, displaying its cylindrical geometry. The detector surrounds almost the entire 4π solid angle around the collision point in the detector centre, it is about 44 m long, measures 25 m in diameter and weighs approximately 7,000 t in total [199].

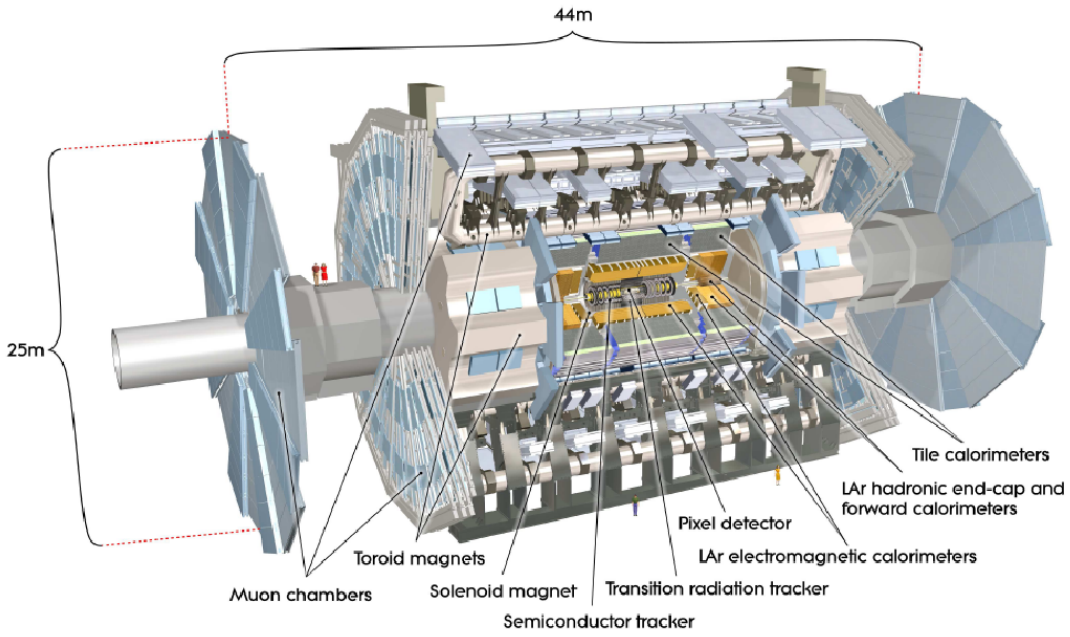

Figure 3.3: Sketch of the ATLAS detector and its subsystems [199].

ATLAS as a multipurpose detector with its large angular coverage and the ability to measure a broad range of particle momenta (from less than one GeV up to a few TeV) is engineered to allow for measurements of a substantial variety of different physics processes. A considerable accuracy in all subdetectors is required to collect collision data of the highest possible quality. It is guaranteed by several requirements which include, for instance, the distinction of multiple interactions from each other due to the high beam intensities to fully reconstruct the underlying collision event.

Particles from the interaction vertices traversing the detectors can be detected and identified by the successive layers of the ATLAS detector characterised by different radiation resistances or granularities and by employing various technologies.
The innermost detector, which is first traversed by the particles, measures charged particles utilising tracking technologies. The particle trajectory is bent in this inner part of the detector caused by

the superconducting solenoid which allows for a measurement of the momentum and the sign of charge of the associated particle, as described in Sec. 3.2.
The electromagnetic (EM) and hadronic calorimeters located around the solenoid magnet measure the energy of the traversing particles. The calorimeter cells record the deposited energy of the particles which lose energy due to interactions with the detector material via a cascade of collisions until they are finally stopped in that detector part. At high particle energies, electrons lose their energy in the EM calorimeter mainly by bremsstrahlung, while photons lose theirs by e^+e^- pair production. Electromagnetic interactions are characterised by the radiation length X_0, the distance over which an electron reduces its energy due to bremsstrahlung by a factor of $1/e$. Hadrons lose only a fraction of their energy in the EM calorimeter and deposit their remaining energy in hadronic calorimeters by a combination of nuclear and ionisation interactions. Thus, a hadronic interaction length λ specifies these interactions, which is, for a given material, often larger than X_0.
Muons, for which ionisation is the dominant energy-loss process, leave the calorimeters as they are minimum ionising particles pursuant to the Bethe-Bloch formula [28]. That is why a muon spectrometer forms the outermost layer of ATLAS which allows for a measurement of the muon momentum and triggers on these leptons after they passed the calorimeters. These measurements exploit the bending of the tracks caused by the toroidal magnetic field giving ATLAS its name.
Particles which are only weakly interacting like neutrinos or certain particles predicted by BSM models do not interact with the detector material and the measured energy imbalance of the event needs to be exploited to deduce their existence.

3.3.1 Inner Detector

The innermost portion of the ATLAS detector, simply called *Inner Detector* (ID), begins a few centimetres from the beam axis and is composed of three systems of subdetectors: the *Pixel Detector*, the *Semiconductor Tracker* (SCT) and the *Transition Radiation Tracker* (TRT). The former two detectors are based on a silicon semiconductor technology whereas the TRT contains a gas mixture of xenon, carbon dioxide and oxygen in which transition radiation is induced. The dimensions of these subdetector layers are given in Fig. 3.4, showing a longitudinal and a transverse section of the Inner Detector. The length of the cylindrical volume of the ID amounts to 6.2 m with a radius of around 1.1 m. The ID is designed in a way to measure particle momenta in a pseudorapidity range of $|\eta| < 2.5$ with an associated momentum resolution of $\sigma_{p_\mathrm{T}}/p_\mathrm{T} = \sqrt{(0.05\%)^2 p_\mathrm{T}^2 + (1\%)^2}$.

The Pixel Detector as the innermost detector part consists of three layers of concentric cylinders in the barrel part and three endcap disks which are vertical to the beam axis and located at each side. As the detector component closest to the beam pipe, it starts 5 cm away from the interaction point which requires a high granularity, given the large particle density originating from the collisions in this region. The layers and disks host 1,744 modules that are composed of more than 80 million readout channels. Each of these channels corresponds to a segment of the Pixel Detector, an n^+-on-n-doped silicon pixel which operates as a sensor. The pixels cover an area of at least 50×400 μm^2 and their thickness amounts to 250 μm. The detector reaches a position resolution of up to 10 μm and,

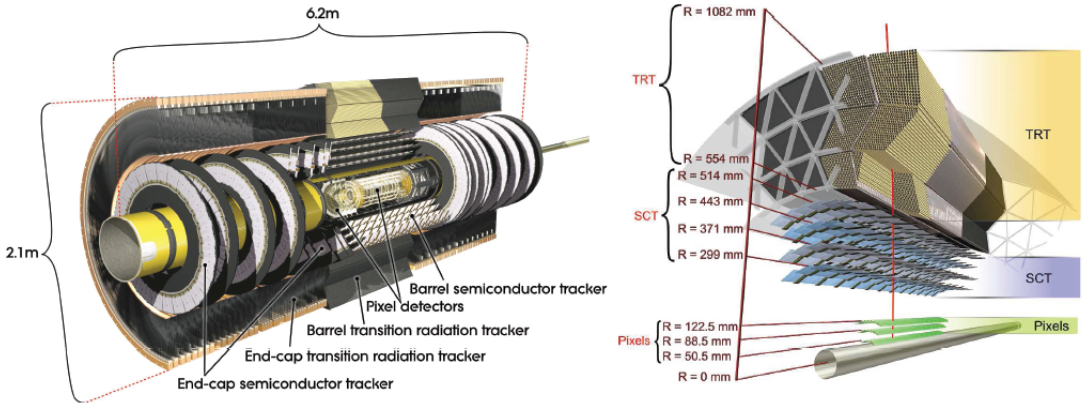

Figure 3.4: The Inner Detector of the ATLAS experiment: The left picture shows the Inner Detector with its different subdetectors. The sketch on the right displays a transverse section of the ID including the distances of the detector layers with respect to the beam line [199].

thus, this pixel structure enables a high precision measurement of tracks as well as the identification of primary and secondary vertices. The latter facilitates the detection of tau leptons or heavy flavour quarks. In particular the identification of b jets, the so-called b-tagging, is used in the analysis presented in this thesis and is discussed in more detail in Sec. 4.5. A pseudorapidity coverage of $|\eta| < 2.5$ is achieved.

The SCT as the next part of the ID is comparable in concept and function but consists of long silicon strips instead of small pixels to cover a larger area. A total of 4,088 modules contain the strips with a width of 80 µm and a length of 126 mm resulting in 6.3 million readout channels. In the barrel region, these strips are arranged parallel to the beam axis in four layers, while the endcap region has nine disks of radially oriented strips. The latter covers a pseudorapidity range of $1.4 < |\eta| < 2.5$, the barrel region comprises $|\eta| < 1.4$. A hit resolution of up to 17 µm is reachable.

350,000 drift tubes constitute the detecting elements of the TRT, so-called straws, which are filled with the gas mixture described above. 73 planes of these straw tubes parallel to the beam axis, having a radius of 2 mm each, form the barrel part. The endcap part contains 160 straw planes with a radial orientation. The TRT, in addition to measuring particle tracks via ionisation, exploits transition radiation for the charged particle identification. Relativistic particles on their way through the detector with high velocity emit photons when they cross the interface of two media which have different dielectric constants ε_r. Different sorts of particles can be distinguished based on the rate of the emitted photons. Heavier particles, like pions, produce merely a small number of photons whereas electrons, related to their low mass, are able to produce a considerable amount of transition radiation. The spatial resolution provided by silicon trackers is considerably better than the one from the TRT. The straw tubes reach resolution values of 130 µm. However, due to the filling gas, the drift time of, for example, electrons is significantly reduced so that neighbouring bunch crossings have a smaller impact. The TRT layout enables a measurement of charged tracks

with a transverse momentum of $p_T > 0.5$ GeV and $|\eta| < 2.0$.
The combination of the three subdetectors, Pixel Detector, the SCT and the TRT, results in 43 measured space points per track, required for a high precision measurement of particle tracks.

For the data-taking periods since 2015 at $\sqrt{s} = 13$ TeV, a new subdetector was added, the *Insertable B-Layer* (IBL) [211] as an additional layer of the Pixel Detector, located even closer to the beam.

3.3.2 Calorimeter System

The Inner Detector is surrounded by two calorimeter systems that cover a large pseudorapidity range of $|\eta| < 4.9$: an inner *electromagnetic calorimeter system* and an outer *hadronic calorimeter system*. These systems are both so-called *sampling calorimeters* whose main characteristic is an alternation of layers composed of active material, which is connected to a readout system, and passive and dense absorber material. The calorimeter system measures the energy deposit of charged and neutral particles by absorbing the particle's energy in the calorimeters with their compact sizes. In most cases, liquid argon (LAr) operates as the active medium, which is used for the particle's energy determination in the ATLAS calorimeters. A broad energy range beginning with a few GeV and reaching the TeV scale as well as the momentum imbalance of a particle reaction can be measured. The latter is caused due to particles that leave the calorimeters without being detected, as, e.g., neutrinos. The entire calorimeter system with its different subcomponents is shown in Fig. 3.5.

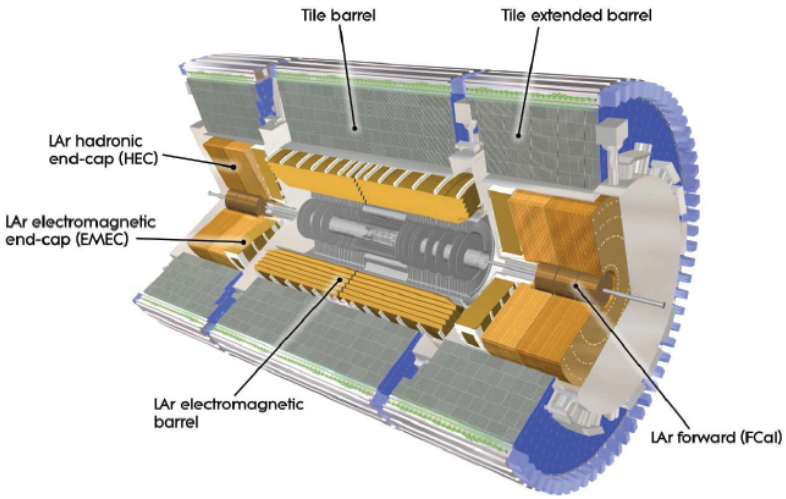

Figure 3.5: The calorimeter system of the ATLAS experiment: The different cells of the electromagnetic and the hadronic calorimeters in the barrel and forward regions are sketched [199].

In order to measure electron and photon energies, the Electromagnetic Calorimeter (ECAL) possesses a fine granularity, concomitant with a very good spatial resolution. An appropriate measurement of jets and the energy imbalance of the underlying event, which requires a large $|\eta|$ coverage, is realised by the hadronic calorimeters which are composed of coarser constituents.
The thickness of the ECAL parts in the barrel region is equivalent to at least 22 radiation lengths

X_0 and reaches 24 or more in the endcap region. These thicknesses depend on the pseudorapidity region of the calorimeter and can rise up to 38 X_0. Taking the hadronic calorimeters into account as well, a particle has to pass about 11 interaction lengths λ (averaged number) which is large enough to adequately suppress punch-through effects to the muon spectrometer.

The ECAL covers the pseudorapidity region $|\eta| < 3.2$ and contains a barrel part ($|\eta| < 1.475$) and two endcap calorimeters ($1.375 < |\eta| < 3.2$). It has an accordion geometry to ensure a uniform and particularly fast response and is based on liquid argon (LAr) as the active medium over which Kapton electrodes are spread. Lead plates are used as the passive absorber material of this sampling calorimeter. All three components (barrel and two endcaps) are placed in their own cryostat. The cell granularity differs between the different calorimeter layers. In η, for example, the granularity is very fine in the first layer and amounts to $\Delta\eta = 0.0031$ while it reaches about $\Delta\eta = 0.025$ to 0.05 in other layers. In ϕ, the granularity ranges from about $\Delta\phi = 0.0245$ to 0.1.
The energy resolution, defined as $\sigma_E/E = a/\sqrt{E} \oplus b$, with a stochastic term a and a constant term b, of the ECAL amounts to [200]:

$$\frac{\sigma_E}{E} = \frac{10\%}{\sqrt{E}} \oplus 0.7\%\,.$$

The hadronic calorimeters (HCAL) are built outside of the ECAL to ensure that showers from hadronic particles and jets penetrating the ECAL are entirely stopped and included in the calorimeter system.
The central region with $|\eta| < 1.7$ is covered by the *Hadronic Tile Calorimeter*, split into a more central barrel part ($|\eta| < 1.0$) and two outer extended barrel regions ($0.8 < |\eta| < 1.7$). This sampling calorimeter is composed of plastic scintillating tiles - according to its name -, having a thickness of 3 mm and iron absorbers. The calorimeter possesses three layers in longitudinal direction with a granularity of $\Delta\eta = 0.1$ in the two inner and $\Delta\eta = 0.2$ in the outermost layers and a segmentation of $\Delta\phi = 0.1$ in all layers.
The *Hadronic Endcap Calorimeter* (HEC) covers the pseudorapidity range $1.5 < |\eta| < 3.2$. Copper plates operate as absorber and liquid argon serves again as active material of this sampling calorimeter. The granularity is between 0.1 and 0.2 for both $\Delta\eta$ and $\Delta\phi$.
The *Forward Calorimeter* (FCAL), finally, provides coverage of the range $3.1 < |\eta| < 4.9$. This sampling calorimeter also uses liquid argon as active material. Copper functions as absorber in an inner and electromagnetic part of this calorimeter, tungsten in the outer hadronic part. In the former, the granularity is about $\Delta\eta \times \Delta\phi = 0.1 \times 0.1$ and reaches $\Delta\eta \times \Delta\phi = 0.2 \times 0.2$ in the latter hadronic part. The large pseudorapidity coverage ensures that all particle energies of a certain event can be recorded. The energy resolution of the hadronic calorimeters in the barrel and endcap region is:

$$\frac{\sigma_E}{E} = \frac{50\%}{\sqrt{E}} \oplus 3\% \quad \text{and amounts to} \quad \frac{\sigma_E}{E} = \frac{100\%}{\sqrt{E}} \oplus 10\% \quad \text{in the FCAL [200].}$$

3.3.3 Muon System

The muon spectrometer (MS) constitutes the outermost part of the ATLAS detector and involves four different types of muon chambers. The momenta of muons leaving the calorimeter system and having energies above 3 GeV can be measured in the pseudorapidity region of $|\eta| < 2.7$. The resulting muon tracks are bent in the magnetic field of the air-core toroidal magnet system. Due to the orientation of the fields in the barrel and the endcap region, these tracks are predominantly perpendicular to the magnetic field lines.
The full layout of the spectrometer is presented in Fig. 3.6, containing both tracking chambers required for precise momentum measurements and trigger systems with fast response times. The barrel part is composed of *Monitored Drift Tubes* (MDT), employed for tracking, and *Resistive Plate Chambers* (RPC) which trigger events. In contrast, the endcap region of the muon system hosts additional MDTs and *Cathode Strip Chambers* (CSC) as tracker as well as *Thin Gap Chambers* (TGC) for trigger purposes. The entire muon system is split into eight octants which overlap in the azimuthal angle ϕ to guarantee a full coverage to detect muons. In both regions, barrel and endcap, muons typically cross three longitudinal spectrometer layers.

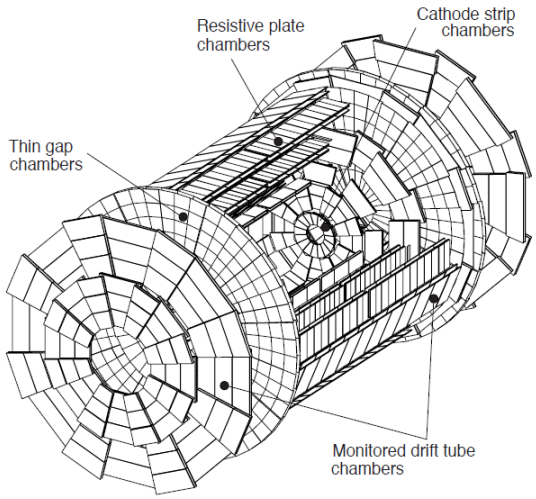

Figure 3.6: The muon system of the ATLAS experiment: The four different parts, tracking chambers as well as trigger systems, are shown [199].

To ensure a high performance during particle reconstruction, a good alignment of the muon system with respect to the chamber position is necessary. The tracking technologies were chosen to obtain a high precision with respect to the measured particle flux whereas the trigger detectors are supposed to respond fast and highly efficiently in both the barrel and endcap regions.

MDTs are assembled in three layers of chambers in the barrel part of the muon system up to $|\eta| < 2.0$ and in most layers of the endcap detectors. MDTs are combined to three to eight layers of tubes and made of aluminium filled with an Ar/CO_2 gas mixture. The tubes with a diameter of 30 mm reach a position resolution of 80 µm.

On the contrary, CSCs are only installed in the innermost endcap layer which covers the forward region of $2.0 < |\eta| < 2.7$. Due to their higher granularity, they allow for a higher precision and can deal better with the higher rates of particles in this detector region. The chambers constitute multiwire proportional chambers which are segmented into strips having orthogonal directions. They are filled with a mixture of the gases argon, CO_2 and CF_4. The position resolution of a single CSC in the bending plane is 40 μm.
RPCs are used in the barrel part of the muon system ($|\eta| < 1.05$) to induce a prompt trigger signal. Each RPC is composed of two bakelite plates and a gas-filled gap in between where $C_2H_2F_4$ is used. The response times of the RPCs and also of the TGCs are about 15-25 ns after the muon traversed the chambers.
The latter chambers, the TGCs, are located in the larger pseudorapidity region of $1.05 < |\eta| < 2.4$. They are built similar to the RPCs and contain two cathode plates with an anode wire in between, filled with a mixture of carbon dioxide and a C_5H_{10}, but they are able to cope with the large particle fluxes in the endcap region.

3.3.4 Forward Detectors

In addition to these main detector components whose recorded data events are used in this thesis, three forward detectors are placed within and around the ATLAS detector in areas close to the beam. They cover the most forward detector regions to obtain information about the particle flux there and allow for luminosity measurements.

The forward detector closest to the interaction point is LUCID (*LUminosity measurement using a Cherenkov Integrating Detector*) whose two symmetric modules have a distance of 17 m to the centre of ATLAS. These modules, which exploit the Cherenkov effect, consist of 20 aluminium tubes each and are filled with C_4F_{10}. The detector arms cover a pseudorapidity range of $5.6 < |\eta| < 5.9$ and measure the luminosity delivered by the LHC.

The *Zero Degree Calorimeter* (ZDC) measures neutral particles (i.e. neutrons and photons) in the very forward region of $|\eta| > 8.3$. It is located at both sides of ATLAS with a distance of ±140 m to the interaction point. It consists of tungsten plates and quartz rods for coordinate and energy measurements. The ZDC measures the energy of the spectator nucleons to estimate the overlap region of the nuclei that collide.

ALFA (*Absolute Luminosity For ATLAS*) intends to measure the luminosity based on the elastic scattering rate at very small angles (around 3 μrad). The two detector parts are ±240 m away from the interaction point and use scintillating fibres for the detection. They cover a pseudorapidity range of $10.6 < |\eta| < 13.5$.

3.3.5 Magnet System

The magnet system of the ATLAS detector aims at bending the particle's trajectories to allow for measuring momenta of charged particles traversing the detector. As already briefly described in the introduction of this section, a solenoid magnet provides a magnetic field in the Inner Detector while barrel and endcap toroidal systems of magnet coils produce a magnetic field in the outer parts of the detector where the muon spectrometer is located. The system relies on superconducting magnets which reach a temperature of around 4.5 K as they are cooled by liquid helium. A schematic of the entire ATLAS magnet system can be found in Fig. 3.7.

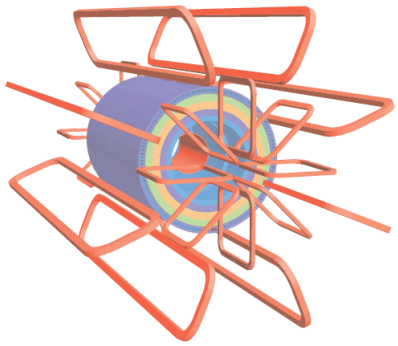

Figure 3.7: The magnet system of the ATLAS experiment with the solenoid in the inner region and the air-core toroids in the barrel and endcap regions of the outer detector areas [199].

The solenoid magnet is built between the Inner Detector and the calorimeter system. In order to minimise energy losses of particles when they pass the solenoid before entering the calorimeter, the magnet was designed to have a low weight and contain as little material as necessary. The axial magnetic field caused by the solenoid, which covers a range of $|\eta| < 2.7$, has a strength of 2 T in the central part of the Inner Detector.
The toroidal magnet system is composed of three air-core toroids, one in the barrel and two in the endcap region which cover together a region of $|\eta| < 2.7$. Each system involves eight superconducting coils inducing a magnetic field with a strength of about 2.5 T in the central part that increases to 3.5 T in the forward regions. The provided bending power amounts to 2 to 6 T·m in the barrel part and ranges from 4 to 8 T·m in the endcap toroids.

3.3.6 Trigger System

Each bunch crossing results in enormously large amounts of data where the vast majority of events are expected to originate from QCD scattering processes. To select processes of interest, the ATLAS experiment utilised a *three-level trigger system* for the data-taking period at a centre-of-mass energy of $\sqrt{s} = 8$ TeV. Besides, the amount of kept data needs to be restricted since the storage capacity is limited and one event requires 1.5 MB of storage space on average. At the design bunch-crossing of 25 ns, a bunch collision rate of 40 MHz is provided which needs to be reduced to design values of around 100 Hz by the trigger levels. The underlying data acquisition system (DAQ) collects the

data taken from all detector components of the ATLAS experiment and retains the events until a trigger decision is in place. The triggers that decide to keep or skip an event are referred to as level-1 trigger (LVL1), level-2 trigger (LVL2) and event filter (EF). The latter two form the high-level trigger (HLT).
The LVL1 is hardware-based and focuses on finding photons, jets, electrons, muons or hadronically decaying tau leptons as well as a high momentum mismatch in the transverse plane. This trigger identifies Regions-of-Interest (RoI) in the η-ϕ-space within 2.5 µs and reduces the event rate to about 75 kHz.
The LVL2 and the EF are both software-based triggers. The former trigger analyses the sort of trigger objects and evaluates the energy and direction based on the RoIs. It decides within up to 40 ms and decreases the event rate further to the order of 1 kHz.
The EF, finally, exploits the full event information and provides an additional drop of the event rate to approximately 400 Hz for $\sqrt{s} = 8$ TeV by using a complex event selection. This is comparable to the following offline selection on which the final event reconstruction is based. The trigger rates can be adjusted by varying thresholds or by the usage of alternative selection cuts.
Fig. 3.8 presents an overview of the ATLAS trigger levels. To be permanently stored and finally reconstructed, all three trigger levels need to be passed by an event.

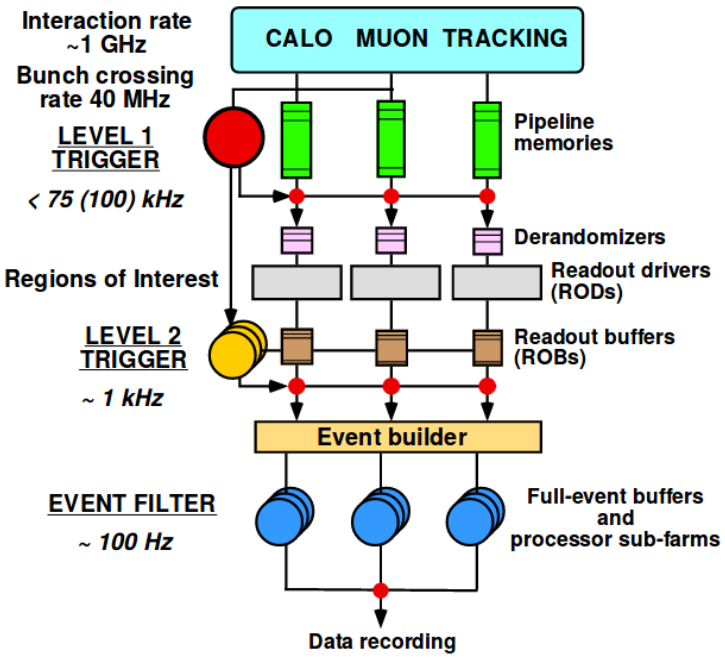

Figure 3.8: Schematic overview of the full ATLAS trigger and DAQ system with the original design event rates after each trigger step [199].

4 Object Definition

The measurement of the top quark decay width requires a reconstruction of the decay products of the $t\bar{t}$ pairs. The ATLAS detector, introduced in Sec. 3.3, measures electronic signals of these physics objects resulting from the top quark decay in its different subdetectors. Based on these signals, the interesting physics objects need to be reconstructed which is done using the reconstruction software of the ATLAS experiment which is called Athena [212].
The performance of the object reconstruction on recorded ATLAS data is compared to Monte Carlo simulated events. The level of (dis)agreement between simulation and data can be modelled by parametrised corrections, referred to as *scale factors* used for the object reconstruction. The evaluation of scale factors is further described in the following subsections. The reconstructed physics objects are commonly called object candidates since their recorded detector signatures can also be produced by an object of a different type.
According to the signature of $t\bar{t}$ decays analysed for the decay width measurement of the top quark, signal events contain the following objects: one electron or muon, four jets, two of which are b-tagged, and missing transverse momentum due to the neutrino which escapes from the detector. After a general introduction of the fundamentals of the object reconstruction, the definition and reconstruction of these physics objects is described in detail. The τ leptons are not explicitly listed in the following as they have a rather short lifetime of around $2.9 \cdot 10^{-13}$ s and thus decay before they can traverse the detector. This heaviest lepton decays with a probability of 65% into hadrons (pions and kaons) and in 35% of all cases leptonically into electrons and muons with the corresponding neutrinos according to: $\tau \to e\bar{\nu}_e\nu_\tau$ and $\tau \to \mu\bar{\nu}_\mu\nu_\tau$. Hence, τ leptons are not part of the object reconstruction of this analysis (see also Sec. 2.2.2), but leptonic τ lepton decays contribute to the measured signal because the signature is the same as for the lepton+jets decay channel of $t\bar{t}$ pairs where the leptonically decaying W boson decays into an electron or muon (and not a τ lepton) due to the additional neutrinos which cannot be detected.

4.1 Fundamentals of the Object Reconstruction

Following the description of Sec. 2.2.1, the decay products of a $t\bar{t}$ decay originate from a hard interaction or hard scattering process, referred to as *parton level*. Not only quarks and gluons, as the name parton indicates, are present at parton level, also other bosons and leptons from the hard interaction are included in the parton level description. Afterwards, these objects shower, and quarks and gluons hadronise later, which then leads to the creation of bound states. Since this level after parton showering and hadronisation contains detectable particles, it is normally called *particle*

level. Often, the parton and the particle level are also denoted as the respective truth level. While traversing the detector, these particles interact with the detector material and leave a characteristic signature. This is the *detector level*. These three levels are visualised in Fig. 4.1. By way of example, jets produced in proton-proton collisions are shown. At detector level, subdetectors as used in the ATLAS detector are illustrated to measure particle tracks or energy deposits.

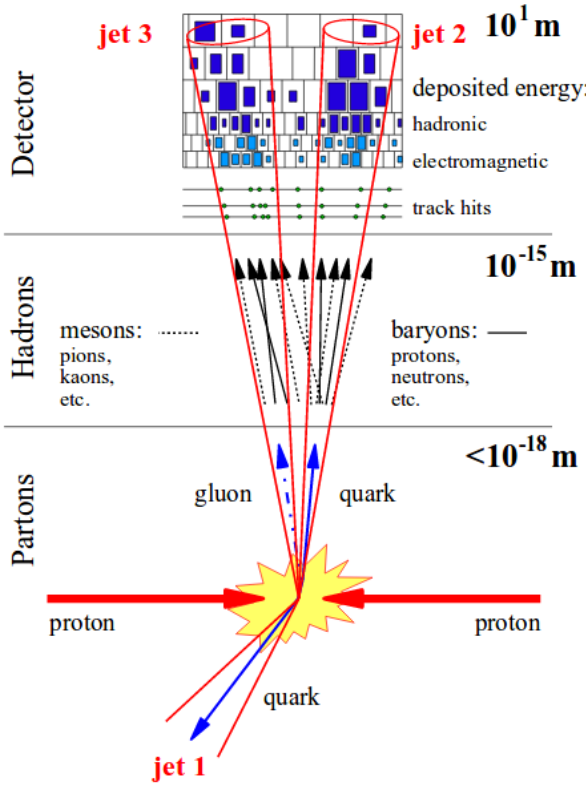

Figure 4.1: The different stages of physics objects with the underlying scales and their descriptions: parton level, particle level and detector level [213].

The detector level reconstruction for particular objects is delineated in the next subsections. Methods employed to reconstruct tracks and vertices in the ATLAS detector are introduced in the following lines.

Tracks created by charged particles in the ATLAS detector are reconstructed based on a χ^2 fit [214]. In the Inner Detector, the tracks are reconstructed in the full available pseudorapidity region of $|\eta| < 2.5$ and the entire transverse plane using hits in all three subcomponents - the Pixel Detector, SCT and TRT. Due to the solenoid magnet around the ID, the particle tracks take a circular trajectory transverse to the beam axis.

Two methods are applied: A so-called inside-out pattern recognition starts with creating three-dimensional space points from seeds in both the silicon pixel and the SCT detector parts. The algorithm propagates to the outer ID parts to also incorporate hits measured in the TRT. The second is an outside-in or back tracking algorithm, which, according to its name, starts with segment seeds

in the TRT and moves to the innermost detector parts to include hits recorded by the silicon-based detectors. The former algorithm mainly serves to reconstruct tracks from primary particles; those directly originating from the pp collision or produced from particles from the pp collision, but with a lifetime shorter than $3 \cdot 10^{-11}$ s. The latter focuses on track reconstruction from secondary interactions. The collected hits then enter a χ^2 fit. In addition, the track candidates need to fulfil quality criteria which impose requirements on so-called impact parameters measured with respect to the beam axis or on the number of hits in the different detector parts. With an increasing rate of collisions and thus larger detector occupancies, stricter requirements for the reconstruction of tracks are utilised to minimise fake tracks [215].

The reconstruction of primary event vertices as the initial interaction points is realised using an algorithm which is part of the high-level trigger and an offline reconstruction algorithm exploiting a maximum-likelihood fit [216]. The latter makes use of the adequate ID track efficiencies and resolutions. The algorithm reaches vertex resolutions of about 23 μm in the transverse direction and around 50 μm in the direction of the beam.
Events considered for this measurement possess at least one reconstructed vertex consistent with the beam collision region in the x-y plane with at least four associated tracks that have $p_{\mathrm{T}} > 400$ MeV. In case more than one vertex exceeds this lower limit, the one having the largest sum of squared momenta from its associated tracks is regarded as the primary vertex (PV).

4.2 Muons

The identification of muon candidates is carried out using information from different detector components. In contrast to electrons, muons act as minimum ionising particles so that merely a small fraction of the muon energy is lost in the ATLAS calorimeters. Consequently, muon tracks are not only recorded in the ID but also in the muon spectrometer as the outermost part of the ATLAS detector. The reconstruction algorithm employed in this analysis to find muon candidates uses track information from both the ID and the MS and considers the small muon energy loss in the calorimeter system as well. The reconstruction of MS tracks relies on first searching for track segments in the chambers and combining information from the different spectrometer components then. This reconstructed MS track needs to match a reconstructed ID track, following the description from above. This algorithm is thus called *combined muon* algorithm. Additional quality criteria on the ID track are imposed, requiring a certain number of hits in all ID subdetectors. Muon candidates passing the combined muon algorithm must also pass cuts on the transverse momentum and the pseudorapidity following the ID acceptance: $p_{\mathrm{T}} > 25$ GeV and $|\eta| < 2.5$.
This algorithm is used as its resolution and efficiency outperforms other approaches like the stand-alone muon algorithm, based on MS and calorimeter information only, the calorimeter-tagged muon algorithm, based on ID and calorimeter information only, or the segment-tagged muon algorithm, which uses basically the ID track reconstruction combined with local track segments recorded by the spectrometer chambers.

Furthermore, a separation criterion between muon candidates and jets is defined: $\Delta R > 0.4$ is required for the distance between the muon and one of the selected jets which reduces background due to non-prompt muons. Muon candidates also need to satisfy a p_{T}-dependent isolation requirement which is track-based and exhibits both good performance under high pile-up conditions and in boosted configurations (efficiency of 97%) where the distance between the muon and a jet is small. The scalar sum of the track p_{T} within a cone having a variable radius of $\Delta R = 10\ \mathrm{GeV}/p_{\mathrm{T}}^{\mu}$ around the muon (without the muon track itself) is required to be below 5% of the muon p_{T} [217]. Both sorts of pile-up, the in-time and out-of-time pile-up, i.e. multiple pp interactions from the same or previous bunch crossings, are considered. The so-called longitudinal impact parameter z_0 related to the muon track defined with respect to the selected event PV must not exceed 2 mm.

The reconstruction, identification and trigger efficiencies of muons differ between data and simulation. Scale factors correct for these discrepancies. They are derived using tag-and-probe techniques on $Z \to \mu^+\mu^-$ data and simulated samples and are applied to MC events [218]. Such tag-and-probe methods for $Z \to \ell^+\ell^-$ are based on *tag leptons* which fulfil tight selection criteria and *probe leptons*, which are investigated once a tag lepton is found, with looser isolation criteria. The number of matched and probe leptons in a sample is used to calculate efficiencies in data ($\varepsilon_{\mathrm{data}}$) and MC samples ($\varepsilon_{\mathrm{MC}}$) to derive scale factors (SF) according to $\mathrm{SF} = \varepsilon_{\mathrm{data}}/\varepsilon_{\mathrm{MC}}$.
Apart from that, reconstructed distributions of $Z \to \mu^+\mu^-$, $J/\psi \to \mu^+\mu^-$ and $\Upsilon \to \mu^+\mu^-$ resonances are used to check the muon momentum scale and resolution in simulation [218].
The reconstruction efficiency of the employed algorithm as a function of p_{T} and η, as used for the parametrisation of the scale factors, is shown in Fig. 4.2.

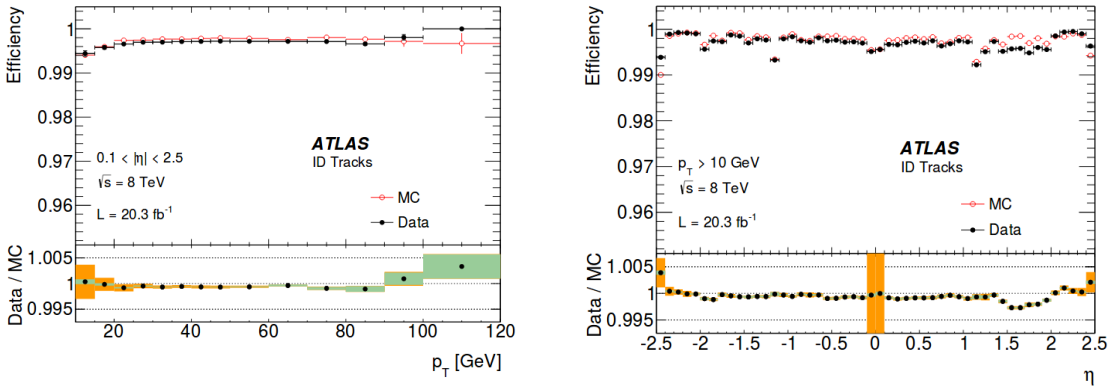

(a) **(b)**

Figure 4.2: The muon reconstruction efficiency of the ID parametrised as a function of (a) p_{T} and (b) η obtained from $Z \to \mu^+\mu^-$ events with muons exceeding a p_{T} of 10 GeV. The bottom panels reflect the ratio between the measured and the predicted efficiencies. The error bars on the efficiency numbers and the green areas in the ratio plot show only the statistical uncertainty whereas the orange bands contain also systematic uncertainties [218].

The scale factors also enter the evaluation of systematic uncertainties, as outlined in Ch. 8.2.

4.3 Electrons

Electrons are absorbed in the ATLAS Electromagnetic Calorimeter as they are supposed to leave their energy by forming electromagnetic showers in the calorimeter material. As electrons are charged, they also cause a measurable track in the Inner Detector so that a combination of calorimeter and ID information serves to identify electron candidates and to measure their deposited energy. Hence, electron candidate reconstruction [219] is based on these energy deposits in the ECAL, so-called clusters, which are associated with reconstructed ID tracks, described in Sec. 4.1.

Depending on the reconstruction criteria which differ in the signal efficiency or the power to reject background contributions due to photons or jets misidentified as electrons, electron candidates are characterised by cut-based selection methods as either loose, medium and tight, usually denoted as *loose++*, *medium++* and *tight++*. Recently, a fourth cut-based selection, called *multilepton*, was introduced which is optimised for low energy electrons in the $H \to ZZ \to 4\ell$ measurement. The additional plus signs indicate updates with respect to former classification criteria used for previous data-taking periods. For example, additional variables were used to improve the classification or cuts were loosened to take the higher instantaneous luminosity of the data taken in 2012 (with respect to former years) with different pile-up contributions into account. This ensures constant classification efficiencies. All electrons classified as tight are also contained in the medium category, and all medium electrons also count as loose ones. At the expense of the selection efficiency, the purity increases with a tighter classification. As a consequence thereof, the tight criteria exploit all tools available for particle identification, use stricter requirements on the track quality and reject non-isolated electron candidates to the largest possible amount. In this analysis, the tight++ ID requirement must be passed by all electron candidates.

The calorimeter clusters associated with the electron candidate are required to have a cluster pseudorapidity of $|\eta_{\text{cluster}}| < 2.47$, with the exclusion of the transition region between the barrel and endcap detector with $1.37 < |\eta_{\text{ cluster}}| < 1.52$, and $E_{\text{T}} > 25$ GeV. The latter quantity is the transverse energy, defined as $E_{\text{T}} = E_{\text{cluster}}/\cosh(\eta_{\text{track}})$. According to the indices, the energy E_{cluster} comes from the calorimeter cluster while the direction η_{track} originates from the ID track information. Moreover, isolation requirements are imposed to minimise the background from non-prompt electrons, produced in jets originating from hadron decays (including heavy flavour). A 90% efficient p_{T}- and η-dependent isolation cut is placed on the sum of the transverse energy and requires this quantity to be deposited within a radius of $\Delta R = 0.2$ around the calorimeter cells related to the electron candidate (called $E_{\text{T}}^{\text{cone20}}$). The sum of the energy deposited around the cells associated with the electron cluster is corrected for leakage from the electron cluster itself. Furthermore, the transverse momentum sum of the energy deposits associated with the track needs to be within a cone of radius $\Delta R = 0.3$ (called $p_{\text{T}}^{\text{cone30}}$) around the electron candidate. This isolation cut has an efficiency of 90% as well. These efficiency numbers are estimated based on a tag-and-probe method [220], as briefly described in Sec. 4.2 but using $Z \to ee$ events. The electron track longitudinal impact parameter z_0 with respect to the PV must be smaller than 2 mm.

Similar to muons, reconstruction, identification and trigger efficiencies need to be estimated for electron candidates to derive corresponding scale factors. Efficiencies are evaluated based on tag-and-probe techniques using $Z \to e^+e^-$ and $J/\psi \to e^+e^-$ events in data and MC samples [220]. The energy scale and resolution for electrons is determined from $Z \to e^+e^-$ decays using again data and MC events. The individual corrections to resolution and electron energy scales are obtained based on a χ^2 minimisation [221]. The energy calibration intends to correct and calibrate the cluster energy of the electron in order to take energy losses in the detector material outside of the calorimeter into account. The achieved calibration using multivariate algorithms is accurate up to 0.05% in most regions of the detector [221].

The reconstruction and identification efficiency of electrons parametrised as a function of E_{T} and η is given in Fig. 4.3.

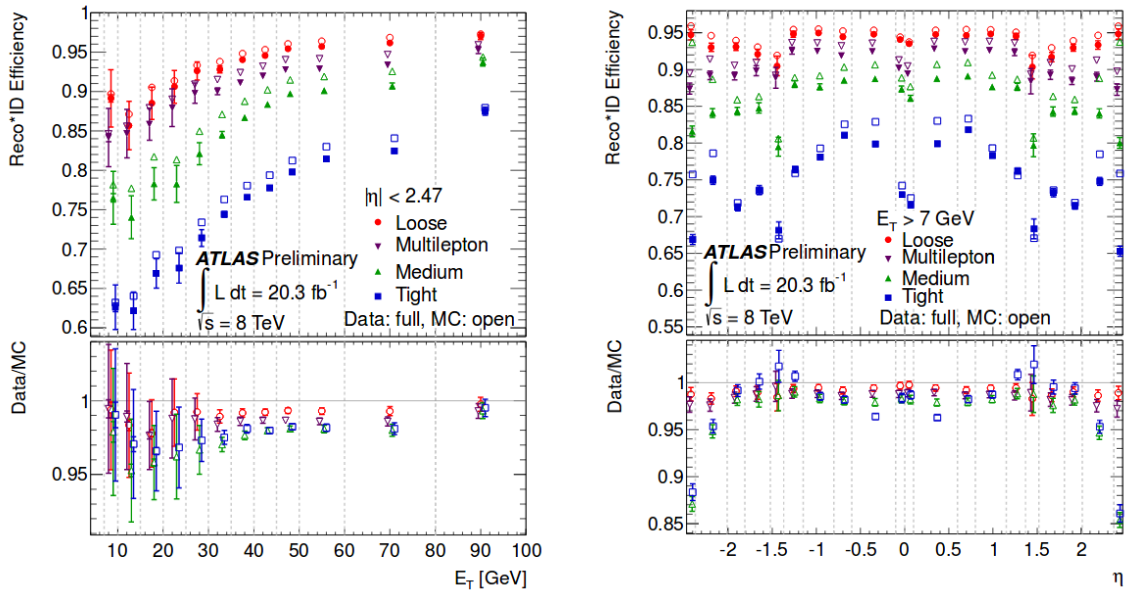

Figure 4.3: The electron reconstruction and identification efficiency parametrised as a function of (a) E_{T} and (b) η obtained from $Z \to e^+e^-$ events for four different cut-based algorithms as introduced in the text. The lower panels show the ratios between data and MC. The shown uncertainties are statistical (inner error bars) or statistical plus systematic (outer error bars) [220].

The systematic uncertainties arising from the scale factors of electrons are outlined in Ch. 8.2.

4.4 Jets

Free partons cannot be detected as discussed in previous chapters since quarks and gluons hadronise when traversing the detector. The particles which are produced in these hadronisation processes deposit their energy in the ATLAS calorimeter system. As the energy deposits are collimated, such collimated streams of energetic particles, so-called jets, can be reconstructed. For this procedure, particle tracks in the ID are used, combined with electromagnetic and hadronic showers in both the ECAL and the HCAL of the ATLAS detector. Since the analysis presented in this thesis is based on $t\bar{t}$ decays in the lepton+jets channel with four jets in the final state according to theory, the jet reconstruction presented in this subsection is very crucial.

There is no possibility to describe a jet in a unique way. A jet needs to be defined by a jet clustering algorithm. A commonly used jet definition includes clustering of calorimeter cells using the (pseudo)rapidity-azimuthal plane. An important criterion for a jet algorithm is infrared and collinear (IRC) safety [222] which means that the jet definition does not depend on the emission of a soft, i.e. infrared, or collinear particle: The jet configuration must be unaffected (a) if a particle i with $p_{\mathrm{T}} \to 0$ is added (IR safe) and (b) if a particle i with momentum p_i is replaced by particles j and k with $p_j + p_k = p_i$ and $|\vec{\rho}_j - \vec{\rho}_k| = 0$ where $\vec{\rho} = (y, \phi)$ (C safe).
In this analysis, the jets are reconstructed using the *anti-k_t algorithm* [223, 224] as a sequential recombination algorithm, defined to be IRC safe and suited for computations in perturbation theory of any desired order. The underlying radius parameter is set to $R = 0.4$. The jet reconstruction, implemented in the FastJet package [225], starts from calibrated topological clusters [226] which are built based on the energy deposits in the calorimeters. Distances d_{ij} between clusters i and j are calculated and the clusters are recombined, i.e. the sum of the two four-momenta is calculated to obtain massive jets, if $d_{ij} \leq R$. The difference d_{ij} is determined via:

$$d_{ij} = \min(p_{\mathrm{T},i}^{2p}, p_{\mathrm{T},j}^{2p}) \cdot \frac{\Delta R_{ij}^2}{R^2} \qquad \text{with} \qquad \Delta R_{ij} = \sqrt{(y_i - y_j)^2 + (\phi_i - \phi_j)^2}\,.$$

The variables p_{T}, y and ϕ denote the transverse momentum, the rapidity and the azimuthal angle of the clusters i and j. These clusters are only combined as long as $d_{ij} < d_{iB} = p_{\mathrm{T},i}^{2p}$. Otherwise, the jet is regarded as being complete. The exponent p is the algorithm parameter set to -1 for the anti-k_t algorithm. According to this parameter value, the algorithm prefers clusterings of hard particles instead of soft ones and leads to almost circular reconstructed jets around the hardest clusters with radius R. Clusterings that favour soft clusters require $p = 1$, while energy-independent ones favour $p = 0$. Due to the fact that the anti-k_t algorithm is based on a combination of energy and angles using distances where collinear particles are by definition clustered in the early iterations of the algorithm, it is IRC safe.

The topological clusters which enter the jet reconstruction algorithm constitute groups of calorimeter cells with a sufficient energy deposit above cell noise. The signal S over noise N ratio needs to be $S/N \geq 4$ for the seed cell and $S/N \geq 2$ for surrounding other cells added to the growing cluster.

The algorithm is able to cope with electronic noise and noise caused by pile-up jets to reduce the impact of in-time and out-of-time pile-up.
In a next step, the clusters need to be calibrated prior to jet finding to correct for effects due to non-compensation, out-of-cluster leakage and dead material. For this purpose, a local cluster weighting (LCW) calibration scheme [227, 228] is applied. Simulations of charged and neutral particles are exploited to estimate these corrections. Generally speaking, the calibration works as follows: At first, quantities like the cluster energy density or the isolation and shower depths in the calorimeter system are exploited to determine the origin of the calorimeter cluster as either being electromagnetic or hadronic. Cluster isolation information is used to calculate the energy deposit outside of clustered cells whereas the energy deposit in inactive detector areas is estimated based on the amount of deposited energy and its position in the various calorimeter regions and layers afterwards. The calibration relies upon factors depending on the pseudorapidity and the energy. The calorimeter clusters were calibrated based on test-beam data using electrons so that the jet energy is initially measured at the electromagnetic scale to provide an estimate of the particle energies originating from EM showers.
Due to the fact that all sorts of hadrons can be contained in a jet, a hadronic jet energy calibration needs to be applied. Based on MC simulation of single pions, the jet energy scale, JES, is corrected for clusters coming from hadronic deposits [229, 230]. This JES calibration is performed using the average jet response which is defined as $R_{\mathrm{JES}} = E_{\mathrm{jet}}^{\mathrm{LCW}} / E_{\mathrm{jet}}^{\mathrm{truth}}$ with the energy for reconstructed LCW jets $E_{\mathrm{jet}}^{\mathrm{LCW}}$ and the energy for MC simulated truth jets $E_{\mathrm{jet}}^{\mathrm{truth}}$. This response factor is displayed in Fig. 4.4 as a function of the pseudorapidity of the jet, measured with respect to the geometric centre of the detector. Further corrections caused by jets not fully covered by the calorimeter system and corrections to minimise response differences between jets initiated by quarks and gluons are considered as well. A last calibration step is applied only to data and relies on in-situ techniques [231]. Different sorts of events are used for the individual calibration levels. Photon+jet and Z+jet events serve to calibrate jets in the central detector region whereas jets in the forward region are calibrated against central jets using dijet events. Multijet events are employed for the calibration of high-p_{T} jets.

Jets are accepted if $p_{\mathrm{T}} > 25$ GeV and $|\eta| < 2.5$ after the final energy calibration. Double-counting of electrons as jets is prevented by requiring that the closest jet within $\Delta R = 0.2$ of the selected electrons is discarded. Leptons from heavy-flavour decays are removed by requiring that no lepton within a cone of $\Delta R = 0.4$ of all remaining jets is present.

A correct event reconstruction is based on the assumption that all jets originate from the primary vertex, whose reconstruction is delineated in Sec. 4.1. A variable called *jet vertex fraction* (JVF) is used to determine whether a jet comes from the PV. By the application of a cut on the JVF variable, jets which are not associated with the hard-scatter PV can be removed from consideration and, thus, effects due to in-time and out-of-time pile-up can be reduced significantly. This variable is defined with respect to each identified PV utilising tracks based on Inner Detector information. The association between tracks and calorimeter jets is realised by a ghost-association procedure [232].

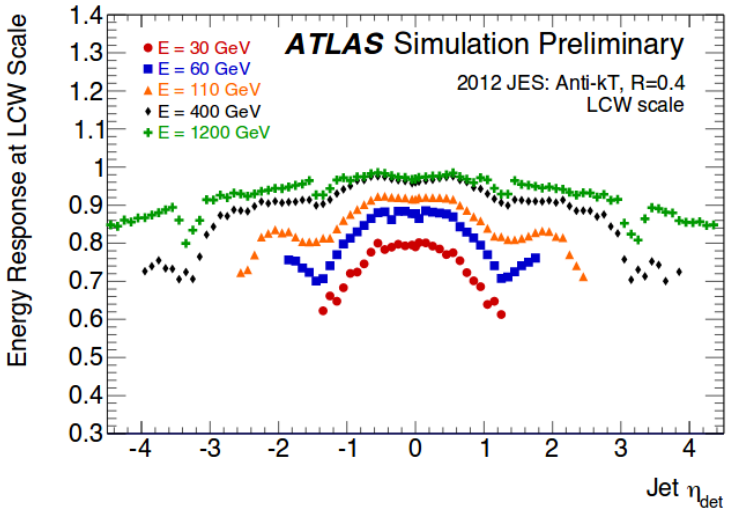

Figure 4.4: Energy response R_{JES} of anti-k_t jets (with $R = 0.4$) after application of the LCW algorithm shown as a function of the pseudorapidity of the jet relative to the geometric centre of the ATLAS detector [230].

The JVF can be described as the ratio of the sum of the p_{T} of tracks associated with the jet and the primary vertex to the sum of p_{T} of all tracks associated with the jet. This is expressed mathematically as follows [233]:

$$\text{JVF}(\text{jet}_i,\text{PV}_j) = \frac{\sum_k p_{\text{T}}(\text{track}_k^{\text{jet}_i}, \text{PV}_j)}{\sum_l \sum_m p_{\text{T}}(\text{track}_m^{\text{jet}_i}, \text{PV}_l)}\,.$$

The index k is used for all tracks originating from PV_i and m for all tracks from PV_l where the index l runs over all primary vertices. According to this definition, JVF values range from 0 to 1. For jets without any associated track, a value of -1 is assigned. The p_{T} of the involved tracks must exceed at least 1 GeV.

The definition of the JVF variable is illustrated in Figure 4.5a. In Figure 4.5b, the JVF variable is shown for pile-up jets (red) and jets after pile-up subtraction and jet energy scale corrections are applied (blue) based on a $Z(\rightarrow ee)$+jets sample.
The different shapes of the distributions for these two kinds of jets are very distinct and thus underline the discriminating power of the JVF variable. Based on such a study, all jets having $p_{\text{T}} < 50$ GeV and $|\eta| < 2.4$ used in the analysis presented in this thesis must satisfy $|\text{JVF}| > 0.5$. Hence, the cut on the JVF variable ensures that 50% of the sum of the p_{T} of tracks associated with a jet belongs to tracks which are compatible with the assumption that these tracks are related to the PV.

The different source of systematic uncertainties related to jets are covered in Sec. 8.2 as the other detector model uncertainties.

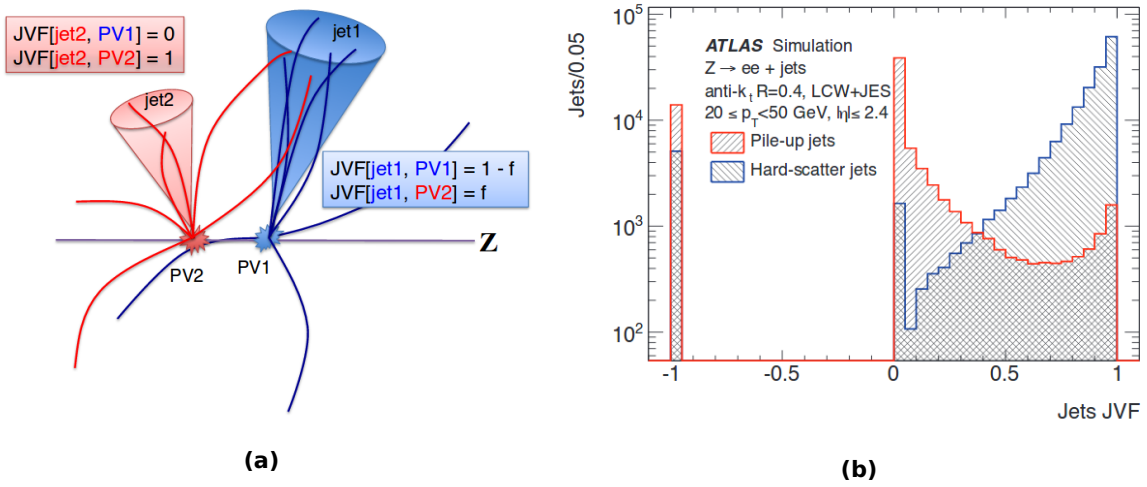

Figure 4.5: (a) Illustration of the definition of the jet vertex fraction. f stands for the fraction of track p_{T} which contributes to jet1 with PV1 although it originates from the vertex PV2. (b) Distributions of the JVF variable for pile-up (red) and hard-scatter (blue) jets in the range $20 \leq p_{\mathrm{T}} \leq 50$ GeV with $|\eta| \leq 2.4$ [233].

4.5 b-Tagging

Jets which originate from bottom quarks possess unique properties allowing for a differentiation between these b jets and those jets coming from the hadronisation of light quarks (u, d and s jets), which hadronise directly at the primary vertex. Top quarks decay almost 100% of the time into a W boson and a bottom quark. Consequently, the identification of b quarks is a vital part of the selection of top quark samples. This section is dedicated to this identification of b jets, the so-called *b-tagging*.

The idea of identifying b jets relies on the fact that these jets contain B hadrons, which may have a decay vertex displaced from the primary one due to its long lifetime of about 1.5 ps [28], as discussed already in Sec. 2.2.2. This results in a measurable flight length path of up to a few millimetres. Hence, the decay of B hadrons can occur at a secondary vertex. Furthermore, a significant amount of B hadron decay products contain the charged leptons e and μ (about 20%) [28], and, due to the high mass of these hadrons, their decay products tend to have a larger transverse momentum with respect to the b quark direction. This leads to relatively broad jets. The differences in the jet properties are exploited by the different existing b-tagging algorithms to discriminate b jets from light jets. These algorithms calculate b-tag weights which correspond to the probability that a jet originated from a b quark. Applying cuts on the b-tagging weights leads to a sample of b-tagged jets with a specific purity and tagging efficiency ε_b. The latter reflects how probable it is to tag a true b jet correctly while the purity is defined by the fraction of correctly tagged b jets in the sample. The fraction of mistagged light and c jets is described by quoting rejection factors of light jets and c jets, R_l and R_c, defined as the inverse of the mistag rates, i.e. the fraction of true light or

c jets which are falsely regarded as being a b jet.

The b-tagging is realised with the ATLAS b-tagger *MV1* [234] in this analysis. It relies on a neural network which combines the information from three high-performance taggers: *IP3D*, *SV1* and *JetFitter*. All three algorithms employ a likelihood ratio technique which is based on the idea of comparing input variables to smoothed normalised distributions obtained from MC simulations for both b jet and light jet hypotheses. The *IP3D* tagger exploits longitudinal and transverse impact parameter significances. The *SV1* tagger rests on the reconstruction of a secondary vertex emerging from the decay products of the B hadron. The third tagger, the *JetFitter*, uses a Kalman filter [235] to find a common line which comprises the position of the PV and of the b- and c-vertices.
The output of the MV1 algorithm is a multivariate discriminant w with values in the range $0 \leq w \leq 1$. The working point of the MV1 tagger is set to 0.7892, i.e. jets are tagged as b jets if w exceeds this value. This is equivalent to an efficiency of $\varepsilon_b = 70\%$ to tag a b quark jet in $t\bar{t}$ events correctly with a light jet rejection factor of $R_l = 136.7$ and a c-jet rejection factor of $R_c = 5$. The purity related to this working point in $t\bar{t}$ events is 92.3%. For b jets having $p_{\mathrm{T}} > 20$ GeV and $|\eta| < 2.5$, these efficiencies and rejection factors are extracted using simulated $t\bar{t}$ events. The general performance of this tagger compared to less sophisticated algorithms is shown in Fig. 4.6.

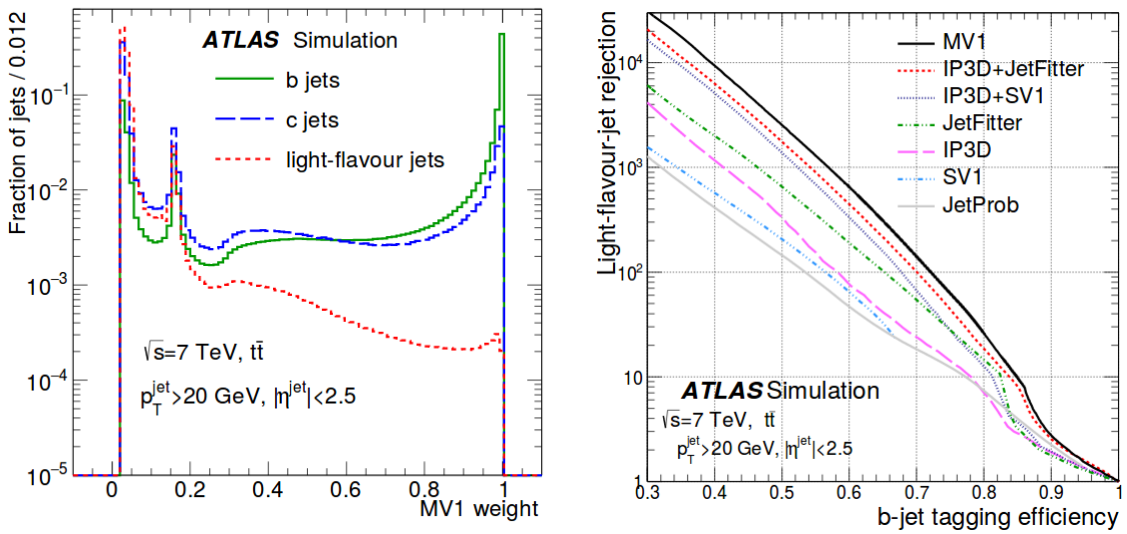

(a) **(b)**

Figure 4.6: (a) Distribution of the b-tagging weight w for the MV1 tagger for three different types of jets. (b) Light jet rejection factor R_l as a function of the b-tagging efficiency ε_b for different tagging algorithms. The MV1 tagger reveals the best performance. Both distributions are based on jets with $p_{\mathrm{T}} > 20$ GeV and $|\eta| < 2.5$ [234].

Scale factors are computed and used in MC samples to properly model the performance in data. The factors are defined as for leptons: $\mathrm{SF} = \varepsilon_{\mathrm{data}}/\varepsilon_{\mathrm{MC}}$, with the tagging efficiencies measured in data ($\varepsilon_{\mathrm{data}}$) and simulation ($\varepsilon_{\mathrm{MC}}$), respectively. To derive these scale factors, the probability density

function calibration method based on a combinatorial likelihood to measure the b-tagging efficiency in a data sample of dileptonic $t\bar{t}$ events is employed [236]. This procedure considers correlations between the measured jets and thus helps to reduce uncertainties related to the b-tagging method. b-tagging efficiencies and computed scale factors are given in Fig. 4.7.

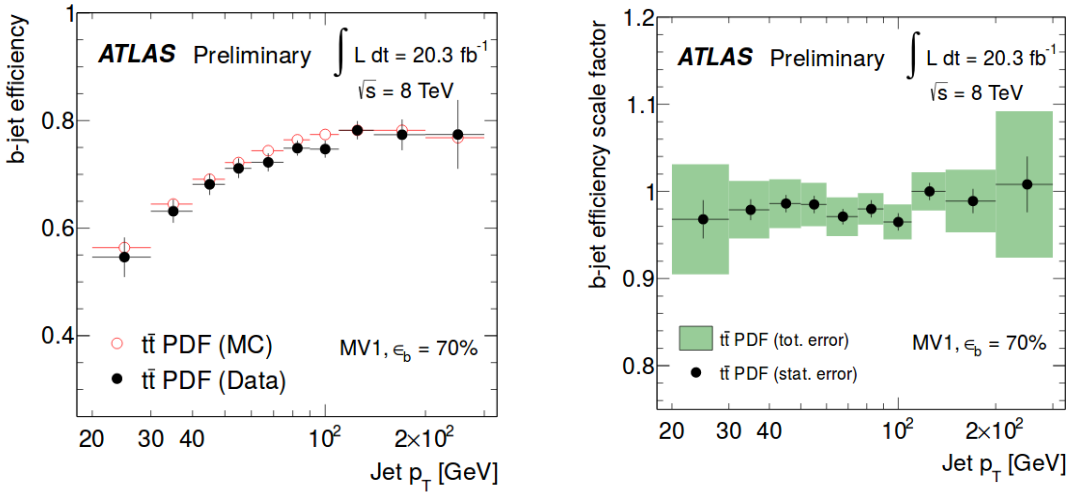

(a) **(b)**

Figure 4.7: (a) b-tagging efficiencies and (b) the corresponding scale factors as a function of the jet transverse momentum. The given values are derived from the MV1 b-tagging algorithm at the working point with $\varepsilon_b = 70\%$. The error bars in (a) include both statistical and systematic components while in (b) the error lines contain only the statistical uncertainty and the green bands both statistical and systematic uncertainties [236].

In a similar fashion, c- and light jet tagging efficiencies and, consequently, corresponding rejection and scale factors can be derived as well [237].

4.6 Missing Transverse Momentum

Particles that do not interact with the detector material need to be reconstructed indirectly. For this purpose, the conservation of momentum in the transverse plane is exploited. The initial full momentum of the pp collision in the centre of the ATLAS detector is not known, but due to the definition of the ATLAS coordinate system, the total transverse momentum of the colliding protons is zero before the collision and needs to be zero afterwards because of transverse momentum conservation. A measured transverse momentum $\neq 0$ hints at particles escaping from being detected, such as neutrinos. This quantity is called *missing transverse momentum* and its magnitude is referred to as $E_{\mathrm{T}}^{\mathrm{miss}}$. In this analysis, $E_{\mathrm{T}}^{\mathrm{miss}}$ serves as a measure of the transverse momentum that is assigned to the neutrino candidate which originates from the leptonically decaying W boson of the $t\bar{t}$ events.

The reconstruction of $E_{\mathrm{T}}^{\mathrm{miss}}$ is based on calibrated physics objects. According to the definition of the transverse plane, components in the x and y axes are used for the calculation [238, 239]:

$$E_{x(y)}^{\mathrm{miss}} = E_{x(y)}^{\mathrm{miss},e} + E_{x(y)}^{\mathrm{miss},\gamma} + E_{x(y)}^{\mathrm{miss},\tau} + E_{x(y)}^{\mathrm{miss,jets}} + E_{x(y)}^{\mathrm{miss},\mu} + E_{x(y)}^{\mathrm{miss,soft}} .$$

Each term is computed as the negative vectorial sum of transverse momenta of energy deposits as well as tracks. Energy deposits in the calorimeters and tracks are matched to reconstructed physics objects in a certain order to avoid double counting. The order is represented by the terms in the above given formula: electrons, photons, the visible parts of the hadronically decaying τ leptons, jets and muons. These terms are collectively referred to as the "hard term" while signals not related to physics objects form a so-called "soft term". The associated magnitude and azimuthal angle are then defined as:

$$E_{\mathrm{T}}^{\mathrm{miss}} = \sqrt{(E_x^{\mathrm{miss}})^2 + (E_y^{\mathrm{miss}})^2} \qquad \text{and} \qquad \phi^{\mathrm{miss}} = \arctan \frac{E_y^{\mathrm{miss}}}{E_x^{\mathrm{miss}}} .$$

Various criteria have to be fulfilled by the objects for the reconstruction of the $E_{\mathrm{T}}^{\mathrm{miss}}$ hard terms. Those include that electrons need to satisfy $p_{\mathrm{T}} > 10$ GeV and $|\eta| < 2.47$ where the transition region between barrel and end-cap EM calorimeters is excluded. Electrons are defined using a medium isolation cut. Photon reconstruction is based on cluster seeds of energy deposited in the EM calorimeter that need to have $p_{\mathrm{T}} > 10$ GeV. For muons, an ID track is matched to an MS track or segment. The latter are used in the region $2.5 < |\eta| < 2.7$ to extend the coverage in the pseudorapidity. The transverse momentum requirement for muons is $p_{\mathrm{T}} > 5$ GeV.
Jets are reconstructed and calibrated as described in Sec. 4.4 using the anti-k_t algorithm and the LCW+JES calibration scheme. The calibrated transverse momentum for jets needs to exceed 20 GeV. Furthermore, a JVF requirement is imposed as well.
Finally, hadronically decaying τ leptons are seeded by calorimeter jets which fulfil $p_{\mathrm{T}} > 10$ GeV and $|\eta| < 2.5$. Similarly to jets, the LCW calibration is employed.

In order to reconstruct the last remaining term of the $E_{\mathrm{T}}^{\mathrm{miss}}$ calculation, the soft term, four reconstruction algorithms are available: The calorimeter Soft Term (CST), the Track Soft Term (TST), the Extrapolated Jet Area with Filter (EJAF) and the Soft Term Vertex Fraction (STVF) $E_{\mathrm{T}}^{\mathrm{miss}}$ algorithm [239].

The soft term reconstruction in this analysis relies on the CST algorithm, which mainly uses calorimeter information but includes also track corrections. The CST reconstruction is based on energy deposits that are not associated with the high-p_{T} physics objects as defined above and used for the other terms. Noise suppression is realised by calculating the soft term using cells that belong to topological clusters calibrated at the LCW scale [227, 228]. In case the track p_{T} resolution is better than the expected calorimeter p_{T} resolution, tracks with $p_{\mathrm{T}} > 0.4$ GeV not matched to the high-p_{T} physics objects are used instead of the calorimeter information. The ΔR significance, defined as $\Delta R/\sigma_{\Delta R}$, with the ΔR resolution $\sigma_{\Delta R}$, serves to quantify the geometrical matching between tracks

and topological clusters. A track is regarded as associated to a cluster in the soft term if the significance minimum fulfils $\Delta R/\sigma_{\Delta R} < 4$. Due to its performance, the CST algorithm for the soft term reconstruction is applied as the standard method in most measurements at $\sqrt{s} = 8$ TeV.

5 Signal and Background Modelling

The modelling of signal and background events is relevant for precision measurements in the field of particle physics at high energies. Many particle physics experiments rely on a comparison of simulations of physics processes and detector responses with measured data. Besides, both theorists and experimentalists exploit simulations to make predictions for future experiments in development. Monte Carlo simulation methods constitute a reliable procedure to model events since the processes on which event simulation is based can be mathematically described by probability density functions. In addition, data-driven methods are also established at the ATLAS experiment to estimate the effect of some processes. After some general remarks on the event simulation, mainly for MC-based simulation, the modelling of the signal and background samples essential for the analysis described in this thesis is discussed. The comparison of simulated and measured data events is covered in Ch. 6 after the analysed dataset is depicted in more detail.

5.1 Fundamentals of the Event Simulation

5.1.1 Stages of the Event Simulation

The simulation of proton-proton collision events at the LHC as realised by an MC generator is composed of several main steps. The structure of such a collision with the two protons coming from the left and right is illustrated in Figure 5.1 showing the stages into which the generation process is usually divided. The *hard-scattering process* of the partons (red circle), the *parton shower* (PS, lines leading to light green ellipses) and the *hadronisation* (light green ellipses) of the partons are the first three steps. The *underlying event* (purple ellipse) consists of secondary interactions of the proton remnants. *Soft photon radiation* (yellow) and *unstable particle decays* (dark green circles) need to be considered for the event generation as well. The different parts of the event generation process are discussed more thoroughly in this section.

The hard collision or hard-scattering process is the primary interaction between the incoming partons from the colliding protons. It is based on a matrix element (ME) which describes the underlying reaction, as the highest momentum transfer process of the event. The simulation of the latter starts with calculating the probability of the process from perturbation theory. For this purpose, parton distribution functions are used to describe partons, and the given order in perturbation theory used for the particular generated process returns probabilistic distributions of the outgoing partons. This computation of the hard collision can be separated from the simulation of non-perturbative QCD effects, as expressed by the QCD factorisation theorem defined in Sec. 2.2.1. That is why specific

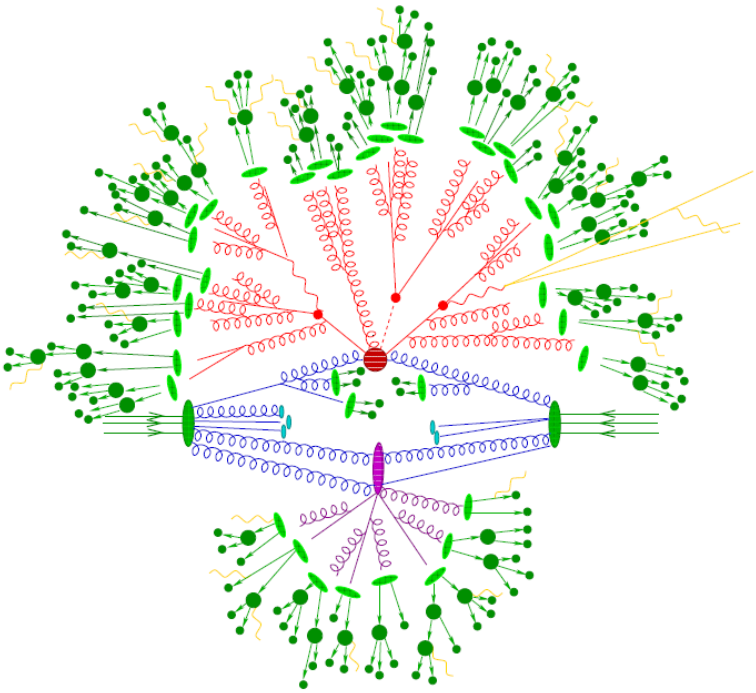

Figure 5.1: Illustration of the structure of a simulated proton-proton collision with the different generation stages as delineated in the text [240].

programmes which simulate the hard process can be interfaced with generators for modelling the evolution of non-perturbative effects involving parton showering and hadronisation.

A parton shower is the cascade of radiation due to QCD processes after the hard-scattering event. The underlying concept of generating the parton shower is the simulation of the cascade of partons produced by QCD interactions and continued in a scattering process. It is differentiated between initial and final state radiation (ISR and FSR). The evolution of the parton shower begins with the hard scatter and proceeds to decreasing momentum scales. At some point, with the progression of this scale, perturbation theory is no longer valid and then hadronisation processes occur.

Hadronisation refers to the formation of hadrons as colour-neutral particles out of the coloured partons contained in the shower, also denoted as jet fragmentation. Hadronisation models serve to describe how partons are confined into hadrons. The two main and frequently used models are called *string model* and *cluster model*. These two models are sketched in Fig. 5.2.
The string fragmentation model [241] relies on the concept of the hadronisation of a colour field. Colour field lines present between a quark-antiquark ($q\bar{q}$) pair are confined in a colour flux tube between these quarks. This tube functions as a string having a certain tension independent of the $q\bar{q}$ separation, responsible for the name of the model. The non-perturbative formation of quark-antiquark pairs according to $q\bar{q} \rightarrow q\bar{q}' + q'\bar{q}$ forces the string to break with proceeding time. The cluster fragmentation model [242], on the contrary, uses colour-singlet clusters of partons.

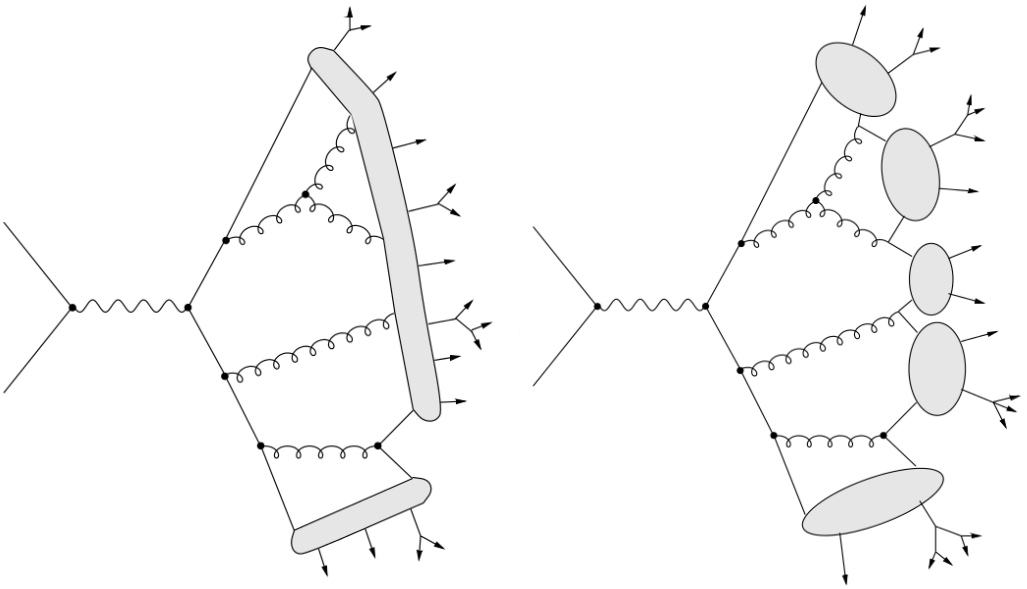

Figure 5.2: Visualisation of the basic concepts of the two main hadronisation models: (a) string model and (b) cluster model [243].

These are built after the parton shower evolution outlined above. The model is based on the idea of pre-confinement; gluons are mainly emitted between partons that are connected (and form the clusters). $q\bar{q}$ pairs are created non-perturbatively from the remaining gluons after the parton shower. The decay of the clusters leads to the observable hadrons.

In the laboratory frame, the two colliding protons are moving towards each other with such a high velocity that they appear to be extremely flattened due to Lorentz contradiction. These flattened protons are completely overlapping in spacetime during the collision resulting in a high probability that other interactions in addition to the hard process take place as well. This is the so-called underlying event, caused by further secondary interactions between remnants of the colliding protons. As the underlying event leads to additional hadrons in the full event signature, as displayed in Figure 5.1, it is overlayed the hard scattering process. This needs to be simulated as well, and phenomenological, non-perturbative models are employed.

At the end of the simulation chain, hadron decays need to be considered in the event generation since many of the produced hadrons are heavy resonances with a very short lifetime. Solely long-lived particles remain and correspond to the particles measured in data. Besides, soft photon radiation, the QED bremsstrahlung, contributes at the different stages of the event simulation.
Particularly non-perturbative models have several free parameters. These are usually constrained using measured data, which is referred to as *tuning*.

5.1.2 Monte Carlo Event Generators and Detector Simulation

Two frequently used matrix element generators which are developed to simulate hard processes are POWHEG [244, 245] and MC@NLO [246, 247]. Both include fixed-order NLO corrections in production and simulate additional radiation of partons based on exact LO matrix element computations and virtual loop corrections. These two generators are typically interfaced with special parton shower generators. Thus, the subsequent softer radiations with decreasing momentum scales are left for these parton shower generators after the hard scattering process is calculated and simulated. The POWHEG generator offers the POWHEG-BOX framework [248] for this purpose.
Two multi-purpose showering and hadronisation generators are PYTHIA [249] and HERWIG [250]. They are able to simulate a large amount of different hard interactions based on leading order matrix elements ($2 \to 1$, $2 \to 2$ but also $2 \to 3$ processes) and cover all aspects of the generation of soft interactions which is why they are often used with POWHEG and MC@NLO. Initial and final state radiation is modelled in PYTHIA based on Q^2- or p_{T}-ordered parton showers and the hadronisation modelling is achieved by using the string model. HERWIG calculates initial and final state radiation with an angular-ordered model for the parton shower and relies on the cluster fragmentation model. In order to simulate the underlying event, HERWIG is often interfaced with JIMMY [251], a generator which utilises the multiple scattering model.
Multi-leg generators like ALPGEN [252] and SHERPA [240] can generate hard processes with several partons by calculating corresponding LO or NLO matrix elements, especially the production processes of vector bosons with several partons. ALPGEN is usually interfaced with PYTHIA or HERWIG whereas SHERPA provides its own implementations to simulate the parton shower, hadronisation and decays. In order to avoid double-counting of the configuration predicted by ME simulation with the parton showering, special ME+PS matching schemes need to be applied. For ALPGEN, the MLM matching scheme [253] is used, while SHERPA relies on the CKKW approach [254], both named after their developers.

After simulating events with generators as described above, the detector response is evaluated [255]. A simulation of the ATLAS detector with its full geometry and detector materials is implemented using the GEANT 4 simulation toolkit [256, 257]. Such a precise detector simulation is relevant for an accurate modelling of the calorimeter response, track reconstruction efficiencies and quantities like missing transverse momentum. The evaluation of systematic effects relies on samples that are passed through a fast simulation which utilises a parametrisation of the performance of both the electromagnetic and hadronic calorimeters [258, 259]. The detector simulation also considers the occurrence of in-time and out-of-time pile-up as multiple pp interactions from the same or neighbouring bunch crossings. A reweighting is applied to the simulated events to match the distribution corresponding to the average number of collisions per bunch crossing measured in data.
In further steps, the events from the detector simulation are digitised and reconstructed to transform the simulated events into the output format used for data events.

5.2 Signal Monte Carlo Samples

The nominal signal $t\bar{t}$ sample used for the direct top quark decay width measurement is generated assuming a top quark mass of $m_t = 172.5$ GeV using the POWHEG generator [244, 245] within the POWHEG-BOX framework [248], version 1. This generator provides NLO QCD matrix element calculations [260] and uses the CT10 parton distribution function PDF set [81]. An additional parameter of the POWHEG generator regulates the radiation at high transverse momentum, the so-called h_{damp} parameter, which is set to m_t here. In order to model parton showering, hadronisation and underlying event, the POWHEG generator is interfaced with PYTHIA 6.427 [249] employing the Perugia 2011C set of tuned parameters [261] and the CTEQ6L1 PDF set [262], a leading order setup used for this showering and hadronisation generator.

The estimation of systematic uncertainties in the modelling of signal events including the choice of the ME generator, the parton shower, the underlying event or factorisation and normalisation scales is based on alternative generators and generator parameters. Such alternative MC generators are MC@NLO [246, 247] and HERWIG 6.520 [250] using JIMMY 4.31 [251] for the underlying event. Further information about the alternative MC samples, the evaluation of these systematic uncertainties and their impact on the total uncertainty of this analysis is provided in Sec.8.4.

All $t\bar{t}$ samples required for this analysis are normalised using the theoretical cross-section of $\sigma_{t\bar{t}} = 253^{+15}_{-16}$ pb, relying on a calculation conducted with the top++2.0 [64–68, 71] programme that consists of NNLO corrections and resums NNLL soft gluon terms. For the calculation of systematic uncertainties, PDF variations, the choice of α_S and the uncertainty in the top quark mass are considered. PDF- and α_S-related systematic uncertainties in the cross-section are determined based on the PDF4LHC prescription [263] with the MSTW2008 68% CL NNLO [69, 70], CT10 NNLO [264] and NNPDF2.3 5f FFN [265] PDF sets. The individual uncertainties are added in quadrature to yield the full quoted uncertainty.

5.3 Background Monte Carlo Samples

5.3.1 Single Top Background

Three mechanisms of single-top-quark production, s-channel, t-channel and associated Wt production, contribute to the single top background. The POWHEG generator [266, 267] is employed to simulate these background processes using the CT10 PDF set. The samples are interfaced with PYTHIA 6.426 (s-channel, Wt production) or PYTHIA 6.427 (t-channel) with the CTEQ6L1 PDF set and the Perugia 2011C tune. Overlap between the $t\bar{t}$ and Wt final states is removed [268] in order to avoid a double-counting of signal processes. The three individual single top quark contributions are normalised to their corresponding approximate NNLO theoretical cross-sections [92, 94] which apply the MSTW 2008 NNLO PDF sets for the evaluation [69, 70]. The top quark mass is set to 172.5 GeV in these samples.

5.3.2 W and Z Boson Background

The ALPGEN 2.14 [252] event generator is used to simulate W or Z boson background events in association with jets utilising the CTEQ6L1 PDF set. ALPGEN is interfaced with PYTHIA 6.426 or PYTHIA 6.427. The samples are generated separately for $W/Z+b\bar{b}$, $W/Z+c\bar{c}$, $W+c$ (all interfaced with PYTHIA 6.427) and W/Z+light jets production (interfaced with PYTHIA 6.426). The MLM parton-jet matching scheme [253] is employed to prevent double-counting of jets generated by the ME calculation in ALPGEN and the evolution of the parton shower with PYTHIA.

Z+jets background events are normalised to the inclusive NNLO theoretical cross-section [269]. For the normalisation of the W+jets events, a data-driven method is used which takes advantage of the asymmetry of $W^{\pm}$ production in the pp collisions at the LHC. The corrections for generator mismodelling are determined for the fractions of three different flavour components. One component comprises $W+b\bar{b}$ and $W+c\bar{c}$ events (in the following denoted as "$W+b\bar{b}/c\bar{c}$"), while $W+c$ and W+light jets events constitute the two further components. The estimation is realised using a sample with the same lepton and $E_{\mathrm{T}}^{\mathrm{miss}}$ selections as utilised for the signal selection but with only two jets and no b-tagging requirement. The heavy-flavour fractions are extracted by using the b-jet multiplicity in conjunction with information about the b-tagging and mistag efficiency. The obtained correction factors, which are used in the measurement, are $K_{b\bar{b}} = K_{c\bar{c}} = 1.50 \pm 0.11$ (stat.+syst.), $K_c = 1.07 \pm 0.27$ (stat.+syst.) and $K_{\mathrm{light}} = 0.80 \pm 0.04$ (stat.+syst.) [270]. The results of the extended likelihood fit to extract these factors are shown in Fig. 5.3. W+jets events constitute the dominant background source in this analysis.

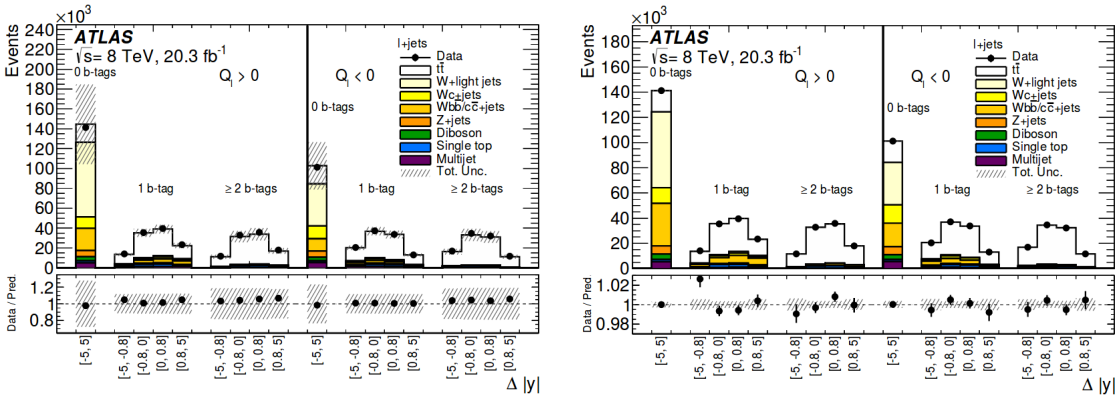

Figure 5.3: Comparison between prediction and data for all 18 analysis bins (divided into rapidity ranges $\Delta|y|$) used in the inclusive charge asymmetry measurement in order to extract the correction factors for the W+jets background components $K_{b\bar{b}}$, $K_{c\bar{c}}$ and K_c (a) before and (b) after a simultaneous unfolding procedure [270].

5.3.3 Diboson Background

For the generation of the relatively small diboson background, the SHERPA 1.4.1 generator [240] with up to three additional partons in the LO matrix elements based on the CT10 PDF set is used. The heavy flavour quarks (b, c) are treated as massive particles during the generation step of diboson samples, which are then normalised using the NLO theoretical cross-sections [271].

5.3.4 Multijet Background

Multijet events may fulfil the selection criteria due to the misidentification of a jet or a photon (from conversions or direct photons) as an electron (called fake lepton) or because of a non-prompt lepton originating from semileptonic decays of heavy-flavour hadrons. The different sources for this background significantly depend on the shape of the detector and the fragmentation processes. The modelling of this background, referred to as multijet background in the following, is thus complicated and, consequently, estimated directly from data using a data-driven matrix method [272]. The matrix method relies on events which satisfy either loose or tight lepton selection requirements, as they are introduced in Sec. 4.2 and Sec. 4.3 for the two charged leptons used in the analysis. The selected tight and loose samples contain real leptons and fake leptons. The total number of events in these samples can be written as:

$$N^{\text{loose}} = N^{\text{loose}}_{\text{real}} + N^{\text{loose}}_{\text{fake}} \qquad \text{and} \qquad N^{\text{tight}} = N^{\text{tight}}_{\text{real}} + N^{\text{tight}}_{\text{fake}} .$$

With the fake and the real efficiency, $\varepsilon_{\text{fake}}$ and $\varepsilon_{\text{real}}$, defined as the ratio of either the number of fake or real leptons classified as tight to the corresponding ones classified as loose, the above equation for the tight sample can be written as:

$$N^{\text{tight}} = \varepsilon_{\text{real}} N^{\text{loose}}_{\text{real}} + N^{\text{tight}}_{\text{fake}} \quad \text{and with } N^{\text{loose}} \text{ rearranged:} \quad N^{\text{tight}} - \varepsilon_{\text{real}} N^{\text{loose}} = \left(1 - \frac{\varepsilon_{\text{real}}}{\varepsilon_{\text{fake}}}\right) N^{\text{tight}}_{\text{fake}} .$$

The number of fake leptons in the tight sample can then be calculated via:

$$N^{\text{tight}}_{\text{fake}} = \frac{\varepsilon_{\text{fake}}}{\varepsilon_{\text{real}} - \varepsilon_{\text{fake}}} \cdot (N^{\text{loose}} \varepsilon_{\text{real}} - N^{\text{tight}}) .$$

The relative efficiencies $\varepsilon_{\text{fake}}$ and $\varepsilon_{\text{real}}$ are estimated based on data, separately for events with electrons and muons. Control samples enriched in real or fake electrons and muons are utilised for this purpose. The control samples need to be kinematically similar to the signal region and are selected accordingly. This allows for the desired application of the measured efficiency, obtained from such a control region, to the signal region used in the analysis.
To be more specific, real efficiencies are extracted with the tag-and-probe method from $Z \to ee$ and $Z \to \mu\mu$ control regions. Both the tag and the probe leptons need to have opposite reconstructed charges, the invariant dilepton mass range is restricted to $80 < m_{\ell^+\ell^-} < 100$ GeV and the events are required to possess at least one jet. The fake efficiencies, on the other hand, require a control region dominated by the multijet fake lepton background. The control regions are composed of events with

solely one lepton and at least one jet. Electron+jets events need to have a low transverse momentum and a low transverse W boson mass. The latter is defined as $m_{\mathrm{T}}^{W} = \sqrt{2p_{\mathrm{T}}^{\ell}E_{\mathrm{T}}^{\mathrm{miss}}(1-\cos\Delta\phi(\ell, E_{\mathrm{T}}^{\mathrm{miss}}))}$ and the selection criteria are $m_{\mathrm{T}}^{W} < 20$ GeV and $m_{\mathrm{T}}^{W} + E_{\mathrm{T}}^{\mathrm{miss}} < 60$ GeV. Muon+jets events need to fulfil a criterion related to the transverse impact parameter d_0. The significance of this quantity, $d_0^{\mathrm{sig}} = d_0/\sigma(d_0)$ with the uncertainty σ, is required to be $|d_0^{\mathrm{sig}}| > 5$ [273].

In practice, the multijet background is evaluated on an event-by-event basis, i.e. the above given equation is transformed into an event weight w_x which is applied to all loose events x according to:

$$w_x = \frac{\varepsilon_{\mathrm{fake}}}{\varepsilon_{\mathrm{real}} - \varepsilon_{\mathrm{fake}}} \cdot (\varepsilon_{\mathrm{real}} - \delta_x),$$

where δ_x equals 1 in case the event is classified as tight and 0 otherwise. Hence, the number of multijet background events in one bin of the observable or kinematic distributions shown in Sec. 6.2 is calculated as the sum over all event weights in that particular bin.

5.4 Summary of Signal and Background Generators

The following table summarises the generators used in this analysis to simulate the $t\bar{t}$ signal and the various background contributions which need to be considered. The individual MC samples used for the $t\bar{t}$ signal and all individual background sources are listed in App. A.

Sample	PDF	Generator	Shower	Normalisation
$t\bar{t}$	CT10	POWHEG	PYTHIA	NNLO+NNLL
Single top	CT10	POWHEG	PYTHIA	aNNLO
W+jets	CTEQ6L1	ALPGEN	PYTHIA	data-driven
Z+jets	CTEQ6L1	ALPGEN	PYTHIA	NNLO
Diboson	CTEQ6L1	SHERPA	SHERPA	NLO
Multijet	data-driven			

Table 5.1: Summary of fundamental generator settings and parameters which are used in this analysis to simulate the nominal $t\bar{t}$ signal and all background events. The estimation of the multijet background and the normalisation of the W+jets background is based on data-driven methods as discussed in the text.

6 Dataset, Event Selection and Reconstruction

The Γ_t measurement is performed using data recorded by the ATLAS detector in 2012. This chapter begins with a description of the used dataset and the related data taking conditions.
A variety of requirements are imposed on the dataset to reduce the fraction of undesired background events. The corresponding cuts to select events used in this analysis are applied to both data and simulated Monte Carlo samples, as introduced in Ch. 5. A comparison of the agreement between the selected data and the simulated events to evaluate the quality of the modelling and to estimate the fraction of background events constitutes a further part of this chapter. This comparison includes distributions of kinematic quantities and of the chosen observables to extract Γ_t.
The selected $t\bar{t}$ events in the lepton+jets decay channel considered in this measurement need to be fully reconstructed to obtain reliable distributions of the observables, required for a precise measurement of Γ_t. The reconstruction of objects at the detector level, as described in Ch. 4, is feasible as the observed signatures are often typical for objects at parton level allowing for a direct association between the two levels. In order to reconstruct events, the present objects at reconstruction level need to be assigned to the parton level objects correctly. In the lepton+jets channel, the relevant task is a correct mapping of four reconstructed jets to the four partons existing in this decay channel. This assignment is achieved using a likelihood-based method. Fundamentals of the event reconstruction, the used and tested reconstruction options and their performances are discussed in detail in the third part of this chapter.

6.1 Dataset

The decay width of the top quark is measured using data recorded by the ATLAS detector in pp collisions at a centre-of-mass energy of $\sqrt{s} = 8$ TeV. The dataset was collected between April and December 2012 and grouped into the data-taking periods A to L with approximately consistent and constant data-taking conditions (excluding periods F and K containing data taken without standard physics run conditions). Runs, which last up to 24 hours depending on the detector performance and the lifetime of the LHC beam, are combined to constitute these periods. Each run consists of luminosity blocks (LBs) lasting one minute each.
During data-taking, the quality of the recorded events is investigated *online* by the shift crew in the ATLAS Control Room where all possible detector parameters and conditions are monitored and constantly inspected, supported by automated systems like the *Data Quality Monitoring Frame-*

work [274]. After further *offline* checks by the detector subgroups and the combined performance groups, events are reconstructed and stored. Data quality criteria require that all detector subsystems are fully operational. In case data quality requirements are not fulfilled, so-called *defects* are assigned to the affected range of luminosity blocks. The decision to store events is thus based on "good" LBs without intolerable defects. Those LBs are summarised in a list, the *good run list* (GRL), used later for the physics analyses.

In total, the LHC delivered data during stable beams corresponding to an integrated luminosity of 22.8 fb^{-1} at $\sqrt{s} = 8$ TeV. The amount of data recorded by the ATLAS detector is 21.3 fb^{-1}. The dataset which passes all quality requirements included in the GRL corresponds to a preliminary integrated luminosity of 20.3 fb^{-1}, which is still used in the official plots but was corrected later to a number of 20.2 fb^{-1} according to latest scale and calibration evaluations [275, 276]. This number is equivalent to around 95% of the recorded data. These luminosities and their evolution as a function of time in 2012 are shown in Figure 6.1a. The integrated luminosity for the individual periods ranges from 0.84 fb^{-1} (period A) to 5.3 fb^{-1} (period B). The individual subcomponents of the ATLAS detector were fully operational in around or even more than 99% of the full data-taking phase in 2012.

The luminosity scale is computed using several luminometers, primarily the BCM (Beam Conditions Monitor) and LUCID, introduced in Sec. 3.3.4. The calibration of these detectors and algorithms in order to determine the final luminosity is done by van der Meer (vdM) scans. Comparisons between them serve to evaluate accuracy, consistency and long-term stability of the resulting values. The uncertainty on the luminosity is estimated to be $\delta\mathscr{L}/\mathscr{L} = \pm 1.9\%$ where the dominant contributions arise from uncertainties due to the luminosity detectors and the vdM calibrations. The calculation is based on the full set of data recorded at $\sqrt{s} = 8$ TeV in 2012 [275]. The obtained value is used to estimate the systematic effect due to the luminosity, as delineated in Sec. 8.7.1.

In-time and out-of-time pile-up events contribute to the recorded dataset. The latter pile-up effect is mainly caused by the calorimeter system of the ATLAS detector which has response times larger than the time difference between two bunch crossings. Fig. 6.1b visualises the mean number of interactions per bunch crossing μ. The mean value is 20.7 and a maximum of up to 40 is observed. Such a plot quantifies the present pile-up conditions and their contribution. The shown interactions are often soft ones, comprising minimum bias events which are characterised by low multiplicity and low transverse momentum. These minimum bias events cause both in-time and out-of-time pile-up and their contribution is luminosity-dependent. Special dedicated algorithms, as outlined in Ch. 5.1.2, account for these effects to avoid detector performance losses. Those events are also considered in the simulation of MC events; minimum-bias interactions are modelled with the PYTHIA 8.1 generator [277] with the MSTW 2008 LO PDF set [69, 70] and the A2 tune [278] and overlaid on hard scatter events.

The recorded dataset is reconstructed with the ATLAS Athena framework [212]. During these

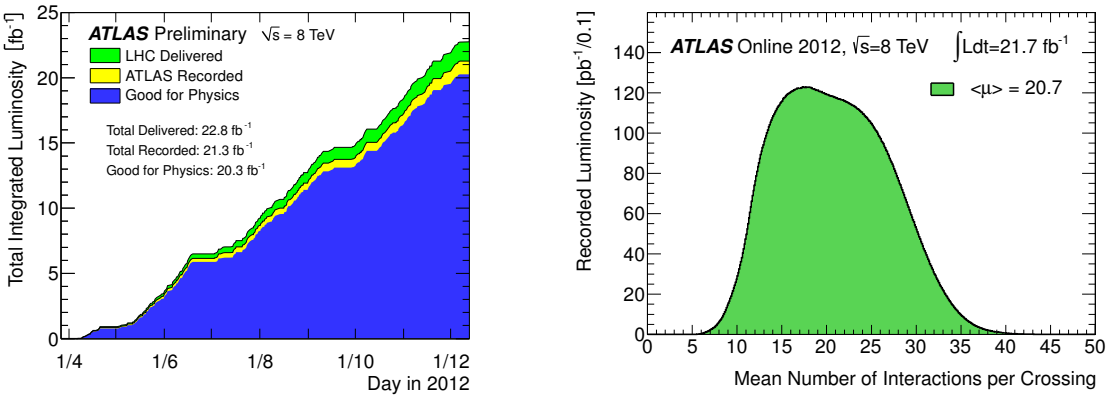

(a) **(b)**

Figure 6.1: (a) Cumulative luminosity versus time delivered by the LHC (green), recorded by the ATLAS detector (yellow), and classified as good quality data in the GRL (blue) during stable beams at $\sqrt{s} = 8$ TeV for pp collisions in 2012. (b) The luminosity-weighted distribution of the mean number of interactions per bunch crossing μ for pp collisions in 2012 with the underlying integrated luminosity and the mean value of μ [209].

processes, the Raw Data Objects are transformed in several steps until they are saved as D3PD (short for "derived physics data") files. This file format can be accessed by the analysis framework ROOT [279] based on C++-code which is used intensively to perform the analysis presented in this thesis.

6.2 Event Selection

According to the requirements of the electron+jets and muon+jets channel of $t\bar{t}$ decays used in this measurement, corresponding events need to be selected out of the given ATLAS dataset described in the previous section. Pursuant to the theory description in Sec. 2.2.2, events are composed of exactly one electron or muon, four jets (two of which are b jets), and $E_{\mathrm{T}}^{\mathrm{miss}}$ because of the neutrino.

A first criterion to select those events refers to single-lepton triggers for electrons and muons. For each of the two lepton types, two triggers are employed having different transverse momentum thresholds. The p_{T} trigger thresholds for electrons are 24 and 60 GeV (trigger chains called `EF_e24vhi_medium1` and `EF_e60_medium1`) while they are set to 24 or 36 GeV for muons (trigger chains called `EF_mu24i_tight` and `EF_mu36_tight`). The electron and muon triggers with the lower p_{T} values impose additional isolation requirements on the lepton in order to retain the trigger rate at a low level. The momentum thresholds of the triggers are similar but a bit looser than the final reconstruction requirements where a p_{T} of 25 GeV for electrons and muons is required. Moreover, an event is rejected if there is a jet with $p_{\mathrm{T}} > 20$ GeV originating from pile-up or from calorimeter noise [280].

In the next step, the events have to meet the requirements on the number of reconstructed objects. In compliance with the above described signature of the chosen decay channel of $t\bar{t}$ pairs, events must have exactly one reconstructed electron or muon and at least four reconstructed jets, at least one of which must be b-tagged. These requirements are imposed to account for the limited object reconstruction and b-tagging algorithm efficiencies and are thus different from the theoretical description of the decay channel. All criteria listed in Ch. 4 must be satisfied by the objects of the selected events. Furthermore, the high-level trigger lepton needs to be matched to the selected electron or muon within a distance of $\Delta R = 0.15$.

Additional cuts are applied to suppress multijet background caused by misidentified leptons. Events with exactly one b-tagged jet must fulfil $E_{\mathrm{T}}^{\mathrm{miss}} > 20$ GeV and $E_{\mathrm{T}}^{\mathrm{miss}} + m_{\mathrm{T}}^{W} > 60$ GeV with the transverse W boson mass $m_{\mathrm{T}}^{W} = \sqrt{2p_{\mathrm{T}}^{\ell}E_{\mathrm{T}}^{\mathrm{miss}}(1-\cos\Delta\phi(\ell, E_{\mathrm{T}}^{\mathrm{miss}}))}$. These two cuts are not imposed on events with at least two b-tagged jets since the multijet background reduced by this cut is mainly present in the low b-tag multiplicity regions. Thus, the usage of these cuts for events with at least two b-tags would not improve the level of agreement between data and Monte Carlo but would reduce the event yield in this region by about 15%-20%.

The reconstruction of the selected events is realised with a likelihood-based method, addressed in Sec. 6.3 and assuming the $t\bar{t}$ lepton+jets decay channel topology. The logarithm of the likelihood from the reconstruction algorithm is required to be $\ln(L) > -50$. This cut reduces background more than signal, thus purifies the selected sample and suppresses a significant portion of combinatorial background due to events which are not correctly reconstructed. Since the fraction of well reconstructed $t\bar{t}$ events is increased, the entire sensitivity of the Γ_t measurement is improved.

Events that pass all these selection criteria are categorised into eight mutually exclusive analysis regions. The selected sample is separated into the electron+jets and muon+jets channel and into two orthogonal b-tag regions to differentiate between events with exactly one and at least two b-tags. Later studies revealed that this division leads to smaller systematic uncertainties, as analysed in detail in Sec. 9.4. These four regions are further split into two pseudorapidity regions, into a central region where all four reconstructed jets associated with the $t\bar{t}$ decay have $|\eta| \leq 1$ and a second one containing the more forward events with at least one jet having $|\eta| > 1$, referred to as $|\eta| \leq 1$ region and $|\eta| > 1$ region, respectively, for the sake of simplicity. The approach of splitting the sample into $|\eta|$ regions exploits the different sensitivity of these regions to detector resolution effects, different pile-up contributions and a varying amount of background events. This choice of analysis regions is justified in a dedicated chapter of this thesis, see Ch. 9.

After the event selection and the determination of events in the different regions, the expected number of background and signal events can be compared to the number of selected events in data. The predicted number of MC events also takes scale factors, corrected trigger, identification, reconstruction and b-tagging efficiencies to data, as well as pile-up corrections into account. The resulting event yields for the prediction and the data in the eight orthogonal analysis channels are

e+jets	$\|\eta\| \leq 1$ region		$\|\eta\| > 1$ region	
Sample	1 b-tag	≥ 2 b-tags	1 b-tag	≥ 2 b-tags
$t\bar{t}$	5850 ± 380	6480 ± 420	29200 ± 1900	27600 ± 1800
Single top	285 ± 48	141 ± 24	1830 ± 310	860 ± 150
W+$b\bar{b}/c\bar{c}$	362 ± 40	81 ± 9	2640 ± 290	506 ± 56
W+c	174 ± 47	8 ± 2	1300 ± 350	56 ± 15
W+light	87 ± 3	3.7 ± 0.2	578 ± 23	26 ± 1
Z+jets	120 ± 58	38 ± 18	1190 ± 570	310 ± 150
Diboson	31 ± 15	4 ± 2	183 ± 88	29 ± 14
Multijet	228 ± 68	38 ± 11	2490 ± 750	540 ± 160
Total expected	7140 ± 400	6790 ± 420	39400 ± 2200	29900 ± 1800
Data	6800	7056	37823	30644

(a) Electron+jets channel.

μ+jets	$\|\eta\| \leq 1$ region		$\|\eta\| > 1$ region	
Sample	1 b-tag	≥ 2 b-tags	1 b-tag	≥ 2 b-tags
$t\bar{t}$	7000 ± 450	7640 ± 490	35900 ± 2300	33500 ± 2200
Single top	369 ± 63	160 ± 27	2110 ± 360	980 ± 170
W+$b\bar{b}/c\bar{c}$	473 ± 52	117 ± 13	3450 ± 380	756 ± 83
W+c	223 ± 60	5 ± 1	1540 ± 420	63 ± 17
W+light	96 ± 4	1.8 ± 0.1	797 ± 32	40 ± 2
Z+jets	74 ± 36	16 ± 8	610 ± 290	159 ± 76
Diboson	37 ± 18	6 ± 3	198 ± 95	32 ± 15
Multijet	195 ± 59	34 ± 10	1870 ± 560	400 ± 120
Total expected	8470 ± 470	7980 ± 490	46400 ± 2500	36000 ± 2200
Data	8274	8193	46275	36471

(b) Muon+jets channel.

Table 6.1: Event yields obtained after the event selection in the (a) electron+jets and (b) muon+jets channel for events with exactly one or at least two b-tagged jets divided into categories where either all four jets of an event associated with the $t\bar{t}$ decay have $|\eta| \leq 1$ or where at least one jet of the event has $|\eta| > 1$. The yield split between the two $|\eta|$ regions is around 1:6. The uncertainties on the given MC signal and background numbers arise from normalisation uncertainties of each sample which are defined in Sec. 7.3. The uncertainties on the W+jets and the multijet background originate from the data-driven methods used to estimate these background sources, the other numbers are based on theory uncertainties.

presented in Table 6.1. The numbers reflect a good agreement between the prediction and the data, comparable to event yields obtained for various other measurements at $\sqrt{s} = 8$ TeV. Event yields before applying the additional cut on the logarithm of the likelihood used for the event selection and before splitting the sample into two pseudorapidity regions are shown in App. B.

Control plots containing the events selected in data and the predicted signal and background contributions for kinematic quantities are given in Figs. 6.2-6.5. Kinematic distributions of the lepton and leading b-tagged jet p_{T}, lepton and leading b-tagged jet η, $E_{\mathrm{T}}^{\mathrm{miss}}$ and m_{T}^{W} for events with exactly one or at least two b-tagged jets in the electron+jets or muon+jets channel, respectively, are shown. Fig. 6.6 and Fig. 6.7 display control plots for the two observables used for the decay width measurement, namely $m_{\ell b}$ and $\Delta R_{\mathrm{min}}(j_b, j_l)$, as briefly defined in Ch. 1 and covered in detail in Sec. 7.1. Distributions in all eight analysis regions are shown. These plots illustrate a good agreement between data and prediction within the assigned uncertainties. The uncertainties shown in the bands include the normalisation uncertainties on the signal and background contributions as well as the signal model systematic uncertainties being the dominant systematic effect.

The distribution of the lepton transverse momentum reveals that this quantity is not well-modelled for low values of p_{T}, especially for events with at least two b-tagged jets before the cut on the logarithm of the reconstruction likelihood is applied. Since such a cut removes more background than signal, background contributions are deemed to be responsible for this visible mismodelling. A closer examination of control plots using logarithmic scales, before the aforementioned cut is imposed, demonstrates that the multijet background is the main source of this modelling issue. To be more specific, the second trigger threshold (at 60 GeV for electrons) is the source of this effect; the multijet fake lepton events have a larger contribution in the small $m_{W,\mathrm{T}}$ and lepton p_{T} regions. The corresponding plots with logarithmic scales are given in Fig. 6.8, the ratio plots in comparison with Figs. 6.2-6.5 clearly show that the modelling improves after applying the cut on the logarithm of the reconstruction likelihood. More control plots without this cut can be found in App. C.

After the event selection, the main background source is due to W bosons produced in association with jets, divided into three components ($W+b\bar{b}/c\bar{c}$,$W+c$, W+light). Other larger contributions originate from multijet events and single top quark production while Z+jets and diboson (WW, WZ, ZZ) production constitute smaller contributions. As can be seen using the absolute numbers in Table 6.1, the fraction of signal $t\bar{t}$ events is larger in the region with at least two b-tags and a larger fraction of background events is present in the region with exactly one b-tag. This implies that the purity is higher in the former region. The W+jets background decreases to a higher degree with regard to other background sources when moving to events with at least two b-tagged jets. The reduction of the remaining background contributions is obvious as well but less effective. The advantages of keeping the events with one b-tagged jet are delineated in the following chapters.

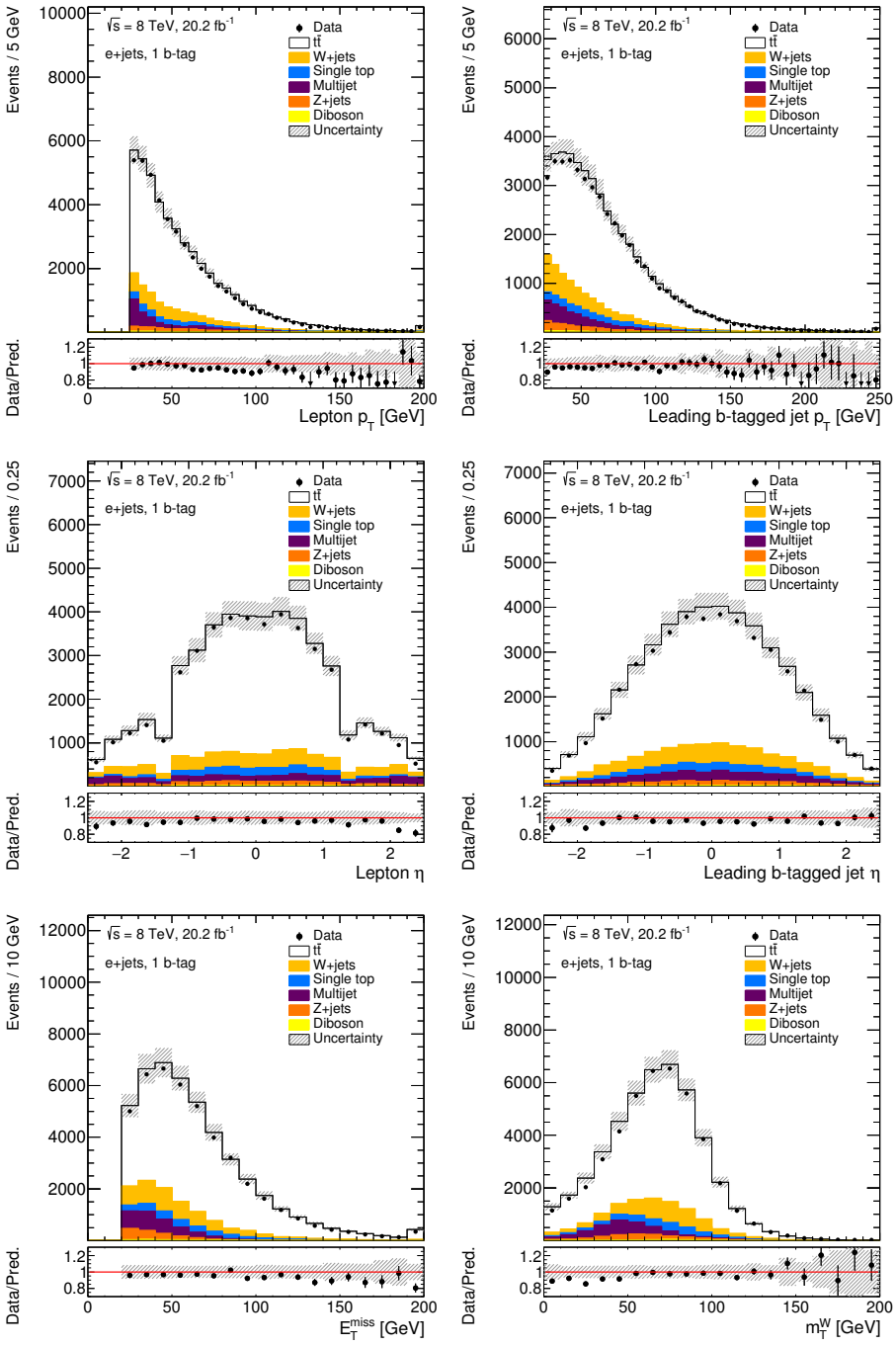

Figure 6.2: Distributions of the lepton and leading b-tagged jet p_{T}, lepton and leading b-tagged jet η, $E_{\mathrm{T}}^{\mathrm{miss}}$ and m_{T}^{W} in the electron+jets channel for events with exactly one b-tagged jet resulting from the event selection. The hatched bands comprise the normalisation uncertainty in the signal and background contributions as well as the signal model systematic uncertainties. The first and last bins include underflow and overflow events, respectively.

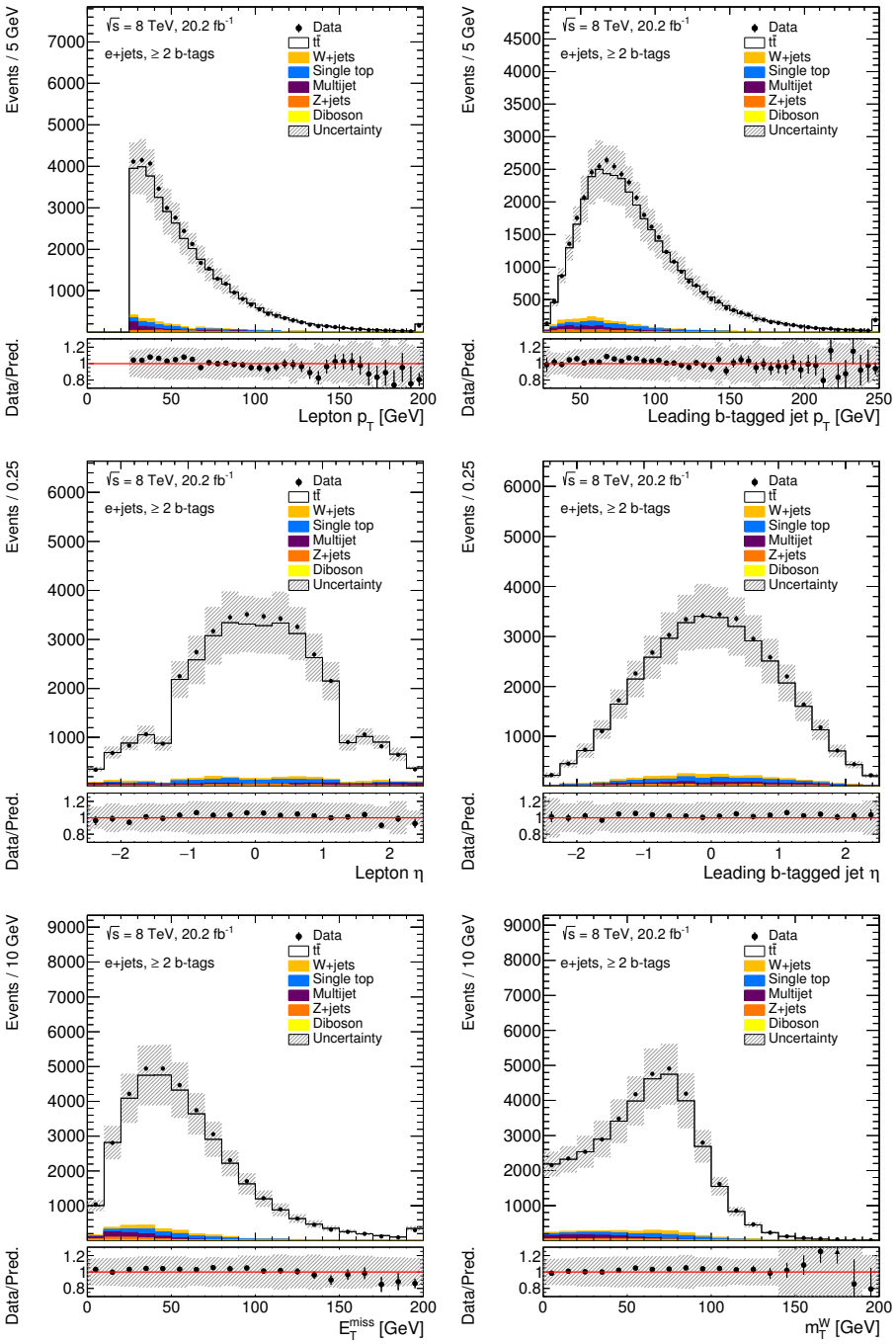

Figure 6.3: Distributions of the lepton and leading b-tagged jet p_{T}, lepton and leading b-tagged jet η, $E_{\mathrm{T}}^{\mathrm{miss}}$ and m_{T}^{W} in the electron+jets channel for events with at least two b-tagged jets resulting from the event selection. The hatched bands comprise the normalisation uncertainty in the signal and background contributions as well as the signal model systematic uncertainties. The first and last bins include underflow and overflow events, respectively.

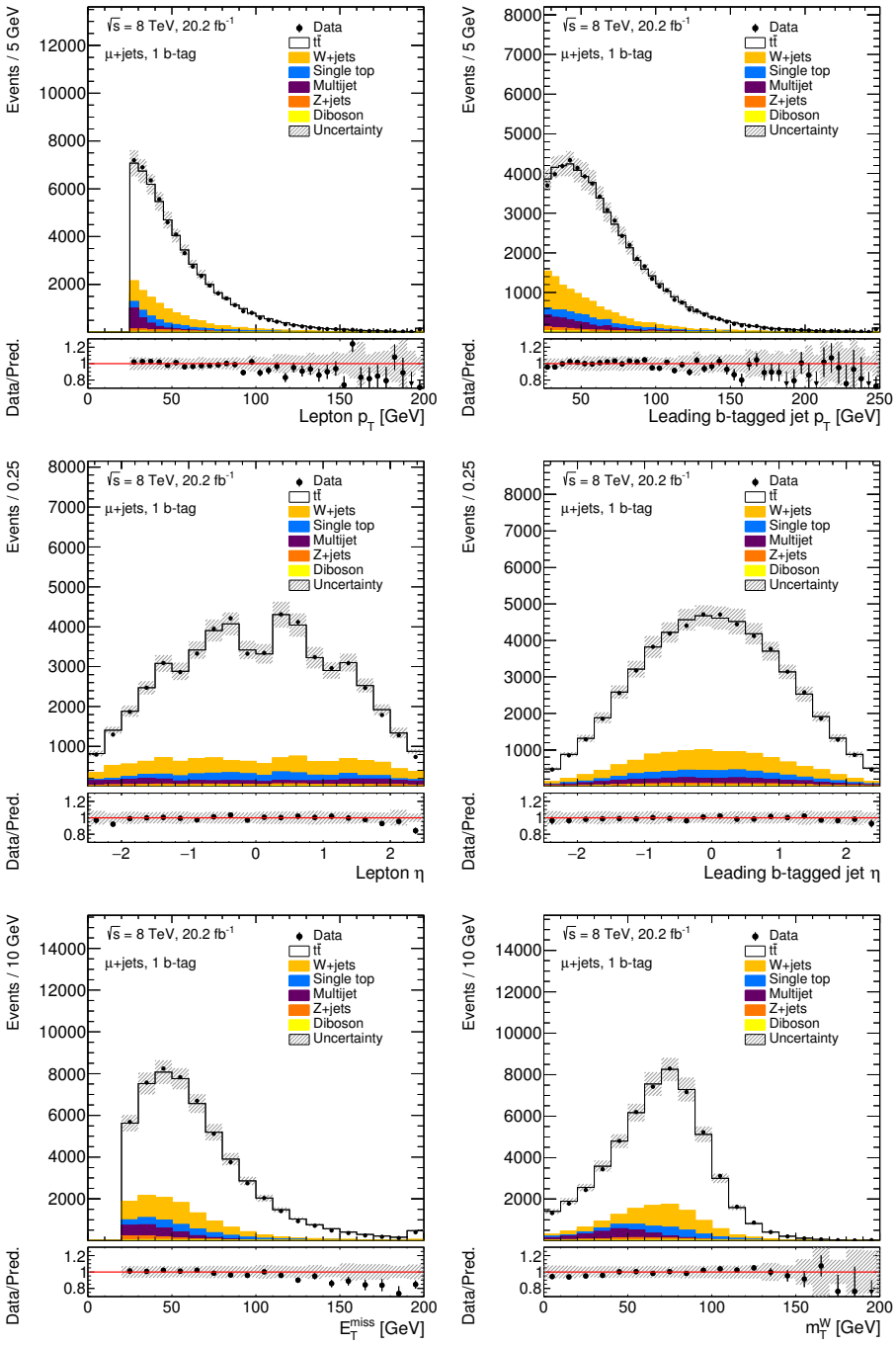

Figure 6.4: Distributions of the lepton and leading b-tagged jet p_{T}, lepton and leading b-tagged jet η, $E_{\mathrm{T}}^{\mathrm{miss}}$ and m_{T}^{W} in the muon+jets channel for events with exactly one b-tagged jet resulting from the event selection. The hatched bands comprise the normalisation uncertainty in the signal and background contributions as well as the signal model systematic uncertainties. The first and last bins include underflow and overflow events, respectively.

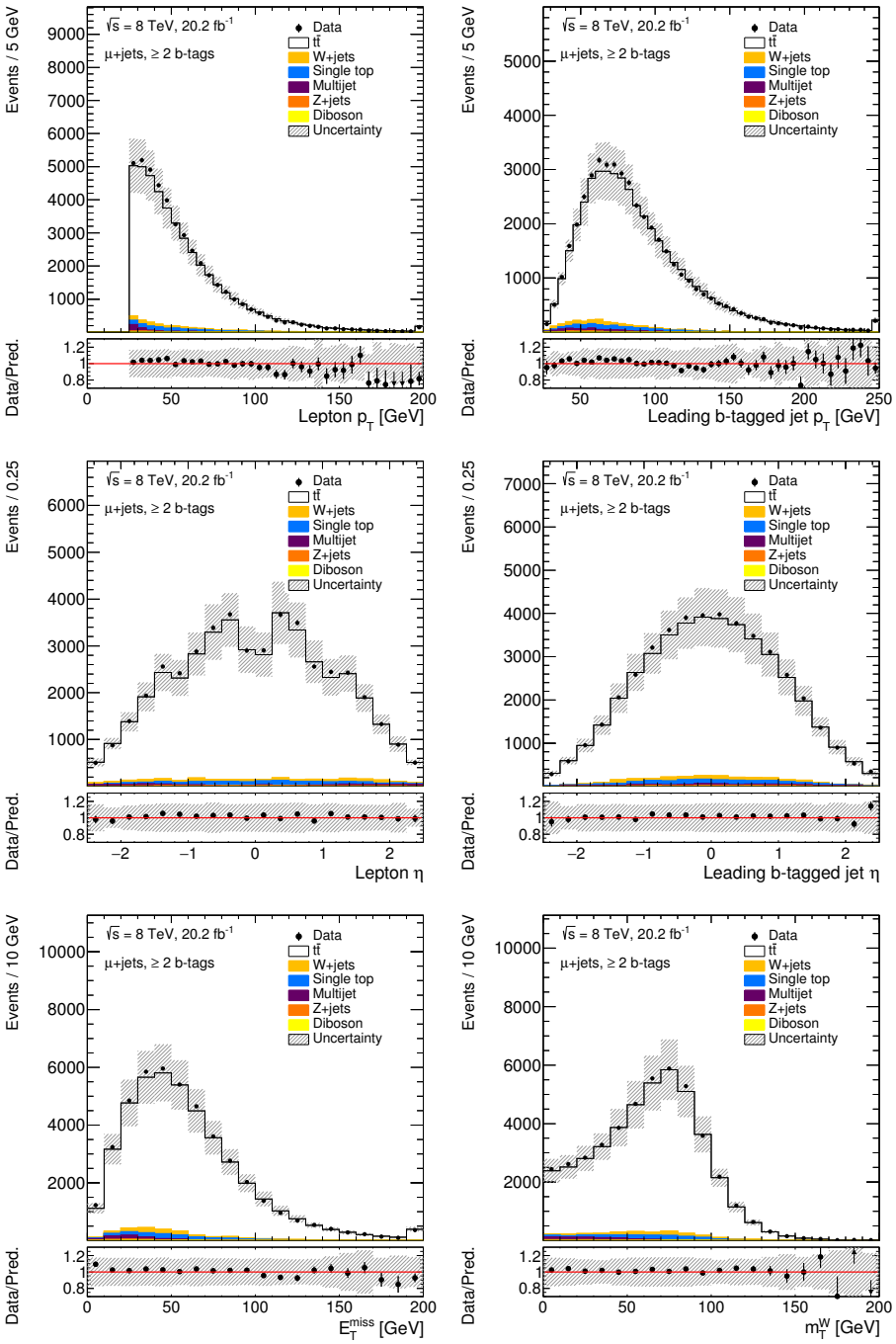

Figure 6.5: Distributions of the lepton and leading b-tagged jet p_{T}, lepton and leading b-tagged jet η, $E_{\mathrm{T}}^{\mathrm{miss}}$ and m_{T}^{W} in the muon+jets channel for events with at least two b-tagged jets resulting from the event selection. The hatched bands comprise the normalisation uncertainty in the signal and background contributions as well as the signal model systematic uncertainties. The first and last bins include underflow and overflow events, respectively.

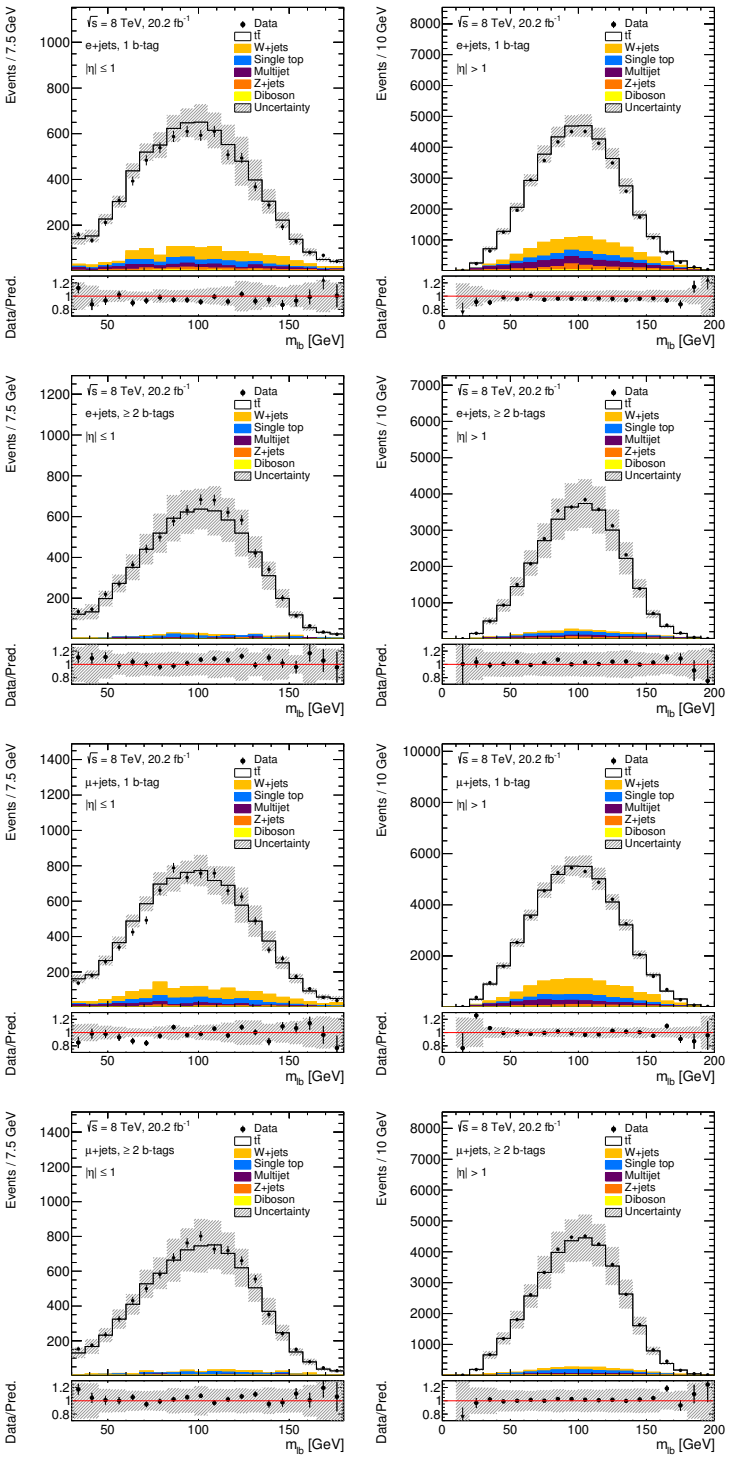

Figure 6.6: Distributions for the observable $m_{\ell b}$ in all eight analysis regions resulting from the event selection, as indicated by the labels. The hatched bands comprise the normalisation uncertainty in the signal and background contributions as well as the signal model systematic uncertainties. The first and last bins include underflow and overflow events, respectively.

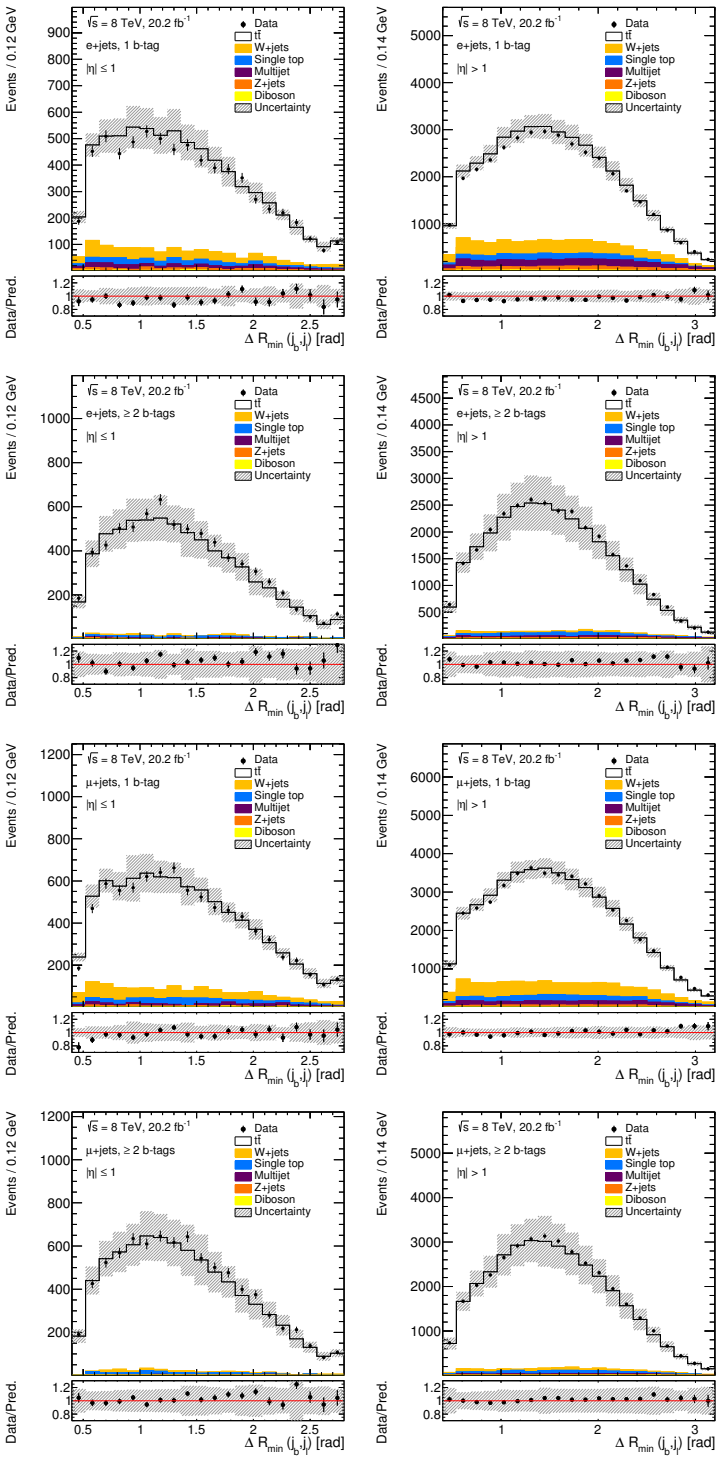

Figure 6.7: Distributions for the observable $\Delta R_{\text{min}}(j_b, j_l)$ in all eight analysis regions resulting from the event selection, as indicated by the labels. The hatched bands comprise the normalisation uncertainty in the signal and background contributions as well as the signal model systematic uncertainties. The first and last bins include underflow and overflow events, respectively.

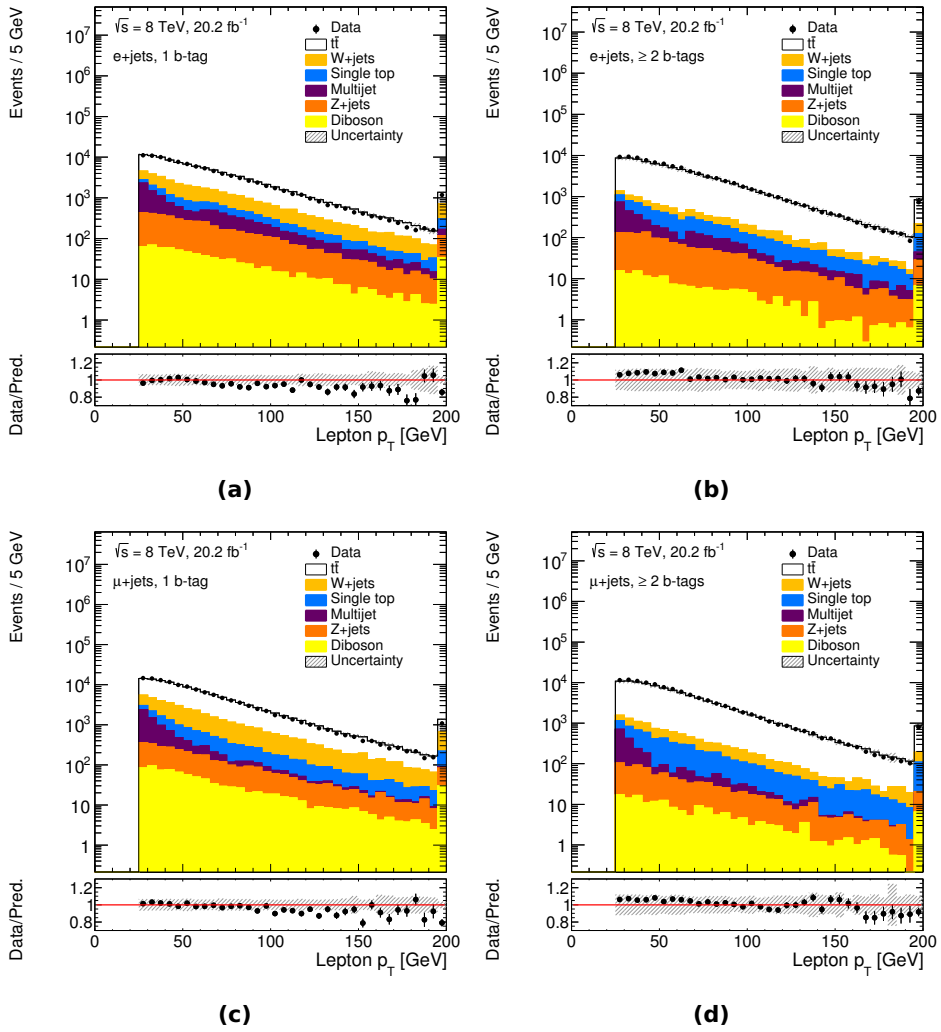

Figure 6.8: Distributions of the transverse momentum of the lepton after event selection using a logarithmic scale for (a,b) electron+jets and (c,d) muon+jets events with (a,c) exactly one and (b,d) at least two b-tagged jets before applying the cut on the likelihood of the event reconstruction algorithm. The effect due to mismodelling for small p_{T} in (b) and (d) is clearly visible although covered by the hatched uncertainty bands. These bands comprise the normalisation uncertainty in the signal and background contributions as well as the signal model systematic uncertainties. The first and last bins include underflow and overflow events, respectively.

6.3 Event Reconstruction

Correct assignment of reconstructed jets to the partons originating from the decay of a $t\bar{t}$ pair is essential for a precise measurement of Γ_t. As the top quark decays before hadronisation, its four-momentum must be reconstructed from its decay products. Since a unique association between jets and final state particles, before hadronisation processes may occur, is not feasible, dedicated reconstruction algorithms are utilised for this purpose. This analysis uses a likelihood-based kinematic fitting technique, the Kinematic Likelihood Fitter (KLFitter) [281], to assign jets to their parton level objects for events that fulfilled and passed the selection criteria delineated above in Sec. 6.2.

6.3.1 Kinematic Likelihood Fit

The reconstruction with the KLFitter framework is based on a certain input decay model, $t\bar{t}$ decays in this analysis, and requires the usage of the Bayesian Analysis Toolkit (BAT) [282]. KLFitter maps the four partons of the $t\bar{t}$ decay in the lepton+jets decay channel to four reconstructed jets using constraints on both the top quark mass m_t and the W boson mass m_W. The four reconstructed jets with the highest p_{T} values are used as input to KLFitter. Further possible configurations are compared in Sec. 6.3.4. For all resulting $4! = 24$ permutations, a likelihood L is maximised, which is of the following form for each permutation:

$$\begin{aligned} L = {} & \mathrm{BW}(m_{q1q2q3}|m_t,\Gamma_t)\cdot\mathrm{BW}(m_{q1q2}|m_W,\Gamma_W)\cdot\mathrm{BW}(m_{q4\ell\nu}|m_t,\Gamma_t)\cdot\mathrm{BW}(m_{\ell\nu}|m_W,\Gamma_W) \\ & \cdot\prod_{i=1}^{4} W(E_i^{\mathrm{meas}}|E_i)\cdot W(E_\ell^{\mathrm{meas}}|E_\ell)\cdot W(E_x^{\mathrm{miss}}|p_x^\nu)\cdot W(E_y^{\mathrm{miss}}|p_y^\nu)\,. \end{aligned} \tag{6.1}$$

The $W(E_P^{\mathrm{meas}}|E_P)$ are transfer functions, described in detail in Sec. 6.3.2, where E_P^{meas} is the measured energy of the reconstructed objects P, E_P is the energy of the corresponding original parton or lepton P, and p_x^ν and p_y^ν stand for the momentum components of the neutrino ν in the transverse plane. The energies E_P and these momentum components are free parameters of the likelihood maximisation. The third neutrino momentum component p_z^ν is initially computed with a W boson mass constraint of $m_W^2 = (p_\nu + p_\ell)^2$ with the four-momenta p_ν and p_ℓ. Then, p_z^ν is another free parameter in the fit after this initial calculation. Transfer functions for electrons, muons (where E is replaced by p_{T}), b-jets, light jets (including c-jets) and $E_{\mathrm{T}}^{\mathrm{miss}}$ are employed.
The $\mathrm{BW}(m_{ij(k)}|m_{t/W},\Gamma_{t/W})$ terms represent Breit-Wigner functions which characterise the probability distribution of the reconstructed W boson or top quark mass given the assumed values for the masses $m_{t/W}$ and the decay widths $\Gamma_{t/W}$. Thus, the BW constraints serve to assign leptons, $E_{\mathrm{T}}^{\mathrm{miss}}$ and jets to the leading order partons/lepton from the hard $t\bar{t}$ decay, and fitted masses of composite reconstructed particles can be evaluated. The indices $q1$-$q4$ refer to the four quarks that are mapped to the reconstructed jets.

The two mass parameters in the BW terms are set to $m_t = 172.5$ GeV and $m_W = 80.4$ GeV while

the parameters for the decay width are fixed to $\Gamma_t = 1.33$ GeV and $\Gamma_W = 2.1$ GeV. Since this analysis uses KLFitter merely to choose the best assignment of jets to partons and does not exploit the fitted parameters of reconstructed particles, as obtained from the kinematic fit, a variation of Γ_t has no influence on the reconstructed distributions and the final result. This possible relationship between the input decay width Γ_t and the resulting reconstructed observable distributions was studied and the results are shown in Sec. 6.3.4.

As described in Sec. 6.2, a cut on the logarithm of the KLFitter likelihood $\ln(L)$, as shown in Eq. (6.1), is applied. Around 56%-58% of events, depending on the analysis region, are removed by this requirement. Combinatorial background due to wrongly reconstructed events, which is mainly present at very small likelihood values, is suppressed to a large extent, as visible in Fig. 6.9. Also, the purity of the selected sample increases as a larger fraction of background events than signal $t\bar{t}$ events is removed. The distributions of the logarithm of the KLFitter likelihood illustrate that events with $\ln(L) < -50$ form a smaller second peak comprising mainly events without a correct match of all four reconstructed jets. The distributions of the reconstructed top quark mass lose their broader tails caused by those not correctly reconstructed events while the general shape of the distributions changes only very slightly when solely fully matched events are plotted.
The cut on $\ln(L)$ also affects the shapes of the distributions of the two observables, $m_{\ell b}$ and $\Delta R_{\text{min}}(j_b, j_l)$. Especially the very large tail at higher mass values of $m_{\ell b}$, which suffers noticeably from the combinatorial background, is reduced after applying the cut. On the contrary, the peak region of the $m_{\ell b}$ distributions hardly change. Later studies showed that the impact of this cut on the final result is covered by the statistical uncertainties, as described in Sec. 10.1.

Fig. 6.10 contains control plots of the logarithm of the likelihood for different analysis regions before the cut on this quantity is imposed. The fully matched events are shown separately. The fraction of events where all four partons are matched correctly increases from 13% to 23% and from 17% to 31% after applying the $\ln(L)$ cut for events with exactly one and at least two b-tagged jets, respectively.
This analysis does not rely on these efficiencies for matching all four jets correctly. The mass observable $m_{\ell b}$, which provides most of the sensitivity to Γ_t, requires solely the reconstruction of the b-jet from the leptonically decaying top quark. The reconstruction efficiency for this jet amounts to 65% and 75% for events with one and at least two b-tagged jets, respectively. The fraction of events with a correctly matched b-jet from the leptonically decaying top quark is highlighted in the $\ln(L)$ distributions contained in Fig. 6.11.
The given figures demonstrate once more to which extent background events and combinatorial background is reduced in order to improve the entire sensitivity of the measurement.

The purely kinematic information in the KLFitter likelihood can be augmented by additional information as, for instance, b-tagging information. The likelihood definition in Eq. (6.1) is modified and converted into a so-called event probability based on such further event properties, outlined in Sec. 6.3.3.

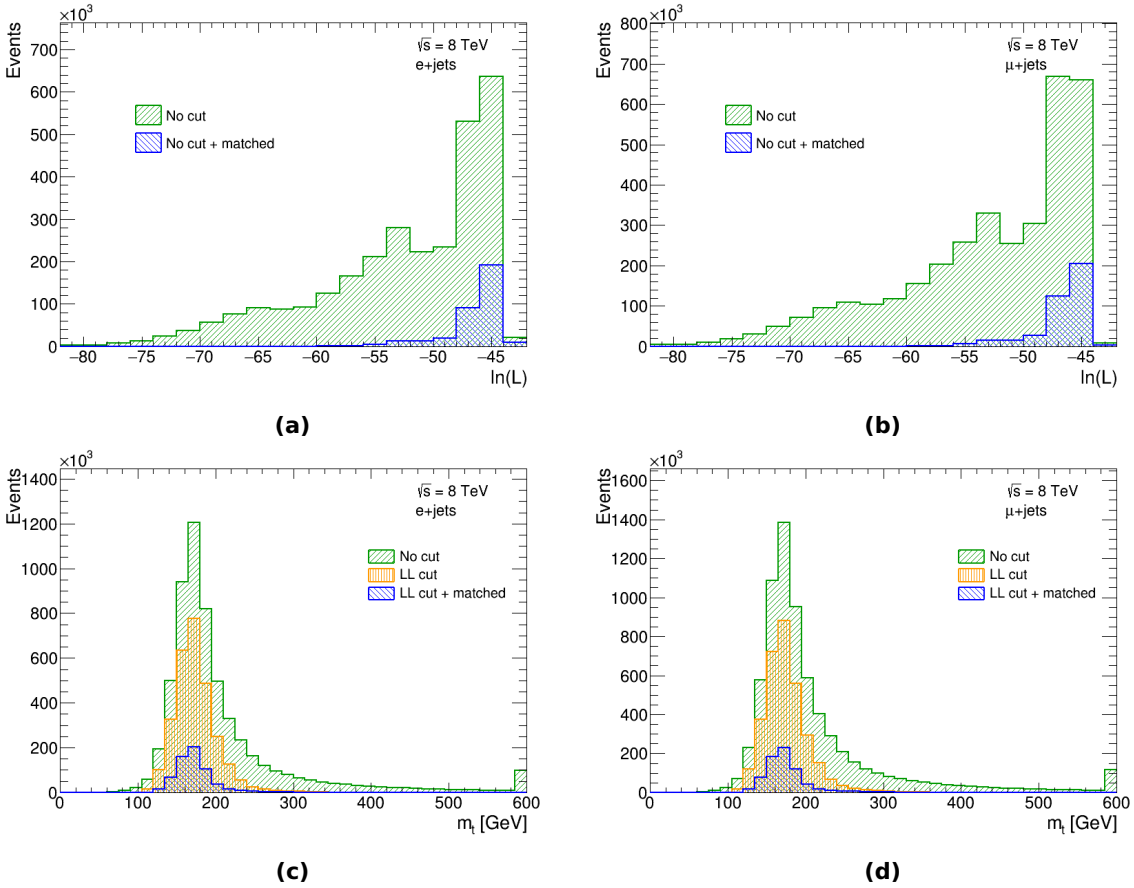

Figure 6.9: Distributions of (a,b) the logarithm of the KLFitter likelihood and (c,d) the reconstructed top quark mass for events with at least one b-tag for (a,c) electron+jets and (b,d) muon+jets events. The distributions in (a) and (b) compare fully matched with not fully matched events while three different options are provided in the top quark mass plots: (1) KLFitter without cut, (2) KLFitter with the likelihood cut ("LL cut") and (3) KLFitter with the likelihood cut for fully matched combinations.

KLFitter determines the likelihood and also the event probability for all permutations in the event. Finally, the permutation with the highest event probability is regarded as the best estimate for the jet-to-particle association and used to reconstruct events entering the decay width measurement.

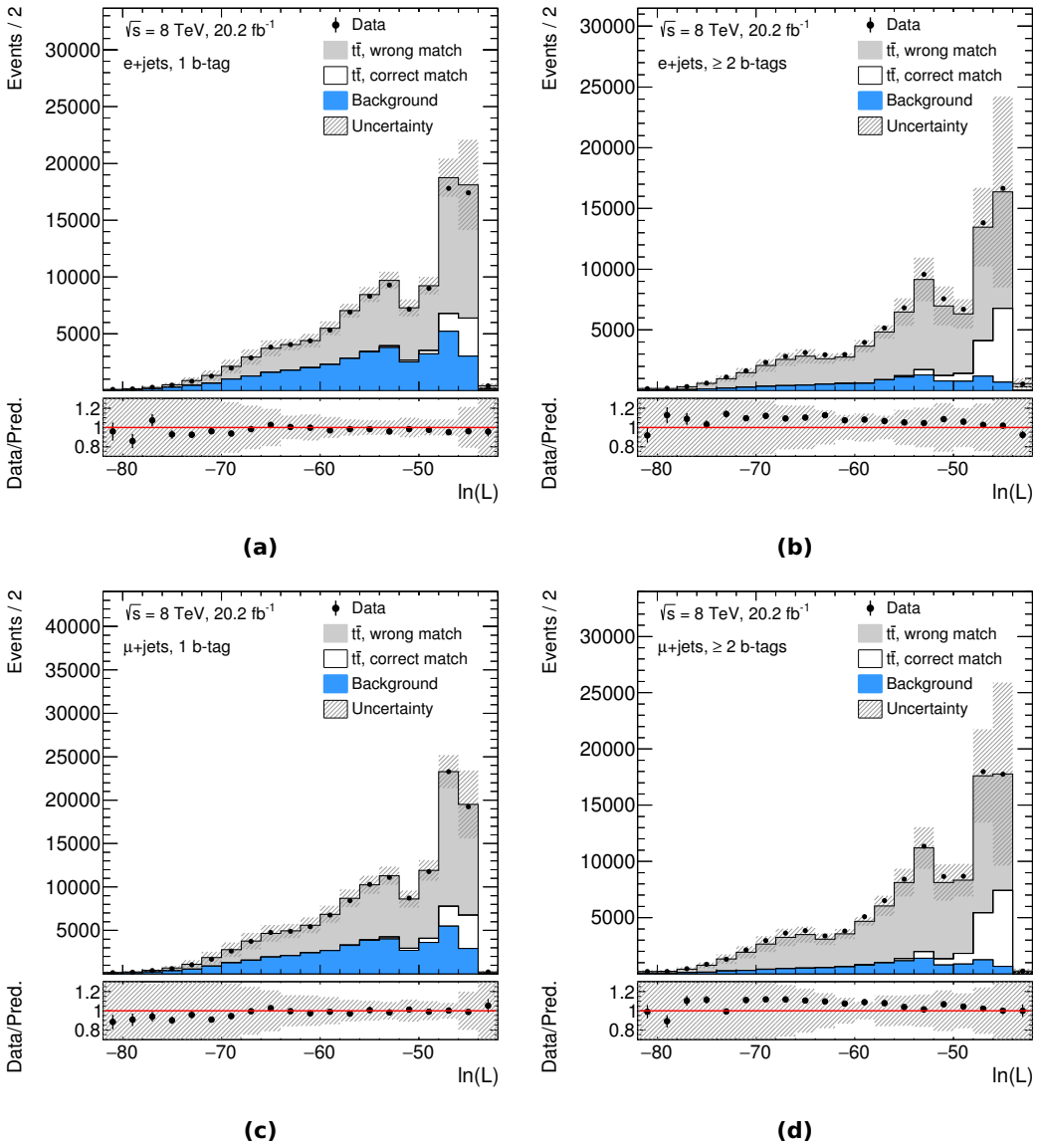

Figure 6.10: Distributions of the logarithm of the likelihood obtained from the event reconstruction algorithm for selected (a,b) electron+jets and (c,d) muon+jets events having (a,c) exactly one and (b,d) at least two b-tagged jets. The events with $\ln(L) < -50$ form a secondary broader peak mainly composed of events that are not properly reconstructed, i.e. events for which not all four jets are correctly matched to partons (“wrong match”). Fully matched events are primarily existent in the larger $\ln(L)$ regions. The hatched bands contain the normalisation uncertainty in the signal and background contributions as well as the signal model systematic uncertainties. The first and last bins include underflow and overflow events, respectively.

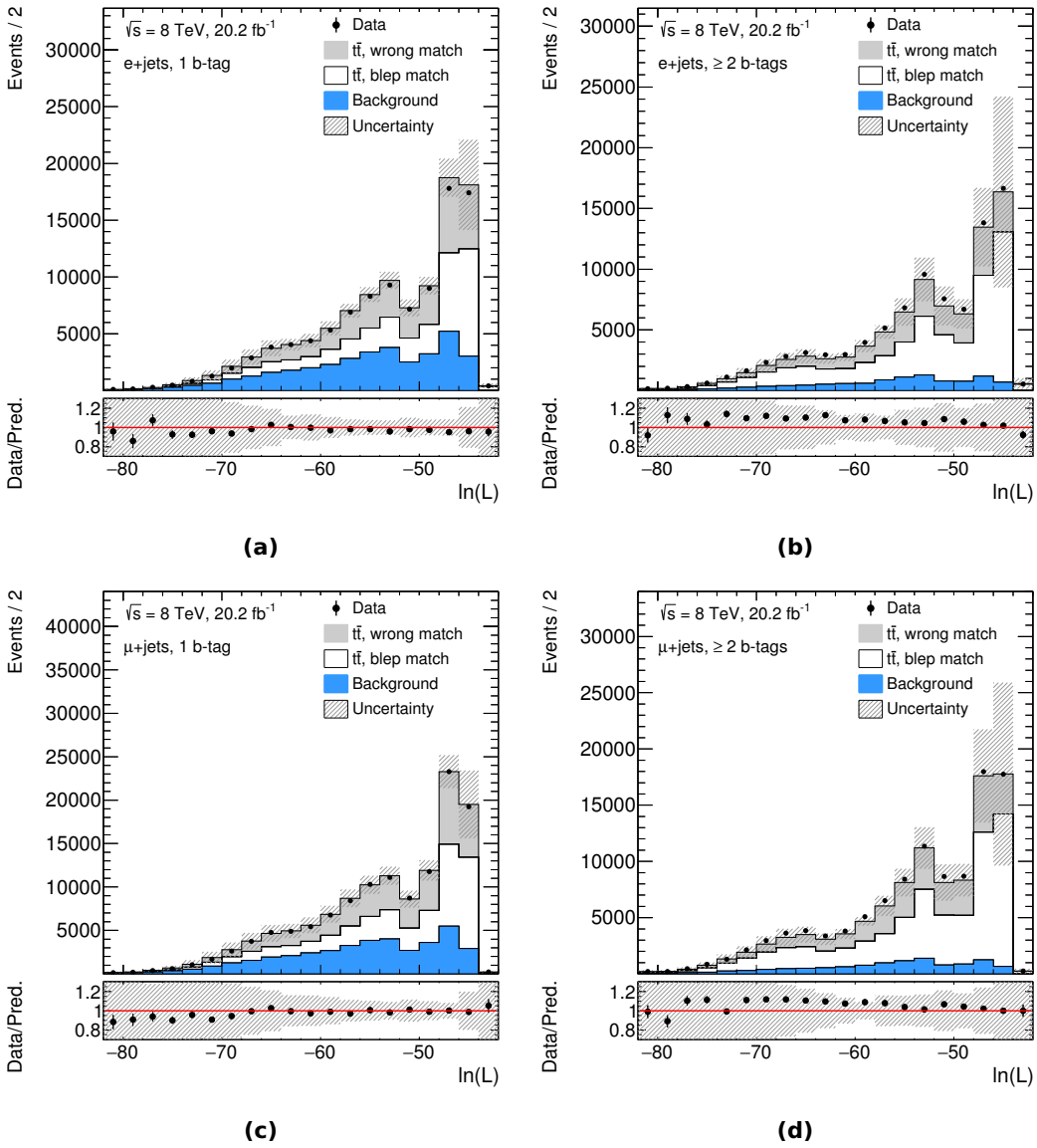

Figure 6.11: Distributions of the logarithm of the likelihood obtained from the event reconstruction algorithm for selected (a,b) electron+jets and (c,d) muon+jets events having (a,c) exactly one and (b,d) at least two b-tagged jets. A large fraction of events possesses a leptonic b jet that is correctly matched to the corresponding parton, in particular in the region of larger $\ln(L)$ values ("blep match"), compared to events without a correct match of this jet ("wrong match"). The hatched bands contain the normalisation uncertainty in the signal and background contributions as well as the signal model systematic uncertainties. The first and last bins include underflow and overflow events, respectively.

6.3.2 Transfer Functions

Transfer functions, which are independent of Γ_t, are part of the KLFitter likelihood in Eq. (6.1) in order to describe reconstructed energies of jets and leptons of the $t\bar{t}$ lepton+jets decay channel affected by detector resolutions. The analysis requires transfer functions for electrons, muons, b-jets, light jets (comprising c-jets) and $E_{\mathrm{T}}^{\mathrm{miss}}$. A transfer function can be characterised, generally speaking, as the conditional probability to get a particular response when matching reconstructed jets and leptons to partons and constitutes a continuous function which describes the relative energy difference between a parton and a reconstructed object as a function of the parton energy according to the LO decay signature. Double-Gaussian functions are used to parametrise the difference between the reconstructed energy and the one at truth or parton level for electrons and jets. Such functions describe the corresponding energy distributions and in particular the tail regions to a good extent and are thus employed despite a better knowledge of the underlying detector physics. The double-Gaussian functions can be expressed as:

$$W(\Delta E) = \frac{1}{\sqrt{2\pi}(p_2 + p_3 p_5)} \left(\mathrm{e}^{\frac{-(\Delta E - p_1)^2}{2p_2^2}} + p_3 \cdot \mathrm{e}^{\frac{-(\Delta E - p_4)^2}{2p_5^2}} \right).$$

The term ΔE constitutes the relative energy difference between these truth and reconstructed energies: $\Delta E = (E_{\mathrm{truth}} - E_{\mathrm{reco}})/E_{\mathrm{truth}}$. For muons, the transverse momentum p_{T} is used instead of the energy. The individual parameters are delineated in more detail in the next paragraphs.

The transfer functions are derived from a simulation of $t\bar{t}$ events using the MC@NLO [246, 247] event generator. Solely objects that are matched to their associated partons from the hard decay are used. A matching criterion of $\Delta R < 0.3$ is applied to the jets to be considered as matched to its partons. This requirement is strengthened to $\Delta R < 0.1$ for leptons. The matching must be bi-unique, which means that one and only one matching for both objects is allowed.

The transfer function parameters p_i depend on the energy of the underlying parton or lepton, p_{T} in case of muons, and are parametrised according to the object type they represent.

A simple linear dependence is used as an approximation for the parameters at leading order, which is adjusted if a physical motivation justifies another parameter dependence. For electrons and jets, the resolution term p_2 is parametrised as $\sim 1/\sqrt{E}$ because this parameter describes the calorimeter resolution due to sampling fluctuations with a definition of the resolution term according to $\sigma_E/E \propto 1/\sqrt{E}$, as given in Sec. 3.3.2. In addition, heuristically determined parametrisations replace failing linear assumptions. Altogether, p_2 and p_4 require such a parametrisation with $1/\sqrt{E}$. For muons, as the resolution is tracking-based, the relationship $\sigma_{p_{\mathrm{T}}}/p_{\mathrm{T}} \propto p_{\mathrm{T}}$ holds so that a linear dependence is kept for all muon parameters. To summarise, the following parametrisations are applied for

electrons and jets:

$$p_1 = a_1 + b_1 \cdot E_{\text{truth}}\,, \quad p_2 = a_2/\sqrt{E_{\text{truth}}} + b_2\,,$$
$$p_3 = a_3 + b_3 \cdot E_{\text{truth}}\,, \quad p_4 = a_4/\sqrt{E_{\text{truth}}} + b_4\,, \quad p_5 = a_5 + b_5 \cdot E_{\text{truth}}\,,$$

while for muons the parametrisation with the linear dependence in all five cases is written as:

$$p_i = a_i + b_i \cdot p_{\text{T,truth}} \quad \text{with } i = 1,2,3,4,5.$$

The different transfer functions for b jets, lighter jets, electrons and muons are defined separately in different $|\eta|$ regions due to detector response changes in those regions and particles with different energy ranges. For light jets and b jets, five $|\eta|$ regions are defined in the range from 0.0 to 4.5. The edges between the regions are $|\eta| = [0.0, 0.8, 1.37, 1.52, 2.5, 4.5]$ with a separate bin for the calorimeter transition region according to the structure of the ATLAS detector with its detector components having different resolutions and efficiencies. The edges of the four electron regions are very similar $|\eta| = [0.0, 0.8, 1.37, 1.52, 2.5]$ although the transition region is excluded because the event selection automatically rejects electrons in that region. For muons, on the contrary, the transfer functions are split into three $|\eta|$ bins with edges at $|\eta| = [0.0, 1.11, 1.25, 2.5]$, to allow for a separation of the barrel and the forward part of the muon spectrometer.
The different factors a_i and b_i of the transfer functions are determined with the help of a global fit to each particle type in all considered η regions separately.

The transfer functions for the missing transverse momentum $E_{\text{T}}^{\text{miss}}$ are defined relying on the approach that the x and y components of the neutrino at parton level are mapped to the measured x and y components of $E_{\text{T}}^{\text{miss}}$. The corresponding transfer functions thus parametrise the difference $E_{x,y}^{\text{miss}} - p_{x,y}^{\nu}$. The $E_{\text{T}}^{\text{miss}}$ is related to the scalar sum of the energy ΣE_{T} that is deposited in the calorimeter which is why the latter quantity is used for the parametrisation with a sigmoid function which was found heuristically [283]:

$$\sigma(\Sigma E_{\text{T}}) = p_0 + \frac{p_1}{1 + \exp[-p_2(\Sigma E_{\text{T}} - p_3)]}\,.$$

Dedicated systematic uncertainties in the transfer function due to the assumption of a particular model are not evaluated. The reason is that uncertainties in the $t\bar{t}$ model are evaluated as part of the systematic uncertainties in this analysis, as described extensively in Ch. 8.4. Nevertheless, the model assumptions on the transfer functions limit their area of validity. With smaller jet energies, pile-up effects may enter to a significant extent and can thus cause deviations from the above given parametrisations, affecting the performance of the kinematic likelihood fit. However, as KLFitter is merely utilised to choose the best assignment of jets to partons without exploiting fitted parameters of the reconstructed particles, the event reconstruction is not affected by such limitations of the transfer functions and yields very reliable results.

6.3.3 Extensions of the Likelihood

The basic definition of the likelihood L, as defined in Sec. 6.3.1, can be complemented by additional information to improve the KLFitter reconstruction. For this purpose, the likelihood expression of Eq. (6.1) is converted into an event probability which, for a certain permutation i, is defined as:

$$P_i = \frac{L_i \prod_j p_{i,j}}{\sum_k L_k \prod_j p_{k,j}} \,. \tag{6.2}$$

The $p_{i,j}$ denote these extensions or weights convoluted with the likelihood for all jets j to properly account for additional information. KLFitter first evaluates the likelihood for each permutation in the event according to Eq. (6.1) and then the P_i. The permutation with the largest event probability is chosen as the best jet-to-parton association at the end.

In this analysis, the likelihood definition of Eq. (6.1) is extended by information about the b-tagged jets from the MV1 tagger, included in the factors $p_{i,j}$, which are calculated for all jets j and multiplied by the likelihood L_i.
The option applied for the direct top quark decay width measurement rests on b-tagging weights so that the $p_{i,j}$ contain the b-tagging efficiency or the rejection factor associated with the b-tagging working point, depending on whether a jet is b-tagged or not. This setup is thus also called *working point option*. With the b-tagging efficiency ε_b and the rejection factor R_l, the weights are defined as:

$$p_{i,j} = \left\{ \begin{array}{c} \varepsilon_b, \; b \text{ jet was } b\text{-tagged} \\ (1-\varepsilon_b), \; b \text{ jet was not } b\text{-tagged} \end{array} \right\} \quad \text{for } b \text{ jets}\,,$$

$$p_{i,j} = \left\{ \begin{array}{c} 1/R_l, \; \text{light jet was } b\text{-tagged} \\ (1-1/R_l), \; \text{light jet was not } b\text{-tagged} \end{array} \right\} \quad \text{for light jets}\,.$$

The corresponding values are set to $\varepsilon_b = 0.7$, equivalent to a b-tagging efficiency of 70%, and the rejection factor amounts to $R_l = 136.7$ (see Sec. 4.5).

A further extension of the KLFitter distinguishes up- and down-type jets originating from the hadronically decaying W boson [130]. In general, such a separation of jets can be based on the flavour difference between the jets and on the V-A structure of the decay vertex of the underlying W boson, which predicts energy differences between the two resulting light jets [284]. In the current implementation of KLFitter, the jet transverse momentum serves as a measure of these differences inferred from the implications of the V-A decay vertex structure. Since particular taggers for c jets are not well-established for analyses at centre-of-mass energies of 8 TeV, the output of the MV1 b-tagging algorithm is used to discriminate between different types of lighter jets. Taking this information into account, the following product of probability extensions for the four participating

jets can be defined and used in Eq. (6.2):

$$\prod_j p_{i,j} = p_\alpha^{b\text{-type}}(p_\mathrm{T}^\mathrm{bhad}) p_\beta^{b\text{-type}}(w_\mathrm{MV1}^\mathrm{bhad}) \cdot p_\alpha^{b\text{-type}}(p_\mathrm{T}^\mathrm{blep}) p_\beta^{b\text{-type}}(w_\mathrm{MV1}^\mathrm{blep}) \cdot \\ \cdot p_\alpha^{u\text{-type}}(p_\mathrm{T}^\mathrm{ujet}) p_\beta^{u\text{-type}}(w_\mathrm{MV1}^\mathrm{ujet}) \cdot p_\alpha^{d\text{-type}}(p_\mathrm{T}^\mathrm{djet}) p_\beta^{d\text{-type}}(w_\mathrm{MV1}^\mathrm{djet}) \,.$$

Complying with the above explanations, p_α denotes the probability of a certain jet to have the measured p_T value and p_β describes the probability of this jet to have the b-tagging weight w_MV1 for the chosen permutation with the four jets assigned to the bottom jets from the hadronically or leptonically decaying top quark (bhad, blep) and to the two light jets (ujet, djet). Although using only the b-tagging weights from the MV1 tagger without c-tagging information, the fraction of events where the up- and down-type jets of the hadronically decaying W boson are correctly matched increased from 50% (arbitrary choice) to around 60%. This setup is enabled for the Γ_t measurement but since this analysis is not sensitive to the interchange of the jets from the hadronically decaying W boson, this choice has no impact on the obtained results discussed later.

6.3.4 Further KLFitter Configurations

The default configuration of KLFitter used for this measurement takes four jets with the highest p_T in the likelihood into account. Due to the presence of additional jets in the event (the event selection in Sec. 6.2 requires at least four jets) caused by processes like initial and final state radiation, KLFitter options based on five jets were studied.
The first option simply uses one more jet with the fifth highest transverse momentum. If only four jets are present in the event, only these four jets enter the kinematic likelihood fit. This option can be compared to a configuration where five jets with a modified ordering are taken into account in the event reconstruction. In this modified ordering, two jets with the highest b-tagging weight from the MV1 tagger and three with the highest p_T of the remaining jets are considered in the likelihood. For events with exactly four jets, only the remaining two jets are added. The number of permutations increases from $4! = 24$ to $5! = 120$ using events with at least five jets for these two options. The effect of these configurations on the reconstruction efficiency and the total uncertainty was evaluated.
The efficiencies of the KLFitter reconstruction for the $t\bar{t}$ decay are shown in Fig. 6.12. These reconstruction efficiencies are evaluated using the nominal POWHEG+PYTHIA signal $t\bar{t}$ MC sample, also used for the comparison between data and prediction in Sec. 6.2. The numbers are given for the reconstruction of individual particles, parts of the $t\bar{t}$ decay chain and the full $t\bar{t}$ topology as reconstructed by KLFitter. The corresponding bin labels are defined and described in Table 6.2.
A KLFitter configuration based on at least five jets used for the reconstruction outperforms the basic option using four jets, as indicated by the efficiency numbers. In most cases, the efficiencies for the five jet option rise by a few percent or are at least comparable. The option where the alternative modified ordering of the four or five jets - if available - is applied in the event reconstruction yields very similar results compared to the simple option with five jets; the efficiencies are only slightly

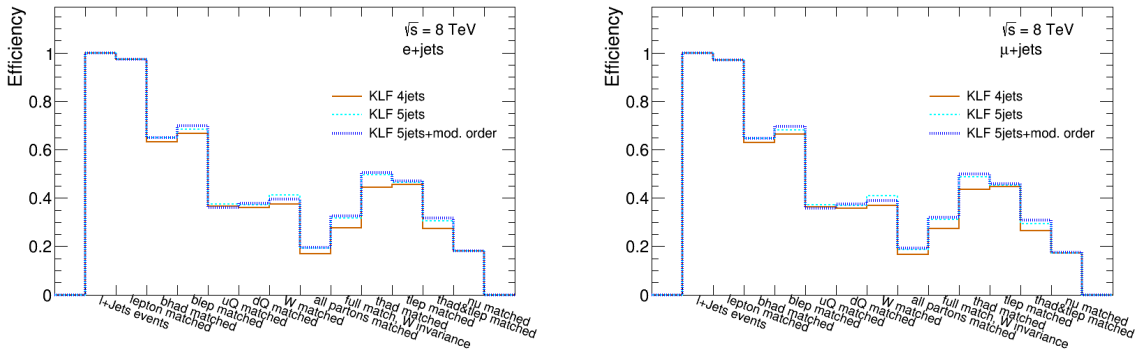

(a) **(b)**

Figure 6.12: KLFitter reconstruction efficiencies for different particles and components of the $t\bar{t}$ decay as described in Table 6.2 in the (a) e+jets and (b) μ+jets channel for events with at least two b-tagged jets. Compared are the KLFitter versions using either four or five jets and also a modified jet ordering ("mod. order") for the event reconstruction, as defined in the text.

higher for the fully matched four partons and for the match of the two top quarks. The increase in reconstruction efficiencies is expected because a jet originating from a parton belonging to the $t\bar{t}$ decay might have the fifth highest p_{T} value but is not considered in the KLFitter configuration with four jets. The configurations with five jets affect in particular the reconstruction of the hadronically decaying top quark where three jets need to be matched correctly while for the leptonically decaying top quark only one jet enters. Thus, the difference between the options is small for this leptonically decaying top quark. This result is similar in all b-tag bins. The magnitude of the different listed efficiencies and their origins are also discussed in Ref. [281].

Even though these studies emphasise the advantages of the reconstruction option with five jets to account for ISR and FSR jets, the measurement of Γ_t is very sensitive to systematic variations caused by initial or final state radiation and the associated systematic uncertainty is significantly larger for events where the KLFitter with more than four jets is used. This is due to the fact that those additional ISR and FSR jets enter the event reconstruction more frequently in a direct way if five instead of four jets are used to assign jets to parton level objects. This effect on the total uncertainty of the top quark decay width outweighs the gain in reconstruction efficiency. Hence, the analysis presented here is based on a KLFitter configuration considering only four jets with the highest transverse momentum. The related studies evaluating the impact of different systematic uncertainties are described in detail in Sec. 9.2.
Based on this option with exactly four jets, the impact of the cut on the logarithm of the KLFitter likelihood was studied. By requiring $\ln(L) > -50$ for all selected events, the reconstruction efficiency improves by about 5% to more than 10% for the individual reconstructed particle or object types. This is illustrated in Fig. 6.13 and constitutes a further justification of this cut.
Events for which the reconstructed jets could not be correctly assigned to partons are mainly

Bin label	Description
l+Jets events	The efficiency of this number is one; only $t\bar{t}$ events decaying via the lepton+jets channel are taken into account here. Used as a reference for further shown numbers.
lepton matched	The reconstructed charged lepton matches the corresponding parton level object with $\Delta R < 0.1$.
bhad matched	The reconstructed b jet from the hadronically decaying top quark matches the corresponding model parton with $\Delta R < 0.3$.
blep matched	The reconstructed b jet from the leptonically decaying top quark matches the corresponding model parton with $\Delta R < 0.3$.
uQ matched	The reconstructed up-type quark jet from the hadr. decaying W boson matches the corresponding model parton with $\Delta R < 0.3$.
dQ matched	The reconstructed down-type quark jet from the hadr. decaying W boson matches the corresponding model parton with $\Delta R < 0.3$.
W matched	The two reconstructed jets assigned to the hadronically decaying W boson match but can be exchanged.
all partons matched	The assignment between reconstructed jets and model partons is correct for all four jets associated with the $t\bar{t}$ decay.
full match, W invar.	The two reconstructed b-jets are correctly matched to model partons and the two light jets are assigned to the hadronically decaying W boson but can be exchanged.
thad matched	The reconstructed hadronically decaying top quark matches the corresponding parton level top quark with $\Delta R < 0.4$.
tlep matched	The reconstructed leptonically decaying top quark matches the corresponding parton level top quark with $\Delta R < 0.4$.
thad&tlep matched	Both reconstructed top quarks are correctly matched to the two top quarks at parton level with $\Delta R < 0.4$.
nu matched	The reconstructed neutrino matches the corresponding neutrino at parton level.

Table 6.2: Definition of bin labels as given in the plots showing the reconstruction efficiencies obtained with KLFitter for different objects and the full $t\bar{t}$ decay.

removed by this cut because the reconstruction efficiencies of the corresponding objects increase the most, for instance, for the reconstruction efficiency of the hadronically decaying top quark. In contrast, the reconstruction efficiency of the leptonically decaying top quark where only one jet is involved increases merely slightly.

KLFitter operates with a fixed top quark decay width in this analysis. As outlined in Sec. 6.3.1, KLFitter only chooses the best assignment of reconstructed particles to corresponding objects at parton level and, hence, the analysis does not rely on the fitted parameters of reconstructed particles. In order to verify that this is indeed appropriate and does not affect the measurement, the impact of a varied decay width in KLFitter was investigated. The default setup is based on $\Gamma_t = 1.33$ GeV corresponding to the value used in the nominal $t\bar{t}$ MC samples. This parameter was set to values

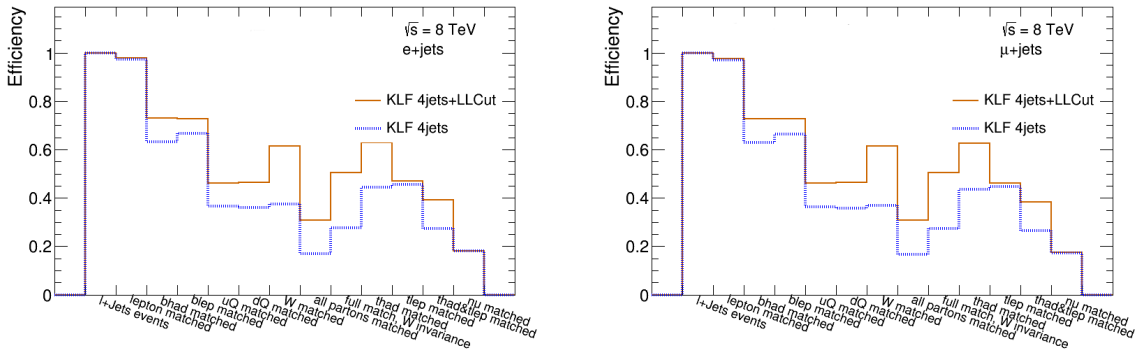

(a) **(b)**

Figure 6.13: KLFitter reconstruction efficiencies for different particles and components of the $t\bar{t}$ decay as described in Table 6.2 in the (a) e+jets and (b) μ+jets channel for events with at least two b-tagged jets. Compared are the KLFitter versions using four jets for the event reconstruction with and without the cut on the KLFitter likelihood ("LLCut").

of $\Gamma_t = 0.6$ GeV and $\Gamma_t = 2.0$ GeV, and the event reconstruction with KLFitter was reperformed for these two alternative options. The resulting observable distributions of both $m_{\ell b}$ and $\Delta R_{\text{min}}(j_b, j_l)$ hardly change with respect to the nominal setup with $\Gamma_t = 1.33$ GeV. Fig. 6.14 and Fig. 6.15 depict the example distributions of the two observables comparing the nominal setting to a KLFitter reconstruction based on $\Gamma_t = 0.6$ GeV. The differences between the distributions are barely visible. The same applies to the comparison with distributions obtained from a KLFitter configuration with $\Gamma_t = 2.0$ GeV so that the usage of a fixed value of $\Gamma_t = 1.33$ GeV for the event reconstruction with KLFitter is well justified.

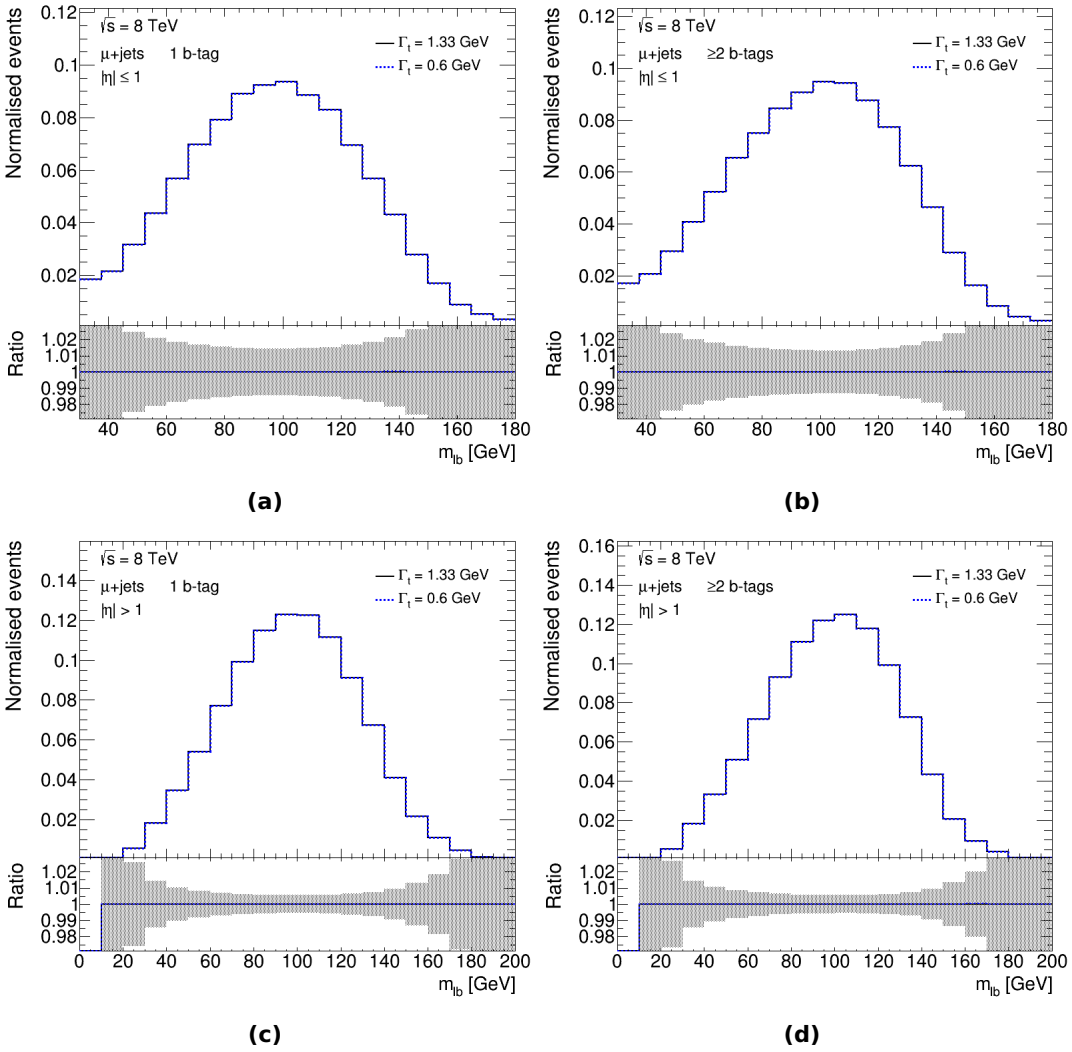

Figure 6.14: Comparison of distributions for the observable $m_{\ell b}$ obtained from event reconstructions with KLFitter configurations where Γ_t is set to 1.33 GeV or 0.6 GeV. Shown are distributions in the (a,b) $|\eta| \leq 1$ analysis region and (c,d) $|\eta| > 1$ analysis region with (a,c) exactly one or (b,d) at least two b-tagged jets in the muon+jets channel. The lower panels contain the ratio between the distributions with respect to the nominal sample with $\Gamma_t = 1.33$ GeV. The shown uncertainty bands contain statistical uncertainties.

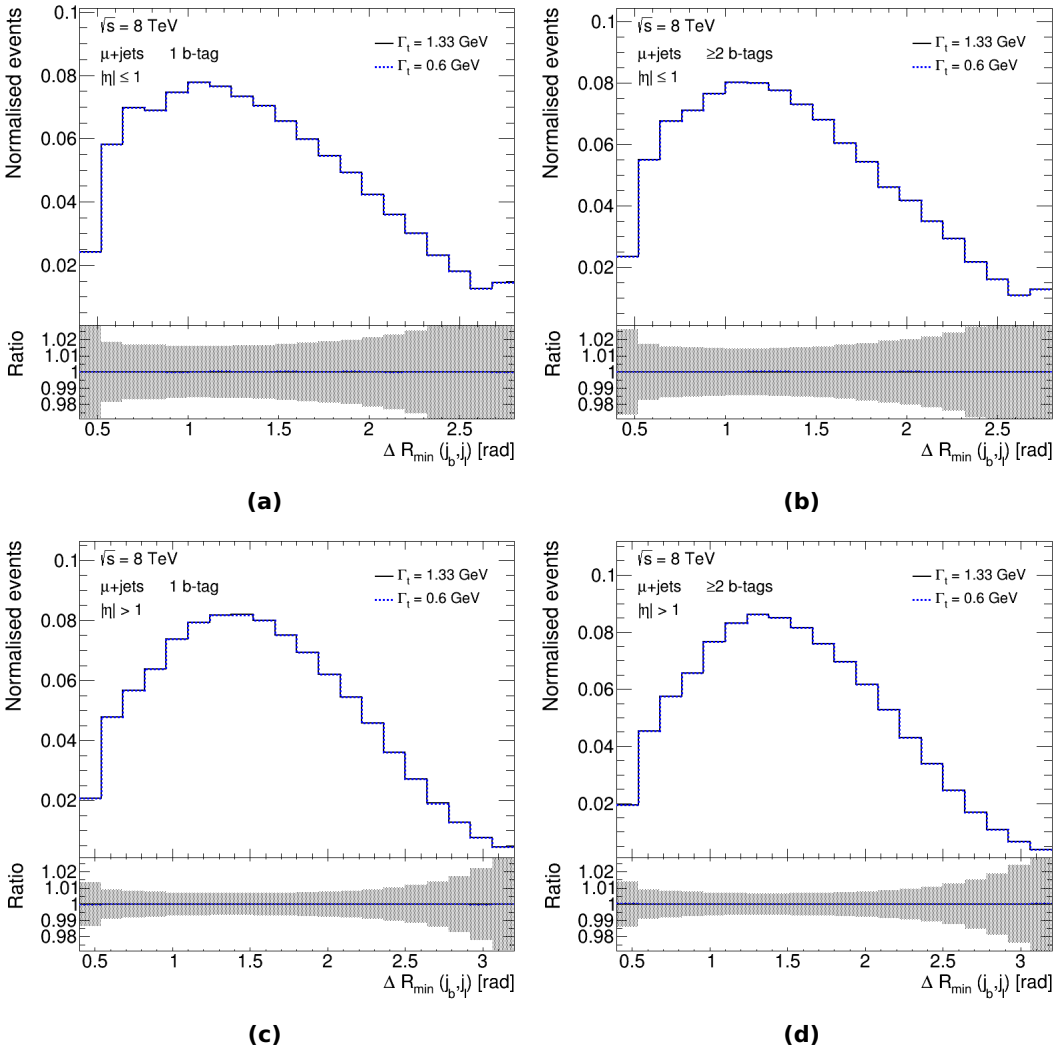

Figure 6.15: Comparison of distributions for the observable $\Delta R_{\text{min}}(j_b, j_l)$ obtained from event reconstructions with KLFitter configurations where Γ_t is set to 1.33 GeV or 0.6 GeV. Shown are distributions in the (a,b) $|\eta| \leq 1$ analysis region and (c,d) $|\eta| > 1$ analysis region with (a,c) exactly one or (b,d) at least two b-tagged jets in the muon+jets channel. The lower panels contain the ratio between the distributions with respect to the nominal sample with $\Gamma_t = 1.33$ GeV. The shown uncertainty bands contain statistical uncertainties.

7 Analysis Strategy

The measurement of the top quark decay width is realised using a binned likelihood template fit of one-dimensional observable distributions. The fit is performed simultaneously with distributions of two observables associated with the hadronic and leptonic decay branches of $t\bar{t}$ events in eight mutually exclusive analysis regions (two lepton flavours, two b-tag regions and two $|\eta|$ regions). The simulated distributions of the observables plus the data-driven estimate of the multijet background are fitted to reconstructed data distributions obtained from the event selection and reconstruction with KLFitter as described in Ch. 6.
This chapter depicts the likelihood template fit with all its features in more detail and thus presents the entire underlying analysis strategy, starting with the choice of observables suited for a template fit to extract Γ_t. The method of producing the required decay width templates is covered in the subsequent section, followed by the definition of the fit procedure itself, the different analysis regions, the description of the determination of uncertainties and the validation of the chosen fit method. At the end, correlations between the chosen observables and tested fit configurations are addressed. The final choice of the best fit configuration is based on dominant systematic uncertainties, presented in Ch. 8. Hence, the detailed discussion of possibly suited fit configurations follows in the subsequent Ch. 9.
In addition, a two-dimensional approach was studied and tested extensively, driven by the idea to estimate and constrain the originally expected largest systematic uncertainty directly in the fit. The corresponding studies and results are summarised in App. I. Comparison studies revealed that a very well optimised one-dimensional setup performs similarly while being far less CPU-intensive.

7.1 Observables Sensitive to the Top Quark Decay Width

Potential observables suited for the measurement of Γ_t were designed in a way to fulfil one or more of the following criteria: a high sensitivity to the top quark decay width, a low sensitivity to dominant (mainly jet-related) systematic uncertainties and a low sensitivity to scale shifts or effects appearing in the tails of the distributions. Since later studies revealed that observables which depend directly on the mass are very sensitive to dominant systematic effects, it was also investigated to which extent it is feasible to design alternative observables with a low sensitivity to the top quark mass. The definition of observables fulfilling one criterion without contradicting at least another one was a very challenging task because a large sensitivity to Γ_t is usually associated with a large sensitivity to m_t. Furthermore, mass-dependent observables from the hadronically decaying top quark especially suffer significantly from jet-related uncertainties. Table 7.1 contains

observables studied in more detail in the course of this analysis.

Observable (formula)	Description
m_t^{had}	Reconstructed mass of the hadronically decaying top quark
$m_{\ell b}$	Reconstructed mass of the b jet from the leptonically decaying top quark and the corresponding lepton
$R_{32} = m_t^{\text{had}}/m_W^{\text{had}}$	Ratio of the reconstructed masses of the top quark and the W boson of the hadronic decay branch
$D_{32} = m_t^{\text{had}} - m_W^{\text{had}}$	Difference of the reconstructed masses of the top quark and the W boson of the hadronic decay branch
$\text{SdR} = \Delta R(j_b, j_{l1}) + \Delta R(j_b, j_{l2}) + \Delta R(j_{l1}, j_{l2})$	Sum of the ΔR of the jets from the hadronically decaying top quark
$\Delta R_{\text{min}}(j_b, j_l)$	ΔR between the b jet j_b and the light jet j_l which is closer to j_b from the hadronically decaying top quark

Table 7.1: Table with observables sensitive to the top quark decay width and thus potentially suited for a direct measurement of Γ_t, studied in more detail in this analysis.

The mass of the hadronically decaying top quark m_t^{had} is included as a reference as its distribution directly contains the decay width by definition. The mass $m_{\ell b}$ is the counterpart for the leptonic decay branch because the neutrino cannot be reconstructed well so that these two components, lepton and b jet, remain. R_{32} is included in the list since it is expected to have only very little sensitivity to the jet energy scale uncertainty due to its definition as a 3-jet mass divided by a 2-jet mass (which is responsible for the observable name). D_{32} denotes the corresponding difference of the two masses, defined such that effects that may influence the tails and thus the width of the two subtracted mass distributions cancel out in the difference. Several other mass-related observables were constructed but exhibited very similar features as the above listed ones which is why they are not discussed separately in this thesis. The observables based on ΔR, namely SdR and $\Delta R_{\text{min}}(j_b, j_l)$, are expected, by construction, to be less sensitive to jet-related uncertainties because they are only derived from angular quantities and do not rely on energy-based parameters. Other angular observables than the ones listed were defined and tested as well. However, SdR as a sum of three angles adds most information to the fit compared to other possible angular observables of the hadronic decay branch while $\Delta R_{\text{min}}(j_b, j_l)$ is much better modelled compared to those alternative angular observables. This is covered in Ch. 9.3. Consequently, the discussion of the angular observables rests on these two variables, SdR and $\Delta R_{\text{min}}(j_b, j_l)$.

Intensive studies of the observables as presented in Ch. 9 revealed that those which are directly related to m_t have a relatively high sensitivity to the width but suffer severely from jet-related or radiation uncertainties. Only the mass $m_{\ell b}$ offers a good sensitivity to Γ_t while being less sensitive to those uncertainties as it uses only one jet unlike the reconstructed masses from the hadronic decay branch. Out of all observables shown in Table 7.1, $m_{\ell b}$ offers the best compromise with a good sensitivity to Γ_t and low sensitivity to systematic effects. In principle, the measurement could be performed with $m_{\ell b}$ as a single observable, but separate studies demonstrated that adding an angular observable improves the general performance of the analysis in terms of uncertainties

significantly. Despite having only little sensitivity to the decay width, the advantages of the angular observables are a small sensitivity to jet-related uncertainties, the addition of information from the hadronic decay branch to the fit and the reduction of leading systematic uncertainties in the combination with $m_{\ell b}$. Particularly $\Delta R_{\text{min}}(j_b, j_l)$ performs promisingly and does not suffer from modelling issues which is why this observable is used in the fit in addition to $m_{\ell b}$. The observable choice is justified and explained in more detail by testing various possible fit configurations in Ch. 9.

7.2 Template Reweighting

This section addresses the derivation of decay width templates required for the fit. Due to the absence of MC simulated $t\bar{t}$ samples with Γ_t values different from the SM expectation of $\Gamma_t = 1.33$ GeV, the signal Γ_t templates were created by a reweighting procedure. On the assumption that the distributions follow a Breit-Wigner shape, verified by additional cross-checks, they were reweighted from the nominal $t\bar{t}$ sample with $\Gamma_t = 1.33$ GeV.

For this purpose, the distributions of reconstructed events based on the nominal $t\bar{t}$ full simulation sample were weighted employing theoretical Breit-Wigner curves for 54 different top quark decay width values. The procedure is explained in the following. The decay width range from $0.1 < \Gamma_t < 5.0$ GeV is covered by 50 templates in steps of $\Delta\Gamma_t = 0.1$ GeV, four additional templates followed from a reweighting to $\Gamma_t = 0.01,\ 6,\ 7,\ 8$ GeV to also account for very small and very large decay width values. The Breit-Wigner function to rescale the distributions on an event-by-event basis is defined as:

$$\text{BW}(x) = \frac{2\sqrt{2} m_t \Gamma_t \sqrt{m_t^2(m_t^2+\Gamma_t^2)}}{\pi\sqrt{m_t^2+\sqrt{m_t^2(m_t^2+\Gamma_t^2)}}\cdot((x^2-m_t^2)^2+m_t^2\Gamma_t^2)}\,. \tag{7.1}$$

The top quark mass is set to $m_t = 172.5$ GeV as the mass of the nominal $t\bar{t}$ MC sample. The truth top quark masses per event are denoted by x. The mass distributions at truth parton level perfectly agree with the shape of a Breit-Wigner curve whereas the distributions are smeared at reconstruction level because of resolution effects. Both top quarks enter the reweighting procedure. For observables of the hadronic decay branch of the $t\bar{t}$ events, only the true MC top quark mass of the hadronic top quark is used to reweight the distributions and, similarly, for observables of the leptonic decay branch only the leptonic top quark mass is used for the reweighting. These truth masses are defined after ISR but before FSR, according to the applied generator definitions.
The weights obtained from the reweighting procedure as a function of m_t are given in Fig. 7.1. The absolute weights per decay width template depicted as histograms are shown in Fig. 7.2. Since the nominal template enters the fit as well, in total 55 templates are used in the fit to extract the best fitted value of Γ_t. The template distributions for the decay widths in the range from 0.7 to 3.0 GeV are shown in Fig. 7.3 and Fig. 7.4 for three example observables at reconstruction level as they are defined in Sec. 7.1.

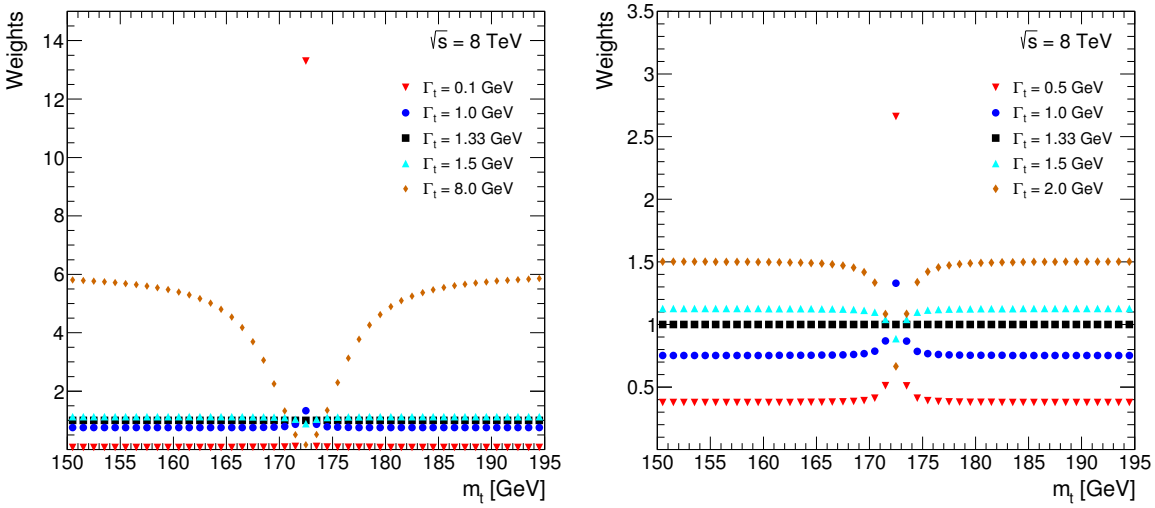

(a) **(b)**

Figure 7.1: MC weights used for the template reweighting as a function of the underlying top quark masses which are passed as arguments to the Breit-Wigner equation. Weights are binned in the plots to allow for a better visibility. (a) also contains the extreme decay width values in the available range, (b) illustrates weights for templates closer to the nominal value of $\Gamma_t = 1.33$ GeV.

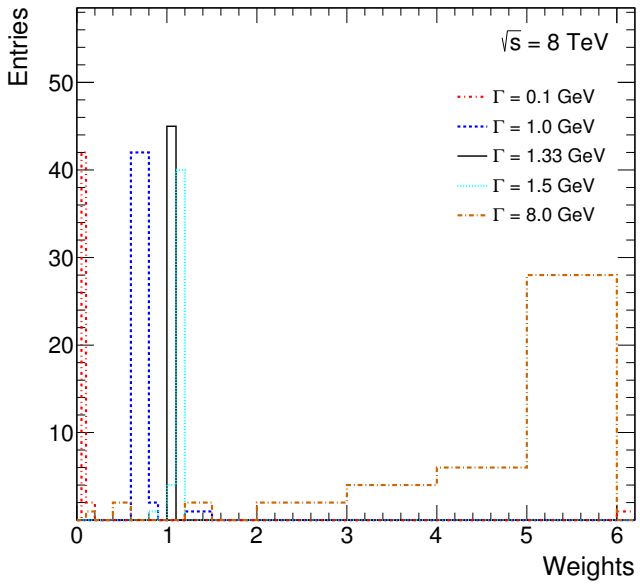

Figure 7.2: MC weights used for the template reweighting filled into histograms for some example top quark decay width values.

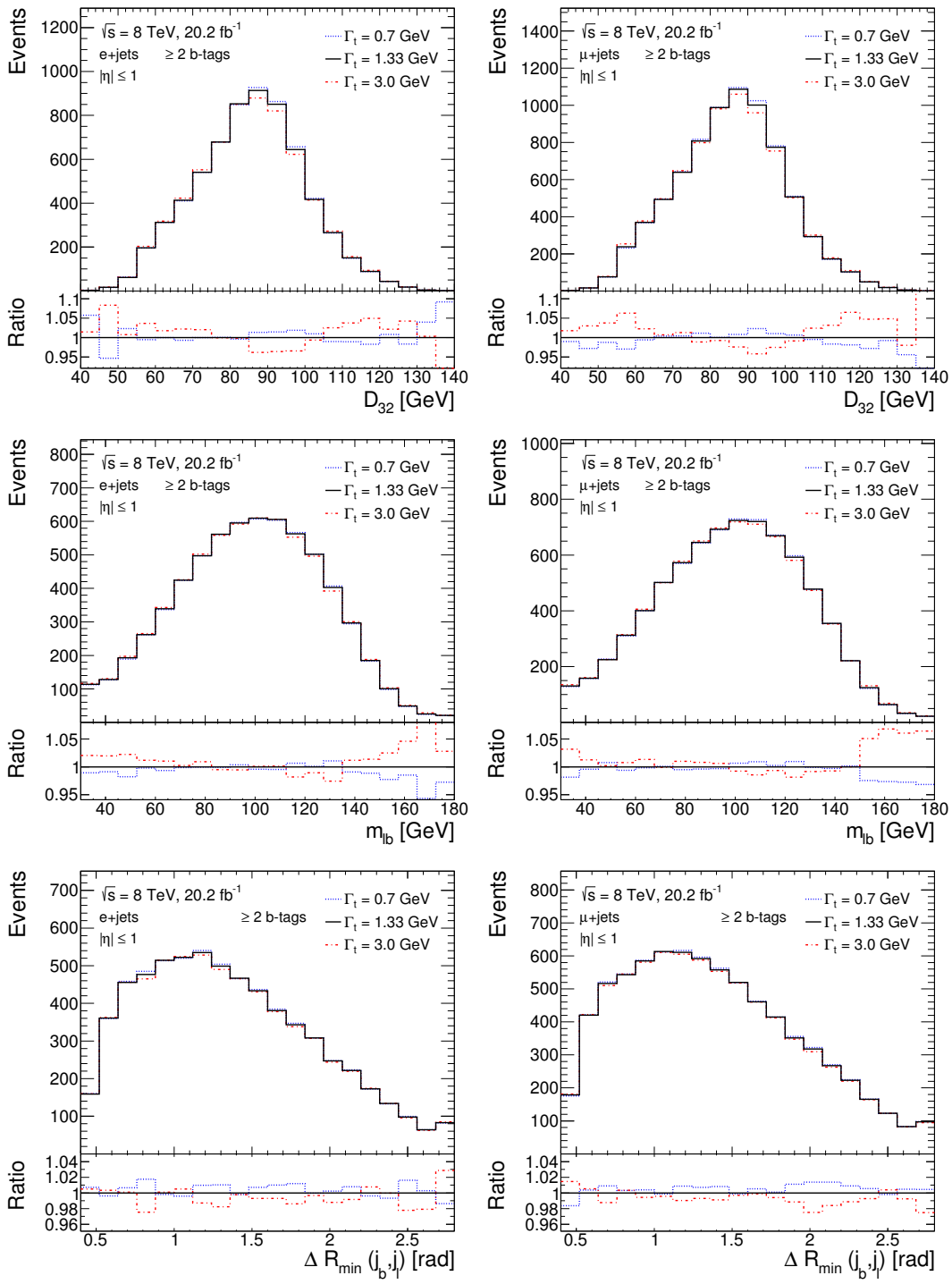

Figure 7.3: Reweighted templates at reconstruction level in the range $0.7 \leq \Gamma_t \leq 3.0$ GeV in the electron+jets (left) and muon+jets (right) channel using events with at least two b-tagged jets in the region $|\eta| \leq 1$. Compared are templates for the observables D_{32}, $m_{\ell b}$ and $\Delta R_{\text{min}}(j_b, j_l)$. The lower panels illustrate the ratio of the reweighted templates with respect to the nominal sample generated at $\Gamma_t = 1.33$ GeV.

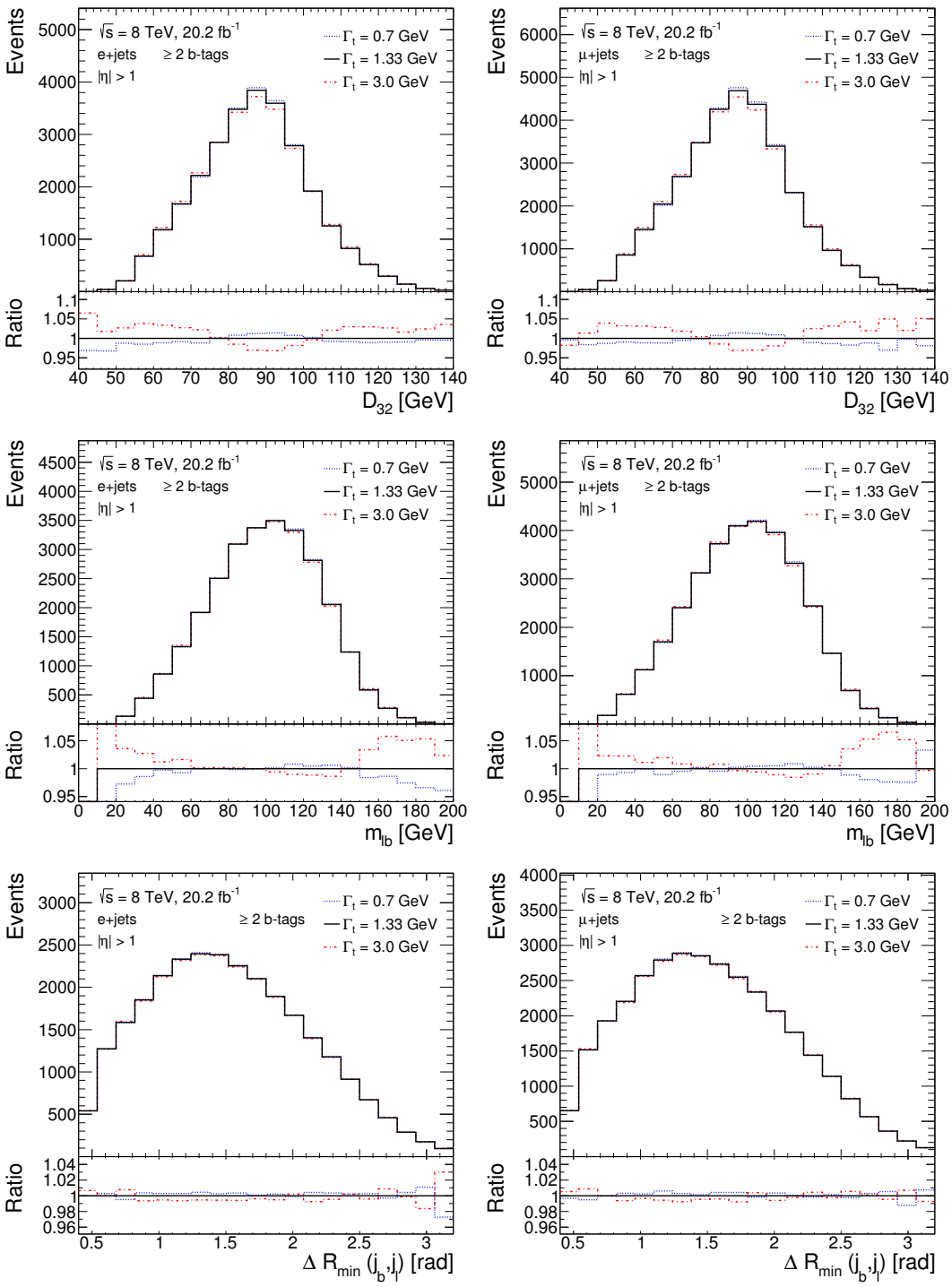

Figure 7.4: Reweighted templates at reconstruction level in the range $0.7 \leq \Gamma_t \leq 3.0$ GeV in the electron+jets (left) and muon+jets (right) channel using events with at least two b-tagged jets in the region $|\eta| > 1$. Compared are templates for the observables D_{32}, $m_{\ell b}$ and $\Delta R_{\text{min}}(j_b, j_l)$. The lower panels illustrate the ratio of the reweighted templates with respect to the nominal sample generated at $\Gamma_t = 1.33$ GeV.

The ratio plots underline the sensitivity of the observables to Γ_t. D_{32} offers the largest differences, but suffers from large systematic uncertainties. The sensitivity of $m_{\ell b}$ to Γ_t is well suited for the desired measurement while $\Delta R_{\text{min}}(j_b, j_l)$ adds only little sensitivity to the decay width which is compensated by the other advantages of using this observable.

The reweighting method was validated using MC $t\bar{t}$ samples generated with POWHEG interfaced with PYTHIA 6, similar to the nominal sample described in Sec. 5.2, but with $h_{\text{hdamp}} = \infty$, based on $\Gamma_t = 0.7$ GeV and $\Gamma_t = 3.0$ GeV. The top quark mass distributions of these alternative samples were compared to corresponding mass distributions obtained from the reweighting procedure at parton level. The good agreement between the reweighted distributions for the alternative Γ_t samples is reflected in Fig. 7.5 and no significant differences beyond the statistical uncertainties in the individual bins are visible. This is also confirmed by results of Kolmogorov-Smirnov (KS) and χ^2 tests which quantify the agreement between the two histograms.

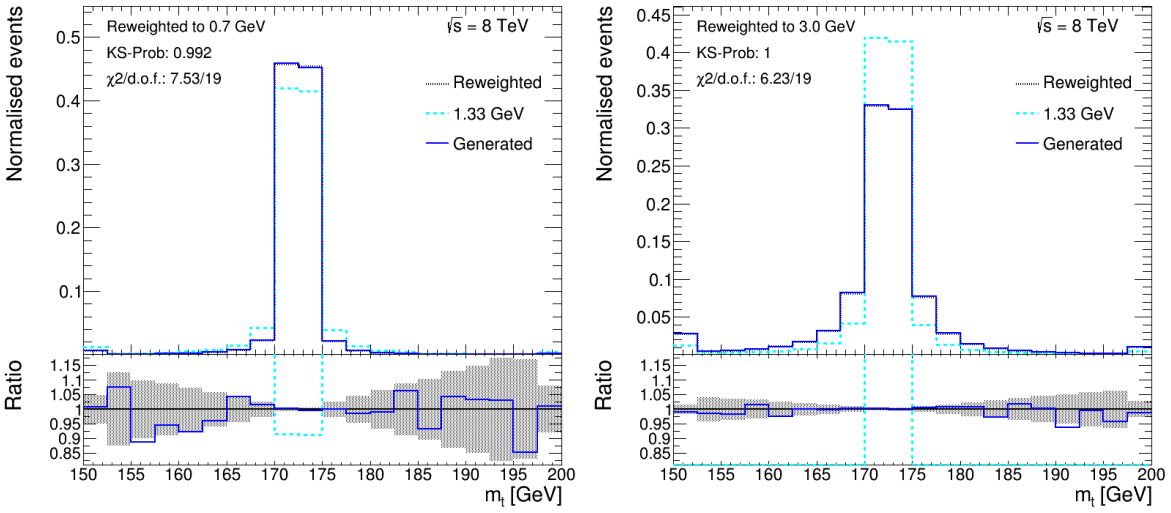

Figure 7.5: Results of a closure test to validate the reweighting method. The nominal sample based on $\Gamma_t = 1.33$ GeV (cyan, dashed) is given and the corresponding reweighted curve (black, dotted), which is compared to a sample with a decay width of (a) $\Gamma_t = 0.7$ GeV and (b) $\Gamma_t = 3.0$ GeV (blue in each case). The plots comprise all events with at least one b-tagged jet after summing up the events in the electron+jets and muon+jets channel. The lower panels contain the ratio with respect to the reweighted sample. The shown uncertainty bands contain statistical uncertainties which cover the differences between the two compared samples.

The Kolmogorov-Smirnov test is designed to check the consistency of one-dimensional distributions and, broadly speaking, quantifies the difference between two probability distributions or histograms, as it is the case here. A resulting KS value of around one verifies a very good agreement between two compared distributions. A bad agreement corresponds to a KS value close to zero. The KS test is particularly suited to compare the shapes of distributions which is why they were initially

defined to compare continuous distributions.

A χ^2 test marks another possibility of checking distances between two distributions or histograms. χ^2 methods rely on bin-by-bin comparisons as such a method requires a discretisation in general. As a consequence thereof, a χ^2 test is more sensitive to statistical fluctuations while a KS test is presumed to yield better results than a χ^2 test in case of histograms with a lack of statistics. The calculation in this thesis is based on the implementation within the ROOT framework [279], resting mainly on Ref. [285] for the KS test and Ref. [286–288] for the χ^2 test. A further discussion would go beyond the scope of this thesis.

This closure test was repeated at reconstruction level for both chosen observables. Reweighted distributions were compared to alternative decay width distributions obtained from the above mentioned MC $t\bar{t}$ samples for $m_{\ell b}$ and $\Delta R_{\text{min}}(j_b, j_l)$. Fig. 7.6 presents example plots confirming the agreement at reconstruction level within the statistical uncertainties.

Distributions for each analysis region are composed of 20 bins for both observables. The associated ranges are chosen depending on the two η regions in order to minimize the number of empty bins or bins which possess very low statistics. The effect of the applied binning was estimated by performing the analysis with less or more than 20 bins in each analysis region for the observables, without modifying the parameter ranges. Halving the number of bins reduces the sensitivity to different decay width templates and thus leads to a larger statistical uncertainty by about 15-20%. An increase in the number of bins above 20 per analysis region results in statistical fluctuations of the fit due to a growing number of bins with low statistics. In summary, a number of 20 constitutes a good compromise.
After reducing the number of bins per analysis region to ten, fluctuations in the bins with a low number of events diminish.

The impact of the chosen binning of the observable templates was evaluated quantitatively by merging the bins in the tail regions with only a very limited number of entries. For this setting, the last six bins were combined to three bins with an equal bin width and, depending on the pseudorapidity region, the first four or two bins were combined into two or only one bin, respectively. Consequently, the resulting distributions per analysis channel contain 15 or 16 bins instead of 20. The bins in the tails are thus twice as large as the bins in the central peak region of the distributions. The fluctuations in the tail regions of the templates decrease, especially for decay width templates outside of the region of extreme decay width values close to 0 GeV. The fit yields a result that differs by 0.12 GeV from the final quoted result, and the statistical uncertainty reduced to 0.02 GeV. Hence, the statistical uncertainty covers the effect due to the binning well.

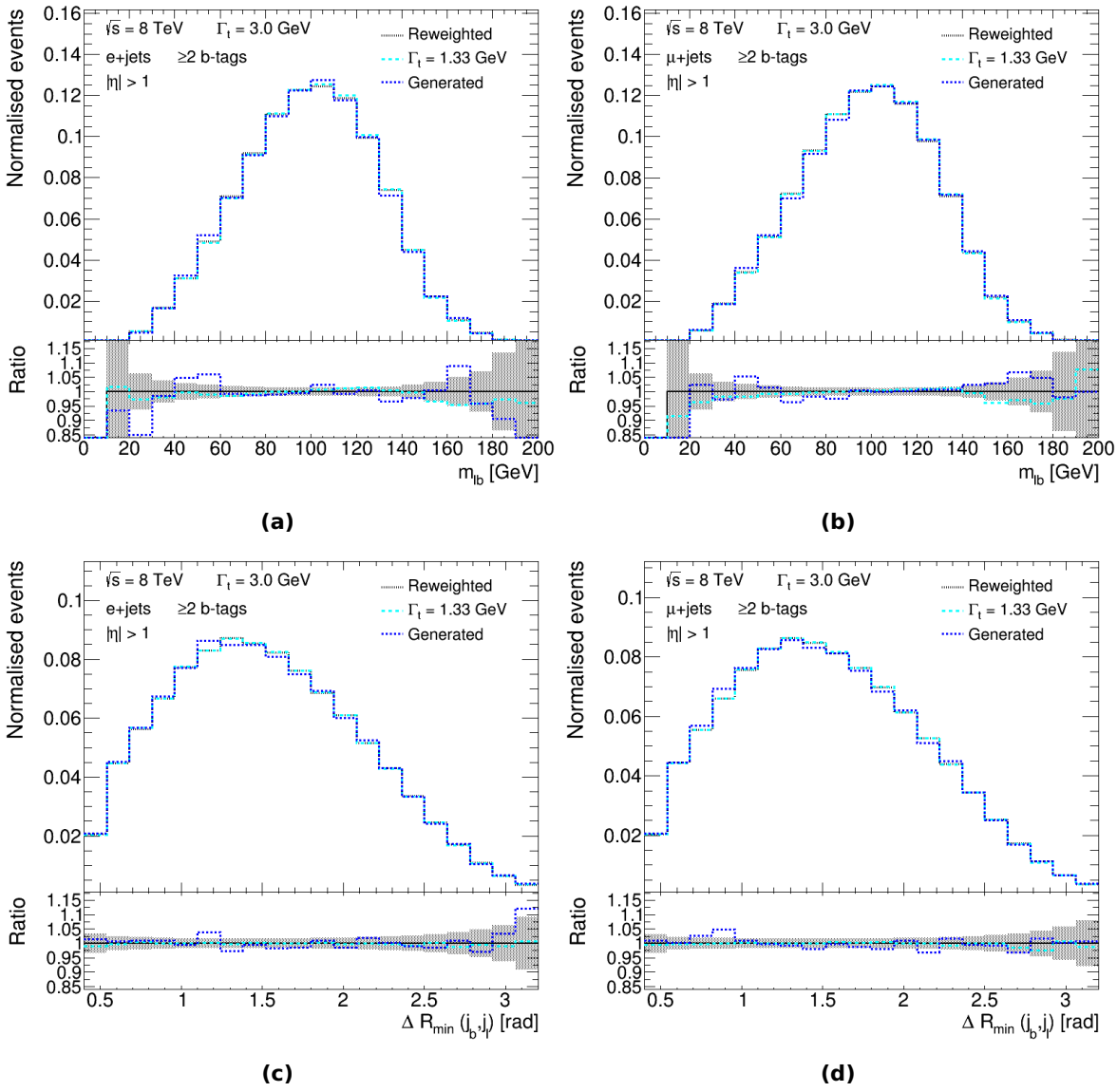

Figure 7.6: Results of a closure test to validate the reweighting method at reconstruction level. The generated sample at $\Gamma_t = 1.33$ GeV (cyan, long dashes) is shown and the corresponding reweighted curve (black, dotted), which is compared to a sample with a decay width of $\Gamma_t = 3.0$ GeV (blue, short dashes) for (a,b) $m_{\ell b}$ and (c,d) $\Delta R_{\text{min}}(j_b, j_l)$. The plots comprise all events with at least two b-tags in the region $|\eta| > 1$ in the (a,c) electron+jets and (b,d) muon+jets channel. The lower panels contain the ratio with respect to the black reweighted sample. The shown uncertainty bands comprise statistical uncertainties that cover the differences between the two compared samples except for a few outliers.

7.3 Definition of the Likelihood

The binned likelihood fit set up to determine Γ_t uses the signal templates defined in the last section for the $t\bar{t}$ contribution. Templates for the background processes, involving the production of single top quarks, are fixed. Those enter the fit with their normalisations and associated uncertainties included in Table 6.1. The influence of missing templates with alternative values of Γ_t for the single top contribution was evaluated separately and is delineated in this section. The implementation of the fit is realised with dedicated commands exploiting the RooFit [289] tool, a part of the ROOT framework [279].

The normalisation of the signal template is a free parameter of the fit while the backgrounds are allowed to vary within Gaussian constraints. The number of expected events as used in the fit equals the sum of all template normalisations and can thus be written as:

$$n_{\text{exp}} = n_{\text{signal}} + n_{\text{singletop}} + n_{W+b\bar{b}/c\bar{c}} + n_{W+c} + n_{W+\text{light}} + n_{Z+\text{jets}} + n_{\text{diboson}} + n_{\text{multijet}} \,.$$

An equivalent expression per bin i yields, after summarising the backgrounds B by the index j:

$$n_{\text{exp},i} = n_{\text{signal},i} + \sum_{j=1}^{\text{B}} n_{\text{bkg},ji} \,.$$

Accordingly, the number of data events per bin is denoted as $n_{\text{data},i}$. Based on these numbers, the likelihood for an observable $\mathcal{O}$ is defined as follows:

$$\mathcal{L}(\mathcal{O}|\Gamma_t) = \prod_{i=1}^{N_{\text{bins}}} \text{Poisson}(\mathcal{O}|n_{\text{data},i}, n_{\text{exp},i}, \Gamma_t) \cdot \prod_{j=1}^{\text{B}} \frac{1}{\sqrt{2\pi}\sigma_{\text{bkg},j}} \exp\left(\frac{-(n_{\text{bkg},j} - \hat{n}_{\text{bkg},j})^2}{2\sigma^2_{\text{bkg},j}}\right). \qquad (7.2)$$

The coefficient N_{bins} specifies the number of bins in the templates where a Poisson regression based on the bin entries is exploited in the fit. The expected number of events from a background source j, $n_{\text{bkg},j}$, is deduced from $n_{\text{bkg},ji}$ by summing over all bins i. The number of background events is allowed to vary in the fit but is constrained by the Gaussian terms of Eq. (7.2) where $\hat{n}_{\text{bkg},j}$ is the expected number of background events for the contribution j and $\sigma_{\text{bkg},j}$ is its uncertainty.

The uncertainties in the background contributions used as constraints or Gaussian priors in Eq. (7.2) are the expected uncertainties of the individual background normalisations. The corresponding numbers of the normalisation of the W+jets background components obtained from the data-driven calibration (as shown in Section 5.3) amount to 7% for $W + b\bar{b}$ and $W + c\bar{c}$, 25% for $W + c$, and 5% for W+light jets events [270]. The uncertainty on the multijet background is 30% and originating from the matrix method [272]. For both diboson and Z+jets events, a 4% theory uncertainty in the inclusive cross-section is applied combined with a 24% uncertainty per additional jet taken in quadrature, which serves to cover the extrapolation to higher jet multiplicities according to MC studies, and adds up to a 48% uncertainty for events having four jets. Finally, the single top

quark background contribution is assigned with an uncertainty of 17%. This number accounts for the variation of initial and final state radiation in the MC samples for t-channel processes and incorporates extra jets in single top quark events. The numbers are summarised in Table 7.2. All background fit parameters n_j are common across the utilised b-tag bins, lepton channels and $|\eta|$ regions, which means that one parameter comprises all eight regions, except for the multijet background. For the latter, each of the eight analysis regions is associated with an individual fit parameter, i.e. the number of multijet events is varied independently in all analysis regions.

Fit parameter	$\sigma_{\text{bkg},j}$
n_{signal}	-
$n_{\text{singletop}}$	0.17
$n_{W+b\bar{b}/c\bar{c}}$	0.07
n_{W+c}	0.25
$n_{W+\text{light}}$	0.05
$n_{Z+\text{jets}}$	0.48
n_{diboson}	0.48
n_{multijet}	0.30

Table 7.2: Signal and background parameters that enter the binned likelihood fit and the relative normalisation uncertainties $\sigma_{\text{bkg},j}$ as used in the Gaussian constraints imposed on the varying background contributions. Shape uncertainties are discussed in Sec. 8.3.

Contrary to the background sources, the number of signal events is left unconstrained in the fit. The uncertainty on the signal normalisation is thus not used in the fit but only considered for the uncertainties presented in Table 6.1. It amounts to 6.43% and is directly taken from the theory calculation [64–68, 71] of the $t\bar{t}$ cross-section at a centre-of-mass energy of 8 TeV presented in Sec. 5.2.
Within the decay width values used for the template reweighting, the difference of the observable distributions in the ratios with respect to the nominal template is up to around 5% or even less in the individual bins, demonstrated in the ratio panels of Fig. 7.3 and Fig. 7.4. As less than 5% of all events in these templates are presumed to originate from single top quarks, the entire effect of the single top events on the Γ_t templates is covered by the MC statistical uncertainty in the single top background. Studies which rest on a change of the single top mass in the event reconstruction with KLFitter also revealed that those mass variations do not bias the result. Because of the presence of one “fake” top quark in single top events these are not reweighted.

The fit is performed for 55 templates, the 54 templates obtained from the reweighting algorithm and the nominal one. The combined likelihood considering both observables is maximised for all available templates of Γ_t. It is defined as the product of two Poisson terms as written in Eq. (7.2), one for each observable, multiplied by the Gaussian constraints. The measured value of Γ_t is derived from the minimum of a quadratic fit to the negative logarithm of the likelihood values from the fits to all templates. The statistical uncertainty of the measurement is extracted from the width of this

likelihood curve at $-2\Delta\ln(\mathscr{L}) = 1$ around the minimum, which is half of the distance between the abscissa positions having a function value of one above the minimum. Thus, the likelihood values are shifted in a way that the minimum coincides with $-2\Delta\ln(\mathscr{L}) = 0$. Such a likelihood curve for the fit to data is shown in Fig. 10.3.

The templates used in the fit constitute concatenated distributions comprising all eight mutually exclusive analysis regions. These distributions are fitted for the two observables using all fit parameters, one for signal and one for each background contribution except for the multijet background, for which eight free parameters are used. The different parameters, the pre-fit numbers of events and the associated uncertainties are summarised in Table 7.3.

Parameter	Norm. unc.	Pre-fit
$t\bar{t}$	6.43%	153138
Single top	17%	6731
W+$b\bar{b}/c\bar{c}$	7%	8381
W+c	25%	3363
W+light	5%	1629
Z+jets	48%	2521
Diboson	48%	522
Multijet e, 1 b-tag, $\|\eta\| \leq 1$	30%	228
Multijet e, 1 b-tag, $\|\eta\| > 1$	30%	2493
Multijet e, $\geq$2 b-tags, $\|\eta\| \leq 1$	30%	41
Multijet e, $\geq$2 b-tags, $\|\eta\| > 1$	30%	538
Multijet μ, 1 b-tag, $\|\eta\| \leq 1$	30%	195
Multijet μ, 1 b-tag, $\|\eta\| > 1$	30%	1873
Multijet μ, $\geq$2 b-tags, $\|\eta\| \leq 1$	30%	46
Multijet μ, $\geq$2 b-tags, $\|\eta\| > 1$	30%	399

Table 7.3: Pre-fit yields in the eight channel combination with the related normalisation uncertainties. The numbers are not rounded in order to directly display the values used in the fit which leads to differences with the numbers listed in Table 6.1. The normalisation uncertainty for the $t\bar{t}$ signal is not used in the fit as the number of $t\bar{t}$ signal events is left unconstrained. However, this percentage number is reflected in the $t\bar{t}$ uncertainties listed in Table 6.1.

From the technical point of view, the different components of Eq. (7.2) are defined as particular RooFit objects, mainly `RooHistPdf` objects, where "Pdf" stands for probability density function. To account for the Gaussian constraints on the background, specific `RooGaussian` objects are available within the RooFit framework. Since the likelihood fit combines Poisson terms for both observables and fits their templates simultaneously, further `RooSimultaneous` objects, which incorporate the RooFit objects for the observables $m_{\ell b}$ and $\Delta R_{\text{min}}(j_b, j_l)$, enter the implementation of the likelihood fit as well.

7.4 Evaluation of Systematic and Expected Statistical Uncertainties

The validation of the fit method and the estimate of expected statistical as well as systematic uncertainties in the Γ_t measurement is realised by performing ensemble tests. Signal templates and background distributions obtained from the MC simulation and the data-driven methods are normalised to the expected number of events in data and used to generate so-called *pseudo-data* distributions. The general treatment, outlined in the following, applies to both nominal templates and templates to evaluate systematic effects. A detailed description of the extraction of systematic uncertainties based on those ensemble tests is provided in Ch. 8.1.
The predicted number of events per bin is assumed to be distributed corresponding to a Poisson distribution. Accordingly, a new pseudo-data set is derived from the observable distributions by fluctuating the bin entries of the distributions. The bin entries are regarded as Poisson-distributed with a mean equalling the original expectation of events for the corresponding bin. Thus, new pseudo-data distributions are created consistent with the statistical fluctuations of the underlying observable distributions. In order to take the Gaussian prior distributions into account, Gaussian fluctuations are imposed on the background distributions. These additional variations originate from a Gaussian distribution with a standard deviation following the $\pm 1\sigma$-range of the underlying parameters and a mean corresponding to the expected values of these parameters.
The original signal templates for the different values of Γ_t and the background templates are then fitted to the resulting pseudo-data distributions. For each pseudo-data distribution for which the template fit is carried out, referred to as one *pseudo-experiment* (PE), a value of the fitted top quark decay width is extracted using a quadratic fit to the likelihood points around the minimum.

Pseudo-experiments are realised in series of about 1,000 or 2,000 pieces (for systematic variations). The obtained fit parameter values and the fitted decay widths for each PE are added to histograms set up for all different fit parameters and the decay width itself. The average fitted value for each single parameter and Γ_t can be evaluated by using the mean value of these histograms that include all pseudo-data results. These numbers are used to validate the fit method in Sec. 7.5.
The number of performed pseudo-experiments per template option (nominal templates or systematic variation) is chosen, on the one hand, because of a considerably large CPU consumption of the simultaneous template fits while, on the other hand, the number is still sufficient to minimise potential statistical effects arising from a limited number of PEs.
The expected statistical uncertainties can be computed in two consistent ways. The statistical uncertainty conforms to the standard deviation σ or "width" of the distribution of fitted decay width values, calculated as $\sigma_{\Gamma_t} = 1/n \cdot \sum_i (\Gamma_{t,i} - \overline{\Gamma_t})^2$, with the number of PEs n, the fitted decay width $\Gamma_{t,i}$ for a pseudo-experiment i and the obtained mean value $\overline{\Gamma_t}$. As described in Sec. 7.3, the statistical uncertainty of Γ_t can also be determined from the width of this likelihood curve at $-2\Delta\ln(\mathscr{L}) = 1$ around the minimum. For reasons of consistency, the latter number is quoted in the following. Pursuant to the definition of the template fit, the statistical uncertainties combine the uncertainty from data statistics and the uncertainty in the different background normalisations.

7.5 Validation of the Fit Method

The fit method is validated using so-called *calibration curves* and *pull distributions*. A calibration curve aims at testing the linearity of the underlying fit. For this purpose, 1,000 pseudo-experiments for decay width values in the range $0.5 \leq \Gamma_t \leq 4.0$ GeV using steps of $\Delta\Gamma_t = 0.5$ GeV were conducted. For the resulting eight calibration points and an additional one for the nominal value, the templates were fitted to pseudo-data distributions obtained from the procedure described in Sec. 7.4. The average measured top quark decay width can be obtained from the mean of the histograms in which the fit results of all pseudo-experiments were filled for the chosen nine input decay width values. The mean values were then plotted as a function of the input values. A linear fit to these points is expected to have a slope of one and an offset of zero - measured as an intercept of the ordinate - as long as the estimator is unbiased. The resulting calibration curve for the final configuration chosen in the template fit is shown in Fig. 7.7.

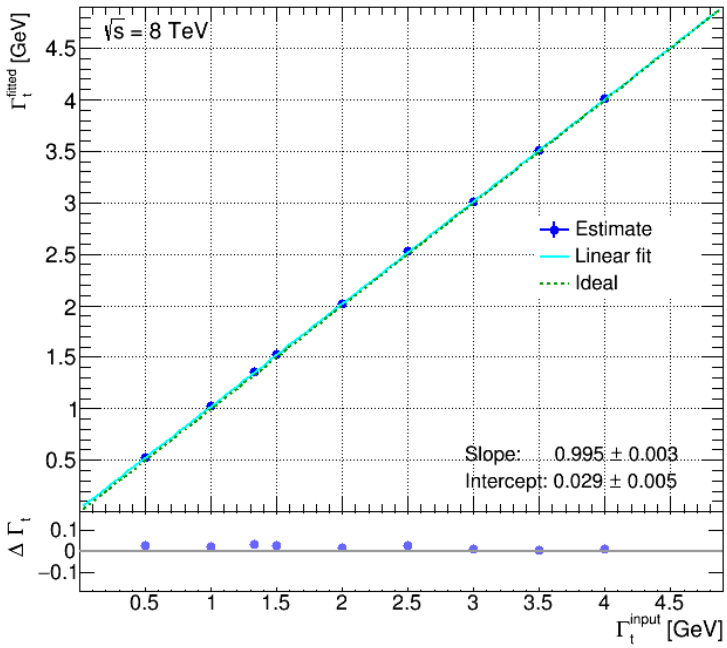

Figure 7.7: Calibration curve for the final fit configuration. The visible deviations from the theoretical expectation in the intercept are well understood and explained in the text. The lower panel shows the difference between the obtained fitted mean values, Γ_t^{fitted}, and the expected input parameter values, Γ_t^{input}.

The linear fit reveals small deviations from the theoretical expectation. The slope is still consistent with one within two standard deviations around the measured slope of 0.995 (the given uncertainty of 0.003 corresponds to 1σ). However, the intercept has an offset and is significantly different from zero. This offset is caused by the slightly shifted mean values of samples with small decay width values because only positive values of Γ_t can be fitted, leading to the edge of Γ_t values at 0 GeV. This effect is thus related to the decay width samples with $\Gamma_t > 0$ GeV and, hence, the resulting

curve follows the expectation for this particular analysis setup. This is further discussed in the next paragraphs.

Pull distributions are employed as well to assess the stability and the modelling of the fit. The pull is calculated as the difference between the fitted value Γ_t and the expected input one Γ_t^{input} divided by the estimated uncertainty on the fit result $\sigma(\Gamma_t)$:

$$\text{Pull} = \frac{\Gamma_t - \Gamma_t^{\text{input}}}{\sigma(\Gamma_t)}.$$

The nine calibration points used for the calibration curve together with three additional points around a decay width of 1.0 GeV were considered with the same number of PEs per input option as before. Based on the definition of the pull, the average fitted pull value is anticipated to be zero, the corresponding pull width to be one. The latter quantity refers again to the standard deviation of the obtained pull distribution. The results of the average fitted pulls and their uncertainties for the tested values of Γ_t are shown in Fig. 7.8a. The mean values of the expected statistical uncertainties $\sigma(\Gamma_t)$ as part of the pull calculation are contained in Fig. 7.8b for the original nine calibration points.

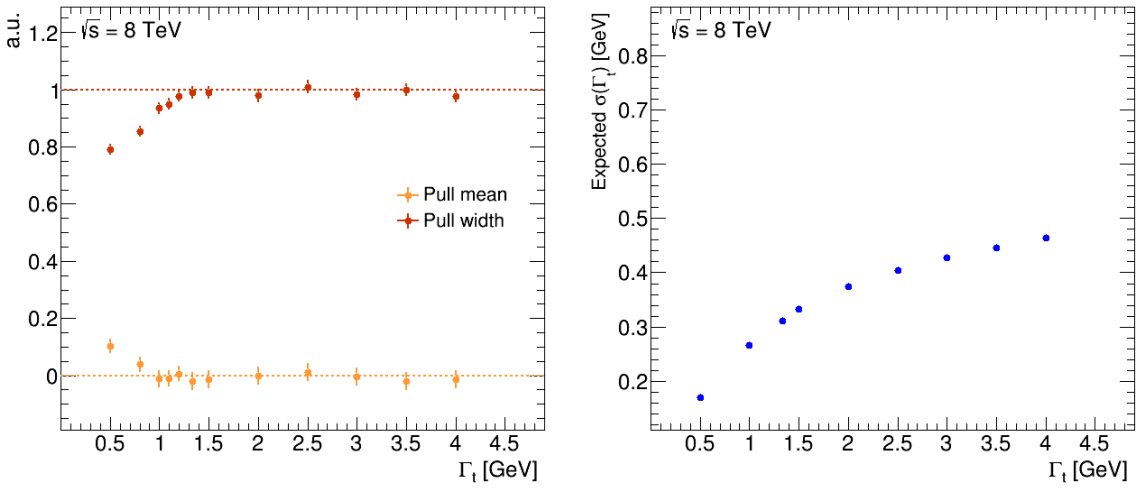

(a) **(b)**

Figure 7.8: Results of the (a) pull distributions and (b) mean expected statistical uncertainties for the final fit setting in the range $0.5 < \Gamma_t < 4.0$ GeV. Small deviations from the expectation can be observed for small decay width values which is why additional pull values are added in the region around $\Gamma_t = 1.0$ GeV. The visible deviations from the theoretical expectation are well understood and explained in the text.

As exhibited by the linear fit for the calibration curve, discrepancies arise from the theoretical expectation for small values of the decay width starting around $\Gamma_t \lesssim 1.1$ GeV. As a result, additional

calibration points were added in this range to better determine the region of possible deviations. Larger input decay widths return mean values included in the 1σ-region around the expectation. The pull mean value is still consistent with zero for $\Gamma_t = 1.0$ GeV while the width values start to deviate in the range $\Gamma_t \lesssim 1.1$ GeV. Since negative decay width values cannot be physically motivated, they are not allowed in the fit and lead to a sharp edge at 0 GeV which explains the deviations visible in the pull values. Besides, according to the definition of the pull, the decrease in the pull width starting slightly above $\Gamma_t \approx 1.0$ GeV during which the mean values are still close to zero hints at an overestimation of uncertainties caused by the physical decay width edge. In other words, the uncertainty assigned to fit results lying in this region emerge from a more conservative uncertainty estimation than required. Apart from that, the region of decay width values around 1.0 or 1.1 GeV is not reached by the fit to data in this measurement and not touched by the associated systematic uncertainties. Consequently, taking all these arguments into account, the entire fit can be regarded as stable and unbiased, and no correction for low values of Γ_t needs to be applied.

Selected output distributions of the fitted decay width values for 1,000 PEs are visualised in Fig. 7.9.

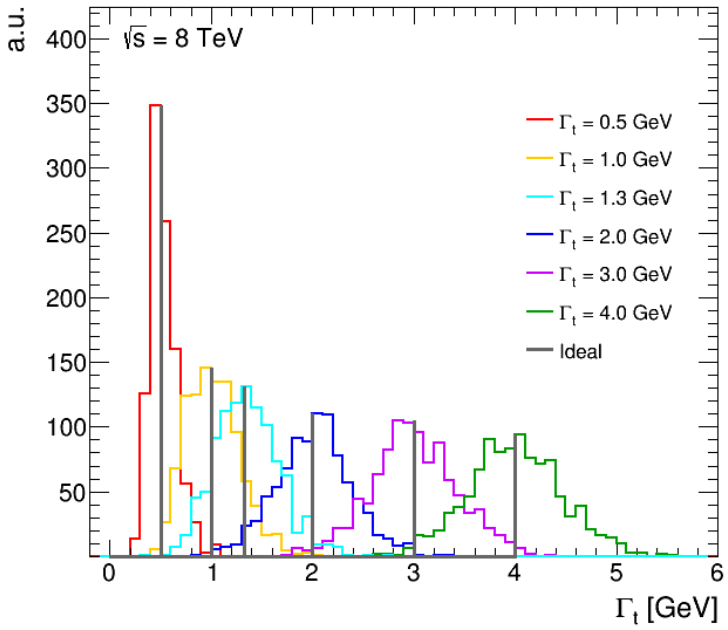

Figure 7.9: Decay width distributions obtained from 1,000 pseudo-experiments with the expected mean values marked in grey in the range $0.5 \leq \Gamma_t \leq 4.0$ GeV. Due to the sharp edge at 0 GeV, the Gaussian-shaped distributions are narrower with more distinct peak regions for smaller values of Γ_t.

The shapes of the histograms support the statements from the last paragraph. They change visibly for decay width values smaller than or around $\Gamma_t = 1$ GeV. The distributions in this Γ_t region have a narrower shape when approaching the limit of 0 GeV, which affects the calibration curves and pull distributions as outlined above. These narrower curves thus possess significantly smaller expected

statistical uncertainties, as illustrated in Fig. 7.8b. The decrease to smaller Γ_t values has a rising slope in $\sigma(\Gamma_t)$ when the region around $\Gamma_t = 1$ GeV and smaller is reached.
The distributions of Fig. 7.9 feature the desired approximate Gaussian shape in the region of larger decay width values. Shifted or otherwise biased distributions apart from the above explained edge effect which might indicate other issues with the fit method are not observed.

7.6 Correlations Between the Observables

Since two observables are fitted simultaneously to extract the decay width of the top quark, a potential correlation between the observables was examined although it is expected to be small. This is due to the fact that one observable originates from the leptonic and one from the hadronic decay branch of the $t\bar{t}$ pair with top quark decays independent of each other. Nevertheless, a correlation may arise due to event reconstruction and charge correlation effects. In case a non-negligible correlation exists, it is not possible to evaluate the uncertainties independently in the different analysis channels.

The correlation between the two observables can be accessed by two-dimensional plots with one observable drawn per axis. These correlation distributions are displayed in Fig. 7.10 for all eight analysis regions with the same binning as used to derive the fit templates. Correlation factors are evaluated individually for all these eight channels. A value of +1 represents a full correlation, -1 full anti-correlation whereas a factor of 0 is associated with completely uncorrelated observables. The correlation factors for the analysis regions are also listed separately in Table 7.4. The difference in correlation between the two pseudorapidity regions is relatively small for the lepton and b-tag bins. The correlation ranges between 0.1-1.2% for events with exactly one b-tag and 1.8-2.7% for events with at least two b-tagged jets. The two-dimensional distributions in Fig. 7.10 comprise all background components. Correlation plots with only signal or only background events for the nominal samples and two-dimensional plots with signal events obtained from alternative MC samples are given in App. D to prove that the correlation is also small for different decay width templates and the samples used to estimate systematic uncertainties in the signal model.

Despite the small correlation factors determined from the two-dimensional observable distributions, a further study was performed to check whether the measured correlation could affect the final fit result. A scenario with a correlation of around 10% between the two observables $m_{\ell b}$ and $\Delta R_{\mathrm{min}}(j_b, j_l)$ was constructed. Events out of the entire MC signal $t\bar{t}$ sample were randomly selected for both observables and filled into new histograms for all considered analysis channels and regions. The number of selected events matches the expectation in data. The resulting distributions for $m_{\ell b}$ and $\Delta R_{\mathrm{min}}(j_b, j_l)$ enter the fit directly without any additional Poisson fluctuations, as applied to the $t\bar{t}$ sample for the standard method validation tests according to Sec. 7.4.
Such a setup implies that the arbitrarily chosen events directly reflect the underlying correlation between the two observables. 1,000 PEs were conducted, equivalent to 1,000 sets of randomly selected events, and the mean fitted decay width value from these PEs was compared to the Standard

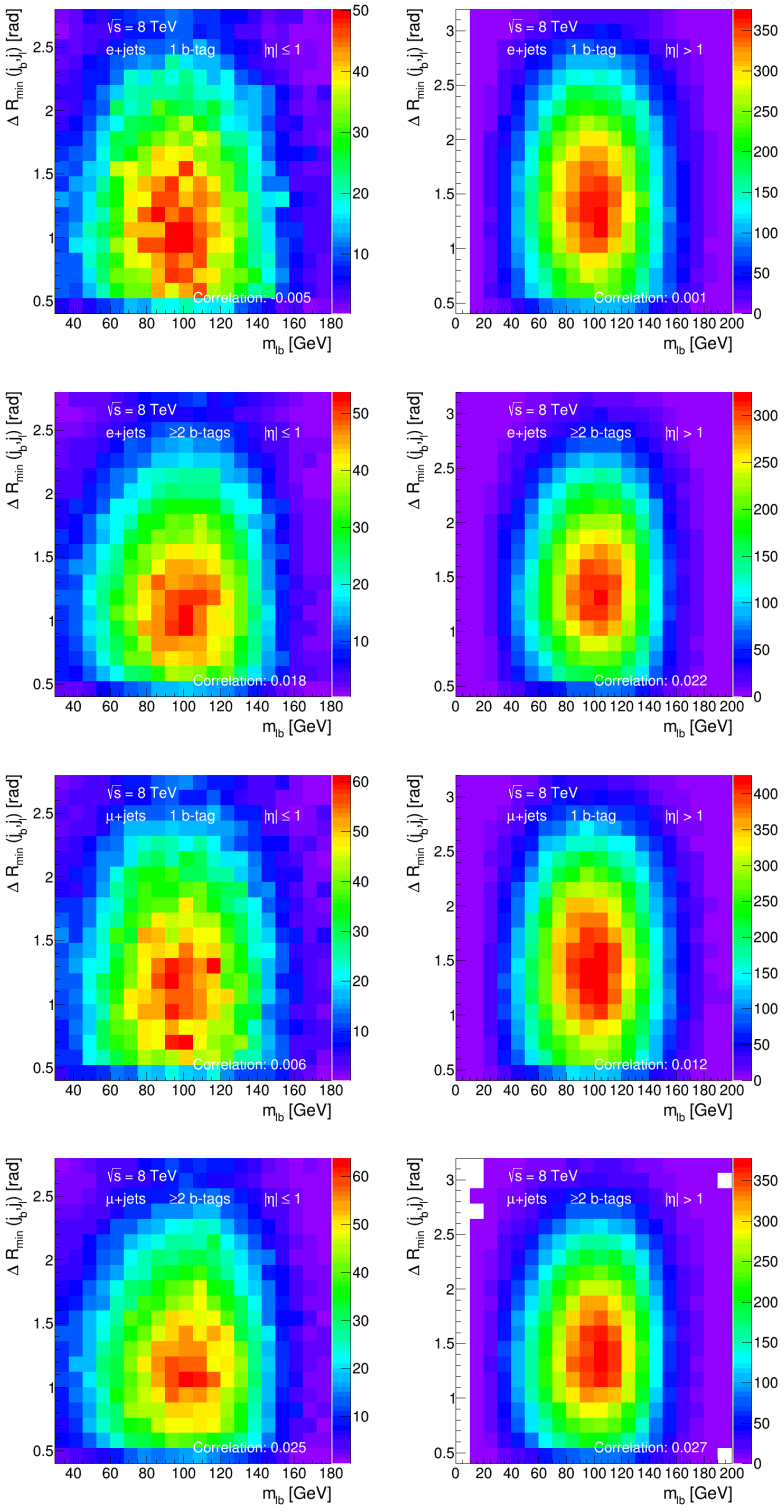

Figure 7.10: Correlation between the two chosen observables $m_{\ell b}$ and $\Delta R_{\text{min}}(j_b, j_l)$ in all eight analysis regions according to the labels. The signal $t\bar{t}$ events and all background contributions are included. The extracted correlation factors are also listed in Table 7.4 for reasons of visibility.

Analysis region	Correlation
e, 1 b-tag, $\|\eta\| \leq 1$	-0.005
e, 1 b-tag, $\|\eta\| > 1$	0.001
e, ≥ 2 b-tags, $\|\eta\| \leq 1$	0.018
e, ≥ 2 b-tags, $\|\eta\| > 1$	0.022
μ, 1 b-tags, $\|\eta\| \leq 1$	0.006
μ, 1 b-tags, $\|\eta\| > 1$	0.012
μ, ≥ 2 b-tags, $\|\eta\| \leq 1$	0.025
μ, ≥ 2 b-tags, $\|\eta\| > 1$	0.027

Table 7.4: Summary of the correlation factors corresponding to the correlation histograms in all eight analysis regions as shown in Fig. 7.10.

Model expectation of $\Gamma_t = 1.33$ GeV. The extracted mean value for this conservative scenario, assuming a correlation that amounts to 10%, is $\Gamma_t^{\text{corr}} = 1.320 \pm 0.009$ GeV, which is in good agreement with the related SM value. Hence, the measured correlation of up to 3% between the observables $m_{\ell b}$ and $\Delta R_{\text{min}}(j_b, j_l)$ for the nominal decay width distributions does not affect the result of the simultaneous template fit and the two observables are treated as independent for the remainder of this measurement.

7.7 Fit Configurations

The actual fit configuration with the two observables $m_{\ell b}$ and $\Delta R_{\text{min}}(j_b, j_l)$, the KLFitter setup with the requirement on the logarithm of the KLFitter likelihood and the split of the input distributions into two $|\eta|$ regions was validated by further studies. Those were driven by the idea to minimise the total (statistical + systematic) uncertainty on the direct measurement of the top quark decay width. Although this chapter and also previous sections provide qualitative arguments for the selected observables and analysis regions, the best possible fit configuration to extract the top quark decay width was also examined quantitatively. Since the decision on the final fit setup is based on dominant systematic uncertainties, presented in Ch. 8, this quantitative discussion follows in the subsequent Ch. 9. For reasons of completeness, an overview of different tested fit configurations, in addition to the analysis of all possibly suited observables defined in Sec. 7.1, is also outlined in this chapter covering the various aspects of the analysis strategy.

Pursuant to the description of the event reconstruction in Sec. 6.3, the KLFitter option which considers up to five jets in the reconstruction step per permutation yields higher reconstruction efficiencies compared to the option which considers only four jets but suffers from larger systematic uncertainties sensitive to the number of jets like uncertainties due to ISR and FSR. Different reconstruction options are compared in Ch. 9 and the setup leading to smaller total uncertainties on the decay width measurement was investigated in combination with additional cuts. A cut on the logarithm of the likelihood value from KLFitter was applied as well as a combination of this cut with a further requirement on the reconstructed hadronic W boson mass - based on the jet assignment from KLFitter.

Namely, a cut value of $\ln(L) > -50$ was found to remove a large portion of undesired combinatorial background due to wrongly reconstructed events while a range of $60 < m_W < 100$ GeV close to the peak of the mass distribution removes the tails with higher background contributions.

The dominant systematic uncertainties of the direct Γ_t measurement are expected to originate from the reconstruction of jets, especially from the jet energy scale (JES) and the jet energy resolution (JER). A split of the observable distributions into two regions based on the pseudorapidity η of the jets or the jet energies E aims at reducing such jet energy reconstruction uncertainties and was examined closer. A region that contains only events where jets have relatively smaller $|\eta|$ values or larger energies may suffer less from undesired detector reconstruction effects and pile-up contributions.
Regarding the split into $|\eta|$ regions, the observable distributions were separated into one region that comprises events where all the four reconstructed jets, i.e two b jets and two light jets originating from the W boson decay, have $|\eta| \leq \eta_C$, denoted as $|\eta| \leq \eta_C$ region. The remaining events where consequently at least one of the four reconstructed jets possesses a pseudorapidity of $|\eta| > \eta_C$ define the second region, referred to as $|\eta| > \eta_C$ region. The resulting total uncertainties were evaluated for values of $\eta_C = 0.8$, 1.0 and 1.2 according to the JES and JER calibration points as given in [230].
Events can also be separated into two different jet energy regions. Events where both b jets have energies of $\mathrm{E}_b > 100$ GeV and light jets values above $\mathrm{E}_{\mathrm{light}} > 50$ GeV constitute the first region, referred to as $E > E_C$ region in the following. The second region is composed of events where b jet energies of $\mathrm{E}_b \leq 100$ GeV or light jet energies $\mathrm{E}_{\mathrm{light}} \leq 50$ GeV can be observed, called the $E \leq E_C$ region accordingly.
A better resolution is assumed for events in the $|\eta| \leq \eta_C$ or $E > E_C$ region. However, still the full set of events was used in all tested configurations. This is due to the fact that by combining the two regions with different resolutions, where all events have the same underlying Γ_t, resolution effects are separated from the resolution-dependent decay width and thus the sensitivity to the latter quantity is increased as intended without removing events. In addition, the combination of analysis regions instead of a simple drop of events may induce a decrease of dominant systematic effects. As a result, the regions are separated in the fits but fitted simultaneously by using concatenated distributions that contain all analysis regions and thus maintain the full event numbers.

Besides, also modelling effects of the tested observables contribute to the selection of the best fit configuration. Before all these tests are presented in more detail, the sources of systematic uncertainty which need to be taken into account for the measurement of Γ_t are introduced.

8 Systematic Uncertainties

Systematic uncertainties affect the normalisation of the $t\bar{t}$ signal and the different background contributions as well as the shape of the observable distributions which are sensitive to the decay width of the top quark. The understanding of systematic effects and their reduction was a vital part of the decay width measurement.
This chapter presents the considered systematic uncertainties and quantifies their impact. After an introduction describing the general procedure applied to estimate systematic effects and listing the various sources of uncertainties, the different effects related to the detector, the background and the signal model are discussed. Since several of these uncertainty components have a severe impact on the final result of the Γ_t measurement, additional studies to understand or reduce those systematic uncertainties are shown as well. A further section is devoted to NLO and off-shell effects in the top quark decay which affect particularly the observable $m_{\ell b}$. The dependence of the decay width on the mass is delineated in another subsequent section and analysed in detail, followed by a definition of remaining smaller systematic uncertainties. The chapter concludes with a summary table listing the quantitative impact of all the systematic effects on the measurement of Γ_t.

8.1 Evaluation of Systematic Uncertainties

The systematic uncertainties considered are summarised in Table 8.1 including the number of components per systematic source, which describe individual systematic effects or shifts combined to an uncertainty listed in the table. This split into components allows for a more accurate treatment of the underlying systematic effects. Labels indicate whether the source of systematic uncertainty affects only the $t\bar{t}$ or background normalisation ("N"), only the shape of the observable distributions ("S") or whether the systematic effect contributes to both normalisation and shape uncertainties ("SN"). The individual sources of systematic uncertainty are regarded as uncorrelated. They are summed in quadrature to obtain the total systematic uncertainty comprising all components. Correlations of systematic uncertainties from the same source are retained for all defined eight analysis regions in the concatenated distributions used in the fit. Some components of the individual systematic variations have a merely small impact on the distributions, i.e. the systematic variation with respect to the nominal distribution is smaller than the statistical uncertainty per bin, and, thus, alternative calculations were performed which exclude some systematic components regarded as not being effective. The resulting uncertainties from such a reduced set of systematic variations are given in App. E, and the total systematic uncertainty decreases slightly as presumed. Such a procedure was applied in several ATLAS measurements in the recent past.

Systematic uncertainty	Type	Components
Detector model		
Electron	SN	5
Muon	SN	6
Missing transverse momentum	SN	2
Jet reconstruction	SN	1
Jet vertex fraction	SN	1
Jet energy scale	SN	26
Jet energy resolution	SN	11
b-tagging efficiency	SN	6
c-tagging efficiency	SN	4
Light jet tagging efficiency	SN	12
Background model		
W+light/$c/b\bar{b}/c\bar{c}$ calibration	N	3
W+jets shape	S	1
Single top normalisation	N	1
Single top modelling	SN	1
Multijet normalisation	N	1
Multijet modelling	SN	3
Z+jets normalisation	N	1
Diboson+jets normalisation	N	1
Signal model		
Radiation	SN	2
ME generator	SN	1
PS/fragmentation	SN	1
Colour reconnection	SN	1
Underlying event	SN	1
PDF	SN	3
Luminosity	N	1
Template statistical uncertainty	SN	1

Table 8.1: Systematic uncertainties considered for the measurement of Γ_t with most of them grouped into detector, background and signal model uncertainties. Depending on the source of systematic uncertainty, only the $t\bar{t}$ or background normalisation, only the shape of the observable distributions or both normalisation and shape of the observable distributions are affected, labelled as "N", "S" or "SN", respectively. The last column indicates the number of individual components per systematic effect.

Pseudo-experiments are conducted according to the general description in Sec. 7.4 to estimate the impact of the various systematic effects. For all components of systematic uncertainties, observable distributions which correspond to the respective up and down variations of the systematic sources are created. These systematic variations account for the possible modifications of the shape and acceptance of the systematic effect under study in accordance with the information given in Table 8.1. Pseudo-data distributions are obtained by applying Poisson fluctuations on all templates as well as Gaussian fluctuations on the background contributions. The latter fluctuations are applied to properly consider the Gaussian constraints imposed on the background sources. This procedure

is adopted bin-by-bin as done for the nominal fit validation studies. The resulting pseudo-data distributions are fitted to the corresponding decay width templates. Sets containing 2,000 of such pseudo-experiments are used for each systematic variation.
For systematic uncertainties having dedicated up and down variations, the differences between the means of the histograms of fitted Γ_t values using the nominal distributions and the up and down variations are quoted as the - usually asymmetric - systematic uncertainty from the respective source. Systematic uncertainties with a solely one-sided variation are determined in the same way based on the differences between the nominal distributions and the available variation. The uncertainty value is then symmetrised, i.e. taken as both the positive and negative uncertainty from this systematic source.

8.2 Uncertainties in Detector Modelling

Detector modelling uncertainties consist of the object reconstruction of the charged leptons, jets and missing transverse momentum. Also, uncertainties in the tagging of *b* jets, *c* jets and light jets are included.

8.2.1 Charged Lepton Uncertainties

Systematic uncertainties arising from charged leptons have the following origins: They are due to the trigger and reconstruction efficiencies, the lepton identification or originate from the lepton momentum and energy scales as well as their resolutions.
Since reconstruction, trigger and identification efficiencies differ between data and MC, scale factors are applied to correct for such discrepancies, as described in Sec. 4.2 for muons and Sec. 4.3 for electrons. These scale factors are varied within their uncertainties to derive the required variation samples for the estimation of the related uncertainties in the efficiencies according to the procedure in Sec. 8.1.
In a similar fashion, the uncertainties for corrections of the lepton momentum or energy scales and of the lepton momentum resolutions are employed to determine variation samples used for the evaluation of resulting systematic uncertainties caused by the lepton resolution and scales.
The given five categories lead to five components of uncertainties for electrons but six for muons because resolution uncertainties from the muon spectrometer and the ID tracking system are determined independently of each other.

8.2.2 Missing Transverse Momentum Uncertainty

The missing transverse momentum $E_{\mathrm{T}}^{\mathrm{miss}}$, as introduced in Sec. 4.6, is reconstructed from the vector sum of terms which are associated with other reconstructed objects. As a result, uncertainties coming from energy scales and resolutions for charged leptons and jets are propagated into the $E_{\mathrm{T}}^{\mathrm{miss}}$ uncertainty estimate. The systematic uncertainty of the $E_{\mathrm{T}}^{\mathrm{miss}}$ soft term is calculated using $Z \to \mu^+\mu^-$ events exploiting the transverse momentum balance of this soft term and the different

physics objects after calibration. Furthermore, the impact of the MC generator and the underlying event modelling in addition to pile-up effects which cause further energy deposits [239] is also considered.
The above sources of uncertainty are combined into two $E_{\mathrm{T}}^{\mathrm{miss}}$ uncertainty components, namely a resolution and a scale component, possessing up and down variations each.

8.2.3 Jet Reconstruction Efficiency

Systematic uncertainties related to jets are due to the reconstruction efficiency, the jet vertex requirement, the jet energy scale and the jet energy resolution. The latter three are described in more detail in the following subsections.
The jet reconstruction efficiency is not simulated correctly by MC generators but instead overestimated. This is taken into account by a dedicated systematic uncertainty. In order to match the efficiency reached in data, jets are randomly chosen and dropped from the selection. In total, 0.2% of jets having $p_{\mathrm{T}} < 30$ GeV are removed and the steps to obtain observable distributions are repeated based on the reduced amount of jets. The difference between this variation and the nominal setup is used to compute the systematic effect due to the jet reconstruction efficiency.

8.2.4 Jet Vertex Fraction

The requirement on the JVF variable implies that all jets used in the analysis must satisfy $|\mathrm{JVF}| > 0.5$. The efficiency per jet to pass this jet vertex fraction cut is estimated using $Z \to \ell^+\ell^-$+1 jet events in both simulation and data [233], which is sufficient to properly account for pile-up jets. The underlying procedure is a comparison between events enriched with jets from the hard-scattering process and events enriched with pile-up jets. The JVF uncertainty is thus determined by increasing or decreasing the cut value by 0.1 to values of 0.6 and 0.4, respectively. Observable distributions are derived for these two alternative values acting as up and down variations to specify this systematic effect.

8.2.5 Jet Energy Scale

The jet energy scale constitutes the largest detector modelling uncertainty in the measurement of Γ_t. The JES and its uncertainty are calculated using the results from LHC collision data, test-beam data and MC simulations [229]. The JES calibration, as delineated in Sec. 4.4, and its uncertainty estimate rely on dijet, multijet or vector boson+jets events, depending on the detector region and the p_{T} range of the jets. These measurements are then combined [230, 231]. The jet energy scale uncertainty itself is split into 26 individual components which are treated independently in the analysis. These components depend on underlying jet transverse momentum and pseudorapidity. The components comprise the in-situ calibration of jets (15 components), pile-up effects (five components), the η intercalibration (two components), the jet flavour composition and the jet flavour response, the b jet energy scale and, finally, one component for high-p_{T} jets.

An eigenvector decomposition is conducted to obtain these components of the JES uncertainty by retaining their correlations. Correlations between transverse momentum and pseudorapidity are accounted for by a correlation matrix defined as a function of p_{T} and $|\eta|$. An eigenvector reduction leads to 26 uncorrelated so-called nuisance parameters which are able to cover and describe all of these correlations and effects relevant for the JES uncertainty.
In order to estimate the underlying systematic uncertainty values, the energy of the jets in MC simulation is smeared by the uncertainty associated with each nuisance parameter variation. This method of propagating uncertainties is repeated for all nuisance parameters and leads to the 26 variations of the observable distribution with respect to the nominal configuration.

The so-called *flavour composition* is one of the dominant sources of the JES uncertainty. This component induces a variation of the jet energy scale with respect to the fraction of jets initiated by gluons as a function of the transverse momentum and the pseudorapidity of jets. In the default configuration of the object reconstruction software, the fraction of gluon-initiated jets is set to 50% and a conservative value of the uncertainty is applied: 0.5 ± 0.5, equivalent to a fraction of $50\% \pm 50\%$. The flavour composition components propagate this uncertainty in the fraction of gluon-initiated jets to the Γ_t measurement.
To reduce the corresponding JES uncertainty, the fraction of gluon-initiated jets and its associated uncertainty value were evaluated separately in this analysis. The implemented procedure relies on events passing the selection criteria given in Sec. 6.2 which are matched to parton level truth events. Reconstructed jets of the selected events are matched to parton level truth jets within a cone of $\Delta R = 0.3$. Based on the information in the truth record of the simulated events, reconstructed jets are classified according to the flavour of the parton that initiated the jet. The fraction of gluon-initiated jets was determined from this classification as a function of p_{T} and $|\eta|$ of the jets. Applying this procedure to the nominal $t\bar{t}$ MC sample yielded the nominal fraction of gluon jets. In the p_{T} and $|\eta|$ regions with most jets the fraction is around 30%-40% with an uncertainty around 5%-10%. In order to obtain the corresponding uncertainty value, this method was repeated for alternative $t\bar{t}$ MC samples, namely a sample with a different amount of ISR/FSR jets, a sample using a different parton shower generator (POWHEG+HERWIG) and a sample with an alternative matrix element generator (MC@NLO). These alternative samples are also used to derive systematic uncertainties in the signal model, as described in more detail in Sec. 8.4. Due to their large impact on top quark measurements this approach can be regarded as a justified estimate of uncertainties. The values for the fraction of gluon jets obtained from these alternative samples were compared to the results from the nominal setup. Differences were summed in quadrature and constitute the required uncertainty in the fraction of gluon jets. The two dimensional distributions of this fraction and its uncertainty representing the dependence on p_{T} and $|\eta|$ of the jets can be found in Fig. 8.1.
To quantify the effect of this modified treatment of the flavour composition component, the resulting JES uncertainty in the flavour composition component is presented in Table 8.2 for the default calculation (0.5 ± 0.5) and for the new setup resting on the actual fraction of gluon jets in the selected event sample. The corresponding JES uncertainty is considerably reduced by the new

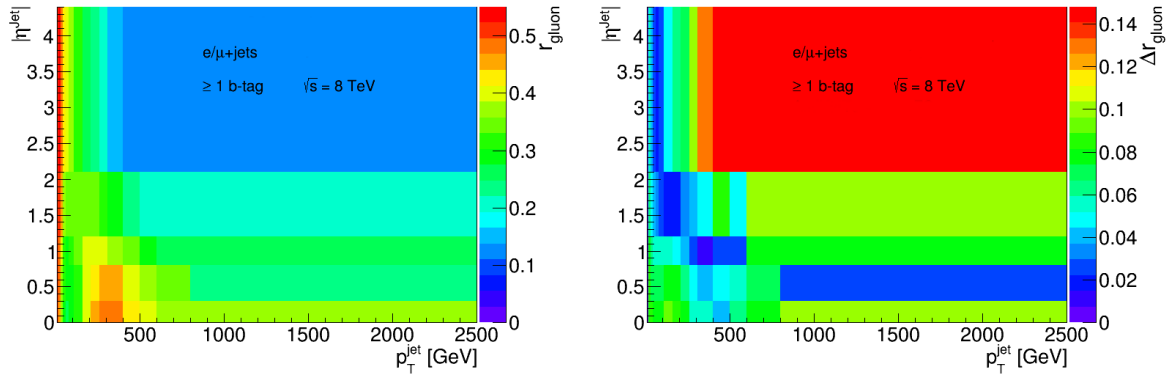

(a) **(b)**

Figure 8.1: Fraction of gluon-initiated jets: (a) nominal central value and (b) associated uncertainty as a function of the jet pseudorapidity and the jet transverse momentum used to evaluate the JES flavour composition uncertainty.

approach with respect to the default setup. Despite this reduction, the JES uncertainty is still the largest systematic uncertainty related to detector modelling underlining the relevance of such additional studies to minimise the impact of systematic effects.

Flavour composition	Uncertainty in Γ_t	
Default treatment	+0.34 GeV	−0.22 GeV
New implementation	+0.04 GeV	−0.02 GeV

Table 8.2: Impact of the modified treatment of the JES flavour composition component on the top quark decay width compared to the default configuration.

8.2.6 Jet Energy Resolution

Another important systematic uncertainty for the measurement of Γ_t is the jet energy resolution. It is estimated separately in simulated events and data employing two in-situ techniques [229]. These are complemented by additional in-situ measurements based on dijet, photon+jet and Z+jets decay processes. The JER uncertainty is mainly driven by pile-up effects for jets having low transverse momentum. This relevant contribution is measured pursuant to the nethod of Ref. [230]. Mathematically, the JER can be expressed by three terms:

$$\frac{\sigma(p_{\mathrm{T}})}{p_{\mathrm{T}}} = \frac{N}{p_{\mathrm{T}}} \oplus \frac{S}{\sqrt{p_{\mathrm{T}}}} \oplus C\,.$$

The first parameter N describes the effect of electronic noise and pile-up contributions, and S parametrises stochastic effects which are due to the sampling nature of the calorimeter system. The last parameter C is a constant term. Based on in-situ measurements involving additional noise

studies, values for N, S and C including parameter uncertainties are extracted. The expected p_{T} resolution for a particular jet is obtained as a function of its transverse momentum and its pseudorapidity.

An eigenvector decomposition is conducted to reduce the related sources of the JER uncertainty as applied for the JES uncertainty. The above described method of propagating uncertainties is conducted for all nuisance parameters and leads to eleven variations of the observable distribution with respect to the nominal configuration.

These up and down variations affecting shape and normalisation of the observables are summed in quadrature and the resulting systematic uncertainty value is symmetrised at the end.

8.2.7 Heavy and Light Flavour Tagging

Systematic uncertainties also arise from the tagging of b and mistagging of c jets, summarised as heavy flavour tagging, and from the mistagging of the light jets, u, d and s. Principles of b-tagging and the related efficiencies including scale factors are discussed in Sec. 4.5.

As mentioned in that chapter, data is used to calibrate efficiencies of the utilised b-tagging algorithms which depend on the jet flavour. The probability density function calibration method [236, 237] corrects the b-tagging efficiency to match the value observed in data. This technique rests on a combinatorial likelihood applied to dileptonic $t\bar{t}$ data events. On the contrary, the mistag rate for c jets is obtained using D^* mesons while the one for light jets relies on measured jets characterised by secondary vertices and impact parameters that conform to a negative lifetime [234, 237].

Scale factors which depend on the transverse momentum correct the efficiencies measured in simulated samples for both b and c jets. The scale factors derived for light jets depend on the jet pseudorapidity in addition. The b-tagging efficiency is affected by six independent sources of scale factor uncertainties, four need to be considered for the tagging of c jets [236]. Twelve uncertainty components which depend on different regions of p_{T} and η describe the uncertainty related to the mistagging of light jets [237].

All these components can be associated with an eigenvector belonging to the matrix which contains uncertainty information about the transverse momentum per bin and about correlations between bins. This complies again with the procedure described above for the JES and JER uncertainty. The systematic uncertainties are regarded as uncorrelated between the different types of jets, i.e. b, c and light jets.

8.3 Uncertainties in Background Modelling

8.3.1 Normalisation Uncertainties

The normalisation of all background contributions enter the list of systematic uncertainties in Table 8.1. The values of these uncertainties are cited in percentages in Sec. 7.3. Following the definition of the likelihood in Eq. (7.2) used in the template fit to extract Γ_t, these normalisation uncertainties are considered directly in the fit by the Gaussian constraints on the backgrounds. Thus, the quoted statistical uncertainty, as directly obtained from the resulting likelihood curve of the fit, does not only contain an uncertainty from data statistics but also comprises the uncertainties in the background normalisation. Further information on this topic are also given in Sec. 7.4. As a consequence, uncertainties affecting the shapes of the background distributions need to be treated separately. The three impacted contributions are described in the following.

8.3.2 W+Jets Shape Uncertainty

Since the W+jets background is split into three flavour components, $W+b\bar{b}/c\bar{c}$, $W+c$ and W+light, each of these components is allowed to vary independently in the fit within its uncertainty that equals the respective calibration factor uncertainty.
The uncertainty in the shape of the W+jets contributions is obtained from the variation of one W+jets component while the other two are fixed to the expected yields. The largest deviation from the nominal distributions constitutes the quoted uncertainty in the W+jets background shape.

8.3.3 Single Top Shape Uncertainty

Two simulated samples are utilised for the evaluation of the shape uncertainty of single top events. In order to correctly account for the overlap of single top events with $t\bar{t}$ decays, a specific *diagram removal technique* [290] is used by the nominal baseline MC generator of Wt events. This nominal sample is compared with an alternative sample which rests on the *inclusive diagram subtraction technique* [290]. The difference between pseudo-experiments for these two setups is symmetrised and taken as uncertainty in the single top background shape.

8.3.4 Multijet Shape Uncertainty

The modelling of the multijet background affecting the shape of the resulting background distributions is evaluated using three systematic variations. A first variation shifts the contribution of MC backgrounds that have to be subtracted to obtain fake rates from a control region, as defined in Sec. 5.3.4, by ±30%, according to the normalisation uncertainty from the matrix method. Those control regions are defined to calculate the efficiencies entering the matrix method. The two further systematic variations are also based on variations of the control regions. They arise from applying alternative techniques to compute either the fake or the real efficiency of the matrix method.

8.4 Uncertainties in Signal Modelling

Various sources of systematic uncertainty affect the shape and acceptance of the $t\bar{t}$ signal distributions. It is noteworthy that alternative MC samples used to estimate those systematic effects are simulated with different values of the h_{damp} parameter, which controls the high-p_{T} radiation damping in the POWHEG generator, than the nominal sample. They are mostly passed through a fast simulation of the detector [258, 259], as described in Sec. 5.1.2. The nominal $t\bar{t}$ sample relies on the full detector simulation though. These two options need to be set consistently between the nominal MC sample and the systematic variation samples for the evaluation of underlying signal model uncertainties.
The effect of different h_{damp} values and alternative detector simulation models, i.e. fast simulation vs. full simulation, was studied separately. The nominal MC $t\bar{t}$ sample using the full detector simulation with $h_{\text{damp}} = m_t$ was compared to a fast simulation $t\bar{t}$ sample with $h_{\text{damp}} = m_t$ and to a full simulation $t\bar{t}$ sample with $h_{\text{damp}} = \infty$. The differences in the mean values of Γ_t deduced from pseudo-experiments for these two tests can be seen in Table 8.3.

Compared simulation settings	Effect on Γ_t
Full vs. fast simulation	0.23 GeV
$h_{\text{damp}} = m_t$ vs. $h_{\text{damp}} = \infty$	0.16 GeV

Table 8.3: Impact of alternative simulation settings on the measured decay width Γ_t, namely the discrepancy between a full and a fast detector simulation as well as between different h_{damp} parameter values.

The effects on the decay width due to different simulation options and h_{damp} parameter choices are significant. Hence, the comparison between alternative MC signal samples and the nominal one to determine systematic uncertainties in the signal model needs to be done using a nominal sample that possesses the same h_{damp} and simulation configurations as the variation samples. The considered signal model uncertainties are delineated in the following.

8.4.1 Radiation Uncertainty

Model uncertainties caused by a different amount of initial and final state radiation are determined with two dedicated POWHEG+PYTHIA samples producing more or less radiation due to modified underlying parameter settings. These modifications include alternative values of the factorisation and normalisation scale, μ_F and μ_R, which are varied by factor 0.5 to 2. The h_{damp} parameter is correlated with these scales and, thus, depending on the scale values, h_{damp} is set to either m_t or $2m_t$. In addition, the coupling parameter α_s affecting initial and final state radiation is also changed in the alternative MC samples; it depends on μ_R but is also varied in different generator *tunes*. The alternative tunes are called `Perugia2012 radHi` (referred to as P2012 radHi) and `Perugia2012 radLo` (P2012 radLo in the following) [261], the nominal tune is P2011C.
Thus, the two alternative MC samples rely on the following parameters: One sample has the values

$\mu_R = \mu_F = 2$ and $h_{\text{damp}} = m_t$ combined with the P2012 radLo tune, the other sample has values of $\mu_R = \mu_F = 0.5$ and $h_{\text{damp}} = 2m_t$ combined with the P2012 radHi tune. These two configurations were chosen based on unfolded data distributions. The variations constitute an envelope of all individual modifications in the resulting distributions.
The nominal $t\bar{t}$ signal sample with $\mu_R = \mu_F = 1$ and $h_{\text{damp}} = m_t$ is compared to these two variation samples again according to the standard procedure using pseudo-experiments. The largest of the resulting differences in the mean values is symmetrised and considered as the systematic uncertainty from ISR and FSR.

Depending on the chosen observables for the Γ_t measurement, the radiation systematic uncertainty reached the order of several GeV, as revealed by comparison studies in Ch. 9. This uncertainty is thus the dominant source of systematic effects for some of the tested observables. Its impact was investigated in more detail.

Three different parameter settings differ from each other between the ISR/FSR samples. But the scales and parameters μ_F, μ_R and h_{damp} as well as the associated PYTHIA tune change only simultaneously. For the detailed study, MC samples containing truth parton and particle level information were generated in which these parameters and tunes are varied independently, also comprising a comparison of the nominal tune P2011C, as the actually used tune, with the tune P2012, which is combined with the "radHi" and "radLo" contributions in the variation samples. Such a setup allows to check whether a certain scale or tune variation is responsible for the large discrepancies and whether the effects observed for the observable distributions at the reconstruction level are also present at parton or particle level.
The two nominal tunes P2012 and P2011C are expected to yield similar observable distributions. Fig. 8.2a and Fig. 8.2b show a comparison between these two tunes for the hadronically decaying top quark mass and the corresponding hadronically decaying W boson mass. The observable m_t^{had} as reconstructed from three jets is very sensitive to the radiation uncertainty. The mass m_W^{had} as the related two-jet mass shows a very similar behaviour as m_t^{had}. Only slight differences between the tunes occur.
An independent variation of h_{damp} and the scales $\mu = \mu_F = \mu_R$ revealed that the differences with respect to the nominal setup are relatively small for changes in the scales and larger for the h_{damp} variation, shown in Figs. 8.2c-8.2f. A value of $h_{\text{damp}} = 0.5m_t$ is actually not used in the two official samples but applied here in order to allow for a comparison with two alternative h_{damp} values. The two nominal Perugia tunes lead to widely consistent results.
A comparison of the two PYTHIA radiation tunes, as the third source of difference between the alternative radiation MC samples unveils significantly larger differences in the obtained m_t^{had} distributions at truth level compared to discrepancies caused by varying the scale or h_{damp} parameters, visualised in Fig. 8.3a and Fig. 8.3b.
In particular, the shape differences between the alternative tunes with regard to the nominal tunes are very distinct. This applies to both nominal tunes P2011C and P2012. Such shape differences are not only present for masses of compound particles such as the three-jet mass m_t^{had} of the top

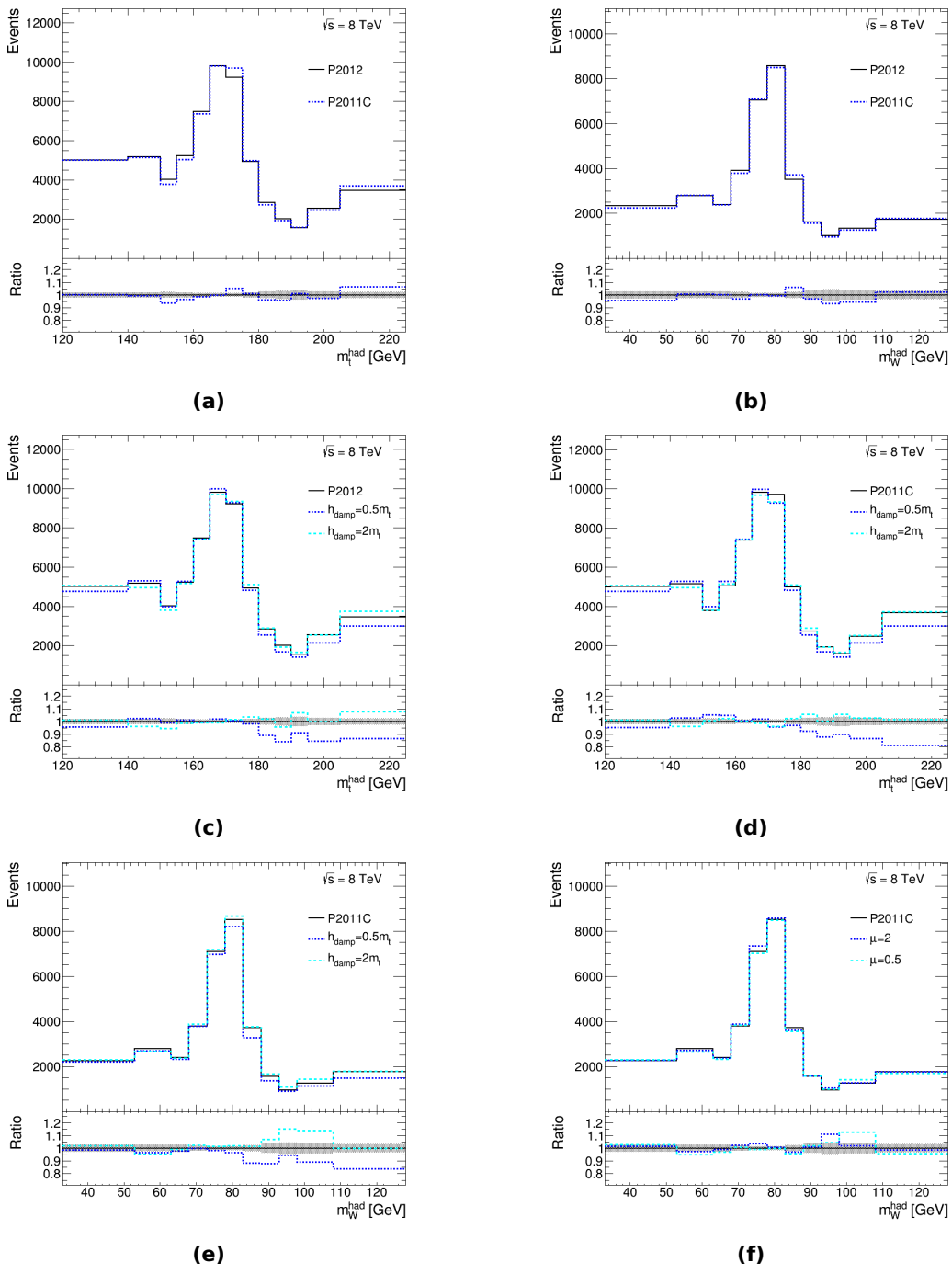

Figure 8.2: (a,b) Particle level mass distributions showing the difference between the two nominal Perugia tunes P2011C and P2012 for the masses m_t^{had} and m_W^{had}. The ratios at the bottom are given with respect to the P2012 tune. (c-f) Parton level mass distributions showing the difference between two different h_{damp} parameter values and between two different values of the renormalisation and factorisation scale μ for the masses m_t^{had} and m_W^{had} with details given in the legends. According to the labels, either the tune P2012 or P2011C is used as reference. The ratios in the lower panels are given with respect to these nominal tunes. The hatched bands in all plots represent the statistical uncertainty of these samples.

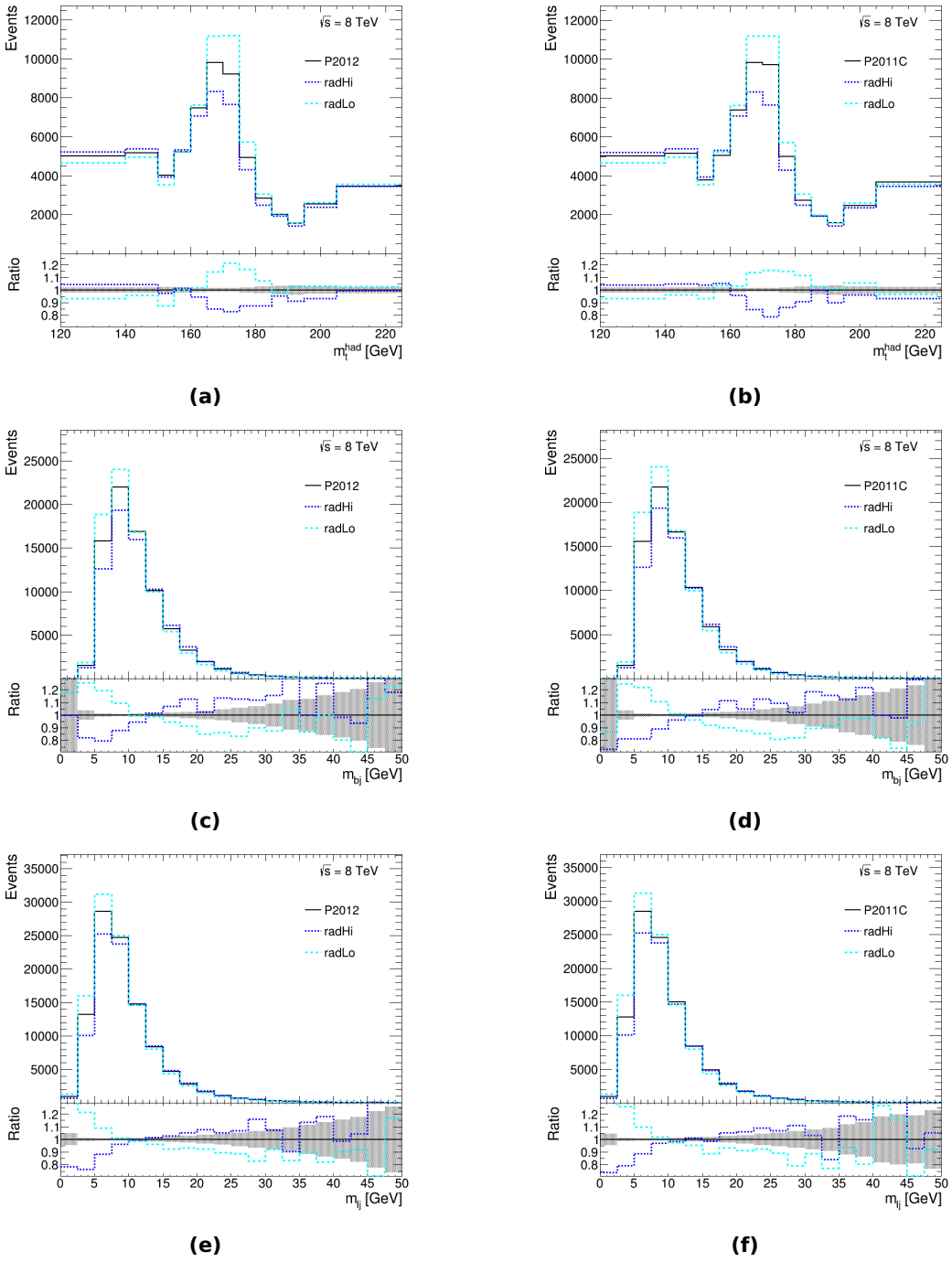

Figure 8.3: Particle level mass distributions showing the difference between the two different radiation tunes P2012 radHi and radLo for (a,b) the mass m_t^{had} as a compound particle as well as (c,d) the masses of the b jet of the hadronically decaying top quark and (e,f) the masses of the light jets of the hadronically decaying top quark. Either the tune P2012 (a,c,e) or the tune P2011C (b,d,f) is used as reference. The ratios in the lower panels are given with respect to these two nominal tunes, the hatched bands represent the statistical uncertainty of these samples.

quark or the two-jet mass m_W^{had} of the W boson but also for masses associated with the jets of the hadronically decaying top quark. The corresponding jet mass distributions at particle level are illustrated in Figs. 8.3c-8.3f for the two nominal tunes used as reference. This demonstrates once more that these shape effects are directly related to the underlying PYTHIA radiation tunes and neither caused by the creation of compound two- or three-jet particles, by the usage of other nominal tunes nor by a certain requirement applied in the event selection or event reconstruction.

This large effect on the mass shapes at truth level is propagated directly to reconstruction level and thus also occurs in the observable distributions used in the fit. The differences between the templates translate into the considerable shifts in the mean values from the pseudo-experiments. Consequently, a lot of effort was spent on designing an analysis configuration where radiation effects do not dominate the total systematic uncertainty to such an extent, shown in Ch. 9.

Since the effect is mainly driven by the radiation tunes, a more careful evaluation of the variation samples based on more precise and better measurements is required in the future, especially for analyses at a centre-of-mass energy of 13 TeV. Besides, the large impact of the radiation also points to the relatively simple description of the top quark decay which is utilised in the three MC $t\bar{t}$ samples available for the comparison in this section. This description relies on LO matrix elements and involves an approximate implementation of interference and finite width effects. The radiation uncertainty is assumed to be reduced further with an adequately tuned setup that considers NLO effects, which is covered more thoroughly in Sec. 8.5.

8.4.2 Matrix Element Generator Uncertainty

The uncertainty due to the choice of the matrix element $t\bar{t}$ generator is evaluated by comparing the nominal ME generator POWHEG with the generator MC@NLO, both interfaced with HERWIG. The resulting uncertainty based on the difference between these two setups is calculated according to the description in Sec. 8.1, as for the other signal model uncertainties. The resulting uncertainty value is symmetrised and represents, after all optimisation studies, the largest signal model uncertainty in this measurement with an effect of around 0.41 GeV due to differences in the region of large $m_{\ell b}$ values. This is also discussed in Sec. 8.8.

8.4.3 Parton Shower and Fragmentation Uncertainty

The choice of the parton shower (PS) generator denotes another source of uncertainty in the signal model. The nominal ME generator POWHEG interfaced with PYTHIA is compared to a generator configuration where POWHEG is interfaced with HERWIG. The h_{damp} parameter is set to infinity in both cases. The resulting uncertainty is the symmetrised value coming from a comparison of these two samples.

8.4.4 Colour Reconnection Uncertainty

A further uncertainty arises from the colour reconnection modelling, defined as formations of colour strings between partons that originate from independent hard scatterings, closely related to the underlying hadronisation models, outlined in Sec. 5.1. The nominal signal generator configuration is compared to a POWHEG+PYTHIA generator with a particular parameter tune for colour reconnection. The resulting difference in Γ_t between the two samples is symmetrised as for the previous uncertainties and quoted as colour reconnection uncertainty.

8.4.5 Underlying Event Uncertainty

The uncertainty due to the underlying event modelling is evaluated in a similar fashion. The nominal $t\bar{t}$ signal sample is compared to a POWHEG+PYTHIA generator that relies on a specific parameter tune for multiparton interactions. Again, the listed uncertainty is obtained from the symmetrised difference between the two generator setups.

8.4.6 PDF Set Uncertainty

The uncertainty due to the choice of the utilised parton distribution functions is estimated as follows. Three different PDF sets are compared for the determination of the uncertainty [263] caused by the choice of the PDF set: CT10 NLO [81], which is the nominal PDF set used in the analysis, MSTW 2008 68% CL NLO [69] as well as NNPDF 2.3 NLO [265]. A reweighting technique for the $t\bar{t}$ signal sample is used for each PDF set. The sets rely on different prescriptions to estimate the uncertainty due to different error sets: the CT10 set employs a symmetric Hessian matrix calculation, the MSTW set an asymmetric Hessian matrix while the NNPDF set utilises a standard deviation for the uncertainty calculation.
The PDF set CT10 consists of 52 individual nuisance parameters, the MSTW set consists of 42 and the NNPDF set possesses 100 nuisance parameters (half of them for up and half of them for down variations). For each of these parameter variations, pseudo-experiments are performed and systematic uncertainties of the decay width are derived following the standard procedure. The resulting systematic shifts $\Delta\Gamma_t$ for all nuisance parameters of the three PDF sets are shown in Fig. 8.4. The total systematic uncertainty due to the PDF set choice is evaluated as half the width of the largest nuisance parameter deviation with respect to the nominal set among all three PDF sets, indicated by the error bar on the right.

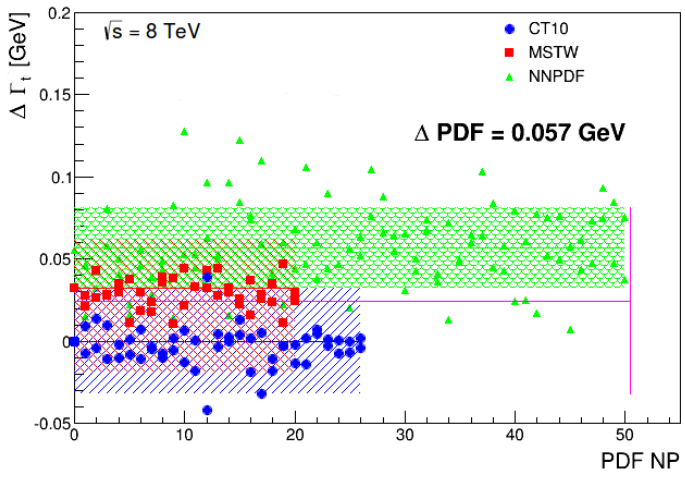

Figure 8.4: Systematic uncertainties on the decay width Γ_t for all individual nuisance parameters (NP) of the three compared PDF sets. The quoted PDF set uncertainty is indicated by the error bar on the right.

8.5 NLO and Off-Shell Effects in the Top Quark Decay

The nominal $t\bar{t}$ MC sample used to derive templates for the decay width measurement is based on a generator setup with NLO matrix elements for the production of $t\bar{t}$ pairs and LO matrix elements for the decay of top quarks, containing an approximate implementation of finite width and interference effects. A recently published theoretical study [291] using the dilepton $e\mu$ decay channel of $t\bar{t}$ pairs indicated that off-shell effects which comprise not only the $t\bar{t}$ contribution but also Wt single top events (plus a negligible contribution of diboson events with $WbWb$ in the final state), in addition to their interference, may have a large impact on mass observables like $m_{\ell b}$. Observables which are only based on angles like $\Delta R_{\text{min}}(j_b, j_l)$ are not affected to a large extent and, thus, the discussion concentrates on $m_{\ell b}$. This can influence precision measurements in the top quark sector as the Γ_t measurement significantly. Since no MC implementation of NLO decay and off-shell effects is available in the lepton+jets decay channel used in this analysis, various studies were conducted in order to investigate the consequences of disregarding NLO and off-shell effects in the $t\bar{t}$ decay, visible in the $m_{\ell b}$ distributions. The results of these tests are discussed in the following.

Several MC generator setups were implemented by theorists in the recent past which consider these additional NLO and off-shell effects in the $t\bar{t}$ decay. However, these generators are still in development and thus neither included in the ATLAS simulation framework nor tuned to data yet because of free parameters in the generator setup. The studies presented in this section are mainly based on those initial test samples.
A new generator implementation that offers NLO precision in $t\bar{t}$ decay but does not allow for a consistent treatment of top quark resonance effects is denoted as `ttb_NLO_dec` [292]. As

the nominal $t\bar{t}$ generators used in this analysis, the new setup is based on the POWHEG-BOX framework. Another, more sophisticated NLO+PS generator was implemented in the POWHEG-BOX-RES framework [293], referred to as `bb4l` [291]. It contains NLO matrix elements for the process $pp \to \ell^+\nu_\ell\ell^-\bar{\nu}_\ell b\bar{b}$, uses the resonance-aware method in POWHEG and is interfaced with PYTHIA8 [277, 294]. The resonance-aware method or resonance-aware matching refers to a general NLO+PS matching technique where resonances are treated consistently, described in Ref. [293]. The physics features of this new generator setup comprise full NLO accuracy in $t\bar{t}$ production and decay, the mentioned NLO+PS treatment of top quark resonances, which involves quantum corrections to propagators of the top quark, and off-shell top quark decay chains. The setup takes exact spin correlation at NLO and interference between NLO radiation from top quark production and decay as well as an improved modelling of b quark kinematics into account. Furthermore, a unified treatment of $t\bar{t}$ and Wt single top processes with NLO interferences is implemented. Such an approach is completely new because previous generations of MC generators rely on simulating each process separately.
The performed studies are based on these two recently developed generators, particularly on the `bb4l` implementation. Although this generator setup is not included in the ATLAS framework, the performed tests are sufficient to make first estimates of the impact of missing NLO and off-shell effects on the current nominal $t\bar{t}$ generators.

Differences between the nominal $t\bar{t}$ generator with LO precision in decay with leading leg corrections (denoted as `tt`) and the `bb4l` setup as provided in [291] are shown in Fig. 8.5a for the parton level. Since an absolute difference between the two distributions originates from the missing Wt events for the standard `tt` setup, the two histograms are normalised to unity to visualise shape differences between the generator approaches.
Very recently the authors of [291] simulated the missing Wt contribution to allow for a more consistent comparison between the LO and NLO generator setups, shown in Fig. 8.5b.
The discrepancies between the two samples in the high mass region of $m_{\ell b}$ are very distinct in case single top Wt events are not included in the `tt` setup. This effect seems to be compensated by the Wt events to a large extent. Currently, efforts by the authors of Ref. [291] aim at a better understanding of these different shape effects, as several mass observables other than $m_{\ell b}$ do not show such shape modifications after adding Wt events. Since severe differences in the region of large $m_{\ell b}$ values are observed in the two plots of Fig 8.5, many studies were realised also in the course of this analysis to understand the impact of the region of large $m_{\ell b}$ values on the measurement of Γ_t.

The first study focussed on the question whether alternative $t\bar{t}$ signal MC samples used to estimate signal model uncertainties reveal similar shape effects as observed in Fig 8.5. With respect to the nominal POWHEG+PYTHIA6 $t\bar{t}$ event generator, most alternative setups introduce less significant shape differences. Only the differences between a POWHEG+PYTHIA6 sample with $h_{\text{damp}} = \infty$ and a POWHEG+HERWIG sample, on which the evaluation of the parton shower and hadronisation model uncertainty is based (Sec. 8.4), are relatively close to the shape effects visible in Fig. 8.5.

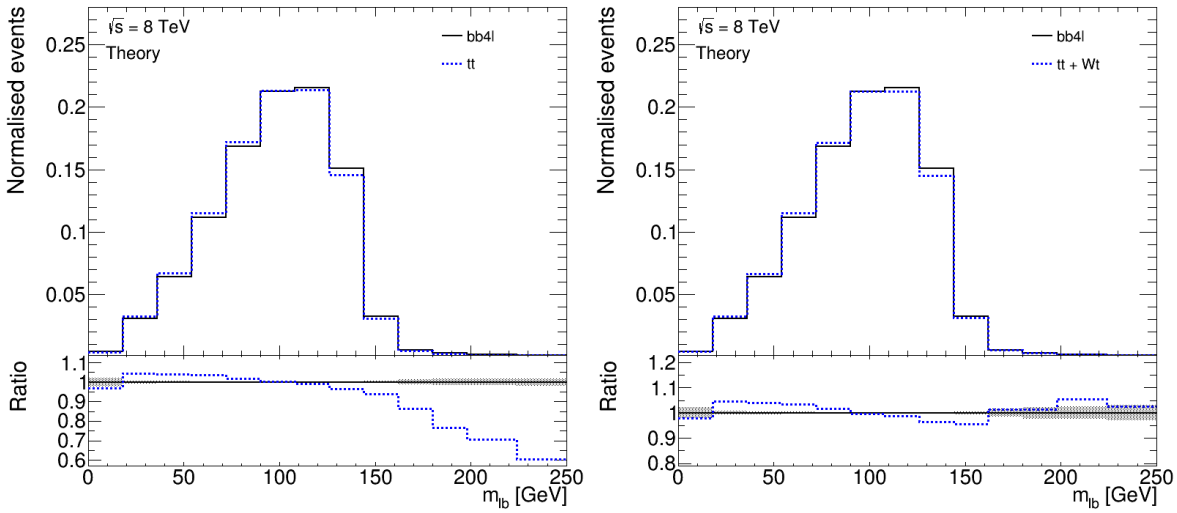

Figure 8.5: Distributions of $m_{\ell b}$ after normalisation to unity for two MC generator setups offering LO precision in $t\bar{t}$ decay (`tt`) or NLO precision (`bb4l`). The `tt` sample is shown (a) without single top Wt events or (b) with the Wt contribution.

Such a comparison is illustrated in Fig. 8.6, underlining that the trend of the shape difference in the high mass region is similar between `bb4l` vs. `tt` and POWHEG+PYTHIA6 vs. POWHEG+HERWIG. However, it cannot be concluded that the differences between the LO and the NLO `bb4l` generator are covered by the parton shower and hadronisation model uncertainty because the discrepancies between the two samples seen at parton level do not translate into large differences between POWHEG+PYTHIA6 and POWHEG+HERWIG at reconstruction level. The relatively small effect at reconstruction level translates into a parton shower and fragmentation model uncertainty of less than 0.1 GeV. As mentioned above, such a reconstruction level analysis is not yet possible for the new generator implementations. Thus, other methods are necessary to estimate the missing NLO and off-shell effects although it is still noteworthy that a POWHEG+HERWIG generator is able to partly describe expected shape variations due to these effects.

Since the shape effects in the region of large $m_{\ell b}$ values are not very well understood yet, the effect of applying cuts on the observable $m_{\ell b}$ in order to remove the right tail was investigated. According to Fig. 8.5a, deviations between `bb4l` and `tt` samples increase more and more for values above $m_{\ell b} = 150$ GeV. In the same region, adding the Wt events has a large impact. Hence, a cut value of 150 GeV was chosen and most systematic uncertainties as defined for the baseline analysis were evaluated using the full $\Delta R_{\text{min}}(j_b, j_l)$ range but only using events with $m_{\ell b} < 150$ GeV. The evaluation revealed that the total systematic uncertainty increases by around 29% after removing the large mass tail. This increase is equivalent to adding a further single systematic uncertainty of around 0.6 GeV, caused by this requirement on $m_{\ell b}$. After having obtained the final result for the fit to data, the influence of removing the large $m_{\ell b}$ tail on data could be estimated. The difference

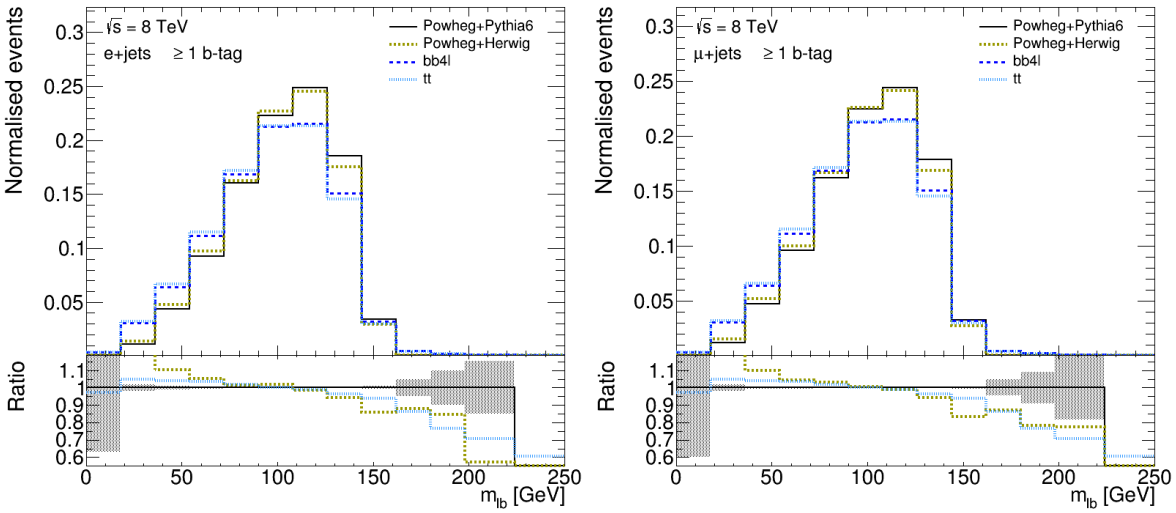

(a) **(b)**

Figure 8.6: Distributions for the observable $m_{\ell b}$ at parton level in the (a) electron+jets and (b) muon+jets channel for events with at least one b-tagged jet. Illustrated are the differences between a Powheg+Pythia6 and a Powheg+Herwig sample which are utilised to derive the parton shower and hadronisation model uncertainty as well as the differences between the two generator setups offering LO precision in decay (`tt`) or NLO precision (`bb4l`). To visualise shape effects and to allow for a better comparison, the distributions are normalised to unity. The lower panels contain the ratio between the Powheg+Pythia6 and a Powheg+Herwig histograms (dark yellow, dotted line) and between the LO and NLO generator approaches (blue, dashed line). The uncertainty bands comprise only statistical uncertainties.

in the final result amounts to 0.45 GeV, stable for cut values of $m_{\ell b}$ between 140 and 160 GeV. This value is slightly smaller than the expected systematic effect of 0.6 GeV determined from pseudo-experiments but is still comparable. Assuming that NLO and off-shell effects are mainly present in the region of large $m_{\ell b}$ values, these studies represent a first rough approximation of those effects missing in the nominal $t\bar{t}$ MC samples.

Due to the fact that these cuts on $m_{\ell b}$ have to be applied to reconstruction level distributions, despite being motivated by the parton level distributions in Fig. 8.5, the correlations between the parton and reconstruction level histograms need to be investigated. Correlation plots for the two considered pseudorapidity regions and b-tag bins are given in Fig. 8.7, as an example for the muon+jets channel.
The two-dimensional distributions reveal, similar to the corresponding electron+jets channel plots, that the reconstruction level masses are slightly shifted to larger values. A cut on $m_{\ell b}$ applied on reconstruction level removes more (and other) events than such a cut applied on parton level. Hence, cutting away events at reconstruction or parton level may lead to slightly different resulting systematic shifts, again emphasising the approximate character of the studies discussed above.

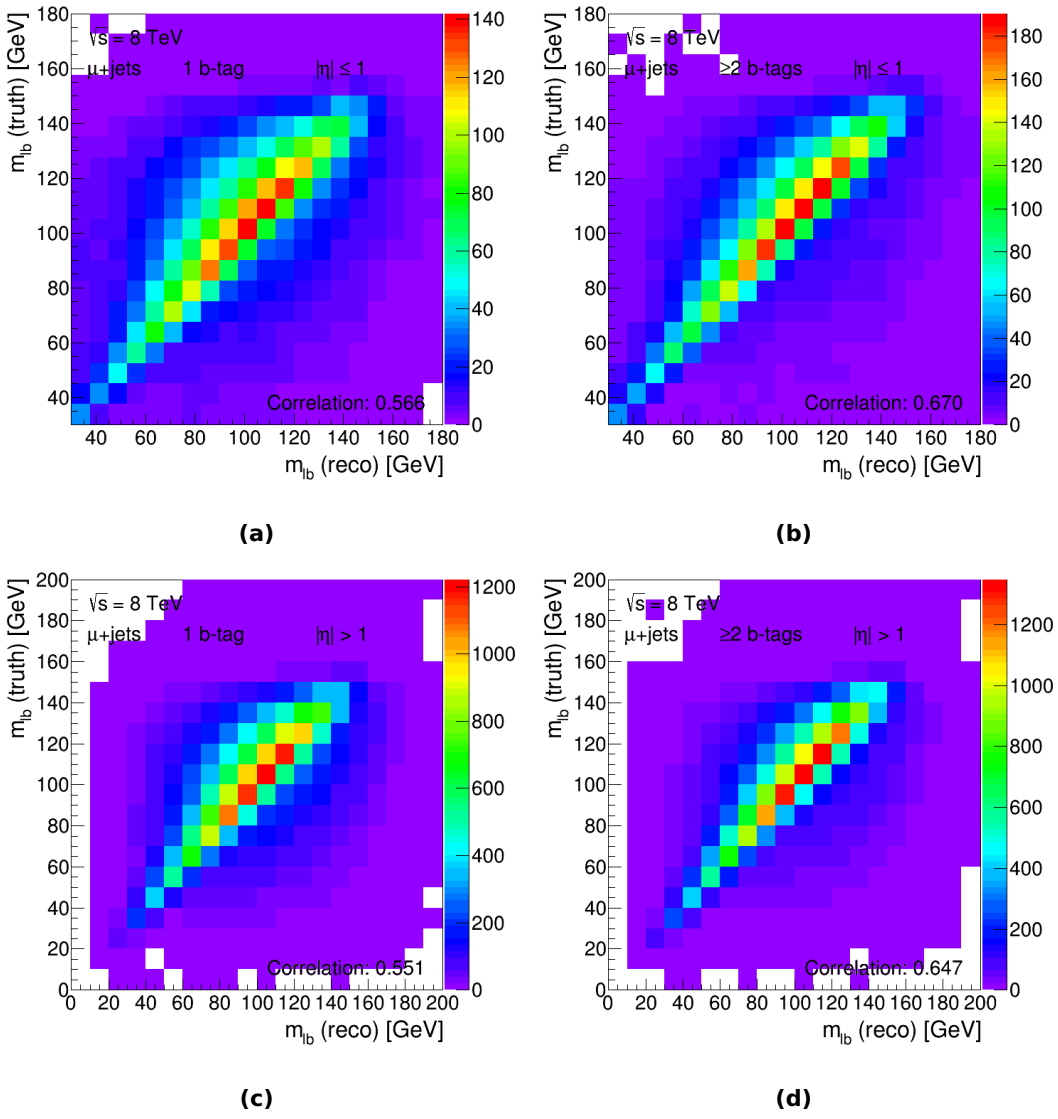

Figure 8.7: Correlation between parton level and reconstruction level distributions of $m_{\ell b}$ in the muon+jets channel. Shown are two-dimensional histograms for events with (a,c) exactly one and (b,d) at least two b-tagged jets as well as events in the two pseudorapidity regions, (a,b) $|\eta| \leq 1$ and (c,d) $|\eta| > 1$, respectively. The correlation values range from 55% to 67%.

Nevertheless, the distributions contained in Fig. 8.7 have considerably large correlation values, and since the above tested values between 140 and 160 GeV for the cut yields similar values, a requirement of $m_{\ell b} < 150$ GeV is justified for such an estimate.

The differences between the two distributions given in Fig. 8.5b after adding the Wt contribution to the `tt` sample are expected to originate from NLO and off-shell effects. Consequently, the deviations visible in the ratio plot can be utilised to reweight the $m_{\ell b}$ distribution of the nominal $t\bar{t}$ sample used in this measurement. The weights derived at truth level were transferred to the corresponding events at reconstruction level to obtain properly reweighted observable templates. These reweighted distributions were treated as a systematic variation so that the standard treatment to evaluate systematic uncertainties as presented in Sec. 8.1 could be applied. 1,000 pseudo-experiments were performed. A comparison of the resulting mean values yields a shift of the measured top quark decay width of -0.42 GeV, a value close to the total signal model uncertainty obtained for this measurement. As the reweighting relies on a sample which has not been validated, the resulting difference is not included in the systematic uncertainties on Γ_t.
Nonetheless, both approaches to estimate the effect of missing NLO precision and further off-shell and non-resonant effects, the cut on $m_{\ell b}$ and the reweighting procedure, can be regarded as first estimates of these effects. As these studies predict differences of around or less than 0.5 GeV, the influence on the final result of such a precision measurement is not negligible. The obtained numbers indicate that ignoring such effects may undersestimate the total systematic uncertainty. Future analyses would thus benefit from MC samples providing an NLO description of the $t\bar{t}$ decay in different channels as well as off-shell effects to allow for well-justified quantitative statements and to verify whether uncertainties are in fact underestimated.

8.6 Impact of the Top Quark Mass

According to the explanations in Sec. 2.3, the top quark decay width depends significantly on the top quark mass. Moreover, the decay width is measured exploiting mass distributions sensitive to Γ_t. It is thus a relevant part of this analysis to quantify the influence of a variation of the top quark mass on the decay width.
For this purpose, alternative MC signal samples based on different masses m_t were employed. The samples with underlying masses closest to the nominal value of $m_t = 172.5$ GeV differ by 2.5 GeV from this reference although latest mass measurements evaluate the top quark mass with a much better precision [111, 123]. These two variations samples with $m_t = 170$ GeV and $m_t = 175$ GeV are based on a full simulation of the ATLAS detector with $h_{\text{damp}} = \infty$. They are treated as systematic variation samples and compared to a full simulation $t\bar{t}$ sample with $h_{\text{damp}} = \infty$ and $m_t = 172.5$ GeV. Pseudo-experiments were conducted as for other systematic uncertainties. The mean values of the distributions resulting from 1,000 pseudo-experiments were compared to infer the effect of the top quark mass on this measurement. The numbers including the standard deviation σ of the resulting Gaussian-shaped distributions are listed in Table 8.4.

m_t	Mean Γ_t
170.0 GeV	2.49 ± 0.49 GeV
172.5 GeV	1.34 ± 0.29 GeV
175.0 GeV	1.21 ± 0.28 GeV

Table 8.4: Results of mean decay width values Γ_t obtained from 1,000 pseudo-experiments based on samples with different underlying top quark masses m_t. The uncertainties correspond to the standard deviations from the Gaussian-shaped distributions that contain the resulting values from the pseudo-experiments.

The value for the alternative mass of 175 GeV is relatively close to the nominal expected decay width of $\Gamma_t = 1.33$ GeV but the smaller mass sample reveals a notable deviation from this expectation. In the following, attempts to parametrise this difference are presented before studies to understand this asymmetric response of Γ_t on the top quark mass variation are discussed.

The three measured values are depicted in Fig. 8.8, together with the simplest possible parametrisation, i.e. linear splines between the points. In addition, decay width values obtained from theory for the three masses $m_t = 170, 172.5, 175$ GeV are included to illustrate discrepancies between the theoretical calculation and the measured numbers. These theory values are computed using a ratio with respect to the nominal value:

$$\frac{\Gamma_t(m_t)}{\Gamma_t(m_{t,0})} = \frac{m_t^3 \cdot \left(1 - 3\left(\frac{m_W}{m_t}\right)^4 + 2\left(\frac{m_W}{m_t}\right)^6\right)}{m_{t,0}^3 \cdot \left(1 - 3\left(\frac{m_W}{m_{t,0}}\right)^4 + 2\left(\frac{m_W}{m_{t,0}}\right)^6\right)}, \tag{8.1}$$

with $m_{t,0} = 172.5$ GeV. Based on this ratio, the values $\Gamma_t(170\text{ GeV})$ and $\Gamma_t(175\text{ GeV})$ are calculated with a reference value that equals 1.33 GeV. The given expression is equivalent to the leading order formula given in Eq. (2.2). NLO or NNLO terms possess only small differences in the given mass range so that these effects cancel out to a significant extent in the ratio. A linear fit between the resulting numbers of $\Gamma_t(170\text{ GeV}) = 1.28$ GeV, $\Gamma_t(172.5\text{ GeV}) = 1.33$ GeV and $\Gamma_t(175\text{ GeV}) = 1.38$ GeV is shown in Fig. 8.8. A reference line with a constant function value of 1.33 GeV is added as well. The measured values do not coincide with the expected behaviour from theory. Instead of an increase in Γ_t, a distinct decrease is observed when going to higher masses.
The mass uncertainty of 0.70 GeV quoted by the latest ATLAS combination [111] can be translated into an uncertainty of Γ_t based on the linear splines. The two clearly different slopes shown in Fig. 8.8 yield a highly asymmetric response of +0.33 GeV and -0.03 GeV.
More complex parametrisations like a quadratic fit using the three mass points were tested as well but were not able to improve the description of the relationship between Γ_t and m_t.

In order to understand the asymmetric response to m_t, further studies were conducted. Pseudo-experiments similar to the ones described above with the alternative mass samples were repeated, based on modified configurations of the template fit. The following options are compared: (a) only

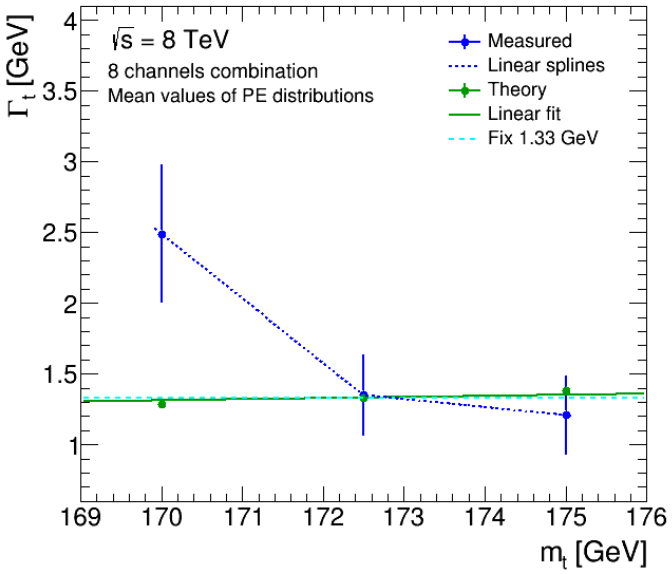

Figure 8.8: Illustration of the asymmetric response of Γ_t to m_t. Shown are mean values of the top quark decay width obtained from pseudo-experiments for different MC mass variation samples at $m_t = 170, 172.5, 175$ GeV, connected by linear splines. The theoretical prediction for the mass dependence of the top quark decay width is drawn as well, which is close to a constant reference line at $\Gamma_t = 1.33$ GeV (dashed), correspondent to a mass of $m_t = 172.5$ GeV. The large difference for the mass value of 170 GeV is too large to be true and the reason for this fit response is explained in the text.

events with at least two b-tagged jets are considered in the fit, (b) the mass in the single top MC samples along with the $t\bar{t}$ samples is set to the alternative values of 170 GeV and 175 GeV, (c) only one observable, either $m_{\ell b}$ or $\Delta R_{\text{min}}(j_b, j_l)$, is used, (d) a cut on the mass observable as introduced in the last section is applied (ignore events with $m_{\ell b} \geq 150$ GeV). The mean values obtained from pseudo-experiments for these four fit configurations performed for the three mass samples are given in Table 8.5. The theoretical predictions for the alternative mass values are shown as well.
In compliance with the expectation, $m_{\ell b}$ is more sensitive to the top quark mass than $\Delta R_{\text{min}}(j_b, j_l)$. The observed asymmetry is mainly caused by $m_{\ell b}$ and increases if only this variable is used in the fit. Particularly the peak region of $m_{\ell b}$ intensifies this effect. The result is almost independent of the used b-tag regions or additional mass variations in the single top event samples. The values of pseudo-experiments relying on fits with only $\Delta R_{\text{min}}(j_b, j_l)$ reveal an almost symmetric response to m_t and the mean values of Γ_t increase with the underlying masses, following the theoretical calculations, although the slope of this rise is more distinct.
These results verify once more that the fit configuration with two observables is mainly driven by the observable which possesses a larger dependence on m_t and Γ_t while $\Delta R_{\text{min}}(j_b, j_l)$ has a clear stabilising effect on the final result and the uncertainty evaluation.
Further tests demonstrated that the observed asymmetry is enhanced by jets in the forward detector

m_t	170.0 GeV	172.5 GeV	175.0 GeV
Γ_t (default option) [GeV]	2.49 ± 0.49	1.34 ± 0.29	1.21 ± 0.28
Γ_t (≥ 2 b-tag bin) [GeV]	2.56 ± 0.77	1.33 ± 0.33	1.44 ± 0.29
Γ_t (mass varied single-top) [GeV]	2.51 ± 0.60	1.34 ± 0.29	1.21 ± 0.24
Γ_t ($m_{\ell b}$ only) [GeV]	2.99 ± 0.60	1.34 ± 0.36	1.09 ± 0.24
Γ_t ($m_{\ell b} < 150$ GeV only) [GeV]	$\sim 6 \pm 0.78$	1.34 ± 0.34	0.77 ± 0.28
Γ_t ($\Delta R_{\text{min}}(j_b, j_l)$ only) [GeV]	1.02 ± 0.43	1.33 ± 0.60	1.56 ± 0.61
Γ_t (theory) [GeV]	1.28	1.33	1.38

Table 8.5: Mean decay width values Γ_t obtained using samples with different top quark masses m_t for various fit configurations and options as described in the text. The uncertainties correspond to the standard deviations from the Gaussian-shaped distributions of the Γ_t values from the pseudo-experiments. The option labelled as "default" is consistent with the fit setup also used for the comparison in Table 8.4. The last row contains the theoretical prediction based on Eq. (8.1). All quoted values are given in units of GeV.

regions and decreases for fit configurations resting on jets in the central region with $|\eta| \leq 1$. In this central pseudorapidity region a mean value of about 2.2 GeV compared to the 2.5 GeV for the default setup is obtained from pseudo-experiments while fits with events from the pseudorapidity region with $|\eta| > 1$ for at least one of the considered jets yield a mean value around 2.8 GeV.

To refute the possibility that the observed asymmetric behaviour is induced by fluctuations in the histogram bins, related to the relatively low statistics in the alternative mass samples with respect to the nominal templates, the number of bins per analysis region was reduced from 20 to 10. However, pseudo-experiments revealed even an increase of the asymmetry, the mean values amount to $\Gamma_t(170\text{ GeV}) \approx 3.1$ GeV and $\Gamma_t(175\text{ GeV}) \approx 1.0$ GeV, respectively.

An interpolation between the nominal observable distributions and those belonging to the 170 GeV and 175 GeV mass variations at reconstruction level, a so-called template morphing, yields a smooth transition between the different templates and pseudo-experiments mean values without unexpected slopes or jumps. This morphing is designed to reproduce the change of the templates in steps of 0.5 GeV in the top quark mass by dividing differences between the nominal and the alternative mass samples per bin by a factor of five. Thus, interpolated or morphed observable distributions for the intermediate masses of $m_t = 170.5, 171, 171.5, 172, 173, 173.5, 174, 174.5$ GeV could be derived. For templates near the nominal value of 172.5 GeV, mean values from pseudo-experiments give decay width values significantly closer to the nominal result, i.e. $\Gamma_t(172\text{ GeV}) \approx 1.52$ GeV and $\Gamma_t(173\text{ GeV}) \approx 1.31$ GeV. The Γ_t mean values for the intermediate mass points from 500 pseudo-experiments in the mass region below 172.5 GeV, where the deviations with regard to the nominal sample are most pronounced, are given in Table 8.6.
To assess the impact of the top quark mass on Γ_t in the range between the nominal and the two alternative mass points, a reweighting using Breit-Wigner functions was tested. For such a study, the procedure defined in Sec. 7.2 for the derivation of decay width templates can be adopted to create

m_t	Mean Γ_t
170.0 GeV	2.49 ± 0.02 GeV
170.5 GeV	2.30 ± 0.03 GeV
171.0 GeV	1.93 ± 0.02 GeV
171.5 GeV	1.71 ± 0.02 GeV
172.0 GeV	1.52 ± 0.02 GeV
172.5 GeV	1.33 ± 0.02 GeV

Table 8.6: Results of mean fitted decay-width values Γ_t including options based on morphed templates for different underlying top quark masses. The values for $m_t = 170$ GeV and $m_t = 172.5$ GeV are obtained from dedicated mass samples, the intermediate values from interpolating or morphing the mass distributions corresponding to $m_t = 170$ GeV and $m_t = 172.5$ GeV as explained in the text. The given uncertainties represent statistical uncertainties on the mean values. The response to the decay width between $m_t = 172.5$ GeV and $m_t = 175$ GeV is similar in the given range from $\Gamma_t = 1.21$ GeV and $\Gamma_t = 1.33$ GeV.

templates based on alternative mass values. Hence, m_t is varied in Eq. (7.1) to create additional mass samples in the range $170 \leq m_t \leq 175$ GeV. But a closure test performed at reconstruction level showed that differences between the rescaled distributions corresponding to $m_t = 170$ GeV and $m_t = 175$ GeV and the respective alternative mass samples are beyond the statistical uncertainties in the bins due to acceptance effects. Since, furthermore, dedicated samples for top quark masses closer to 172.5 GeV are not available for the current analyses, the above delineated template morphing is the best approach to access the m_t range close to the nominal value of $m_t = 172.5$ GeV. These masses comply with uncertainties quoted in latest measurements of m_t.

According to the above listed studies, neither the binning nor specific b-tag, jet pseudorapidity or $m_{\ell b}$ regions are solely responsible for the observed asymmetric response to the top quark mass although some of these parameters amplify the observed asymmetry. The differences between the mass samples are of a similar order in the eight exclusive analysis regions, there is no obvious shift or fluctuation in one certain region between the two alternative mass distributions explaining why the fits behave so asymmetricly. This is highlighted in Fig. 8.9 for plots in the eight regions with the nominal sample as reference. Different values of Γ_t were tested and reflect the same behaviour.

To understand the asymmetric fit response, templates based on $\Gamma_t = 1.33$ GeV obtained from the alternative mass sample with $m_t = 170$ GeV were compared with templates from the nominal sample with $m_t = 172.5$ GeV that correspond to $\Gamma_t = 1.0$ GeV and $\Gamma_t = 2.5$ GeV. The resulting plots are shown in Fig. 8.10 for the pseudorapidity region with $|\eta| > 1$, also including plots for the alternative sample with $m_t = 175$ GeV. App. F comprises further plots also for the $|\eta| \leq 1$ region. The distributions contrasted in Fig. 8.10 verify that the templates derived at $m_t = 172.5$ GeV are not able to cover the $m_{\ell b}$ distribution of the $t\bar{t}$ mass samples of 170 GeV and 175 GeV. Since the alternative mass distributions are beyond the covered range of the nominal $m_t = 172.5$ GeV templates, the fit is not able to reproduce a symmetric response to m_t. This stresses the large sensitivity

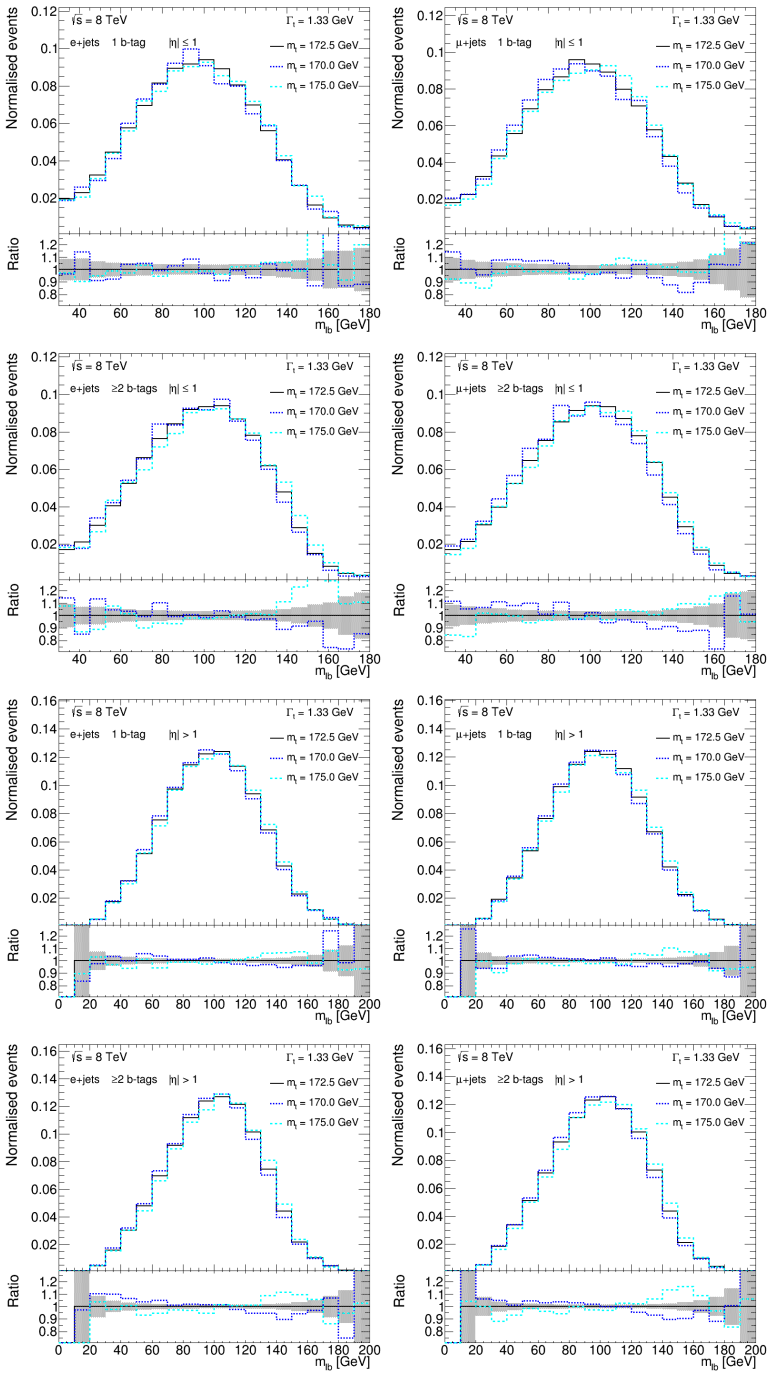

Figure 8.9: Distributions of the observable $m_{\ell b}$ in the eight exclusive analysis regions according to the labels. Templates based on $\Gamma_t = 1.33$ GeV are compared for the nominal sample with $m_t = 172.5$ GeV and for the alternative top quark masses of 170 and 175 GeV. The lower panels illustrate the ratio of the presented histograms with respect to the nominal signal sample.

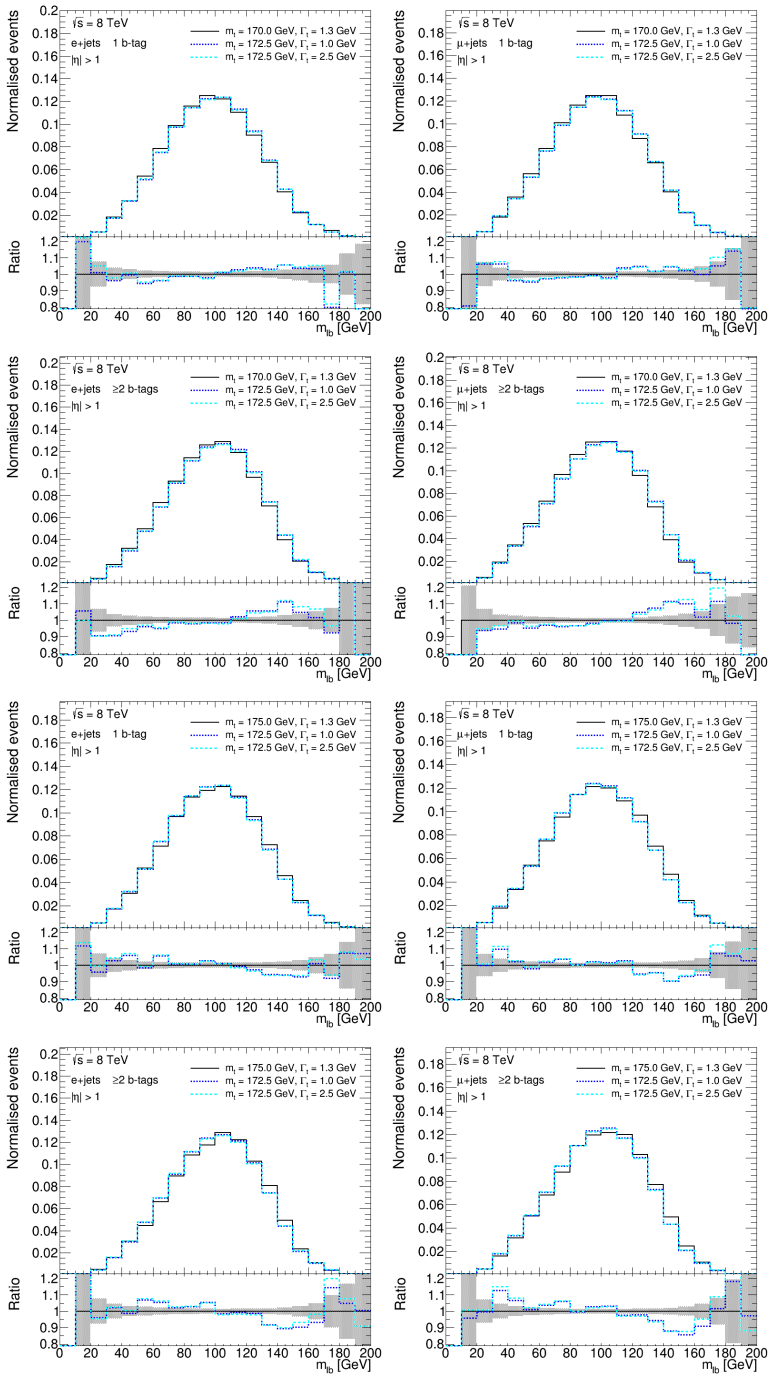

Figure 8.10: Distributions of the observable $m_{\ell b}$ in the four $|\eta| > 1$ analysis regions. Templates based on $\Gamma_t = 1.33$ GeV for the alternative mass sample with $m_t = 170$ GeV (upper half) and with $m_t = 175$ GeV (lower half) are compared to templates for two different decay width values, namely $\Gamma_t = 1.0$ GeV and $\Gamma_t = 2.5$ GeV, from the nominal sample with $m_t = 172.5$ GeV. The lower panels illustrate the ratio of the presented histograms with respect to the alternative $t\bar{t}$ samples at $m_t = 170$ GeV and $m_t = 175$ GeV.

of $m_{\ell b}$ to the mass. For the determination of other systematic uncertainties, as described in the previous sections of this chapter, the different decay width templates encompass the systematic shifts, and thus reliable estimates of the underlying systematic uncertainty can be made.
These conclusions are supported by χ^2 tests, as introduced in Sec. 7.2. Fits of nominal templates to pseudo-data distributions of the nominal $t\bar{t}$ sample at $m_t = 172.5$ GeV, which yield the expected mean value of around 1.33 GeV, are characterised by χ^2 values of around 0.6, after dividing by the numbers of degrees of freedom (ndf). Fits to pseudo-data distributions of the two alternative mass samples have χ^2/ndf values of around 1.4 (for $m_t = 170$ GeV) and of around 1.6 (for $m_t = 175$ GeV), reflecting that the goodness of the fit is significantly worse, following the expectations pertaining to Fig. 8.10.

For the fit configurations implemented and compared so far, the nominal 172.5 GeV templates were fitted to pseudo-data distributions of the 170 GeV and 175 GeV samples, as it is the recommended procedure for systematic uncertainties described in Sec. 8.1. In contrast to this default procedure, the decay width templates derived from the 170 GeV and 175 GeV mass samples can be fitted to pseudo-data distributions of the nominal 172.5 GeV sample. This leads to mean values of $\Gamma_t = 1.28$ GeV for a configuration with $m_t = 170$ GeV templates fitted to $m_t = 172.5$ GeV pseudo-data histograms while a mean value of $\Gamma_t = 1.38$ GeV is measured for the other possible setup with $m_t = 175$ GeV templates fitted to $m_t = 172.5$ GeV pseudo-data distributions. In this particular case, the potential effect of the decay width on m_t is far less distinct in comparison to the values in Table 8.5 and even symmetric around the expectation of 1.33 GeV related to the nominal top quark mass.
A similar approach relies on the idea of fitting $m_t = 170$ GeV templates directly to $m_t = 175$ GeV pseudo-data histograms and vice versa. The resulting mean values from pseudo-experiments are around 1.25 GeV and 1.6 GeV. Despite the difference of $\Delta m_t = 5$ GeV between the two compared samples, the resulting difference in Γ_t is smaller compared to the numbers in Table 8.5 where the difference between the samples is merely $\Delta m_t = 2.5$ GeV.
These further cross-checks confirm the above description that the fit is not able to properly account for the differences between the alternative mass samples because the different decay width templates do not cover the mass differences. Hence, the resulting numbers are so different for the various cross-checks without a clear tendency for the preference of a certain template.

As a consequence, a precise estimate of the impact of the top quark mass on the Γ_t measurement requires alternative MC mass samples much closer to the nominal value of $m_t = 172.5$ GeV so that the resulting observable distributions can be covered by the different decay width templates. The most reliable approach available for $\sqrt{s} = 8$ TeV is the template morphing for which a shift in the decay width of up to 0.2 GeV can be deduced from a mass variation of ±0.5 GeV around the nominal value.
The top quark mass dependence is not included as an uncertainty in many analyses but given as a parametrisation. According to the above described studies, a parametrisation is not possible for this measurement and the final result of Γ_t is quoted for a top quark mass of 172.5 GeV.

8.7 Other Systematic Uncertainties

8.7.1 Luminosity Uncertainty

An uncertainty of 1.9% is assigned to the integrated luminosity [210], as outlined in Sec. 6.1, equivalent to a value of 0.4 fb^{-1}. To evaluate the corresponding systematic effect on the Γ_t measurement, distributions based on a variation of the luminosity of ±1.9% are built. These systematic variation samples are then compared to the nominal distributions by using pseudo-experiments as for previous uncertainties and the measured difference in Γ_t is quoted as luminosity uncertainty.

8.7.2 Template Statistical Uncertainty

The systematic uncertainty that is due to the limited size of the employed MC samples is taken into account by varying the content of each bin of the signal and background templates within its statistical uncertainty. The fit to fixed nominal distributions with the varied templates is repeated and 2,000 ensemble tests were performed. The standard deviation of the distribution of Γ_t values coming from this particular type of ensemble tests is taken as systematic uncertainty due to the limited template statistical uncertainty.

8.8 Total Systematic Uncertainty

The resulting systematic uncertainties evaluated according to the descriptions in this chapter are summarised in Table 8.7, obtained from 2,000 pseudo experiments each. The individual sources of systematic uncertainty considered in this analysis are summed in quadrature to determine the total systematic uncertainty given in the last row.
Since each selected event in this analysis contains at least four jets and since the decay width Γ_t is extracted from templates where resolution effects may play a major role, the jet energy scale and the jet energy resolution constitute dominant systematic uncertainties. Another substantial contribution comes from the ME generator uncertainty which is by far the dominant signal model uncertainty, around two times larger than the second largest effect which is caused by the colour reconnection model. This is due to the fact that the two samples which are compared to estimate the ME generator uncertainty possess very significant differences in the region of large $m_{\ell b}$ values. Removing this region from the fit affects the result by at least 0.45 GeV, as studied in Sec. 8.5. Additional investigations revealed that an MC generator setup with MC@NLO describes the data worse than the nominal POWHEG+PYTHIA setup, which may also explain a significant systematic effect when comparing these two ME generators.

Source	Uncertainty [GeV]	
Detector model		
Electron	+0.14	−0.07
Muon	+0.11	−0.06
Missing transverse momentum	+0.01	−0.01
Jet energy scale	+0.42	−0.30
Jet energy resolution	+0.27	−0.27
Jet vertex fraction	+0.13	−0.03
Jet reconstruction efficiency	+0.03	−0.03
Heavy and light flavour tagging	+0.32	−0.24
Signal model		
ME generator	+0.41	−0.41
Colour reconnection	+0.19	−0.19
Underlying event	+0.11	−0.11
Radiation	+0.07	−0.07
PDF	+0.06	−0.06
PS/fragmentation	+0.05	−0.05
Background model		
Multijet	+0.04	−0.00
W+jets	+0.02	−0.02
Single top	$<+0.01$	<-0.01
Template statistical uncertainty	+0.07	−0.07
Luminosity	+0.03	−0.00
Total systematic uncertainty	+0.79	−0.68

Table 8.7: Summary of all systematic uncertainties for the top quark decay width measurement. The resulting total systematic uncertainty is given in the last row.

9 Comparison of Fit Configurations and Observables

Various observables and configurations of the fit method are potentially suited for a direct measurement of the top quark decay width. The previous chapter indicated, see, for instance, Sec. 8.5 or Sec. 8.6, that the understanding of systematic effects and their reduction constitutes a very important part of this analysis.
A brief and general motivation of the two observables $m_{\ell b}$ and $\Delta R_{\mathrm{min}}(j_b, j_l)$ and the split into two pseudorapidity and b-tag regions is addressed in preceding chapters. The observable $m_{\ell b}$ offers the best compromise with a good sensitivity to Γ_t and low sensitivity to jet-related and radiation systematic effects while angular observables of the hadronic decay branch of $t\bar{t}$ events like $\Delta R_{\mathrm{min}}(j_b, j_l)$ contribute to the reduction of other leading systematic uncertainties in the combination with $m_{\ell b}$. The idea of splitting the sample into two mutually exclusive $|\eta|$ regions takes advantage of the different sensitivity of these regions to detector resolution effects, exploits different pile-up contributions and varying portions of background events. The usage of two orthogonal b-tag regions is also motivated by the reduction of systematic uncertainties, like the one due to ISR and FSR.
The subsequent sections are dedicated to verify that the chosen observables and analysis regions lead to a fit configuration that, in contrast to others, minimises dominant systematic uncertainties the most. The comparison studies were performed for the systematic uncertainties which dominate the total uncertainty in the Γ_t measurement according to the descriptions in Ch. 8 and Table 8.7, namely the jet energy scale, the jet energy resolution and the signal model uncertainties.
This chapter begins with an analysis of fits based on single observables before dominant systematic uncertainties are evaluated and compared for a large variety of template fits with two observables fitted simultaneously. A further section focuses on the modelling of different suited observables, which is also taken into account for the final observable choice, before the chapter concludes with a comparison of fits for which only events with at least two b-tagged jets are used.

9.1 Comparison of Fits with One Observable

Dominant systematic uncertainties are first compared for template fits with only one observable. The tested observables are listed and defined in Table 7.1. The implementation of the fit follows the description in Ch. 7, and the systematic uncertainties are estimated pursuant to the general strategy given in Sec. 8.1 and the more detailed definitions of individual sources of systematic uncertainty in the subsequent sections of Ch. 8. Since the jet energy scale and the jet energy resolution are

composed of 26 and 11 subcomponents, respectively, only the three largest components of the JES and the largest component of the JER are considered for the comparison shown here. Since these components dominate the full JES and JER uncertainty values to a high degree, this approach yields a reliable estimate of the full effect, in due consideration of the very high CPU consumption and runtime of all these studies. Besides, the following five signal model uncertainties are used in the comparison as well: the radiation systematic uncertainty, the matrix element generator uncertainty, the parton shower and fragmentation model uncertainty as well as the uncertainties due to the underlying event and the colour reconnection modelling, delineated in Sec. 8.4.
The resulting uncertainty numbers for these sources of systematic uncertainty are summarised in Table 9.1, including expected statistical uncertainties which are calculated as described in Sec. 7.4. The last row shows the total uncertainty obtained from the total systematic and the expected statistical uncertainty added in quadrature. These numbers are derived from a fit without a cut on the logarithm of the KLFitter likelihood and without the split into pseudorapidity regions in order to compare variables with only the basic selection criteria applied.

Source	Uncertainties [GeV] for m_t^{had}	$m_{\ell b}$	R32	D32	SdR	$\Delta R_{\mathrm{min}}(j_b, j_l)$
JES (3 components)	$^{+3.04}_{-1.16}$	$^{+0.76}_{-0.59}$	$^{+0.26}_{-0.24}$	$^{+1.32}_{-0.85}$	$^{+0.41}_{-0.37}$	$^{+0.04}_{-0.09}$
JER (1 component)	±0.61	±0.32	±0.94	±0.66	±0.09	±0.17
Radiation	±2.97	±0.17	±2.60	±1.31	±1.69	±1.31
ME generator	±0.24	±0.52	±1.40	±0.38	±0.70	±0.16
Colour reconnection	±0.07	±0.16	±0.58	±0.31	±0.05	±0.03
Underlying event	±0.10	±0.13	±0.08	±0.16	±0.09	±0.33
PS/fragmentation	±0.03	±0.09	±0.77	±0.54	±0.32	±0.38
Total syst. uncertainty	$^{+4.31}_{-3.26}$	$^{+1.01}_{-0.89}$	$^{+3.26}_{-3.26}$	$^{+2.11}_{-1.85}$	$^{+1.91}_{-1.90}$	$^{+1.42}_{-1.43}$
Exp. stat. uncertainty	±0.29	±0.31	±0.36	±0.23	±0.60	±0.65
Total uncertainty	$^{+4.32}_{-3.27}$	$^{+1.06}_{-0.95}$	$^{+3.28}_{-3.28}$	$^{+2.12}_{-1.86}$	$^{+2.00}_{-2.00}$	$^{+1.56}_{-1.57}$

Table 9.1: Dominant systematic and expected statistical uncertainties for fits using different observables. The individual sources of systematic uncertainty are summed in quadrature to obtain the total systematic uncertainty. The quadratic sum of this value and the expected statistical uncertainty yields the total uncertainty given in the last row. The numbers are compared in the text. The uncertainties on these numbers amount to around 0.01-0.02 GeV and originate from the finite number of pseudo-experiments performed (1,000 pseudo-experiments).

The shown results indicate that the total uncertainty becomes very large for observables from the hadronic decay branch of the $t\bar{t}$ events. They all suffer from very large radiation uncertainties. By construction, R_{32} has a small JES uncertainty due to its definition as a mass ratio but larger signal model uncertainties, in contrast to m_t^{had} and D_{32} with very high JES uncertainties. The uncertainties

determined for the angular observables are mainly driven by the large radiation uncertainty value. The large expected statistical uncertainties hint at a relatively low sensitivity to the decay width Γ_t. The observable $m_{\ell b}$, however, possesses reasonably small dominant systematic uncertainties while the expected statistical uncertainty is comparable to that of the other mass-based observables of the hadronic decay branch, stressing the good sensitivity of $m_{\ell b}$ to the top quark decay width. A detailed discussion of all shown numbers in this chapter would go beyond the scope of this thesis.

9.2 Comparison of Fits with Two Observables

Since the results of the previous section verify that $m_{\ell b}$ offers by far the best performance in terms of the total uncertainty, the fit configurations tested with two observables in this section rely on $m_{\ell b}$ as the first observable.
Setting up such a fit aims at reducing the total systematic uncertainty further because systematic effects that impact both observables may cancel out in the combination. In addition, a simultaneous likelihood fit using two observables from the different branches of the $t\bar{t}$ pair decay exploits most information from this decay while the two observables have only small correlations, as shown in Sec. 7.6.
The dominant systematic uncertainties as well as the expected statistical uncertainties were evaluated in the exact same manner as delineated in Sec. 9.1 for the one observable setup. The combinations of $m_{\ell b}$ with the remaining five observables from the hadronic decay branch were tested and the results can be seen in Table 9.2.

Merely the combination of $m_{\ell b}$ with the angular observables SdR and $\Delta R_{\text{min}}(j_b, j_l)$ provide smaller total uncertainties compared to the one observable fits. The combinations of $m_{\ell b}$ with the other three observables that depend directly on masses still suffer from sizeable JES, JER and radiation uncertainties. Although these uncertainty values decrease with regard to the one observable results for m_t^{had}, R_{32} and D_{32}, they still exceed the results for the fit with $m_{\ell b}$ only. The combination of $m_{\ell b}$ with angular observables reduces the impact of the JER and in particular of the JES as the largest systematic uncertainty of this measurement eminently. Moreover, also the statistical uncertainty as a measure of the sensitivity to the underlying top quark decay width is still comparable to other observable combinations. Especially the combination of $m_{\ell b}$ with $\Delta R_{\text{min}}(j_b, j_l)$ results in a substantial decrease of the total uncertainty with respect to the fit setup with $m_{\ell b}$ only.

Based on these findings, the effect of splitting the samples into two orthogonal jet pseudorapidity regions was investigated. Since only combinations of $m_{\ell b}$ with an angular observable are suited for a precise Γ_t measurement with acceptably small total uncertainties, the studies presented in the following are based on two observable fits with $m_{\ell b}$ and SdR or $\Delta R_{\text{min}}(j_b, j_l)$.
As outlined in Sec. 7.7, three values of η_C that cut the sample into two jet pseudorapidity regions were tested: $\eta_C = 0.8$, 1.0 and 1.2, in compliance with the JES and JER calibration points defined in [230].
The resulting uncertainties obtained from these three fit configurations are presented in Table 9.3

Source	Uncertainties [GeV] for $m_{\ell b}$+				
	$+m_t^{\mathrm{had}}$	+R32	+D32	+SdR	$+\Delta R_{\mathrm{min}}(j_b, j_l)$
JES (3 components)	$+2.47$ -1.17	$+0.52$ -0.42	$+1.25$ -0.85	$+0.60$ -0.47	$+0.46$ -0.43
JER (1 component)	± 0.50	± 0.67	± 0.59	± 0.28	± 0.26
Radiation	± 1.82	± 0.81	± 1.00	± 0.49	± 0.22
ME generator	± 0.22	± 0.57	± 0.29	± 0.05	± 0.08
Colour reconnection	± 0.06	± 0.05	± 0.19	± 0.01	± 0.06
Underlying event	± 0.06	± 0.14	± 0.01	± 0.10	± 0.14
PS/fragmentation	± 0.03	± 0.36	± 0.43	± 0.25	± 0.14
Total syst. uncertainty	$+3.12$ -2.23	$+1.36$ -1.33	$+1.79$ -1.54	$+0.87$ -0.78	$+0.64$ -0.61
Exp. stat. uncertainty	± 0.26	± 0.28	± 0.22	± 0.30	± 0.28
Total uncertainty	$+3.13$ -2.25	$+1.39$ -1.36	$+1.81$ -1.55	$+0.92$ -0.84	$+0.70$ -0.68

Table 9.2: Dominant systematic and expected statistical uncertainties for simultaneous fits of two observables. The observable $m_{\ell b}$ is shown in combination with the different observables from the hadronic decay branch of $t\bar{t}$ events. The individual sources of systematic uncertainty are summed in quadrature to obtain the total systematic uncertainty. The quadratic sum of this value and the expected statistical uncertainty yields the total uncertainty given in the last row. The numbers are compared in the text. The uncertainties on these numbers amount to around 0.02-0.03 GeV and originate from the finite number of pseudo-experiments performed.

for the observable combinations $m_{\ell b}$+SdR and $m_{\ell b}+\Delta R_{\mathrm{min}}(j_b, j_l)$. Other observable combinations led to similar results as already presented in Table 9.2 and are thus not listed separately.

Furthermore, the distributions were separated into two categories by the jet energies with cut values E_C defined in Sec. 7.7. The uncertainties extracted for this fit configuration are listed in Table 9.4 for both observable combinations of $m_{\ell b}$ with the angular variables.

The conducted studies show that splitting the samples into two $|\eta|$ regions or two energy regions leads in all cases to smaller total uncertainties for the observable combination $m_{\ell b}$+SdR. The decrease in estimated uncertainty values is larger for the split into two pseudorapidity regions and mainly caused by a reduction of jet-related uncertainties. This follows the expectation that the jet resolution uncertainty goes down by performing the fit in two regions with different underlying detector resolutions. For a combination of $m_{\ell b}$ and $\Delta R_{\mathrm{min}}(j_b, j_l)$, a decrease in the total uncertainty is merely observed for a split into two $|\eta|$ regions with $\eta_C = 1$, but the size of the total uncertainty is already relatively small for this observable combination without applying the $|\eta|$ split. Taken as a whole, the two observable combinations associated with splitting the observable distributions into two pseudorapidity regions with $\eta_C = 1$ results in smallest total uncertainty values. Hence, the studies presented in the following for the combinations of $m_{\ell b}$+SdR and $m_{\ell b}+\Delta R_{\mathrm{min}}(j_b, j_l)$ are

Source	Uncert. [GeV], $m_{\ell b}$+SdR			Uncert. [GeV], $m_{\ell b}$+$\Delta R_{\mathrm{min}}(j_b, j_l)$		
	$\eta_C = 0.8$	$\eta_C = 1.0$	$\eta_C = 1.2$	$\eta_C = 0.8$	$\eta_C = 1.0$	$\eta_C = 1.2$
JES (3 components)	$^{+0.41}_{-0.40}$	$^{+0.43}_{-0.32}$	$^{+0.38}_{-0.35}$	$^{+0.57}_{-0.29}$	$^{+0.39}_{-0.32}$	$^{+0.45}_{-0.32}$
JER (1 component)	±0.21	±0.21	±0.26	±0.30	±0.27	±0.22
Radiation	±0.32	±0.32	±0.35	±0.29	±0.26	±0.20
ME generator	±0.14	±0.04	±0.02	±0.26	±0.23	±0.30
Colour reconnection	±0.01	±0.10	±0.19	±0.03	±0.13	±0.22
Underlying event	±0.09	±0.00	±0.12	±0.07	±0.12	±0.18
PS/fragmentation	±0.19	±0.16	±0.21	±0.10	±0.06	±0.14
Total syst. uncertainty	$^{+0.61}_{-0.61}$	$^{+0.61}_{-0.53}$	$^{+0.66}_{-0.64}$	$^{+0.76}_{-0.59}$	$^{+0.62}_{-0.58}$	$^{+0.69}_{-0.62}$
Exp. Stat. uncertainty	±0.30	±0.27	±0.26	±0.24	±0.22	±0.27
Total uncertainty	$^{+0.68}_{-0.68}$	$^{+0.66}_{-0.60}$	$^{+0.70}_{-0.69}$	$^{+0.81}_{-0.65}$	$^{+0.66}_{-0.62}$	$^{+0.74}_{-0.67}$

Table 9.3: Dominant systematic and expected statistical uncertainties for fits with the observables $m_{\ell b}$ and SdR (column 2-4) or $m_{\ell b}$ and $\Delta R_{\mathrm{min}}(j_b, j_l)$ (column 5-7) in combination with a split of the input distributions into two jet pseudorapidity regions. Compared are configurations with $\eta_C = 0.8$, $\eta_C = 1$ and $\eta_C = 1.2$. The individual sources of systematic uncertainty are summed in quadrature to obtain the total systematic uncertainty. The quadratic sum of this value and the expected statistical uncertainty yields the total uncertainty given in the last row. The uncertainties on these numbers amount to around 0.02-0.03 GeV and originate from the finite number of pseudo-experiments performed.

based on this particular $|\eta|$ split. Apart from that, the statistical uncertainty decreases noticeably for the configurations with $\eta_C = 1$, pointing at a larger sensitivity to the underlying Γ_t, another purpose of utilising the split.

Further tested fit configurations comprise the application of a cut on the logarithm of the KLFitter likelihood and an additional cut on the reconstructed hadronic W boson mass. A cut on the KLFitter likelihood - chosen is a requirement of $\ln(L) > -50$ - increases the purity of the event reconstruction since a significant portion of combinatorial background due to events which are not correctly reconstructed is suppressed. This requirement is combined with a cut on the reconstructed hadronic W boson mass. A range of $60 < m_W^{\mathrm{had}} < 100$ GeV is kept to dismiss the tails with higher background pollutions.
These two cut options were tested for a fit setup where the events entering the fit are reconstructed by a KLFitter setup using four jets in the event reconstruction. In order to check the impact of systematic uncertainties on a fit with events reconstructed by a KLFitter configuration based on five jets - if the event contains more than four -, the dominant systematic uncertainties were also calculated for such a setup. The results are summarised in Table 9.5.

Since these additional fit configurations correspond to fits of the combinations $m_{\ell b}$+SdR and

Source	Uncertainties [GeV], Energy split	
	$m_{\ell b}$+SdR	$m_{\ell b}$+$\Delta R_{\mathrm{min}}(j_b, j_l)$
JES (3 components)	+0.55 −0.48	+0.56 −0.38
JER (1 component)	±0.15	±0.21
Radiation	±0.40	±0.32
ME generator	±0.18	±0.07
Colour reconnection	±0.05	±0.10
Underlying event	±0.02	±0.17
PS/fragmentation	±0.06	±0.09
Total syst. uncertainty	+0.72 −0.67	+0.72 −0.59
Exp. stat. uncertainty	±0.30	±0.28
Total uncertainty	+0.78 −0.73	+0.77 −0.65

Table 9.4: Dominant systematic and expected statistical uncertainties for fits with the observables $m_{\ell b}$ in combination with SdR or $\Delta R_{\mathrm{min}}(j_b, j_l)$ associated with a split of the input distributions into two jet energy regions. The individual sources of systematic uncertainty are summed in quadrature to obtain the total systematic uncertainty. The quadratic sum of this value and the expected statistical uncertainty yields the total uncertainty given in the last row. The uncertainties on these numbers amount to around 0.02-0.03 GeV and originate from the finite number of pseudo-experiments performed.

$m_{\ell b}$+$\Delta R_{\mathrm{min}}(j_b, j_l)$ associated with a pseudorapidity split of $\eta_C = 1$, the obtained values need to be compared to columns No. 3 and No. 6 of Table 9.3. For a better comparability, these columns are copied to Table 9.5, added as an additional column on the right.

The numbers indicate that the additional jet used in a reconstruction with five jets causes severely larger radiation uncertainties. As also other uncertainties increase, the total uncertainty is around 50% larger with respect to fits based on the KLFitter that considers only four jets in the reconstruction step. Thus, a fit with an event reconstruction using five jets in combination with additional cuts on $\ln(L)$ or the W boson mass is not explicitly given in Table 9.5.
A comparison of the fit configurations based on a KLFitter version with four jets reveals that the uncertainties increase slightly after applying a cut on $\ln(L)$ and even further with the second cut on the W boson mass. The statistical uncertainties increase because of the event loss due to the cuts. As a result, a raw comparison of uncertainty numbers would give preference to a fit without further cuts. However, apart from the fact that at least the cut on the logarithm of the KLFitter likelihood purifies the sample by removing combinatorial background, also modelling issues need to be taken into account to justify the final fit configuration used for the Γ_t measurement, delineated in the next section.

Source	Uncertainties [GeV], $m_{\ell b}$+SdR			
	4 jets + LL	4 jets + LL & m_W^{had}	5 jets	4 jets
JES (3 components)	$^{+0.32}_{-0.31}$	$^{+0.38}_{-0.33}$	$^{+0.38}_{-0.36}$	$^{+0.43}_{-0.32}$
JER (1 component)	±0.16	±0.10	±0.28	±0.21
Radiation	±0.05	±0.26	±0.55	±0.32
ME generator	±0.42	±0.53	±0.03	±0.04
Colour reconnection	±0.09	±0.08	±0.15	±0.10
Underlying event	±0.19	±0.03	±0.11	±0.00
PS/fragmentation	±0.21	±0.33	±0.64	±0.16
Total syst. uncertainty	$^{+0.63}_{-0.62}$	$^{+0.79}_{-0.76}$	$^{+0.99}_{-0.98}$	$^{+0.61}_{-0.53}$
Exp. stat. uncertainty	±0.28	±0.32	±0.27	±0.27
Total uncertainty	$^{+0.69}_{-0.68}$	$^{+0.85}_{-0.83}$	$^{+1.02}_{-1.02}$	$^{+0.66}_{-0.60}$

(a)

Source	Uncertainties [GeV], $m_{\ell b}$+$\Delta R_{\text{min}}(j_b, j_l)$			
	4 jets + LL	4 jets + LL & m_W^{had}	5 jets	4 jets
JES (3 components)	$^{+0.41}_{-0.29}$	$^{+0.46}_{-0.32}$	$^{+0.46}_{-0.37}$	$^{+0.39}_{-0.32}$
JER (1 component)	±0.22	±0.13	±0.18	±0.27
Radiation	±0.07	±0.13	±0.52	±0.26
ME generator	±0.41	±0.54	±0.08	±0.23
Colour reconnection	±0.19	±0.37	±0.09	±0.13
Underlying event	±0.11	±0.22	±0.17	±0.12
PS/fragmentation	±0.05	±0.16	±0.48	±0.06
Total syst. uncertainty	$^{+0.66}_{-0.60}$	$^{+0.86}_{-0.80}$	$^{+0.89}_{-0.84}$	$^{+0.62}_{-0.58}$
Exp. stat. uncertainty	±0.30	±0.32	±0.28	±0.22
Total uncertainty	$^{+0.70}_{-0.67}$	$^{+0.93}_{-0.86}$	$^{+0.93}_{-0.89}$	$^{+0.66}_{-0.62}$

(b)

Table 9.5: Dominant systematic and expected statistical uncertainties for fits with the two observable combinations (a) $m_{\ell b}$+SdR and (b) $m_{\ell b}$+$\Delta R_{\text{min}}(j_b, j_l)$ where the input distributions are split into two jet pseudorapidity regions with $\eta_C = 1$. Fit configurations relying on different KLFitter setups used for the event reconstruction are compared. The option with four jets in the reconstruction, as shown in Table 9.3, is displayed in the last column ("4jets") and compared to KLFitter setups with additional cuts on $\ln(L)$ and the hadronic W boson mass ("4jets + LL" and "4jets + LL & m_W^{had}") and to a KLFitter setup based on five jets in the reconstruction ("5jets"). The individual sources of systematic uncertainty are summed in quadrature to obtain the total systematic uncertainty. The quadratic sum of this value and the expected statistical uncertainty yields the total uncertainty given in the last row. The uncertainties on these numbers amount to around 0.03 GeV and originate from the finite number of pseudo-experiments performed.

9.3 Modelling of the Observables

The modelling of the observables in the different analysis regions is important and was also checked in the course of this analysis. An observable is regarded as well-modelled if the predicted signal and background distributions agree well with the distributions measured in data for the entire range of observable values. The agreement between data and prediction can be quantified using a χ^2 test. The obtained χ^2 values are divided by the numbers of degrees of freedom (based on the number of histogram bins here) so that values close to one reflect a good agreement between data and prediction whereas larger χ^2 values considerably above one hint at a mismodelling of the respective observable.

A test of the observables $m_{\ell b}$ and SdR corresponding to the option with smallest total uncertainties, listed in Table 9.3, yields values of $\chi^2/\text{ndf}(m_{\ell b}) \approx 3.44$ and $\chi^2/\text{ndf}(\text{SdR}) \approx 5.30$, derived from a concatenated histogram of all eight exclusive analysis regions. This comparatively poor χ^2/ndf value for SdR is reflected in the ratio of data events divided by predicted events per bin. Most analysis regions have clear slopes with a ratio steadily increasing from below one to above one. Despite the better agreement between data and prediction for $m_{\ell b}$, such a mismodelling of SdR might introduce a bias in the fit to data.
The application of the cut on the logarithm of the KLFitter likelihood reduces the χ^2 values to $\chi^2/\text{ndf}(m_{\ell b}) \approx 1.86$ and $\chi^2/\text{ndf}(\text{SdR}) \approx 3.23$ but the slopes in the ratio of the SdR distributions in the different analysis regions remain to a large extent. A closer look at the second angular observable exhibits that $\Delta R_{\text{min}}(j_b, j_l)$ suffers from slight slopes in the data over prediction ratios which almost vanish after applying the cut on the logarithm of the KLFitter likelihood. The related χ^2 values of $\chi^2/\text{ndf}(m_{\ell b}) \approx 1.86$ and $\chi^2/\text{ndf}(\Delta R_{\text{min}}(j_b, j_l)) \approx 2.08$ underline that both observables are reasonably well-modelled, required for a stable and unbiased fit. These quantitative statements are also supported by Kolmogorov-Smirnov tests. The corresponding observable plots including the χ^2 test and Kolmogorov-Smirnov test results are presented in Appendix G.

To conclude, based on all the studies described on the previous pages, the observable combination of $m_{\ell b}$ and $\Delta R_{\text{min}}(j_b, j_l)$ combined with a split of the distributions into two jet pseudorapidity regions and a cut on the logarithm of the KLFitter likelihood is used in the final fit to data, referred to as default configuration in the following. Because of the separate lepton channels and the two considered b-tag regions, which are addressed in the next subsection, the input distributions that enter the fit consist of the eight concatenated regions. This configuration constitutes a very good compromise with small systematic uncertainties compared to the other tested options and an adequate modelling which does not introduce a bias in the fit to data.

A further investigation of the mismodelling of angular-based variables indicates that the mismodelling tends to be larger if all three ΔR values of the sum SdR are small. As $\Delta R_{\text{min}}(j_b, j_l)$ depends on only one angle and not all three ΔR values of the jets resulting from the hadronically decaying top quark, as SdR, where such a small sum of these ΔR values enters directly, the mismodelling is more

distinct for SdR than for $\Delta R_{\text{min}}(j_b, j_l)$. These findings may be due to not sufficiently well-modelled highly boosted top quarks, where all ΔR angles between the decay particles of the top quark are relatively small. The impact of parton showering offers a further explanation for a discrepancy between data and prediction of angular quantities. If the matrix element generator POWHEG is interfaced with HERWIG instead of PYTHIA, the agreement between data and prediction is better. The same observation was made during initial observable studies at a centre-of-mass energy of $\sqrt{s} = 13$ TeV.

9.4 Comparison of Results Using Events with at Least 2 b-Tags

In the final fit configuration, two b-tag regions composed of events that possess at least two b-tagged jets or exactly one b-tagged jet are considered. The latter region has a larger fraction of background events and also the KLFitter reconstruction efficiency is larger for events with at least two b-tagged jets. To validate to which extent events with exactly one b-tag are relevant for the analysis, this section serves to compare the final fit setup with eight concatenated fit regions to a corresponding setup excluding the events with exactly one b-tag. Thus, the number of individual channels in the concatenated distributions is reduced from eight to four (two lepton channels divided into two $|\eta|$ regions each).
Dominant systematic uncertainties and expected statistical uncertainties were determined for this four channel setup. For reasons of completeness, fits based on merely one observable were conducted as well. The results are listed in Table 9.6. The values for the default option are taken from Table 9.5 and added to the last column to facilitate the comparison.

After removing events with exactly one b-tag, the systematic as well as the expected statistical uncertainties increase. In particular, the signal model uncertainties such as the uncertainty due to ISR and FSR increase significantly. The differences between the samples used and the nominal signal sample are much smaller in the region of events with exactly one b-tag. Hence, adding this b-tag region helps to reduce some of these dominant signal model uncertainties. The total uncertainty increases by a factor of around two if only the events with at least two b-tagged jets are taken into account. A similar increase is observed for the fits using only one observable. In contrast to the fits with both b-tag regions, the fit based on $m_{\ell b}$ only results in slightly smaller uncertainties compared to the respective two observable option in this particular case.
To conclude, considering events with one b-tagged jet is essential for keeping systematic uncertainties at a low level and, thus, such events are used in the analysis with eight analysis regions in total.

Source	Uncertainties [GeV], ≥ 2 b-tagged jets			
	$m_{\ell b}$ only	$\Delta R_{\text{min}}(j_b, j_l)$ only	$m_{\ell b}$+$\Delta R_{\text{min}}(j_b, j_l)$	Default
JES (3 components)	$^{+0.62}_{-0.42}$	$^{+0.10}_{-0.13}$	$^{+0.47}_{-0.34}$	$^{+0.41}_{-0.29}$
JER (1 component)	± 0.33	± 0.24	± 0.39	± 0.22
Radiation	± 0.83	± 1.30	± 0.93	± 0.07
ME generator	± 0.57	± 1.72	± 0.79	± 0.41
Colour reconnection	± 0.03	± 0.27	± 0.11	± 0.19
Underlying event	± 0.15	± 0.57	± 0.23	± 0.11
PS/fragmentation	± 0.31	± 0.79	± 0.42	± 0.05
Total syst. uncertainty	$^{+1.28}_{-1.19}$	$^{+2.39}_{-2.39}$	$^{+1.45}_{-1.42}$	$^{+0.66}_{-0.60}$
Exp. stat. uncertainty	± 0.43	± 0.89	± 0.39	± 0.30
Total uncertainty	$^{+1.35}_{-1.27}$	$^{+2.55}_{-2.55}$	$^{+1.50}_{-1.47}$	$^{+0.70}_{-0.67}$

Table 9.6: Dominant systematic and expected statistical uncertainties for fits based on one observable - $m_{\ell b}$ or $\Delta R_{\text{min}}(j_b, j_l)$- and based on the observable combination $m_{\ell b}$+$\Delta R_{\text{min}}(j_b, j_l)$ using events with at least two b-tagged jets compared to the default configuration applied in this analysis, as given in Table 9.5. The individual sources of systematic uncertainty are summed in quadrature to obtain the total systematic uncertainty. The quadratic sum of this value and the expected statistical uncertainty yields the total uncertainty given in the last row. The uncertainties on these numbers amount to around 0.03-0.04 GeV and originate from the finite number of pseudo-experiments performed.

10 Results

In order to extract the top quark decay width, the binned likelihood template fit is applied to data using the concatenated distributions of both observables, $m_{\ell b}$ and $\Delta R_{\text{min}}(j_b, j_l)$, in the eight exclusive analysis regions. This chapter presents the results of this fit and the value of Γ_t obtained for this measurement.
After a discussion of the results including various figures that show, for instance, post-fit distributions of the observables as well as the likelihood curve deduced from the fit, a further section is dedicated to the impact of the W+jet background, the dominant background source. The chapter concludes with a study of the statistical significance of this measurement.

10.1 Results of the Fit to Data

According to the definition of the binned likelihood template fit in Ch. 7, the fit to data is performed. The concatenated observable distributions comprising all eight regions which enter the fit ("pre-fit") are shown in Fig. 10.1, the observable distributions based on the fit results with the best-fit templates ("post-fit") are illustrated in Fig. 10.2. For reasons of visibility, the eight analysis regions are split into two rows with the $|\eta| \leq 1$ region in the first row and the $|\eta| > 1$ region in the second. The agreement between data and the event yields improves after performing the fit, as expected. The observed differences in the individual bins are well-covered by the given statistical and systematic uncertainties included in the uncertainty bands. Further post-fit plots in the individual analysis regions are added to Appendix H.

The pre- and post-fit yields of the $t\bar{t}$ signal and all background sources are listed in Table 10.1. The relative differences between these two numbers with respect to the pre-fit values are also given in percentages and multiples of the standard deviation σ, which equals the normalisation uncertainties summarised in Table 7.3. Since eight individual fit parameters are used for the multijet background, the associated pre- and post-fit numbers as well as the relative differences are displayed separately in Table 10.2.

The pre- and post-fit yields agree very well, deviations are mostly below 1σ. Solely the post-fit numbers of two components of the W+jets background differ by more than 1σ from the initial pre-fit values. However, these discrepancies for two of the largest background contributions do not impact the final result significantly and thus do not cause a bias of the fit to data, as it is discussed and cross-checked in Sec. 10.2.

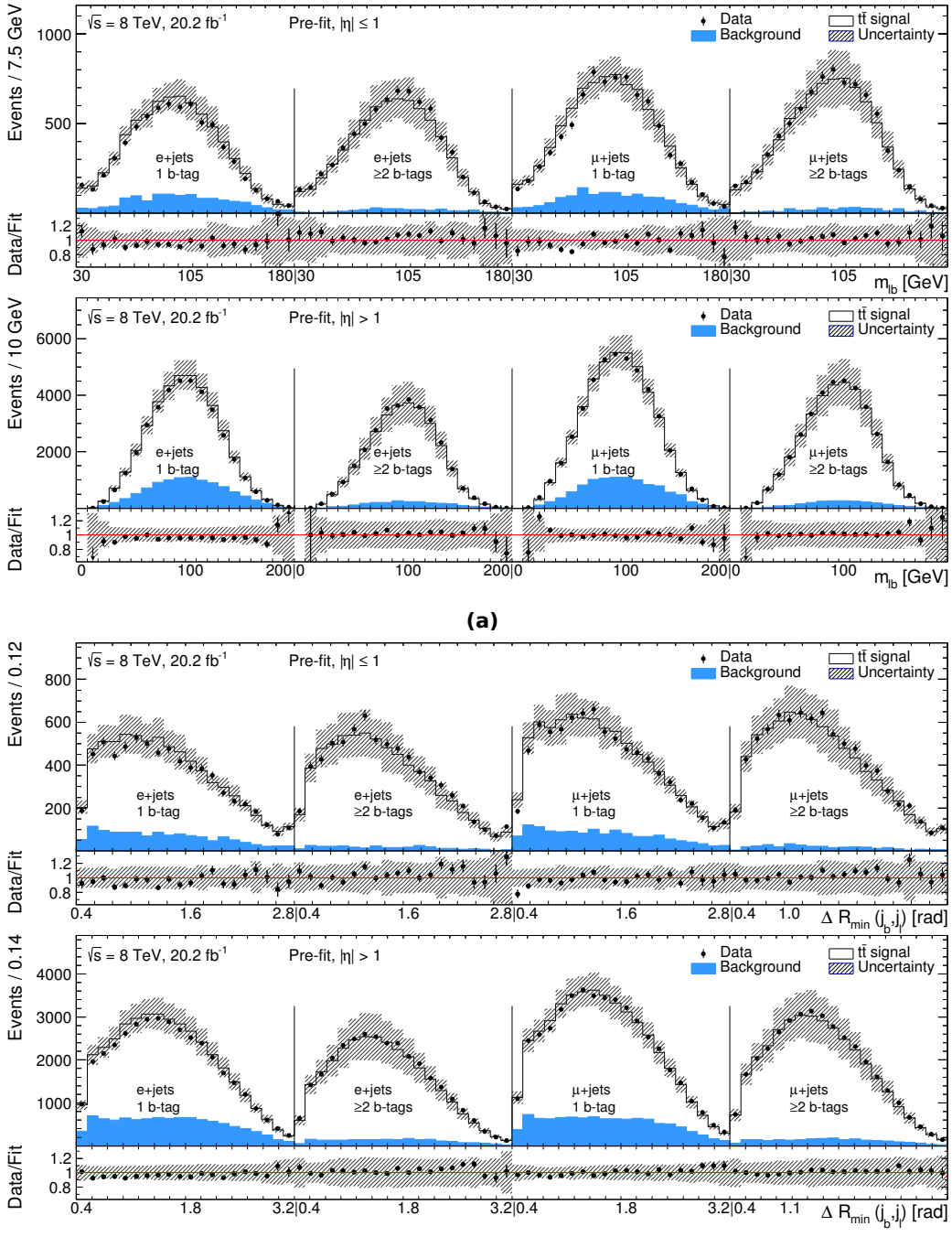

Figure 10.1: Pre-fit distributions based on the nominal templates with $\Gamma_t = 1.33$ GeV for both observables, (a) $m_{\ell b}$ and (b) $\Delta R_{\text{min}}(j_b, j_l)$, in all eight analysis regions corresponding to different lepton flavours, b-tag multiplicities and jet pseudorapidities. The lower panels show the ratio of data over the expected $t\bar{t}$ signal and background contributions, which are combined in the upper main panels. The vertical lines mark the boundaries between the binned observables in the lepton and b-tag regions. The hatched bands represent the total uncertainty. The systematic uncertainties are derived bin-by-bin based on the systematic variations by adding differences in quadrature. Finally, statistical and systematic uncertainties are added in quadrature to obtain the total uncertainty given in the bands.

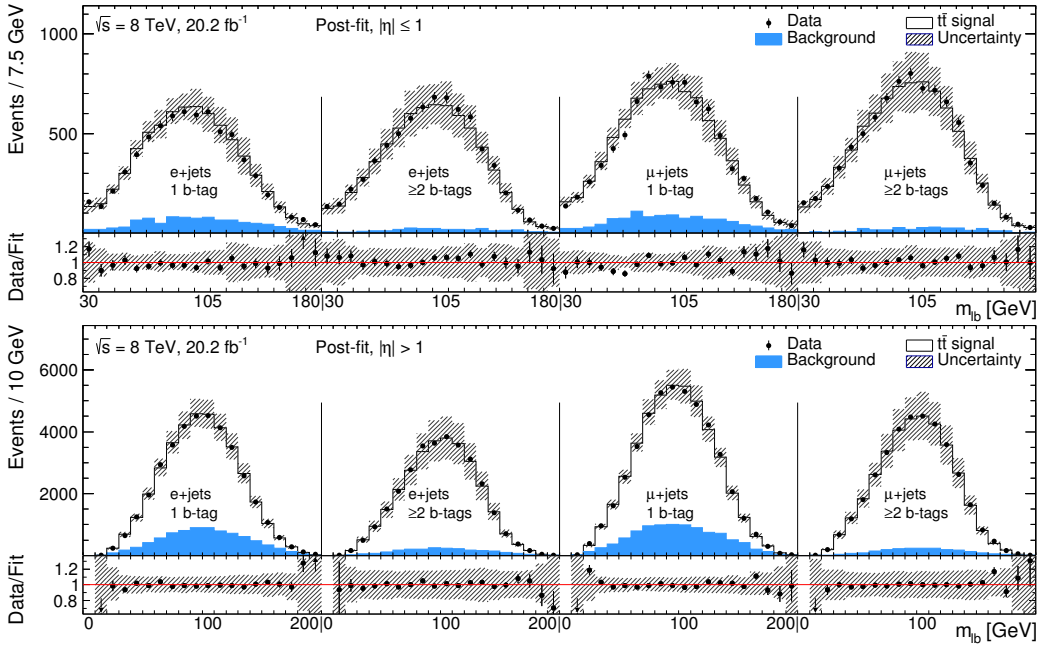

(a)

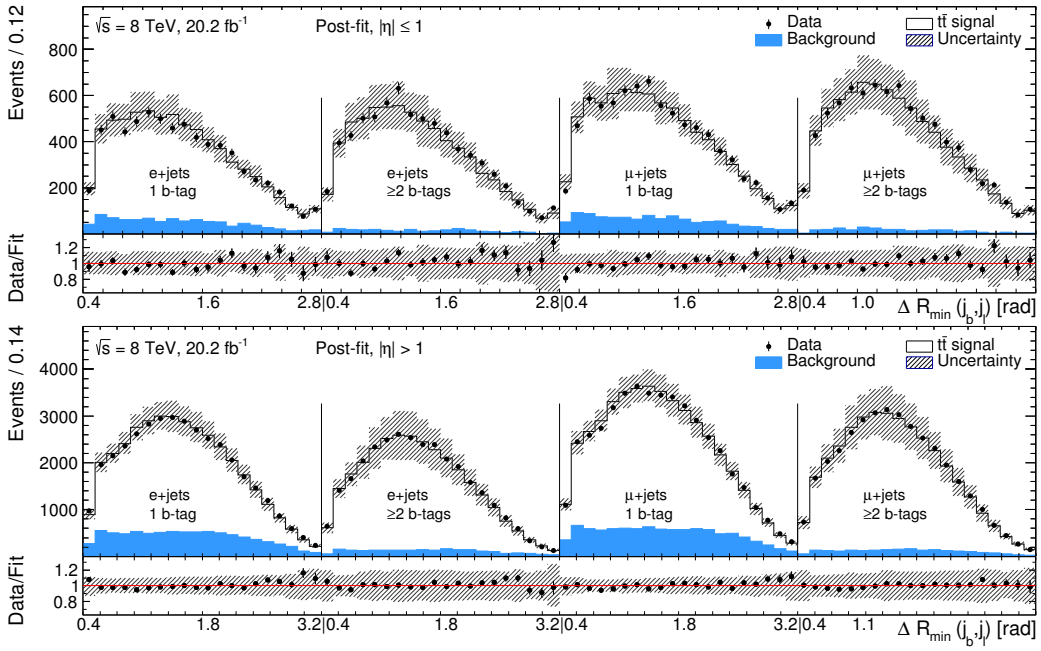

(b)

Figure 10.2: Post-fit distributions based on the best-fit templates for both observables, (a) $m_{\ell b}$ and (b) $\Delta R_{\text{min}}(j_b, j_l)$, in all eight analysis regions corresponding to different lepton flavours, b-tag multiplicities and jet pseudorapidities. The lower panels show the ratio of data over the expected $t\bar{t}$ signal and background contributions, which are combined in the upper main panels. The vertical lines mark the boundaries between the binned observables in the lepton and b-tag regions. The hatched bands represent the total uncertainty. The systematic uncertainties are derived bin-by-bin based on the systematic variations by adding differences in quadrature. Finally, statistical and systematic uncertainties are added in quadrature to obtain the total uncertainty given in the bands.

Sample	Pre-fit yields	Post-fit yields	Rel. difference	Rel. difference [σ]
$t\bar{t}$	153138 ± 9847	156363 ± 750	+2.1%	+0.33
Single top	6731 ± 1144	5704 ± 925	-15.3%	-0.90
W+$b\bar{b}/c\bar{c}$	8381 ± 922	7063 ± 507	-15.7%	-1.43
W+c	3363 ± 908	1650 ± 550	-50.9%	-1.89
W+light	1629 ± 65	1603 ± 81	-1.6%	-0.40
Z+jets	2521 ± 1210	2772 ± 710	+10.0%	+0.21
Diboson	522 ± 251	322 ± 241	-38.3%	-0.80
Multijet	5810 ± 1739	6074 ± 377	+4.5%	+0.15
Total	182083 ± 10160	181551 ± 1640	-0.3%	-0.05

Table 10.1: Pre-fit and post-fit yields for $t\bar{t}$ signal and all background contributions. The given numbers represent the sum of the yields in the eight analysis regions. Relative differences between pre-fit and post-fit yields are calculated with respect to the pre-fit uncertainties and presented in percentage and in σ, corresponding to the normalisation uncertainties as listed in Table 7.3.

Multijet in region	Pre-fit yields	Post-fit yields	Rel. difference	Rel. difference [σ]
e, 1 b-tag, $\|\eta\| \leq 1$	228 ± 69	98 ± 45	-57.0%	-1.88
e, 1 b-tag, $\|\eta\| > 1$	2493 ± 748	1845 ± 269	-26.0%	-0.87
e, $\geq$2 b-tags, $\|\eta\| \leq 1$	41 ± 12	43 ± 12	+4.9%	+0.17
e, $\geq$2 b-tags, $\|\eta\| > 1$	538 ± 162	704 ± 101	+30.9%	+1.02
μ, 1 b-tag, $\|\eta\| \leq 1$	195 ± 59	127 ± 43	-34.9%	-1.15
μ, 1 b-tag, $\|\eta\| > 1$	1873 ± 562	2742 ± 216	+46.4%	+1.55
μ, $\geq$2 b-tags, $\|\eta\| \leq 1$	46 ± 14	50 ± 13	+8.7%	+0.29
μ, $\geq$2 b-tags, $\|\eta\| > 1$	399 ± 120	465 ± 91	+16.5%	+0.55
Total	5810 ± 1739	6074 ± 377	+4.5%	+0.15

Table 10.2: Pre-fit and post-fit yields for the multijet background in the individual eight analysis regions with the eight fit parameters. Relative differences between pre-fit and post-fit yields are calculated with respect to the pre-fit uncertainties and presented in percentage and in σ, corresponding to the normalisation uncertainty of 30%.

The predicted number of $t\bar{t}$ signal events in the lepton+jets decay channel corresponds to a cross-section of $\sigma_{t\bar{t}} = 253^{+15}_{-16}$ pb [64–68]. The post-fit value obtained from the fit leads to a measured $t\bar{t}$ cross-section of 258.3 pb, well within the uncertainties of the theoretical prediction.

The likelihood curve coming from the fit with the resulting likelihood values for all 55 utilised templates is illustrated in Fig. 10.3a. The region around the minimum is highlighted in Fig. 10.3b, including a quadratic fit to the likelihood points which follow the parabolic shape well. The likelihood values are given as twice the negative logarithm and shifted so that the minimum corresponds to $-2\Delta\ln(\mathscr{L}) = 0$. This allows for the extraction of the statistical uncertainty which comprises contributions from the data statistics and the uncertainties in the normalisation of all backgrounds, according to the definition of the fit in Sec. 7.3. The uncertainty is derived from the width of the fitted likelihood curve at $-2\Delta\ln(\mathscr{L}) = 1$ around the minimum.

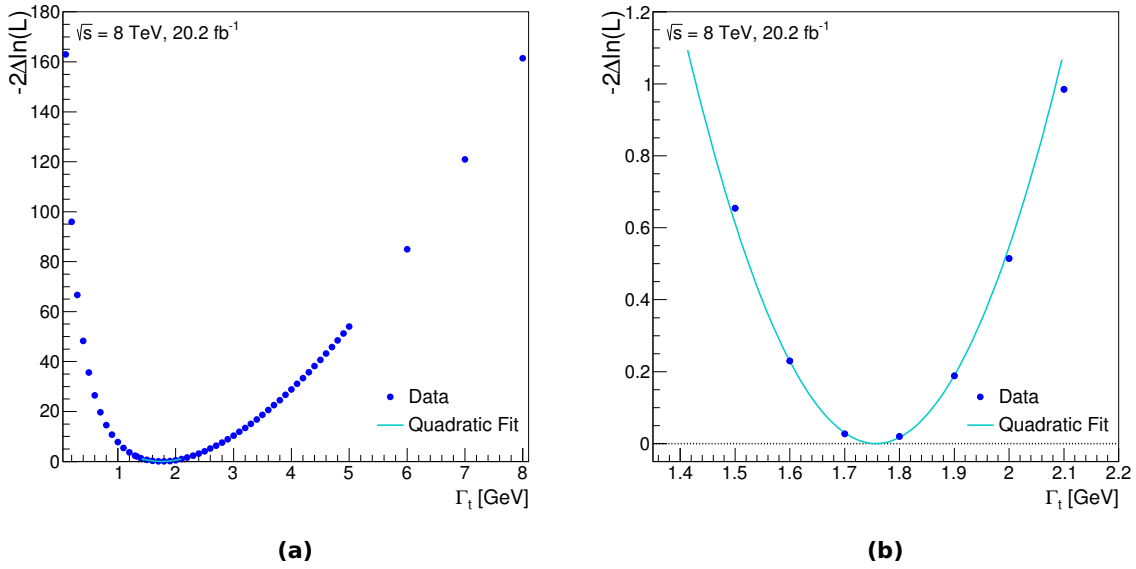

Figure 10.3: Likelihood curves obtained from the binned likelihood template fit to data: Twice the negative logarithm of the likelihood given for (a) the full range of available decay width templates and (b) around the fitted minimum to demonstrate the parabolic behaviour. Thus, a quadratic fit is performed around the minimum. Both plots show the same fitted curve restricted to the smallest likelihood values.

The fitted curve is also shown in Fig. 10.3a, restricted to the area close to the minimum. Distortions of this shape are caused by the edge of decay width values at 0 GeV, leading to the distinct slope in the left part of the parabola. Since the shape is symmetric in the range around the minimum which covers the size of individual systematic effects and the statistical uncertainty, these shape differences for very small decay width values do not bias the result, as already verified by the pull distribution studies whose results are shown in Fig. 7.8a.

The decay width measured for a top quark mass of 172.5 GeV used in the signal templates amounts to:

$$\Gamma_t = 1.76 \pm 0.33\ (\text{stat.})\ ^{+0.79}_{-0.68}\ (\text{syst.})\ \text{GeV} = 1.76^{+0.86}_{-0.76}\ \text{GeV}\,.$$

This result is in good agreement with the Standard Model expectation of 1.322 GeV using available NLO and NNLO corrections [172] and well-covered by the statistical and systematic uncertainties determined for this analysis. All systematic uncertainties entering this final result are listed in Table 8.7.

The measurement was repeated in individual b-tag and observable regions to confirm that the measured central value is consistent within the statistical uncertainty. The relevance of adding events with only one b-tagged jet is proven in Sec. 9.4, leading to significantly smaller systematic uncertainties compared to a fit using only the analysis regions with at least two b-tagged jets.
The impact of the cut applied to the logarithm of the KLFitter likelihood is also covered by the statistical uncertainty.
A fit utilising merely the observable $m_{\ell b}$ results in total uncertainties that are about 0.3 GeV larger than the ones for the chosen fit configuration, in compliance with the studies presented in Ch. 9.

A comparison with previous direct measurements of Γ_t, outlined in Sec. 2.3.2, reveals that the total uncertainty evaluated for this ATLAS measurement is by a factor of two smaller than the one quoted by the CDF Collaboration [14] and of a similar order of the preliminary result by the CMS Collaboration [15].

Although the final fit configuration yields, in comparison to other shown setups, satisfactory results, it is still less precise than indirect measurements. Hence, it is not yet possible to rule out alternative BSM models, predicting Γ_t values different from the SM expectation, as briefly discussed in Sec. 2.3.3, with the currently achieved sensitivity.

The Γ_t templates used for this fit to data rely on a top quark mass of $m_t = 172.5$ GeV, and the quoted result is given for this mass value since observables which are very sensitive to the top quark decay width are by construction also sensitive to the top quark mass. The detailed studies in Sec. 8.6 indicated that the most reliable approach to estimate the relationship between m_t and Γ_t in a range close to this nominal mass value is obtained from a template morphing procedure. A shift in the decay width of up to 0.2 GeV could be inferred from this method, based on a mass variation of ±0.5 GeV around the nominal value.

10.2 Impact of the W+Jets Background

The post-fit yields of two components of the W+jets background differ by more than 1σ from the pre-fit values, as listed in Table 10.1, although the W+jets yield is based on a data-driven estimate. This section is dedicated to evaluate the impact of such discrepancies in the yields on the final result.

As a first study, the fit was reperformed with additional nuisance parameters for the normalisation of the W+jets background components. Instead of only one fit parameter for each of the three W+jets components, fit parameters were defined for the individual analysis regions, equivalent to the procedure applied to the multijet background. Two options were tested: (a) As differences between the electron+jets and the muon+jets channel are not expected, four fit parameters are used for each of the three W+jets components, i.e. one parameter for each of the two $|\eta|$ and the two b-tag regions. (b) Eight fit parameters for all eight analysis regions and all three W+jets contributions enter the binned likelihood fit, corresponding to the number of fit parameters used for the multijet background. The results of both approaches, (a) and (b), are consistent, the fitted central values of Γ_t are shifted by approximately 0.07 GeV with respect to the nominal fit result quoted in the last section, i.e. the measured value amounts to $\Gamma_t = 1.69$ GeV.
The deviation from the expectation of the normalisation of the $W+b\bar{b}/c\bar{c}$ and $W+c$ components reduces from 1.4σ and 1.9σ to values around 0.7σ. However, the reduced shifts in the yields of these two background components are compensated by other smaller background sources. The $t\bar{t}$ signal yield is stable but differences between the pre- and post-fit yields rise above 1σ for the single top and Z+jets backgrounds. Hence, applying more fit parameters to account for the differences in the W+jets background yields does not change the fit result significantly and deviations are still present or even larger for other background sources. The obtained yields for a fit setup with eight parameters per W+jets component are summarised in Table 10.3. The resulting numbers are similar to the ones for the option with four fit parameters per contribution, according to the initial expectation.

One test realised for the multijet background can also be redone for the W+jets components. For the estimate of the multijet background, a parametrisation of the jet pseudorapidity is not available because the impact is expected to be minor. But in order to parametrise the fake efficiencies used for the multijet background estimation with the matrix method, lepton p_{T} and η are actually used. Since the multijet events are decorrelated between the analysis regions, the fake estimate is effectively η-dependent within the assigned uncertainty of 30%. To verify that the effect is indeed negligible for this analysis, the uncertainty was increased to 90% and the central value of the fitted decay width changed by merely 0.04 GeV.
In a similar fashion, the Gaussian constraints on the W+jets components were increased by a factor of three for the above introduced setup with eight fit parameters per region and W+jets contribution. The performed fit shows hardly any change, the fitted central value of Γ_t shifts by less than 0.03 GeV.

Sample	Pre-fit yields	Post-fit yields	Rel. difference	Rel. difference [σ]
$t\bar{t}$	153138 ± 9847	156213 ± 752	+2.0%	+0.31
Single top	6731 ± 1144	4977 ± 905	-26.1%	-1.53
W+$b\bar{b}/c\bar{c}$	8381 ± 922	7749 ± 287	-7.5%	-0.69
W+c	3363 ± 908	2689 ± 394	-20.0%	-0.74
W+light	1629 ± 65	1622 ± 49	-0.4%	-0.11
Z+jets	2521 ± 1210	2300 ± 703	-8.8%	-0.18
Diboson	522 ± 251	249 ± 240	-52.3%	-1.09
Multijet	5810 ± 1739	5769 ± 449	-0.7%	-0.02
Total	182083 ± 10160	181568 ± 1542	-0.3%	-0.05

Table 10.3: Pre-fit and post-fit yields for $t\bar{t}$ signal and all background contributions for the fit option with eight fit parameters for each of the three W+jets background components. The given numbers represent the sum of the yields in the eight analysis regions. Relative differences between pre-fit and post-fit yields are calculated with respect to the pre-fit uncertainties and presented in percentage and in σ, corresponding to the respective normalisation uncertainties.

To substantiate that the changes of the W+jets background yields do not influence or bias the final result, variations of the individual W+jets components were investigated. The following options were studied: (a) A fit with all three W+jets components fixed while other backgrounds are allowed to vary as in the default setup, (b) only W+$b\bar{b}/c\bar{c}$ fixed, (c) only W+c fixed, and (d) only W+light fixed. For the options (b)-(d) all other fit parameters vary as in the default fit configuration. The results are shown in Table 10.4, listing the fitted values of the decay width and the yields for the $t\bar{t}$ signal and the background components as well as the total yield.

Fit option:	Default fit to data	All W+jets fixed	Only W+$b\bar{b}/c\bar{c}$ fixed	Only W+c fixed	Only W+light fixed
Γ_t [GeV]	1.76 ± 0.33	1.71 ± 0.31	1.70 ± 0.32	1.78 ± 0.33	1.76 ± 0.34
W+$b\bar{b}/c\bar{c}$	7063 ± 507	8381 ± 922	8381 ± 922	6594 ± 484	7059 ± 507
W+c	1650 ± 550	3363 ± 908	1223 ± 525	3363 ± 908	1642 ± 549
W+light	1603 ± 81	1629 ± 65	1597 ± 81	1589 ± 81	1629 ± 65
Single top	5704 ± 905	4198 ± 870	5364 ± 915	5000 ± 898	5697 ± 925
Z+jets	2772 ± 710	1801 ± 678	2613 ± 706	2262 ± 690	2770 ± 710
Diboson	322 ± 241	146 ± 238	285 ± 240	238 ± 239	322 ± 241
Multijet	6074 ± 377	5468 ± 356	5962 ± 374	5763 ± 364	6068 ± 376
$t\bar{t}$	156363 ± 750	156602 ± 737	156137 ± 746	156756 ± 739	156366 ± 750
Total	181551 ± 1640	181588 ± 1903	181562 ± 1795	181565 ± 1756	181553 ± 1638

Table 10.4: Different fitted decay width values Γ_t (given with statistical uncertainties) obtained from a fit to data to estimate the influence of the three W+jets background components on the final result. The post-fit yields of each W+jets component are listed first, followed by other background contributions, the signal and the total event yields. The given numbers represent the sum of the yields in each of the eight analysis regions. The compared options are explained in more detail in the text, the first column refers to the standard option as displayed in Table 10.1.

The obtained values of Γ_t indicate only slight shifts of the fit result. Depending on the chosen option,

the changes are within a range of 0.08 GeV close to the result of the original fit configuration with $\Gamma_t = 1.76$ GeV. A comparison of the individual numbers illustrate that fixed W+jets components are compensated by other small background sources so that the $t\bar{t}$ signal yield as well as the total yield are relatively stable and result in fitted values close to the original setup.

To conclude, the discrepancies between pre- and post-fit yields for dominant W+jets background contributions do not bias the outcome of the fit. The different tested configurations reveal changes in the final result of not more than 25% of the statistical uncertainty. Consequently, the effect of the fitted W+jets yields on the result is small and proven to be not significant.

10.3 Statistical Significance

In an additional and final analysis step, the statistical significance is estimated to verify that indeed a non-zero decay width of the top quark is measured. For this purpose, a p-value is extracted based on ensemble tests as a measure of the statistical significance. As the Γ_t measurement is performed with templates based on positive decay width values, p-values are determined for such values of $\Gamma_t > 0$ GeV and extrapolated to zero. Templates for $\Gamma_t = 0$ GeV were not generated as such a decay width value is not physical and, thus, only positive decay width values were considered for the reweighting based on Breit-Wigner distributions.

Systematic uncertainties are included in this evaluation. The input distribution for each single pseudo-experiment is randomly changed pursuant to the sources of systematic uncertainty. Random numbers for the individual components of systematic uncertainties are used to choose the corresponding systematic source, and the input distribution entering the fit is modified accordingly. Based on such pseudo-data distributions, the fit is performed following the regular procedure for pseudo-experiments, as described in Sec. 7.4, with the default fit configuration.

The resulting fitted Γ_t values from the pseudo-experiments are filled into a histogram used to calculate the p-value. This value is defined as the the integral from the observed decay width in data, $\Gamma_t = 1.76$ GeV, to infinity of the corresponding normalised pseudo-data distribution. This is illustrated by the normalised histogram for an example input decay width in Fig. 10.4a. Input values of the decay width are $\Gamma_t = 0.2, 0.3, 0.4, 0.5, 0.6, 0.7$ GeV as well as $\Gamma_t = 1.8$ GeV, which complies with the decay width of the template closest to the result of the fit to data. For each value of Γ_t, 50,000 pseudo-experiments were carried out and the p-values were determined from the resulting histograms. The obtained p-values are visualised in Fig. 10.4b. According to the theory expectation, such p-values follow a Gauss error function, which was fitted to the derived values.

The fitted curve describes the measured points well and can be extrapolated to extract a p-value for a decay width of zero in order to circumvent the non-existence of templates at $\Gamma_t = 0$ GeV. The function yields a p-value of 0.0035 for $\Gamma_t = 0$ GeV which corresponds to a significance of 2.7σ. Since the integral is calculated from $\Gamma_t = 1.76$ GeV to infinity, the Gaussian-shaped distribution

obtained from the pseudo-experiments for an input decay width of $\Gamma_t = 1.8$ GeV has a p-value of around 0.5, as presented in Fig. 10.4a.

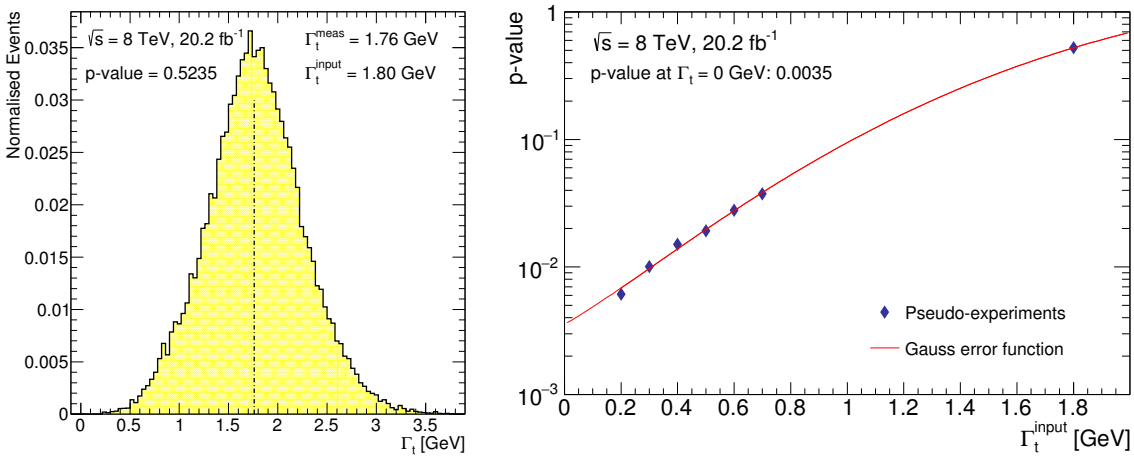

(a) **(b)**

Figure 10.4: Results from pseudo-experiments to extract a p-value as a measure of the statistical significance to measure a non-zero decay width. (a) Normalised histogram containing the fitted decay width values from 50,000 pseudo-experiments based on an input decay width value of 1.8 GeV. The black, dashed line corresponds to the measured value of 1.76 GeV which defines the lower limit of the integral to extract the p-value, as explained in the text. (b) Illustration of p-values obtained from pseudo-experiments for different values of $\Gamma_t > 0$ GeV including a fit with a Gauss error function to extrapolate to the desired value of zero.

For the three smallest considered decay width values of $\Gamma_t = 0.2, 0.3, 0.4$ GeV, the resulting distributions from the pseudo-experiments reveal a two-peak structure. This is due to the inclusion of systematic uncertainties which cause such shape effects close to the natural edge of 0 GeV. If these three values are removed from the Gauss error function fit of Fig. 10.4b, the measured p-value for a decay width of zero decreases to 0.009, which is equivalent to a significance of around 3.1σ, a similar significance value as obtained for the more conservative approach above.
From this one can infer that a true decay width value close to 0 GeV is unlikely, very consistent with the measured central value of $\Gamma_t = 1.76$ GeV and its uncertainties, as quoted in Sec. 10.1.

11 Summary and Conclusion

This thesis presented a direct measurement of the decay width of the top quark with ATLAS data. Due to the unique properties of the top quark, a large variety of precision measurements has been performed in the past few years in the field of top quark physics. The top quark decay width Γ_t, however, is one of the fundamental properties which has not been measured with a high precision directly yet. An important motivation for such a direct measurement is a reduced dependence on Standard Model assumptions in comparison to indirect approaches which rely on SM predictions for partial top quark decay widths or single top t-channel cross-sections and presume certain branching ratios. A direct measurement is therefore based on far less assumptions leading to a potential sensitivity to BSM physics.
Nevertheless, performing such a direct measurement is very demanding which is why, in particular, indirect measurements of Γ_t have been published in the last years. Hence, a pivotal part of this thesis was devoted to the finding and the optimisation of a well-suited and sophisticated analysis setup to extract the decay width out of the given dataset and ease the effort of such a measurement. The first part of this final chapter focuses on summarising the obtained results and concluding the thesis with an emphasis on the relevant and most challenging aspects of this analysis while the second part is dedicated to an outlook covering prospects for future direct measurements of the top quark decay width.

11.1 Summary of the Obtained Results

The performed measurement of the decay width of the top quark is based on LHC proton-proton collision data recorded with the ATLAS detector at a centre-of-mass energy of $\sqrt{s} = 8$ TeV, corresponding to an integrated luminosity of 20.2 fb^{-1}, and exploits $t\bar{t}$ events in the lepton+jets channel with one hadronically and one leptonically decaying top quark.
The measurement was realised by using a binned likelihood template fit to data which rests on two observables related to the hadronic and the leptonic decay branch of $t\bar{t}$ events to extract Γ_t. The templates that enter the likelihood fit were generated by a reweighting method. One observable originates from the hadronic decay branch while the other depends on quantities of the leptonically decaying top quark. The first observable with a good sensitivity to Γ_t is $m_{\ell b}$, the reconstructed invariant mass of the system formed by the b jet associated with the leptonically decaying top quark and the charged lepton ℓ. The second observable, which serves to significantly constrain systematic uncertainties in the combination with $m_{\ell b}$, is $\Delta R_{\text{min}}(j_b, j_l)$, the angular distance between the b jet j_b associated with the hadronic top quark and the closest light jet j_l from the hadronically decaying

W boson. The events entering the fit were split into events where the charged lepton is either an electron or a muon, into events where exactly one or at least two jets are tagged as originating from a b quark and into two pseudorapidity regions in order to obtain a region which suffers less from detector resolution effects and pile-up contributions. Thus, concatenated distributions composed of eight individual regions constitute the templates employed in the likelihood fit.
The fit to data yielded a decay width of

$$\Gamma_t = 1.76 \pm 0.33\ (\text{stat.})\ ^{+0.79}_{-0.68}\ (\text{syst.})\ \text{GeV} = 1.76^{+0.86}_{-0.76}\ \text{GeV}$$

for $m_t = 172.5$ GeV, which agrees well with SM predictions and represents the first direct decay width measurement of the top quark with the ATLAS detector.

The evaluated total uncertainty is by a factor of two smaller than the latest one published by the CDF Collaboration [14] and of a similar order of the preliminary result quoted by the CMS Collaboration [15]. Despite such a satisfactory uncertainty, the direct measurements are still less precise than indirect ones so that the currently achieved sensitivity is not sufficient yet to support or rule out alternative BSM models, predicting decay width values of the top quark which are different from the SM expectation. Due to the limited detector precision and resolution of objects used to define observables, the measured values constitute the best possible result currently reachable.

A first task of the analysis involved the development of the fit framework to conduct the binned likelihood template fit in one or two dimensions with one or two observables fitted simultaneously. The performance and strength of the self-implemented code relying on dedicated ROOT and RooFit commands was examined in detail and the chosen fit setup was tested with its distinct features extensively, as summarised in Ch. 7. The fit method was validated successfully using calibration curves and pull distributions following the presumed behaviour, and very acceptable statistical uncertainties could be derived, indicating a good sensitivity to Γ_t.

The analysis challenges do not only comprise the implementation of the fit framework and its validation but also detailed studies on systematic uncertainties. According to the above quoted result of Γ_t, the total uncertainty is dominated by systematic uncertainties. Consequently, a relevant part of the thesis was dedicated to understand and reduce dominant systematic uncertainties. As described in Ch. 8, a new treatment of the uncertainty related to the jet flavour composition was employed to decrease the size of the dominant JES uncertainty, and a separate section delineated the understanding of the large uncertainty due to ISR and FSR. Substantial studies served to investigate the impact of NLO and off-shell effects in the top quark decay and the impact of the top quark mass, which is both important for future measurements, as outlined in the next section below. Variations of the top quark mass of ±0.5 GeV shifted Γ_t by around 0.2 GeV while approaches to estimate the impact of the missing description of NLO and off-shell effects in the current MC samples yielded values of around or less than 0.5 GeV.
In Ch. 9, the focus was laid on finding an adequate analysis configuration in order to reduce

dominant systematic uncertainties to a significant extent. This included the choice of observables, the split of analysis regions by jet pseudorapidity or energy and further analysis cuts. Moreover, the optimisation of the fit setup was also carried out with respect to the KLFitter configuration utilised to reconstruct the $t\bar{t}$ events for this measurement. The comparison studies, taking the observable modelling into account, verified that the fit configuration with the two fit observables $m_{\ell b}$ and $\Delta R_{\mathrm{min}}(j_b, j_l)$ and the eight exclusive analysis regions yield the most promising results. This substantiates the potential of these comprehensive studies to reduce systematic uncertainties and to optimise event reconstruction efficiencies.
The obtained results allow to deduce that the general analysis strategy with the underlying implementation of a template fit is very well suited to access the top quark decay width. However, there is still room for possible modifications in future measurements which is addressed in the following.

11.2 Outlook

Future direct measurements of the top quark decay width will profit from the intensive studies performed in the course of the analysis presented in this thesis. The basic analysis strategy using a template fit to extract Γ_t will also be a valuable choice for a measurement using, for instance, $\sqrt{s} = 13$ TeV data, corresponding to the current centre-of-mass energy of the LHC.

In due consideration of the obtained results, potential modifications are primarily useful in the context of the evaluation of systematic uncertainties. The approach of determining systematic uncertainties using pseudo-experiments was widely used in the field of top quark physics in analyses based at $\sqrt{s} = 8$ TeV. Latest measurements at $\sqrt{s} = 13$ TeV, however, applied profile likelihood fits with nuisance parameters as additional fit parameters to estimate systematic uncertainties directly during the fit. This method of constraining systematic uncertainties in the measurement may lead to a further reduction of the corresponding uncertainties. For each considered systematic effect, such a nuisance parameter is added. The size of the corresponding systematic uncertainty is adjusted by these parameters since the fitted values from the fit constitute the values which best fit the data.
Initial studies at $\sqrt{s} = 8$ TeV in order to constrain the radiation systematic uncertainty by such an approach with nuisance parameters were conducted and led to promising results.
With an updated description of the uncertainty due to ISR and FSR for $\sqrt{s} = 13$ TeV analyses, such a profile likelihood fit may even yield acceptable results for observables that suffered heavily from the radiation uncertainty in this measurement, as shown in Ch. 9.
Further prospects for a future measurement also include updated configurations of the event reconstruction with KLFitter. Because of the above mentioned uncertainty due to ISR and FSR, the event reconstruction was carried out with exactly four jets in the event reconstruction step. With an updated description of the radiation uncertainty, the usage of at least five jets for the event reconstruction or further analysis cuts in combination with new KLFitter transfer functions for $\sqrt{s} = 13$ TeV may be applicable and increase the reconstruction efficiencies further.
Additional optimisations regarding the choice of the observables, the number of utilised b-tag

regions or the $t\bar{t}$ decay channel can be considered in the future as well. In the analysis presented here, analysis regions composed of events with exactly one b-tag were added as this constrained dominant systematic uncertainties to a higher degree. If future analyses are not affected in a similar way, a Γ_t measurement can be performed with events having at least two b-tagged jets to improve the purity of the sample by further reducing the fraction of background events. Apart from that, more sophisticated b-taggers and even c-tagging algorithms are and will be available for future measurements, facilitating the identification of those jets. The IBL, as the new innermost part of the ATLAS detector, will improve the corresponding efforts. Since $m_{\ell b}$ offers a good sensitivity to Γ_t while suffering less from systematic uncertainties, a fit configuration using the dilepton $t\bar{t}$ channel can be contemplated as well.
Special emphasis needs to be put on the impact of the top quark mass and the missing NLO precision comprising off-shell effects in the $t\bar{t}$ decay. For a more precise evaluation of those effects, it will be beneficial to have alternative MC samples with masses close to the current nominal value of $m_t = 172.5$ GeV and an MC simulation that provides an NLO description of the $t\bar{t}$ decay, also accounting for off-shell effects. This will eliminate the need for the elaborate studies required to roughly estimate such effects for this measurement at $\sqrt{s} = 8$ TeV.

The consideration of such analysis items for future direct Γ_t measurements may lead to an improvement of the precision reached in this thesis and may in particular allow for a more reliable evaluation of the impact of NLO and off-shell effects in the top quark decay and the influence of the top quark mass. The results shown in this thesis obtained after intensive studies and comparisons correspond to the currently best available estimate.

A significant fraction of fundamental studies and test setups established in the framework of this measurement can be used for future approaches. In this thesis, a template fit associated with well-motivated observables and adequate analysis regions was proven to provide an excellent opportunity to perform precision measurements and access underlying quantities like the top quark decay width although the limited detector resolution of objects needed to design potential observables translates into observable resolutions which are around one order of magnitude larger.

A Monte Carlo Samples

This appendix comprises a list of MC samples used for the distributions of $t\bar{t}$ signal events and the different background contributions.

$t\bar{t}$ Signal Samples

Nominal signal sample

mc12_8TeV.110404.PowhegPythia_P2011C_ttbar_hdamp172p5[...]NTUP_COMMON.e3151_s1773_s1776_r4485_r4540_p1575

Samples required to estimate systematic signal model uncertainties

Nominal sample based on a fast simulation

mc12_8TeV.110404.PowhegPythia_P2011C_ttbar_hdamp172p5_nonallhad.merge.NTUP_COMMON.e3151_a220_a205_r4540_p1575

Nominal sample with $h_{\mathbf{damp}} = \infty$, full and fast simulation

mc12_8TeV.117050.PowhegPythia_P2011C_ttbar.merge.NTUP_COMMON.e1728_s1581_s1586_r3658_r3549_p1575
mc12_8TeV.117050.PowhegPythia_P2011C_ttbar.merge.NTUP_COMMON.e1727_a188_a171_r3549_p1575

Samples used to estimate the radiation uncertainty

mc12_8TeV.110407.PowhegPythia_P[...]2012radLo_ttbar_hdamp172p5[...]NTUP_COMMON.e3876_a220_a263_a264_r4540_p1770
mc12_8TeV.110408.PowhegPythia_P[...]2012radHi_ttbar_hdamp345p0[...]NTUP_COMMON.e3876_a220_a263_a264_r4540_p1770

Samples used to estimate the colour reconnection and the underlying event uncertainty

mc12_8TeV.117426.PowhegPythia_P2012loCR_TTbar.merge.NTUP_COMMON.e2710_a220_a205_r4540_p1575
mc12_8TeV.117429.PowhegPythia_P2012mpiHi_TTbar.merge.NTUP_COMMON.e2710_a220_a205_r4540_p1575
mc12_8TeV.117428.PowhegPythia_P2012_TTbar.merge.NTUP_COMMON.e2710_a220_a205_r4540_p1575

Samples used to estimate the ME generator and the parton shower uncertainty

mc12_8TeV.105200.McAtNloJimmy_CT10_ttbar_LeptonFilter.merge.NTUP_COMMON.e1513_a159_a171_r3549_p1575
mc12_8TeV.105860.PowhegJimmy_AUET2CT10_ttbar_LeptonFilter.merge.NTUP_COMMON.e1576_a159_a171_r3549_p1575

Samples based on alternative top quark masses

mc12_8TeV.117840.TTbar_MT1700_nonallhad_PowHeg_Pythia[...]NTUP_COMMON.e2051_s1581_s1586_r3658_r3549_p1562
mc12_8TeV.117842.TTbar_MT1750_nonallhad_PowHeg_Pythia[...]NTUP_COMMON.e2051_s1581_s1586_r3658_r3549_p1562

Samples based on alternative top quark decay widths

mc12_8TeV.117272.PowhegPythia_P2011C_ttbar[...]_twidth0p7GeV.merge.NTUP_COMMON.e3168_a220_a205_r4540_p1575
mc12_8TeV.117273.PowhegPythia_P2011C_ttbar[...]_twidth3GeV.merge.NTUP_COMMON.e3168_a220_a205_r4540_p1575

Single Top Samples

mc12_8TeV.110090.PowhegPythia_P2011C_[...]tchan_lept_top[...]NTUP_COMMON.e2575_s1773_s1776_r4485_r4540_p1575
mc12_8TeV.110091.PowhegPythia_P2011C_[...]tchan_lept_antitop[...]NTUP_COMMON.e2575_s1773_s1776_r4485_r4540_p1575
mc12_8TeV.110119.PowhegPythia_P2011C_st_schan_lep.merge.NTUP_COMMON.e1720_s1581_s1586_r3658_r3549_p1575
mc12_8TeV.110140.PowhegPythia_P2011C_st_Wtchan_incl_DR.merge.NTUP_COMMON.e1743_s1581_s1586_r3925_r3549_p1575
mc12_8TeV.110142.PowhegPythia_P2011C_st_Wtchan_incl_DS.merge.NTUP_COMMON.e1743_s1581_s1586_r3925_r3549_p1575

Diboson Samples

mc12_8TeV.177997.Sherpa_CT10_llnunu_WW_MassiveCB.merge.NTUP_COMMON.e2098_s1581_s1586_r4485_r4540_p1575
mc12_8TeV.183734.Sherpa_CT10_WWtoenuqq_MassiveCB.merge.NTUP_COMMON.e2347_s1581_s1586_r4485_r4540_p1575
mc12_8TeV.183736.Sherpa_CT10_WWtomunuqq_MassiveCB.merge.NTUP_COMMON.e2347_s1581_s1586_r4485_r4540_p1575
mc12_8TeV.183738.Sherpa_CT10_WWtotaunuqq_MassiveCB.merge.NTUP_COMMON.e2347_s1581_s1586_r4485_r4540_p1575
mc12_8TeV.183586.Sherpa_CT10_ZZtoeeqq_MassiveCB.merge.NTUP_COMMON.e2370_s1581_s1586_r4485_r4540_p1575
mc12_8TeV.183588.Sherpa_CT10_ZZtomumuqq_MassiveCB.merge.NTUP_COMMON.e2370_s1581_s1586_r4485_r4540_p1575
mc12_8TeV.183590.Sherpa_CT10_ZZtotautauqq_MassiveCB.merge.NTUP_COMMON.e2370_s1581_s1586_r4485_r4540_p1575
mc12_8TeV.179975.Sherpa_CT10_lnununu_WZ_MassiveCB.merge.NTUP_COMMON.e2203_s1581_s1586_r4485_r4540_p1575
mc12_8TeV.183735.Sherpa_CT10_WZtoenuqq_MassiveCB.merge.NTUP_COMMON.e2347_s1581_s1586_r4485_r4540_p1575
mc12_8TeV.183737.Sherpa_CT10_WZtomunuqq_MassiveCB.merge.NTUP_COMMON.e2347_s1581_s1586_r4485_r4540_p1575
mc12_8TeV.183739.Sherpa_CT10_WZtotaunuqq_MassiveCB.merge.NTUP_COMMON.e2347_s1581_s1586_r4485_r4540_p1575
mc12_8TeV.183585.Sherpa_CT10_ZWtoeeqq_MassiveCB.merge.NTUP_COMMON.e2370_s1581_s1586_r4485_r4540_p1575
mc12_8TeV.183587.Sherpa_CT10_ZWtomumuqq_MassiveCB.merge.NTUP_COMMON.e2370_s1581_s1586_r4485_r4540_p1575
mc12_8TeV.183589.Sherpa_CT10_ZWtotautauqq_MassiveCB.merge.NTUP_COMMON.e2370_s1581_s1586_r4485_r4540_p1575
mc12_8TeV.189608.Sherpa_CT10_llll_ZZ_MassiveCB.merge.NTUP_COMMON.e2859_s1773_s1776_r4485_r4540_p1575
mc12_8TeV.185397.Sherpa_CT10_lllnu_WZ_l10_MassiveCB.merge.NTUP_COMMON.e2486_s1773_s1776_r4485_r4540_p1575
mc12_8TeV.179974.Sherpa_CT10_lllnu_WZ_MassiveCB.merge.NTUP_COMMON.e2203_s1581_s1586_r4485_r4540_p1575
mc12_8TeV.177999.Sherpa_CT10_llnunu_ZZ_MassiveCB.merge.NTUP_COMMON.e2136_s1581_s1586_r4485_r4540_p1680

W+Jets Samples

mc12_8TeV.147025.AlpgenPythia_Auto_P2011C_WenuNp0.merge.NTUP_COMMON.e1879_s1581_s1586_r3658_r3549_p1575
mc12_8TeV.147026.AlpgenPythia_Auto_P2011C_WenuNp1.merge.NTUP_COMMON.e1879_s1581_s1586_r3658_r3549_p1575
mc12_8TeV.147027.AlpgenPythia_Auto_P2011C_WenuNp2.merge.NTUP_COMMON.e1879_s1581_s1586_r3658_r3549_p1575
mc12_8TeV.147028.AlpgenPythia_Auto_P2011C_WenuNp3.merge.NTUP_COMMON.e1879_s1581_s1586_r3658_r3549_p1575
mc12_8TeV.147029.AlpgenPythia_Auto_P2011C_WenuNp4.merge.NTUP_COMMON.e1879_s1581_s1586_r3658_r3549_p1575
mc12_8TeV.147030.AlpgenPythia_Auto_P2011C_WenuNp5incl.merge.NTUP_COMMON.e1879_s1581_s1586_r3658_r3549_p1575
mc12_8TeV.147033.AlpgenPythia_Auto_P2011C_WmunuNp0.merge.NTUP_COMMON.e1880_s1581_s1586_r3658_r3549_p1575
mc12_8TeV.147034.AlpgenPythia_Auto_P2011C_WmunuNp1.merge.NTUP_COMMON.e1880_s1581_s1586_r3658_r3549_p1575
mc12_8TeV.147035.AlpgenPythia_Auto_P2011C_WmunuNp2.merge.NTUP_COMMON.e1880_s1581_s1586_r3658_r3549_p1575
mc12_8TeV.147036.AlpgenPythia_Auto_P2011C_WmunuNp3.merge.NTUP_COMMON.e1880_s1581_s1586_r3658_r3549_p1575
mc12_8TeV.147037.AlpgenPythia_Auto_P2011C_WmunuNp4.merge.NTUP_COMMON.e1880_s1581_s1586_r3658_r3549_p1575
mc12_8TeV.147038.AlpgenPythia_Auto_P2011C_WmunuNp5incl.merge.NTUP_COMMON.e1880_s1581_s1586_r3658_r3549_p1575
mc12_8TeV.147041.AlpgenPythia_Auto_P2011C_WtaunuNp0.merge.NTUP_COMMON.e1881_s1581_s1586_r3658_r3549_p1575
mc12_8TeV.147042.AlpgenPythia_Auto_P2011C_WtaunuNp1.merge.NTUP_COMMON.e1881_s1581_s1586_r3658_r3549_p1575
mc12_8TeV.147043.AlpgenPythia_Auto_P2011C_WtaunuNp2.merge.NTUP_COMMON.e1881_s1581_s1586_r3658_r3549_p1575
mc12_8TeV.147044.AlpgenPythia_Auto_P2011C_WtaunuNp3.merge.NTUP_COMMON.e1881_s1581_s1586_r3658_r3549_p1575
mc12_8TeV.147045.AlpgenPythia_Auto_P2011C_WtaunuNp4.merge.NTUP_COMMON.e1881_s1581_s1586_r3658_r3549_p1575
mc12_8TeV.147046.AlpgenPythia_Auto_P2011C_WtaunuNp5incl.merge.NTUP_COMMON.e1881_s1581_s1586_r3658_r3549_p1575

Dedicated $W+c\bar{c}$ Samples

mc12_8TeV.200156.AlpgenPythia_Auto_P2011C_WccNp0.merge.NTUP_COMMON.e2384_s1581_s1586_r3658_r3549_p1575
mc12_8TeV.200157.AlpgenPythia_Auto_P2011C_WccNp1.merge.NTUP_COMMON.e2384_s1581_s1586_r3658_r3549_p1575
mc12_8TeV.200158.AlpgenPythia_Auto_P2011C_WccNp2.merge.NTUP_COMMON.e2384_s1581_s1586_r3658_r3549_p1575

mc12_8TeV.200159.AlpgenPythia_Auto_P2011C_WccNp3incl.merge.NTUP_COMMON.e2384_s1581_s1586_r3658_r3549_p1575

Dedicated $W+c$ Samples

mc12_8TeV.200056.AlpgenPythia_Auto_P2011C_WcNp0.merge.NTUP_COMMON.e2384_s1581_s1586_r3658_r3549_p1575
mc12_8TeV.200057.AlpgenPythia_Auto_P2011C_WcNp1.merge.NTUP_COMMON.e2384_s1581_s1586_r3658_r3549_p1575
mc12_8TeV.200058.AlpgenPythia_Auto_P2011C_WcNp2.merge.NTUP_COMMON.e2384_s1581_s1586_r3658_r3549_p1575
mc12_8TeV.200059.AlpgenPythia_Auto_P2011C_WcNp3.merge.NTUP_COMMON.e2384_s1581_s1586_r3658_r3549_p1575
mc12_8TeV.200060.AlpgenPythia_Auto_P2011C_WcNp4incl.merge.NTUP_COMMON.e2384_s1581_s1586_r3658_r3549_p1575

Dedicated $W+b\bar{b}$ Samples

mc12_8TeV.200256.AlpgenPythia_Auto_P2011C_WbbNp0.merge.NTUP_COMMON.e2384_s1581_s1586_r3658_r3549_p1575
mc12_8TeV.200257.AlpgenPythia_Auto_P2011C_WbbNp1.merge.NTUP_COMMON.e2384_s1581_s1586_r3658_r3549_p1575
mc12_8TeV.200258.AlpgenPythia_Auto_P2011C_WbbNp2.merge.NTUP_COMMON.e2384_s1581_s1586_r3658_r3549_p1575
mc12_8TeV.200259.AlpgenPythia_Auto_P2011C_WbbNp3incl.merge.NTUP_COMMON.e2384_s1581_s1586_r3658_r3549_p1575

Z+Jets Samples

mc12_8TeV.147105.AlpgenPythia_Auto_P2011C_ZeeNp0.merge.NTUP_COMMON.e1879_s1581_s1586_r3658_r3549_p1575
mc12_8TeV.147106.AlpgenPythia_Auto_P2011C_ZeeNp1.merge.NTUP_COMMON.e1879_s1581_s1586_r3658_r3549_p1575
mc12_8TeV.147107.AlpgenPythia_Auto_P2011C_ZeeNp2.merge.NTUP_COMMON.e1879_s1581_s1586_r3658_r3549_p1575
mc12_8TeV.147108.AlpgenPythia_Auto_P2011C_ZeeNp3.merge.NTUP_COMMON.e1879_s1581_s1586_r3658_r3549_p1575
mc12_8TeV.147109.AlpgenPythia_Auto_P2011C_ZeeNp4.merge.NTUP_COMMON.e1879_s1581_s1586_r3658_r3549_p1575
mc12_8TeV.147110.AlpgenPythia_Auto_P2011C_ZeeNp5incl.merge.NTUP_COMMON.e1879_s1581_s1586_r3658_r3549_p1575
mc12_8TeV.147113.AlpgenPythia_Auto_P2011C_ZmumuNp0.merge.NTUP_COMMON.e1880_s1581_s1586_r3658_r3549_p1575
mc12_8TeV.147114.AlpgenPythia_Auto_P2011C_ZmumuNp1.merge.NTUP_COMMON.e1880_s1581_s1586_r3658_r3549_p1575
mc12_8TeV.147115.AlpgenPythia_Auto_P2011C_ZmumuNp2.merge.NTUP_COMMON.e1880_s1581_s1586_r3658_r3549_p1575
mc12_8TeV.147116.AlpgenPythia_Auto_P2011C_ZmumuNp3.merge.NTUP_COMMON.e1880_s1581_s1586_r3658_r3549_p1575
mc12_8TeV.147117.AlpgenPythia_Auto_P2011C_ZmumuNp4.merge.NTUP_COMMON.e1880_s1581_s1586_r3658_r3549_p1575
mc12_8TeV.147118.AlpgenPythia_Auto_P2011C_ZmumuNp5incl[...]NTUP_COMMON.e1880_s1581_s1586_r3658_r3549_p1575
mc12_8TeV.147121.AlpgenPythia_Auto_P2011C_ZtautauNp0.merge.NTUP_COMMON.e1881_s1581_s1586_r3658_r3549_p1575
mc12_8TeV.147122.AlpgenPythia_Auto_P2011C_ZtautauNp1.merge.NTUP_COMMON.e1881_s1581_s1586_r3658_r3549_p1575
mc12_8TeV.147123.AlpgenPythia_Auto_P2011C_ZtautauNp2.merge.NTUP_COMMON.e1881_s1581_s1586_r3658_r3549_p1575
mc12_8TeV.147124.AlpgenPythia_Auto_P2011C_ZtautauNp3.merge.NTUP_COMMON.e1881_s1581_s1586_r3658_r3549_p1575
mc12_8TeV.147125.AlpgenPythia_Auto_P2011C_ZtautauNp4.merge.NTUP_COMMON.e1881_s1581_s1586_r3658_r3549_p1575
mc12_8TeV.147126.AlpgenPythia_Auto_P2011C_ZtautauNp5incl.merge.NTUP_COMMON.e1881_s1581_s1586_r3658_r3549_p1575

Dedicated $Z+b\bar{b}$ Samples

mc12_8TeV.200332.AlpgenPythia_Auto_P2011C_ZeebbNp0.merge.NTUP_COMMON.e2384_s1581_s1586_r3658_r3549_p1575
mc12_8TeV.200333.AlpgenPythia_Auto_P2011C_ZeebbNp1.merge.NTUP_COMMON.e2384_s1581_s1586_r3658_r3549_p1575
mc12_8TeV.200334.AlpgenPythia_Auto_P2011C_ZeebbNp2.merge.NTUP_COMMON.e2384_s1581_s1586_r3658_r3549_p1575
mc12_8TeV.200335.AlpgenPythia_Auto_P2011C_ZeebbNp3incl.merge.NTUP_COMMON.e2384_s1581_s1586_r3658_r3549_p1575
mc12_8TeV.200340.AlpgenPythia_Auto_P2011C_ZmumubbNp0.merge.NTUP_COMMON.e2385_s1581_s1586_r3658_r3549_p1575
mc12_8TeV.200341.AlpgenPythia_Auto_P2011C_ZmumubbNp1.merge.NTUP_COMMON.e2385_s1581_s1586_r3658_r3549_p1575
mc12_8TeV.200342.AlpgenPythia_Auto_P2011C_ZmumubbNp2.merge.NTUP_COMMON.e2385_s1581_s1586_r3658_r3549_p1575
mc12_8TeV.200343.AlpgenPythia_Auto_P2011C_ZmumubbNp3incl[...]NTUP_COMMON.e2385_s1581_s1586_r3658_r3549_p1575
mc12_8TeV.200348.AlpgenPythia_Auto_P2011C_ZtautaubbNp0.merge.NTUP_COMMON.e2386_s1581_s1586_r3658_r3549_p1575
mc12_8TeV.200349.AlpgenPythia_Auto_P2011C_ZtautaubbNp1.merge.NTUP_COMMON.e2386_s1581_s1586_r3658_r3549_p1575
mc12_8TeV.200350.AlpgenPythia_Auto_P2011C_ZtautaubbNp2.merge.NTUP_COMMON.e2386_s1581_s1586_r3658_r3549_p1575
mc12_8TeV.200351.AlpgenPythia_Auto_P2011C_ZtautaubbNp3incl[...]NTUP_COMMON.e2386_s1581_s1586_r3658_r3549_p1575

Dedicated Z+$c\bar{c}$ Samples

mc12_8TeV.200432.AlpgenPythia_Auto_P2011C_ZeeccNp0.merge.NTUP_COMMON.e2384_s1581_s1586_r3658_r3549_p1575
mc12_8TeV.200433.AlpgenPythia_Auto_P2011C_ZeeccNp1.merge.NTUP_COMMON.e2384_s1581_s1586_r3658_r3549_p1575
mc12_8TeV.200434.AlpgenPythia_Auto_P2011C_ZeeccNp2.merge.NTUP_COMMON.e2384_s1581_s1586_r3658_r3549_p1575
mc12_8TeV.200435.AlpgenPythia_Auto_P2011C_ZeeccNp3incl.merge.NTUP_COMMON.e2384_s1581_s1586_r3658_r3549_p1575
mc12_8TeV.200440.AlpgenPythia_Auto_P2011C_ZmumuccNp0.merge.NTUP_COMMON.e2385_s1581_s1586_r3658_r3549_p1575
mc12_8TeV.200441.AlpgenPythia_Auto_P2011C_ZmumuccNp1.merge.NTUP_COMMON.e2385_s1581_s1586_r3658_r3549_p1575
mc12_8TeV.200442.AlpgenPythia_Auto_P2011C_ZmumuccNp2.merge.NTUP_COMMON.e2385_s1581_s1586_r3658_r3549_p1575
mc12_8TeV.200443.AlpgenPythia_Auto_P2011C_ZmumuccNp3incl[...]NTUP_COMMON.e2385_s1581_s1586_r3658_r3549_p1575
mc12_8TeV.200448.AlpgenPythia_Auto_P2011C_ZtautauccNp0.merge.NTUP_COMMON.e2386_s1581_s1586_r3658_r3549_p1575
mc12_8TeV.200449.AlpgenPythia_Auto_P2011C_ZtautauccNp1.merge.NTUP_COMMON.e2386_s1581_s1586_r3658_r3549_p1575
mc12_8TeV.200450.AlpgenPythia_Auto_P2011C_ZtautauccNp2.merge.NTUP_COMMON.e2386_s1581_s1586_r3658_r3549_p1575
mc12_8TeV.200451.AlpgenPythia_Auto_P2011C_ZtautauccNp3incl[...]NTUP_COMMON.e2386_s1581_s1586_r3658_r3549_p1575

Dedicated Z+Jets Samples with Low Dilepton Masses (Unfiltered)

Dilepton events with an invariant mass range of 10 GeV < $m_{\ell\ell}$ < 40 GeV

mc12_8TeV.178354.AlpgenPythia_P2011C_ZeeNp0Excl_Mll10to40[...].NTUP_COMMON.e2373_s1581_s1586_r4485_r4540_p1575
mc12_8TeV.178355.AlpgenPythia_P2011C_ZeeNp1Excl_Mll10to40[...].NTUP_COMMON.e2371_s1581_s1586_r4485_r4540_p1575
mc12_8TeV.178356.AlpgenPythia_P2011C_ZeeNp2Excl_Mll10to40[...].NTUP_COMMON.e2371_s1581_s1586_r4485_r4540_p1575
mc12_8TeV.178357.AlpgenPythia_P2011C_ZeeNp3Excl_Mll10to40[...].NTUP_COMMON.e2371_s1581_s1586_r4485_r4540_p1575
mc12_8TeV.178358.AlpgenPythia_P2011C_ZeeNp4Incl_Mll10to40[...].NTUP_COMMON.e2371_s1581_s1586_r4485_r4540_p1575
mc12_8TeV.178359.AlpgenPythia[...]ZmumuNp0Excl_Mll10to40[...].NTUP_COMMON.e2373_s1581_s1586_r4485_r4540_p1575
mc12_8TeV.178360.AlpgenPythia[...]ZmumuNp1Excl_Mll10to40[...].NTUP_COMMON.e2371_s1581_s1586_r4485_r4540_p1575
mc12_8TeV.178361.AlpgenPythia[...]ZmumuNp2Excl_Mll10to40[...].NTUP_COMMON.e2371_s1581_s1586_r4485_r4540_p1575
mc12_8TeV.178362.AlpgenPythia[...]ZmumuNp3Excl_Mll10to40[...].NTUP_COMMON.e2371_s1581_s1586_r4485_r4540_p1575
mc12_8TeV.178363.AlpgenPythia[...]ZmumuNp4Incl_Mll10to40[...].NTUP_COMMON.e2371_s1581_s1586_r4485_r4540_p1575
mc12_8TeV.178364.AlpgenPythia[...]ZtautauNp0Excl_Mll10to40[...].NTUP_COMMON.e2373_s1581_s1586_r4485_r4540_p1575
mc12_8TeV.178365.AlpgenPythia[...]ZtautauNp1Excl_Mll10to40[...].NTUP_COMMON.e2371_s1581_s1586_r4485_r4540_p1575
mc12_8TeV.178366.AlpgenPythia[...]ZtautauNp2Excl_Mll10to40[...].NTUP_COMMON.e2371_s1581_s1586_r4485_r4540_p1575
mc12_8TeV.178367.AlpgenPythia[...]ZtautauNp3Excl_Mll10to40[...].NTUP_COMMON.e2371_s1581_s1586_r4485_r4540_p1575
mc12_8TeV.178368.AlpgenPythia[...]ZtautauNp4Incl_Mll10to40[...].NTUP_COMMON.e2371_s1581_s1586_r4485_r4540_p1575

Dilepton events with an invariant mass range of 40 GeV < $m_{\ell\ell}$ < 60

mc12_8TeV.178369.AlpgenPythia_P2011C_ZeeNp0Excl_Mll40to60[...].NTUP_COMMON.e2373_s1581_s1586_r4485_r4540_p1575
mc12_8TeV.178370.AlpgenPythia_P2011C_ZeeNp1Excl_Mll40to60[...].NTUP_COMMON.e2371_s1581_s1586_r4485_r4540_p1575
mc12_8TeV.178371.AlpgenPythia_P2011C_ZeeNp2Excl_Mll40to60[...].NTUP_COMMON.e2371_s1581_s1586_r4485_r4540_p1575
mc12_8TeV.178372.AlpgenPythia_P2011C_ZeeNp3Excl_Mll40to60[...].NTUP_COMMON.e2371_s1581_s1586_r4485_r4540_p1575
mc12_8TeV.178373.AlpgenPythia_P2011C_ZeeNp4Incl_Mll40to60[...].NTUP_COMMON.e2371_s1581_s1586_r4485_r4540_p1575
mc12_8TeV.178374.AlpgenPythia[...]ZmumuNp0Excl_Mll40to60[...].NTUP_COMMON.e2373_s1581_s1586_r4485_r4540_p1575
mc12_8TeV.178375.AlpgenPythia[...]ZmumuNp1Excl_Mll40to60[...].NTUP_COMMON.e2371_s1581_s1586_r4485_r4540_p1575
mc12_8TeV.178376.AlpgenPythia[...]ZmumuNp2Excl_Mll40to60[...].NTUP_COMMON.e2371_s1581_s1586_r4485_r4540_p1575
mc12_8TeV.178377.AlpgenPythia[...]ZmumuNp3Excl_Mll40to60[...].NTUP_COMMON.e2371_s1581_s1586_r4485_r4540_p1575
mc12_8TeV.178378.AlpgenPythia[...]ZmumuNp4Incl_Mll40to60[...].NTUP_COMMON.e2371_s1581_s1586_r4485_r4540_p1575
mc12_8TeV.178379.AlpgenPythia[...]ZtautauNp0Excl_Mll40to60[...].NTUP_COMMON.e2373_s1581_s1586_r4485_r4540_p1575
mc12_8TeV.178380.AlpgenPythia[...]ZtautauNp1Excl_Mll40to60[...].NTUP_COMMON.e2371_s1581_s1586_r4485_r4540_p1575
mc12_8TeV.178381.AlpgenPythia[...]ZtautauNp2Excl_Mll40to60[...].NTUP_COMMON.e2371_s1581_s1586_r4485_r4540_p1575
mc12_8TeV.178382.AlpgenPythia[...]ZtautauNp3Excl_Mll40to60[...].NTUP_COMMON.e2371_s1581_s1586_r4485_r4540_p1575
mc12_8TeV.178383.AlpgenPythia[...]ZtautauNp4Incl_Mll40to60[...].NTUP_COMMON.e2371_s1581_s1586_r4485_r4540_p1575

Dedicated Z+$c\bar{c}$ Samples with Dileptons in the Invariant Mass Range of 10 GeV < $m_{\ell\ell}$ < 60 GeV

mc12_8TeV.178384.AlpgenPythia_P2011C_ZeeccNp0_Mll10to60[...].NTUP_COMMON.e2371_s1581_s1586_r4485_r4540_p1575
mc12_8TeV.178385.AlpgenPythia_P2011C_ZeeccNp1_Mll10to60[...].NTUP_COMMON.e2371_s1581_s1586_r4485_r4540_p1575
mc12_8TeV.178386.AlpgenPythia_P2011C_ZeeccNp2_Mll10to60[...].NTUP_COMMON.e2371_s1581_s1586_r4485_r4540_p1575
mc12_8TeV.178387.AlpgenPythia_P2011C_ZeeccNp3_Mll10to60[...].NTUP_COMMON.e2371_s1581_s1586_r4485_r4540_p1575
mc12_8TeV.178388.AlpgenPythia[...]ZmumuccNp0_Mll10to60[...].NTUP_COMMON.e2371_s1581_s1586_r4485_r4540_p1575
mc12_8TeV.178389.AlpgenPythia[...]ZmumuccNp1_Mll10to60[...].NTUP_COMMON.e2371_s1581_s1586_r4485_r4540_p1575
mc12_8TeV.178390.AlpgenPythia[...]ZmumuccNp2_Mll10to60[...].NTUP_COMMON.e2371_s1581_s1586_r4485_r4540_p1575
mc12_8TeV.178391.AlpgenPythia[...]ZmumuccNp3_Mll10to60[...].NTUP_COMMON.e2371_s1581_s1586_r4485_r4540_p1575
mc12_8TeV.178392.AlpgenPythia[...]ZtautauccNp0_Mll10to60[...].NTUP_COMMON.e2371_s1581_s1586_r4485_r4540_p1575
mc12_8TeV.178393.AlpgenPythia[...]ZtautauccNp1_Mll10to60[...].NTUP_COMMON.e2371_s1581_s1586_r4485_r4540_p1575
mc12_8TeV.178394.AlpgenPythia[...]ZtautauccNp2_Mll10to60[...].NTUP_COMMON.e2371_s1581_s1586_r4485_r4540_p1575
mc12_8TeV.178395.AlpgenPythia[...]ZtautauccNp3_Mll10to60[...].NTUP_COMMON.e2371_s1581_s1586_r4485_r4540_p1575

Dedicated Z+$b\bar{b}$ Samples with Dileptons in the Invariant Mass Range of 10 GeV < $m_{\ell\ell}$ < 60 GeV

mc12_8TeV.178396.AlpgenPythia_P2011C_ZeebbNp0_Mll10to60[...].NTUP_COMMON.e2371_s1581_s1586_r4485_r4540_p1575
mc12_8TeV.178397.AlpgenPythia_P2011C_ZeebbNp1_Mll10to60[...].NTUP_COMMON.e2371_s1581_s1586_r4485_r4540_p1575
mc12_8TeV.178398.AlpgenPythia_P2011C_ZeebbNp2_Mll10to60[...].NTUP_COMMON.e2371_s1581_s1586_r4485_r4540_p1575
mc12_8TeV.178399.AlpgenPythia_P2011C_ZeebbNp3_Mll10to60[...].NTUP_COMMON.e2371_s1581_s1586_r4485_r4540_p1575
mc12_8TeV.178400.AlpgenPythia[...]ZmumubbNp0_Mll10to60[...].NTUP_COMMON.e2371_s1581_s1586_r4485_r4540_p1575
mc12_8TeV.178401.AlpgenPythia[...]ZmumubbNp1_Mll10to60[...].NTUP_COMMON.e2371_s1581_s1586_r4485_r4540_p1575
mc12_8TeV.178402.AlpgenPythia[...]ZmumubbNp2_Mll10to60[...].NTUP_COMMON.e2371_s1581_s1586_r4485_r4540_p1575
mc12_8TeV.178403.AlpgenPythia[...]ZmumubbNp3_Mll10to60[...].NTUP_COMMON.e2371_s1581_s1586_r4485_r4540_p1575
mc12_8TeV.178404.AlpgenPythia[...]ZtautaubbNp0_Mll10to60[...].NTUP_COMMON.e2371_s1581_s1586_r4485_r4540_p1575
mc12_8TeV.178405.AlpgenPythia[...]ZtautaubbNp1_Mll10to60[...].NTUP_COMMON.e2371_s1581_s1586_r4485_r4540_p1575
mc12_8TeV.178406.AlpgenPythia[...]ZtautaubbNp2_Mll10to60[...].NTUP_COMMON.e2371_s1581_s1586_r4485_r4540_p1575
mc12_8TeV.178407.AlpgenPythia[...]ZtautaubbNp3_Mll10to60[...].NTUP_COMMON.e2371_s1581_s1586_r4485_r4540_p1575

B Additional Event Yield Tables

e+jets	All events	Analysis region	
Sample	≥ 0 b-tags	1 b-tag	≥ 2 b-tags
$t\bar{t}$	162000 ± 10000	69500 ± 4500	74100 ± 4800
Single top	10960 ± 350	5520 ± 180	3650 ± 120
$W+b\bar{b}/c\bar{c}$	38300 ± 4200	11800 ± 1300	2800 ± 310
$W+c$	16900 ± 4600	4500 ± 1200	271 ± 73
W+light	45200 ± 1800	2449 ± 98	102 ± 4
Z+jets	16800 ± 8000	3800 ± 1800	1270 ± 610
Diboson	4200 ± 2000	780 ± 380	169 ± 81
Multijet	26500 ± 7900	6900 ± 2100	2050 ± 620
Total expected	321000 ± 17000	105100 ± 5600	84500 ± 4900
Data	310747	101859	88915
Deviation [%]	3.2	3.2	5.0

Table B.1: Event yields obtained in the electron+jets channel for all events (≥ 0 b-tags) and for events with exactly one or at least two b-tags before applying the cut on the logarithm of the KLFitter likelihood and before splitting the signal and background distributions into two jet pseudorapidity regions. The uncertainties on the given MC signal and background numbers arise from normalisation uncertainties of each sample, which are defined in Sec. 7.3. The uncertainties on the W+jets and the multijet background originate from the data-driven methods used to estimate these background sources, the other numbers are based on theory uncertainties. The predicted yields agree within 1σ with the events measured in data. In addition to the requirements listed in Sec. 6.2, events without any b-tagged jet need to have $E_{\mathrm{T}}^{\mathrm{miss}} > 40$ GeV and also fulfil the triangular cut of $E_{\mathrm{T}}^{\mathrm{miss}} + m_{\mathrm{T}}^{W} > 60$ GeV.

μ+jets	All events	Analysis region	
Sample	≥ 0 b-tags	1 b-tag	≥ 2 b-tags
$t\bar{t}$	202000 ± 13000	87000 ± 5600	91900 ± 5900
Single top	13270 ± 430	6660 ± 210	4410 ± 140
$W+b\bar{b}/c\bar{c}$	52500 ± 5800	16000 ± 1800	3980 ± 440
$W+c$	21500 ± 5800	5500 ± 1500	326 ± 88
W+light	61000 ± 2400	3230 ± 130	174 ± 7
Z+jets	11700 ± 5600	2400 ± 1200	730 ± 350
Diboson	5000 ± 2400	900 ± 430	179 ± 86
Multijet	17000 ± 5100	5300 ± 1600	1455 ± 44
Total expected	384000 ± 17000	127000 ± 6400	103100 ± 5900
Data	379098	125455	107472
Deviation [%]	1.2	1.2	4.0

Table B.2: Event yields obtained in the muon+jets channel for all events (≥ 0 b-tags) and for events with exactly one or at least two b-tags before applying the cut on the logarithm of the KLFitter likelihood and before splitting the signal and background distributions into two jet pseudorapidity regions. The uncertainties on the given MC signal and background numbers arise from normalisation uncertainties of each sample, which are defined in Sec. 7.3. The uncertainties on the W+jets and the multijet background originate from the data-driven methods used to estimate these background sources, the other numbers are based on theory uncertainties. The predicted yields agree within 1σ with the events measured in data. In addition to the requirements listed in Sec. 6.2, events without any b-tagged jet need to have $E_{\mathrm{T}}^{\mathrm{miss}} > 40$ GeV and also fulfil the triangular cut of $E_{\mathrm{T}}^{\mathrm{miss}} + m_{\mathrm{T}}^{W} > 60$ GeV.

C Additional Control Plots

This appendix comprises additional control plots for kinematic quantities. Shown in Figs. C.1-C.4 are kinematic distributions of the lepton and leading b-tagged jet p_{T}, lepton and leading b-tagged jet η, $E_{\mathrm{T}}^{\mathrm{miss}}$ and m_{T}^{W} for events with exactly one or at least two b-tagged jets in the electron and muon channel where the cut on the logarithm of the likelihood from the reconstruction algorithm $\ln(L)$ is not yet applied.
A comparison with the corresponding control plots where the cut is applied, presented in Figs. 6.2-6.5, reveals that the modelling of kinematic quantities, in particular for the shown transverse momenta, improves with the application of this cut on $\ln(L)$.

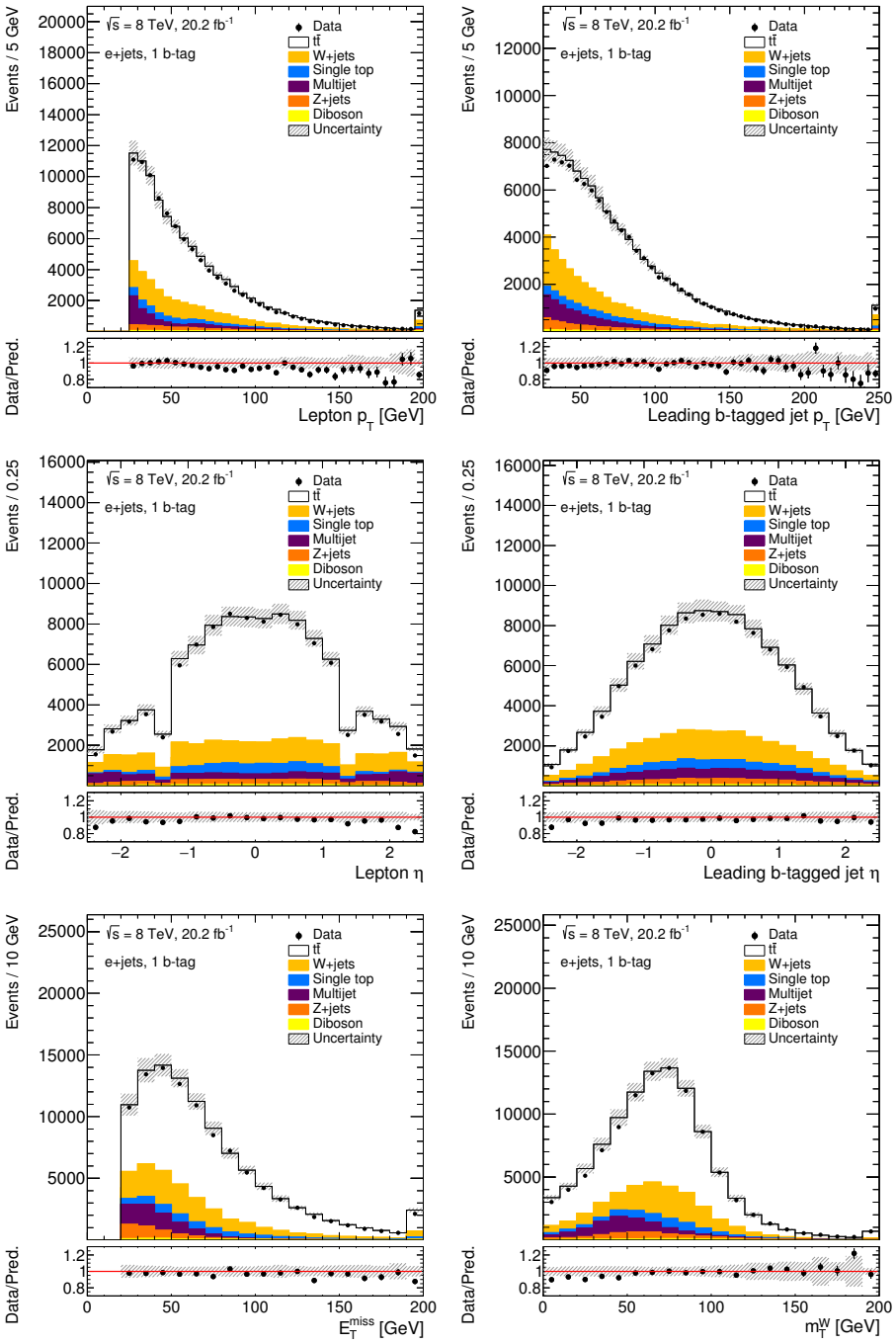

Figure C.1: Distributions of the lepton and leading b-tagged jet p_{T}, lepton and leading b-tagged jet η, $E_{\mathrm{T}}^{\mathrm{miss}}$ and m_{T}^{W} in the electron+jets channel for events with exactly one b-tagged jet before applying the cut on the logarithm of the reconstruction likelihood. The hatched bands comprise the normalisation uncertainty in the signal and background contributions as well as the signal model systematic uncertainties. The first and last bins include underflow and overflow events, respectively.

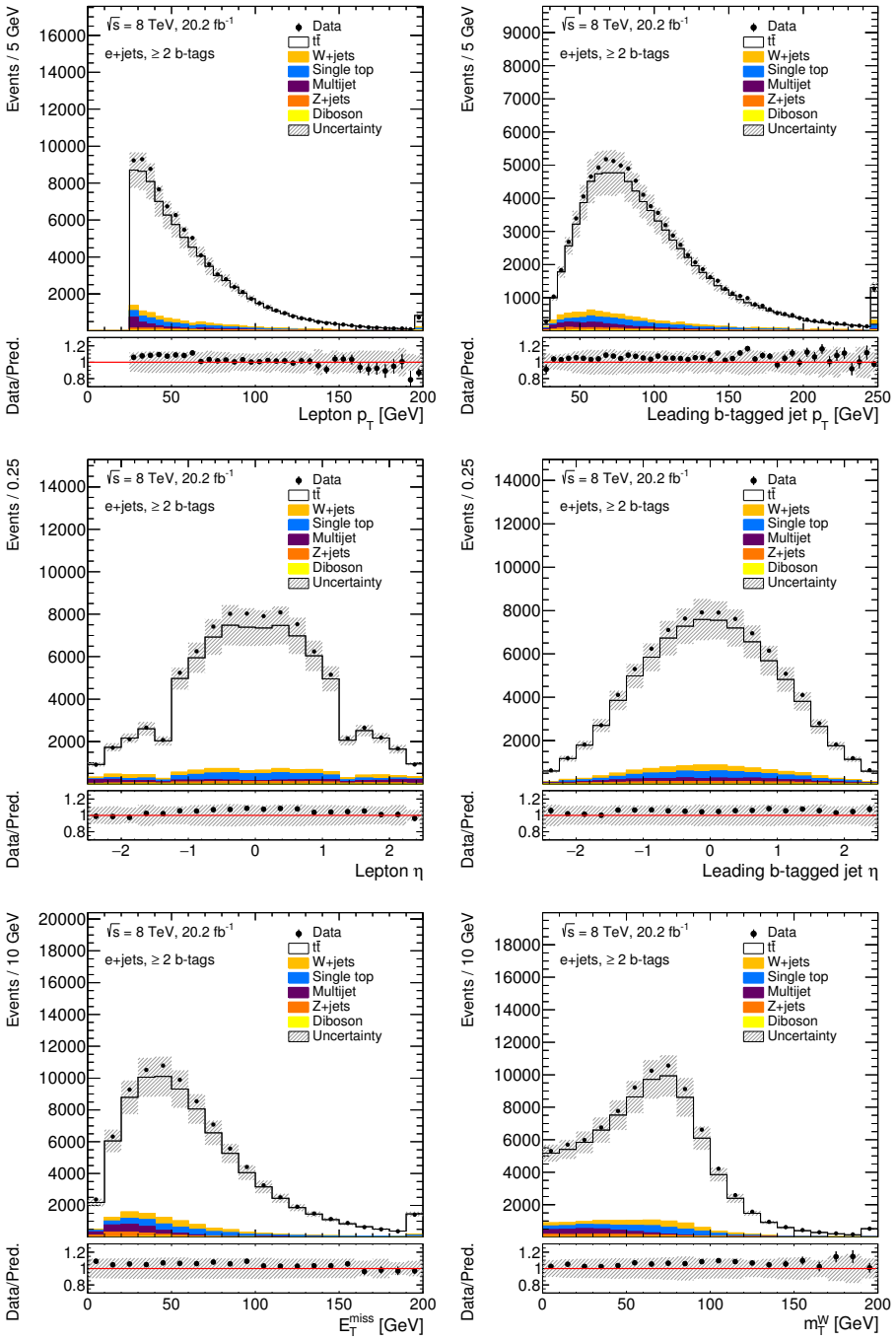

Figure C.2: Distributions of the lepton and leading b-tagged jet p_{T}, lepton and leading b-tagged jet η, $E_{\mathrm{T}}^{\mathrm{miss}}$ and m_{T}^{W} in the electron+jets channel for events with at least two b-tagged jets before applying the cut on the logarithm of the reconstruction likelihood. The hatched bands comprise the normalisation uncertainty in the signal and background contributions as well as the signal model systematic uncertainties. The first and last bins include underflow and overflow events, respectively.

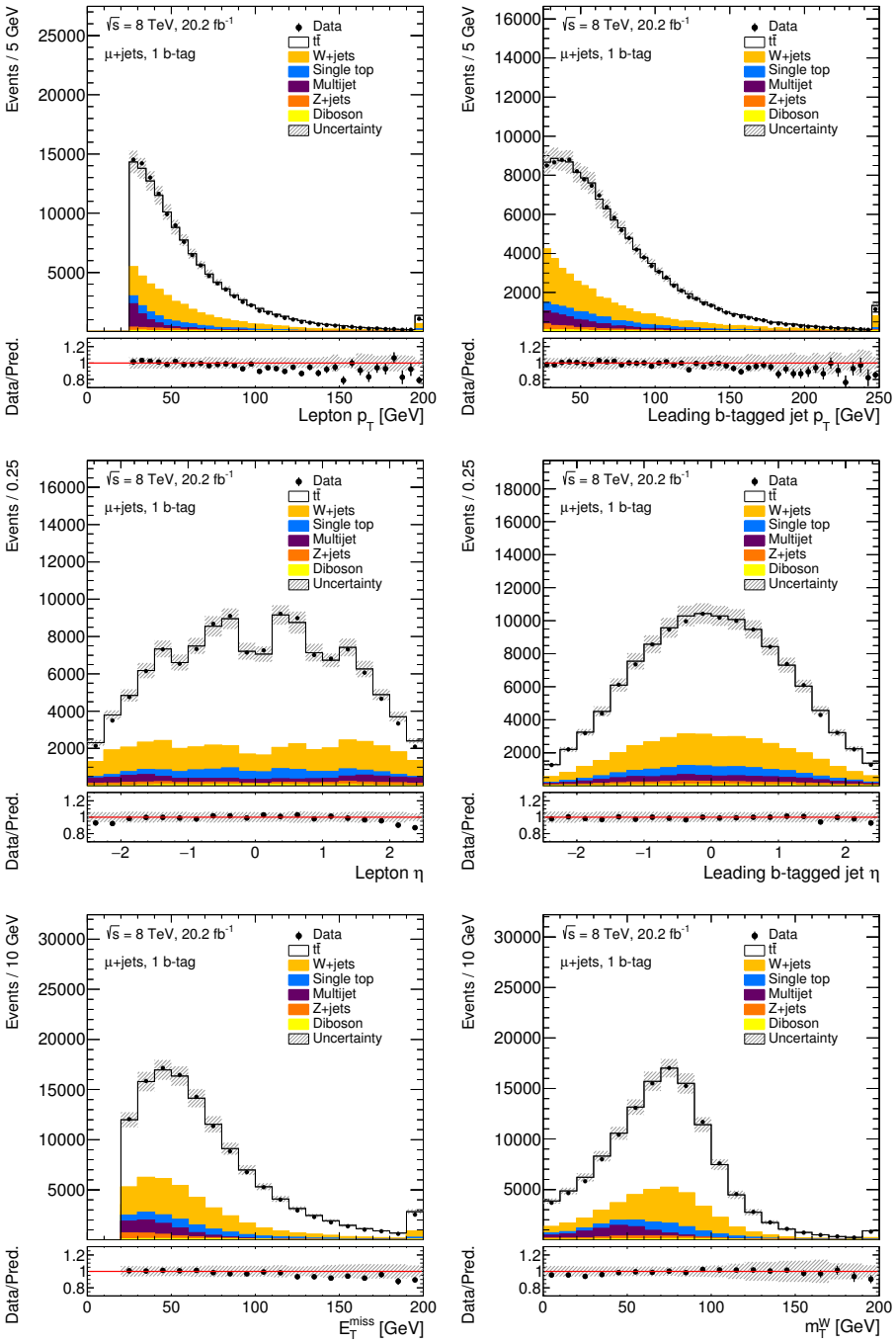

Figure C.3: Distributions of the lepton and leading b-tagged jet p_{T}, lepton and leading b-tagged jet η, $E_{\mathrm{T}}^{\mathrm{miss}}$ and m_{T}^{W} in the muon+jets channel for events with exactly one b-tagged jet before applying the cut on the logarithm of the reconstruction likelihood. The hatched bands comprise the normalisation uncertainty in the signal and background contributions as well as the signal model systematic uncertainties. The first and last bins include underflow and overflow events, respectively.

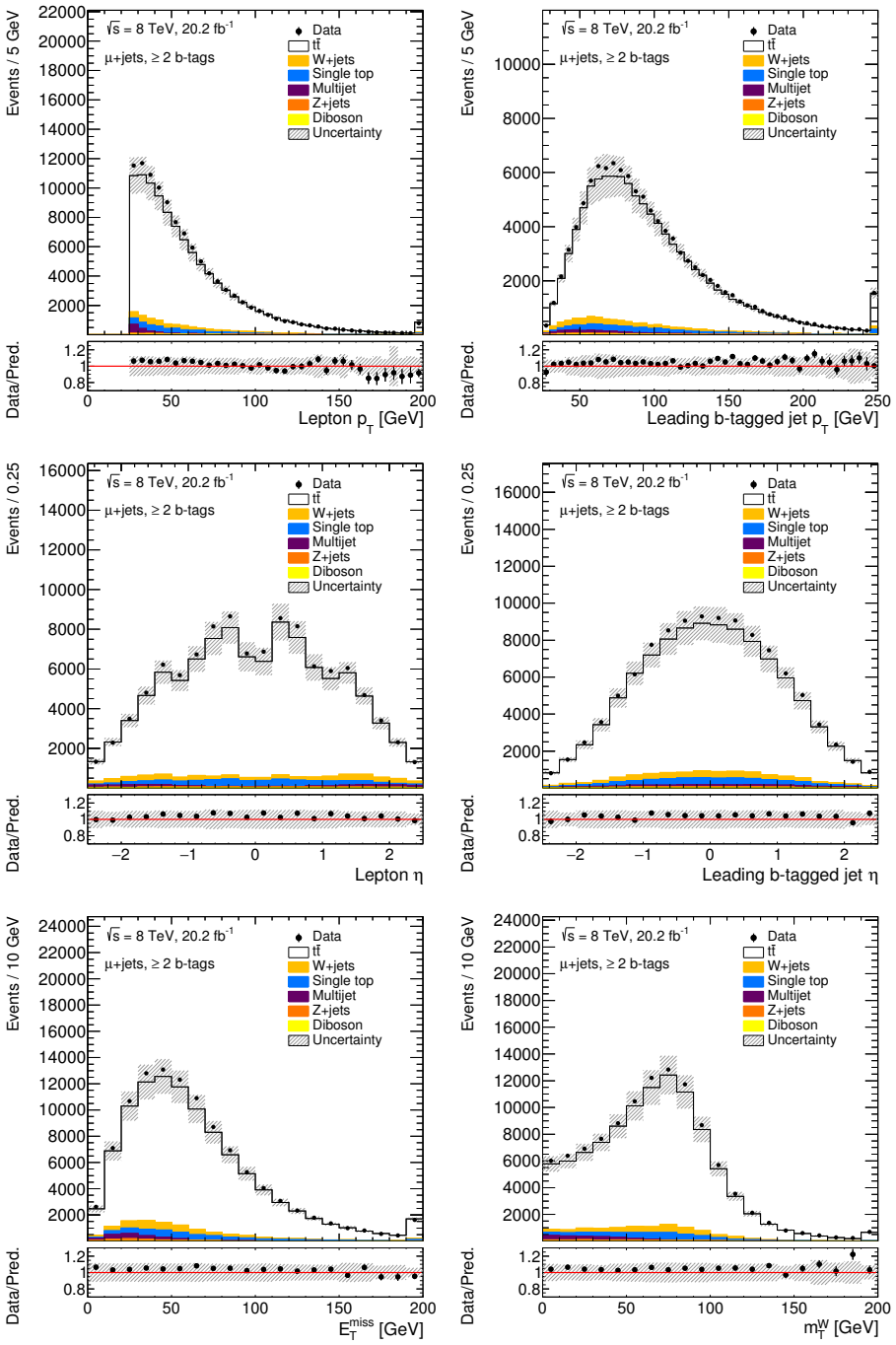

Figure C.4: Distributions of the lepton and leading b-tagged jet p_{T}, lepton and leading b-tagged jet η, $E_{\mathrm{T}}^{\mathrm{miss}}$ and m_{T}^{W} in the muon+jets channel for events with at least two b-tagged jets before applying the cut on the logarithm of the reconstruction likelihood. The hatched bands comprise the normalisation uncertainty in the signal and background contributions as well as the signal model systematic uncertainties. The first and last bins include underflow and overflow events, respectively.

D Additional Correlation Plots

Two-dimensional histograms to evaluate the correlation between the two observables $m_{\ell b}$ and $\Delta R_{\text{min}}(j_b, j_l)$ in all eight analysis regions are shown in Fig. 7.10. These histograms correspond to the distributions directly used in the fit comprising signal and all background contributions. The correlation is found to be between 0.1-1.2% for events with exactly one b-tag and 1.8-2.7% for events with at least two b-tagged jets.

This appendix provides additional correlation plots for signal only and background only samples as well as correlation plots based on alternative decay width MC samples and alternative MC $t\bar{t}$ samples to demonstrate that the correlation between the two observables is indeed small for all these various options.

Fig. D.1 presents correlation plots for signal events based on the nominal sample with $\Gamma_t = 1.33$ GeV. Correlation histograms for signal samples based on the alternative decay width values of $\Gamma_t = 0.7$ GeV and $\Gamma_t = 3.0$ GeV are given in Fig. D.2 and Fig. D.3 while Fig. D.4 contains histograms for the sum of the background contributions. Correlation distributions for two alternative $t\bar{t}$ signal generator setups, namely POWHEG+HERWIG and MC@NLO+HERWIG, are summarised in Fig. D.5 and Fig. D.6.

The correlation factors included in the plots are also listed separately in Table D.1 to allow for an easier comparison of the values. Correlation factors range from 0.2% to 6.4% which is reasonable small pursuant to the explanations and tests outlined in Sec. 7.6.

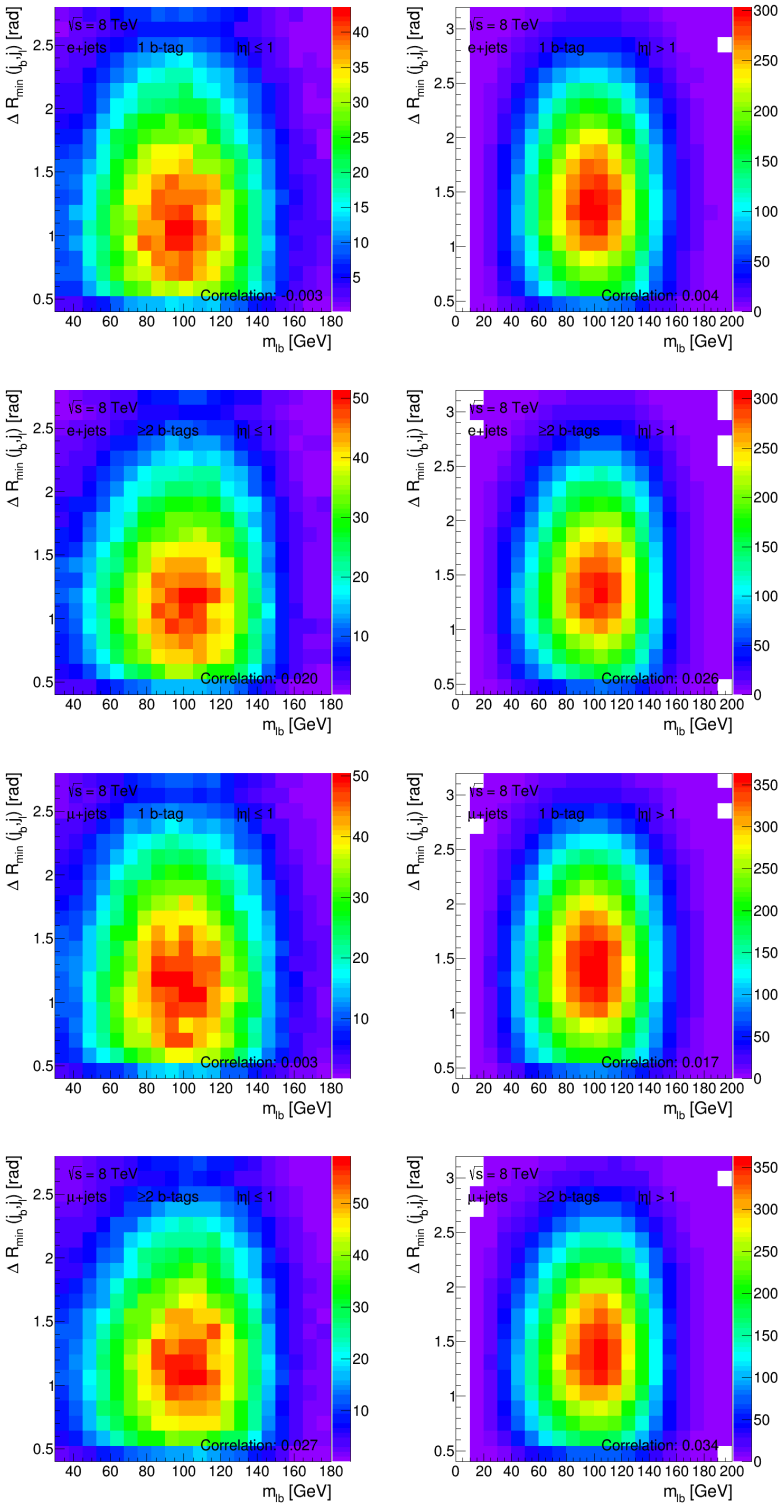

Figure D.1: Correlation between the two observables $m_{\ell b}$ and $\Delta R_{\text{min}}(j_b, j_l)$ in all eight analysis regions according to the labels. Signal $t\bar{t}$ events based on the nominal sample with $\Gamma_t = 1.33$ GeV are shown. The extracted correlation factors are also listed in Table D.1.

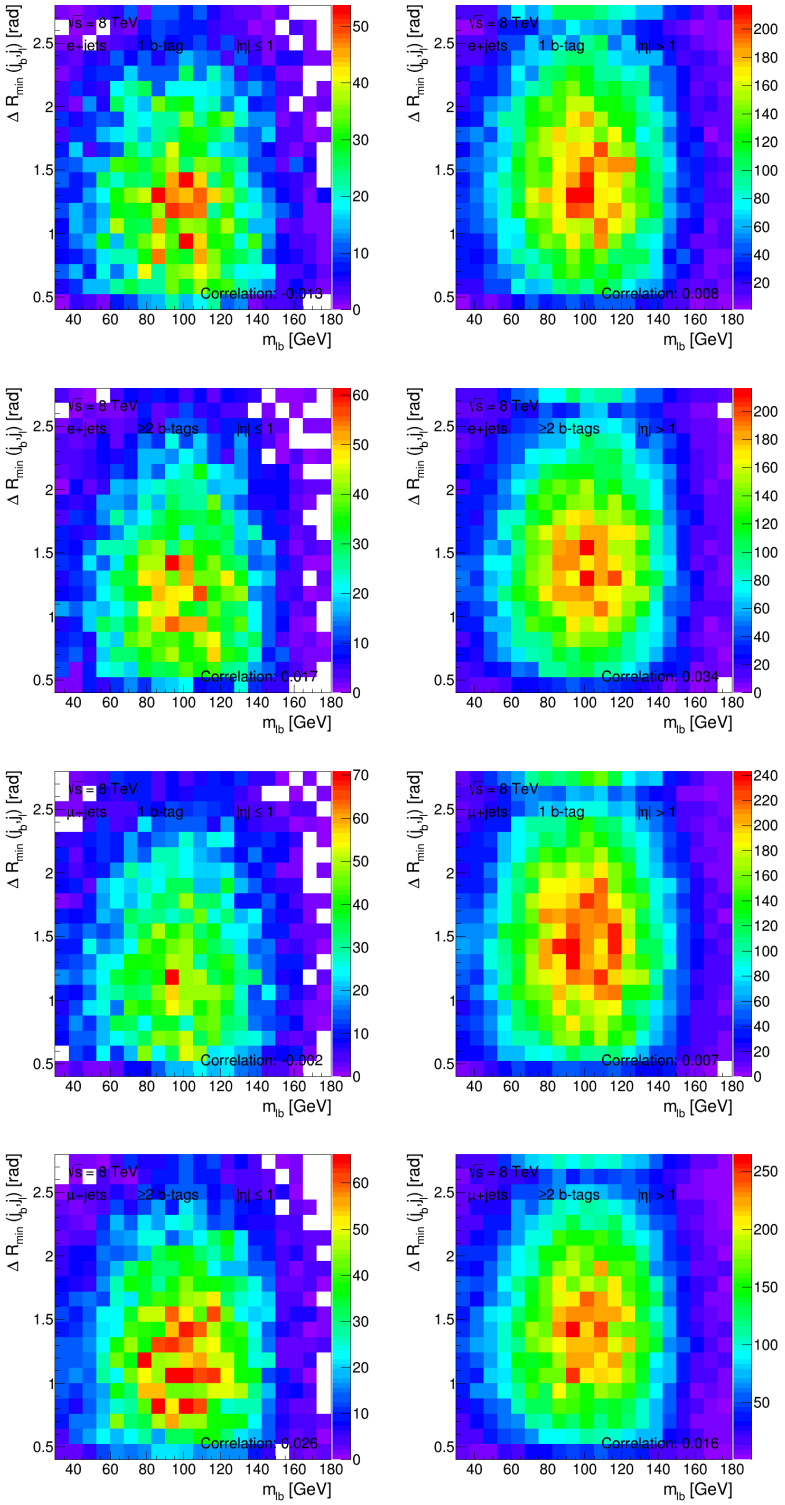

Figure D.2: Correlation between the two observables $m_{\ell b}$ and $\Delta R_{\text{min}}(j_b, j_l)$ in all eight analysis regions according to the labels. Signal $t\bar{t}$ events based on a sample with $\Gamma_t = 0.7$ GeV are shown. The extracted correlation factors are also listed in Table D.1.

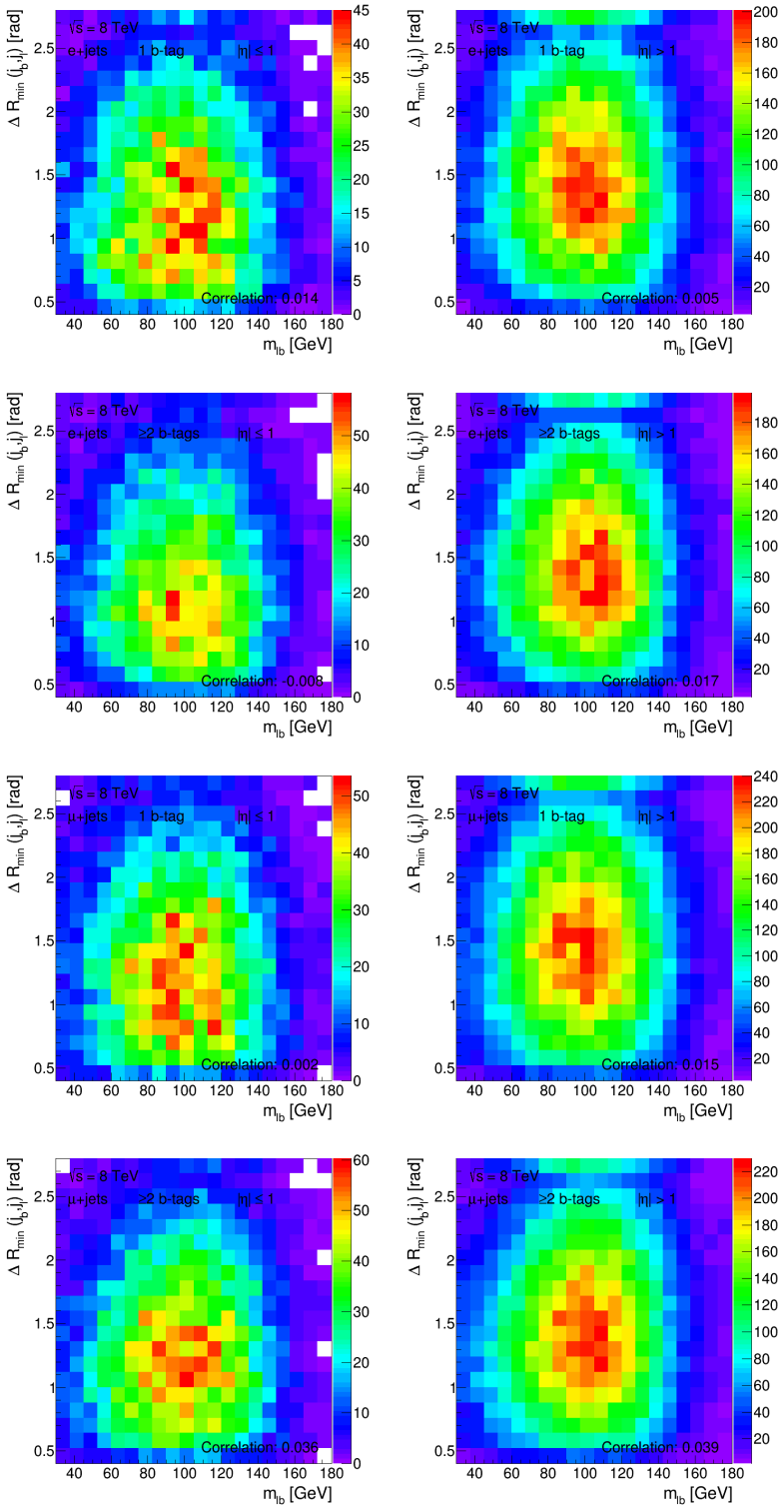

Figure D.3: Correlation between the two observables $m_{\ell b}$ and $\Delta R_{\text{min}}(j_b, j_l)$ in all eight analysis regions according to the labels. Signal $t\bar{t}$ events based on a sample with $\Gamma_t = 3.0$ GeV are shown. The extracted correlation factors are also listed in Table D.1.

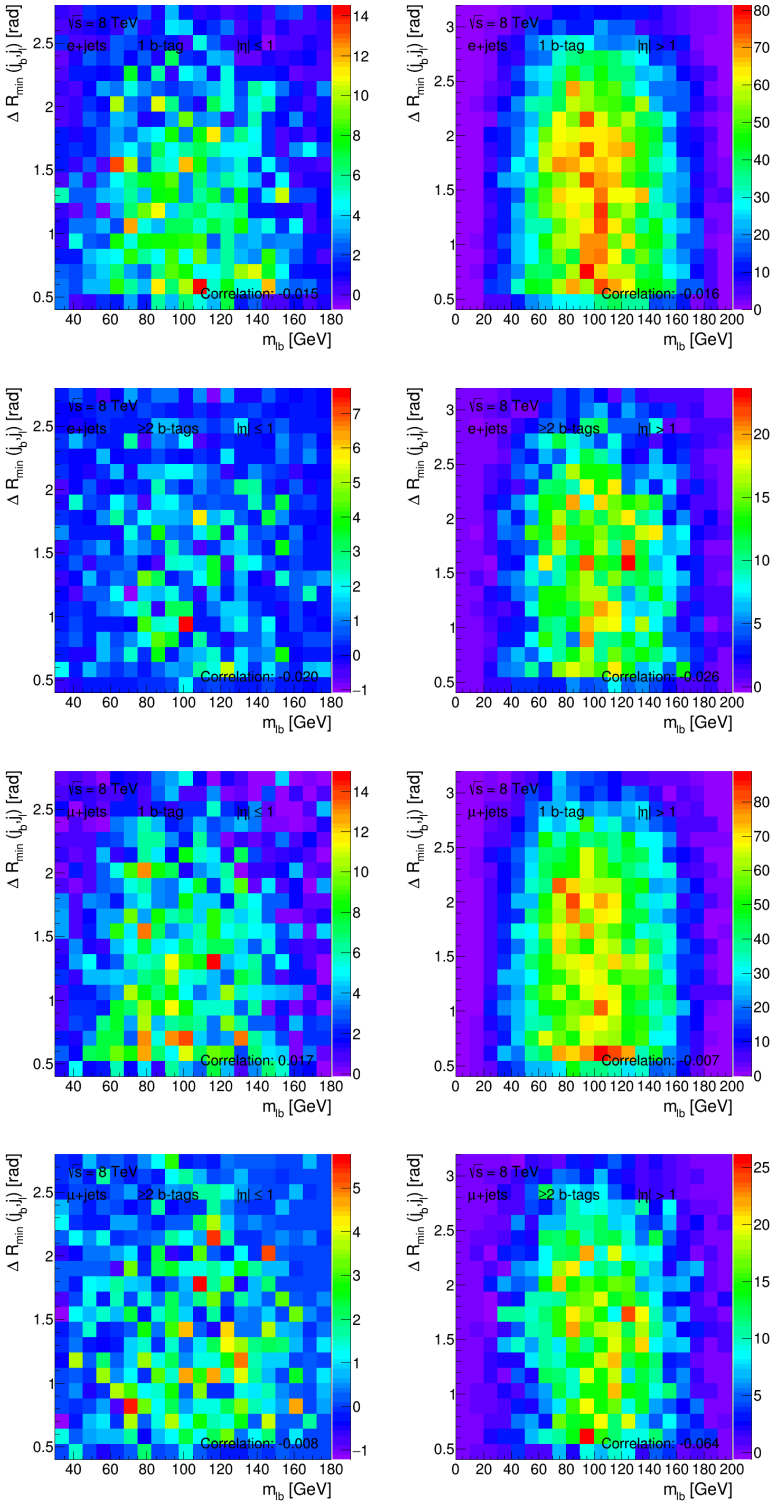

Figure D.4: Correlation between the two observables $m_{\ell b}$ and $\Delta R_{\text{min}}(j_b, j_l)$ in all eight analysis regions according to the labels. The sum of the different background contributions is shown. The extracted correlation factors are also listed in Table D.1.

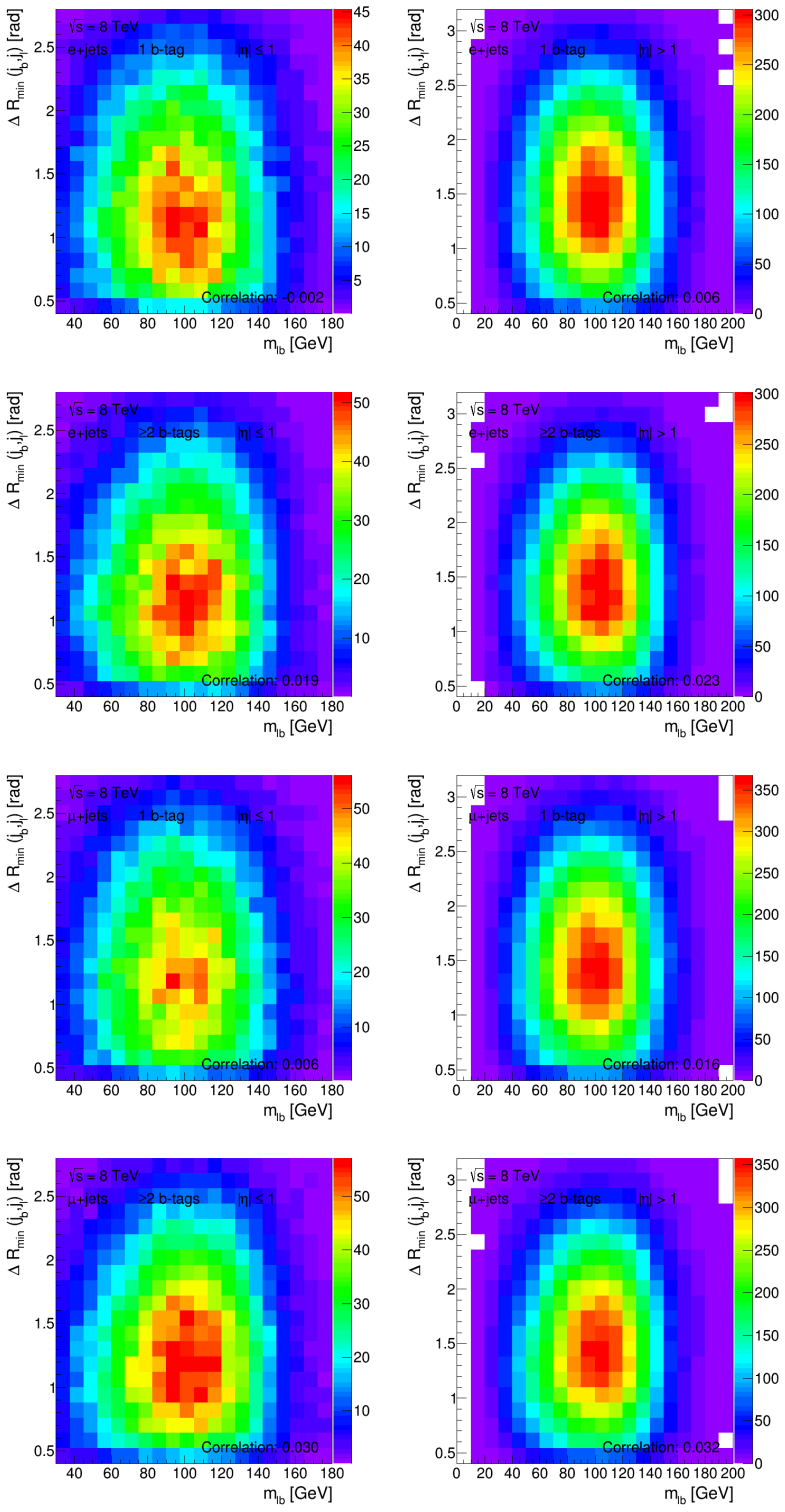

Figure D.5: Correlation between the two observables $m_{\ell b}$ and $\Delta R_{\text{min}}(j_b, j_l)$ in all eight analysis regions according to the labels. Signal $t\bar{t}$ events based on an alternative signal sample generated with Powheg+Herwig are shown. The extracted correlation factors are also listed in Table D.1.

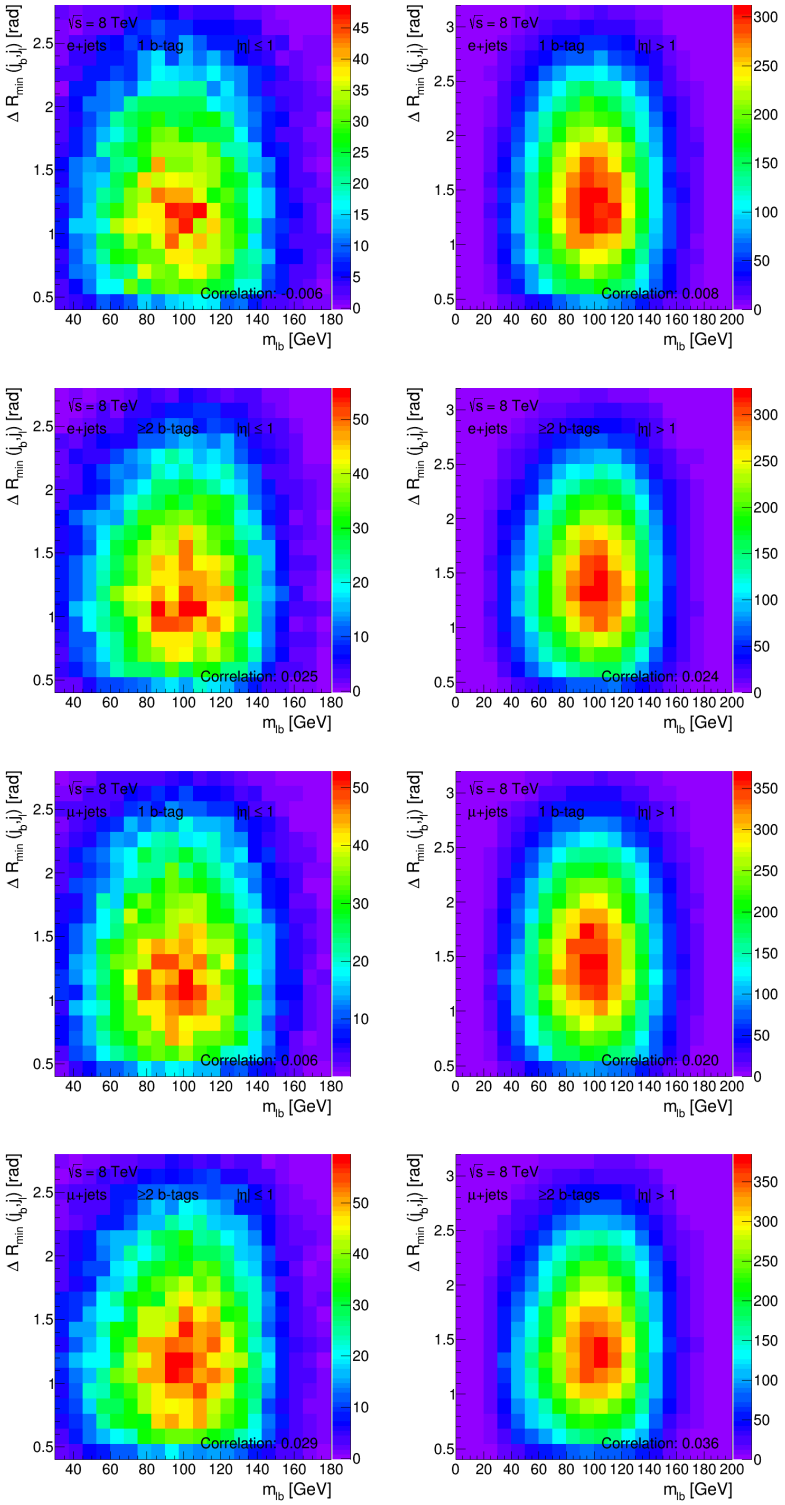

Figure D.6: Correlation between the two observables $m_{\ell b}$ and $\Delta R_{\text{min}}(j_b, j_l)$ in all eight analysis regions according to the labels. Signal $t\bar{t}$ events based on an alternative signal sample generated with MC@NLO+Herwig are shown. The extracted correlation factors are also listed in Table D.1.

Analysis region	Correlation		
	Signal $\Gamma_t = 1.33$ GeV	Signal $\Gamma_t = 0.7$ GeV	Signal $\Gamma_t = 3.0$ GeV
e, 1 b-tag, $\|\eta\| \leq 1$	-0.003	-0.013	0.014
e, 1 b-tag, $\|\eta\| > 1$	0.004	0.008	0.005
e, ≥ 2 b-tags, $\|\eta\| \leq 1$	0.020	0.017	-0.008
e, ≥ 2 b-tags, $\|\eta\| > 1$	0.026	0.034	0.017
μ, 1 b-tag, $\|\eta\| \leq 1$	0.003	-0.002	0.002
μ, 1 b-tag, $\|\eta\| > 1$	0.017	0.007	0.015
μ, ≥ 2 b-tags, $\|\eta\| \leq 1$	0.027	0.026	0.036
μ, ≥ 2 b-tags, $\|\eta\| > 1$	0.034	0.016	0.039
	Background	POWHEG+HERWIG	MC@NLO+HERWIG
e, 1 b-tag, $\|\eta\| \leq 1$	-0.015	-0.002	-0.006
e, 1 b-tag, $\|\eta\| > 1$	-0.016	0.006	0.008
e, ≥ 2 b-tags, $\|\eta\| \leq 1$	-0.020	0.019	0.025
e, ≥ 2 b-tags, $\|\eta\| > 1$	-0.026	0.023	0.024
μ, 1 b-tag, $\|\eta\| \leq 1$	0.017	0.006	0.006
μ, 1 b-tag, $\|\eta\| > 1$	-0.007	0.016	0.020
μ, ≥ 2 b-tags, $\|\eta\| \leq 1$	-0.008	0.030	0.029
μ, ≥ 2 b-tags, $\|\eta\| > 1$	-0.064	0.032	0.036

Table D.1: Overview of the correlation factors corresponding to the correlation histograms in all eight analysis regions for signal only and background only samples as well as for alternative decay width MC samples and systematic MC samples as shown in Figs. D.1-D.6 and explained in more detail in the text.

E Systematic Uncertainties with Effective Components

The estimation of systematic uncertainties as described in detail in Ch. 8 considers all possible components of systematic uncertainties, e.g., also the large number of components of the jet energy scale and resolution uncertainties.
Since some of these components have a very small impact on the final uncertainty value, an additional study was performed to test a reduced setup which does not treat those systematic components as being effective and thus does not include them in the calculation of the total uncertainty. Such an approach was also used for other measurements in the past.

A single systematic effect corresponding to one systematic component is considered as being effective if the systematic variation with respect to the nominal sample is larger than the statistical uncertainty of this nominal sample in at least three bins per analysis region of the observables with 20 bins per region. If this criterion is fulfilled in one of the eight analysis regions, the systematic component is considered, i.e. used in the estimate with all eight concatenated analysis regions. Sources of systematic uncertainty that only reweight the nominal sample like uncertainties based on scale factors are always considered and regarded as effective. The list of uncertainties with the full number of effective components is given in Table E.1.

Tab. E.2 contains the summary of systematic uncertainties after the components which are not effective are removed from the calculation. The inclusion of all systematic variations does not increase the total systematic uncertainty remarkably. Since the total uncertainty values are so similar, the measurement is realised with the full number of components as the most conservative approach.

Systematic uncertainty	Type	Components	
Detector model		Total	Effective
Electron	SN	5	4
Muon	SN	6	3
Missing transverse momentum	SN	2	0
Jet reconstruction	SN	1	0
Jet vertex fraction	SN	1	1
Jet energy scale	SN	26	9
Jet energy resolution	SN	11	6
b-tagging efficiency	SN	6	6
c-tagging efficiency	SN	4	4
Light jet tagging efficiency	SN	12	12
Background model		Total	Effective
W+light/c/$b\bar{b}$/$c\bar{c}$ calibration	N	3	3
W+jets shape	S	1	1
Single top cross-section	N	1	1
Single top modelling	SN	1	0
Multijet normalisation	N	1	1
Multijet modelling	SN	3	1
Z+jets normalisation	N	1	1
Diboson+jets normalisation	N	1	1
Signal model		Total	Effective
Radiation	SN	2	2
ME generator	SN	1	1
PS/fragmentation	SN	1	1
Colour reconnection	SN	1	1
Underlying event	SN	1	1
PDF	SN	3	3
Luminosity	N	1	1
Template statistical uncertainty	SN	1	1

Table E.1: Systematic uncertainties considered for the measurement of Γ_t mostly grouped into detector, background and signal model uncertainties. Depending on the source of systematic uncertainty, only the $t\bar{t}$ or background normalisation, only the shape of the observable distributions or both normalisation and shape of the observable distributions are affected, labelled as "N", "S" or "SN", respectively. The last two columns indicate the number of individual components per systematic effect and the number of components which are effective according to the definition in the text.

Source	Uncertainty [GeV]	
Detector model		
Electron	+0.13	−0.07
Muon	+0.11	−0.05
Jet energy scale	+0.40	−0.29
Jet energy resolution	+0.25	−0.25
Jet vertex fraction	+0.13	−0.03
Heavy and light flavour tagging	+0.32	−0.24
Signal model		
ME generator	+0.41	−0.41
Colour reconnection	+0.19	−0.19
Underlying event	+0.11	−0.11
Radiation	+0.07	−0.07
PDF	+0.06	−0.06
PS/fragmentation	+0.05	−0.05
Background model		
Multijet	+0.03	−0.00
W+jets	+0.02	−0.02
Template statistical uncertainty	+0.07	−0.07
Luminosity	+0.03	−0.00
Total systematic uncertainty	+0.77	−0.67

Table E.2: Summary of all systematic uncertainties for the top quark decay width measurement estimated from components which are effective according to the definition in the text. The resulting total systematic uncertainty is given in the last row.

F Additional Plots for the Estimation of the Impact of the Top Quark Mass

According to the explanations in Sec. 2.3, the definition of the top quark decay width depends significantly on the top quark mass. The decay width is measured exploiting $m_{\ell b}$ mass distributions sensitive to Γ_t. Several studies and tests to assess the impact of Γ_t on the top quark mass are described thoroughly in Sec. 8.6.
The differences between the nominal and the alternative mass samples are of a similar order in the eight exclusive analysis regions. This is shown in Fig. 8.9 for the mass distributions based on the nominal decay width of $\Gamma_t = 1.33$ GeV. For the sake of completeness, Fig. F.1 and Fig. F.2 contain those mass distributions, again comparing the nominal samples to the alternative mass samples in all eight analysis regions, based on different decay width values of $\Gamma_t = 0.5$ GeV and $\Gamma_t = 2.0$ GeV. These plots, independent of the underlying decay width, reflect the same behaviour as the nominal width samples, i.e. also for alternative values of Γ_t no obvious shift or fluctuation can be observed between the various mass distributions.

In order to understand the asymmetric response of Γ_t to the top quark mass, templates based on $\Gamma_t = 1.33$ GeV obtained from the alternative mass sample with $m_t = 170$ GeV are compared with templates from the nominal sample with $m_t = 172.5$ GeV that correspond to $\Gamma_t = 1.0$ GeV and $\Gamma_t = 2.5$ GeV. The resulting plots for the pseudorapidity region with $|\eta| > 1$ are given in Fig. 8.10, the corresponding plots for the $|\eta| \leq 1$ region are illustrated in Fig. F.3.
Also the distributions in this smaller pseudorapidity region demonstrate that the templates derived at $m_t = 172.5$ GeV are not able to cover the $m_{\ell b}$ distribution of the comparison values of 170 GeV and 175 GeV.

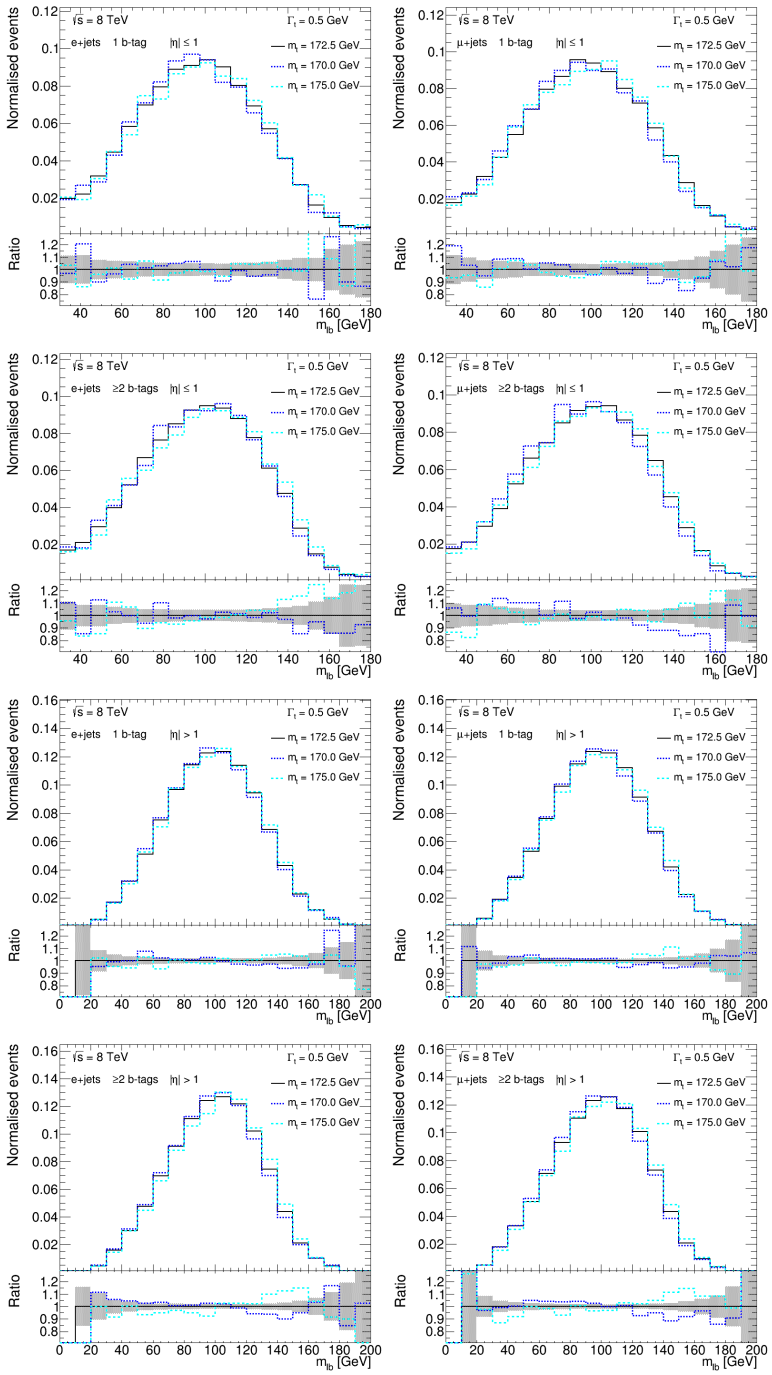

Figure F.1: Distributions of the observable $m_{\ell b}$ in the eight exclusive analysis regions according to the labels. Templates based on $\Gamma_t = 0.5$ GeV are compared for the nominal sample with $m_t = 172.5$ GeV and for the alternative top quark masses of $m_t = 170$ and 175 GeV. The lower panels illustrate the ratio of the presented histograms with respect to the nominal signal sample.

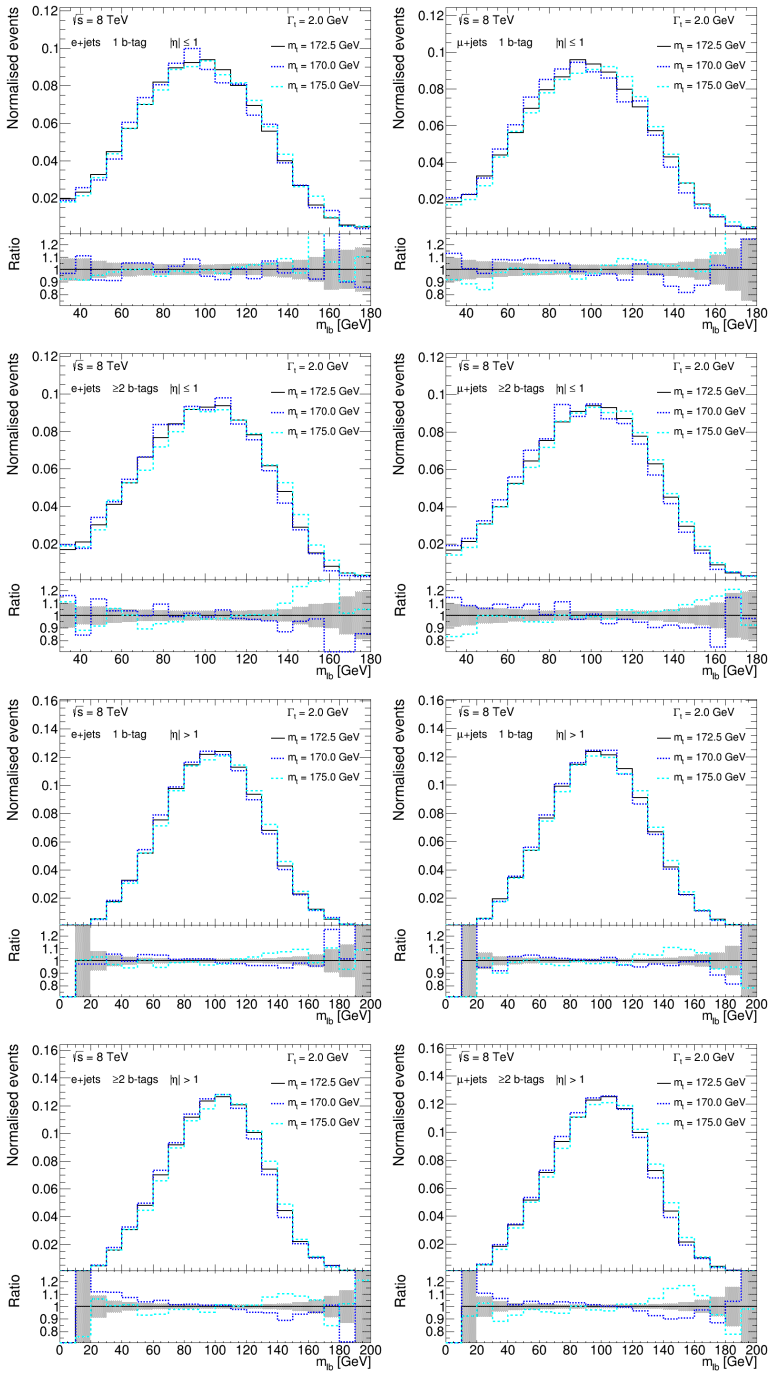

Figure F.2: Distributions of the observable $m_{\ell b}$ in the eight exclusive analysis regions according to the labels. Templates based on $\Gamma_t = 2.0$ GeV are compared for the nominal sample with $m_t = 172.5$ GeV and for the alternative top quark masses of $m_t = 170$ and 175 GeV. The lower panels illustrate the ratio of the presented histograms with respect to the nominal signal sample.

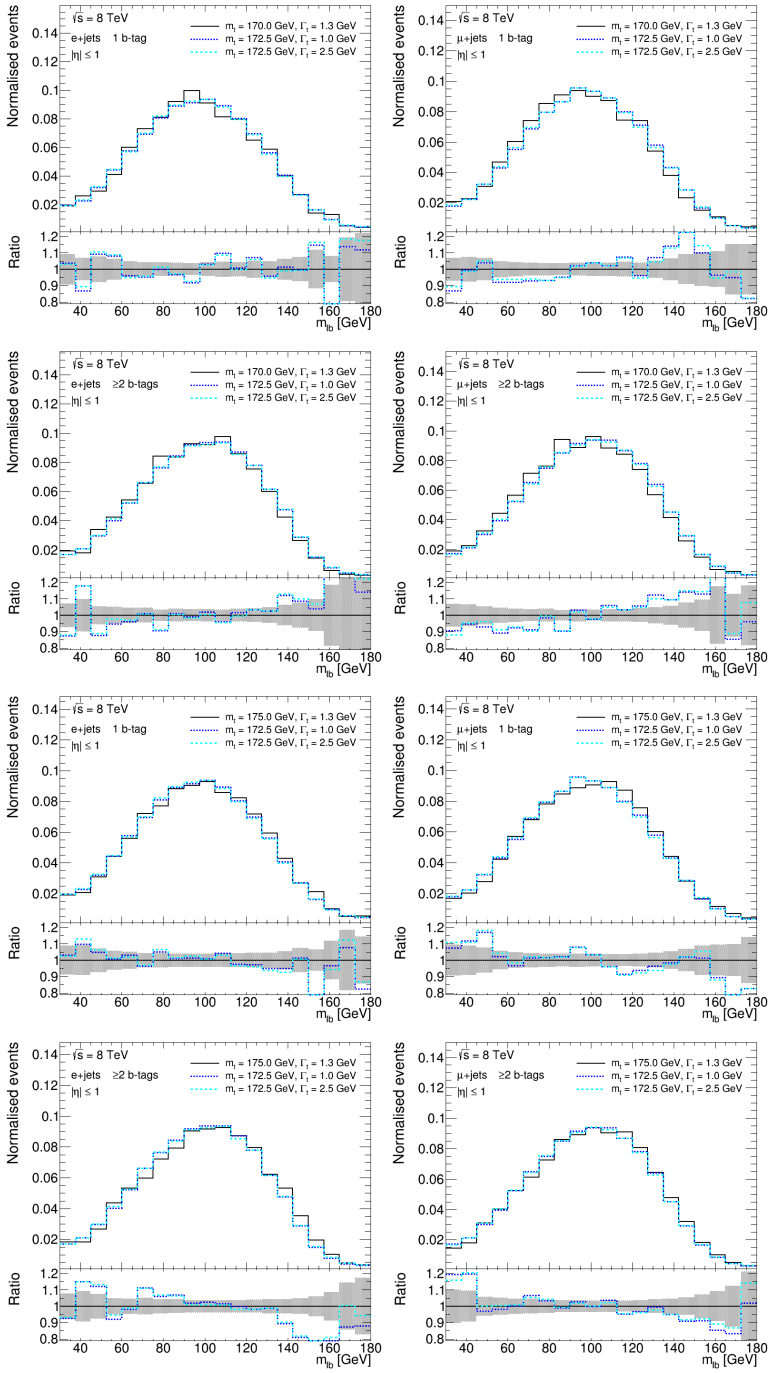

Figure F.3: Distributions of the observable $m_{\ell b}$ in the four $|\eta| \leq 1$ analysis regions. Templates based on $\Gamma_t = 1.33$ GeV for the alternative mass sample with $m_t = 170$ GeV (upper half) and with $m_t = 175$ GeV (lower half) are compared to templates for two different decay width values, namely $\Gamma_t = 1.0$ GeV and $\Gamma_t = 2.5$ GeV, from the nominal sample with $m_t = 172.5$ GeV. The lower panels illustrate the ratio of the presented histograms with respect to the alternative $t\bar{t}$ samples at $m_t = 170$ GeV and $m_t = 175$ GeV.

G Pre-Fit Plots to Test the Observable Modelling

Observable distributions of $m_{\ell b}$, $\Delta R_{\text{min}}(j_b, j_l)$ and SdR are presented in this appendix to test the modelling of these observables. The agreement between prediction and data is quantified by χ^2 tests and Kolmogorov-Smirnov tests, whose results are given in the plots as well. Shown in Fig. G.1 and Fig. G.2 are pre-fit plots for the observables $\Delta R_{\text{min}}(j_b, j_l)$, $m_{\ell b}$ and SdR after the cut on the logarithm of the KLFitter likelihood is applied. Observable distributions before this cut is applied are given in Fig. G.3 to underline to which extent the modelling improves by such a requirement. The results of the modelling tests are discussed thoroughly in Sec. 9.3.

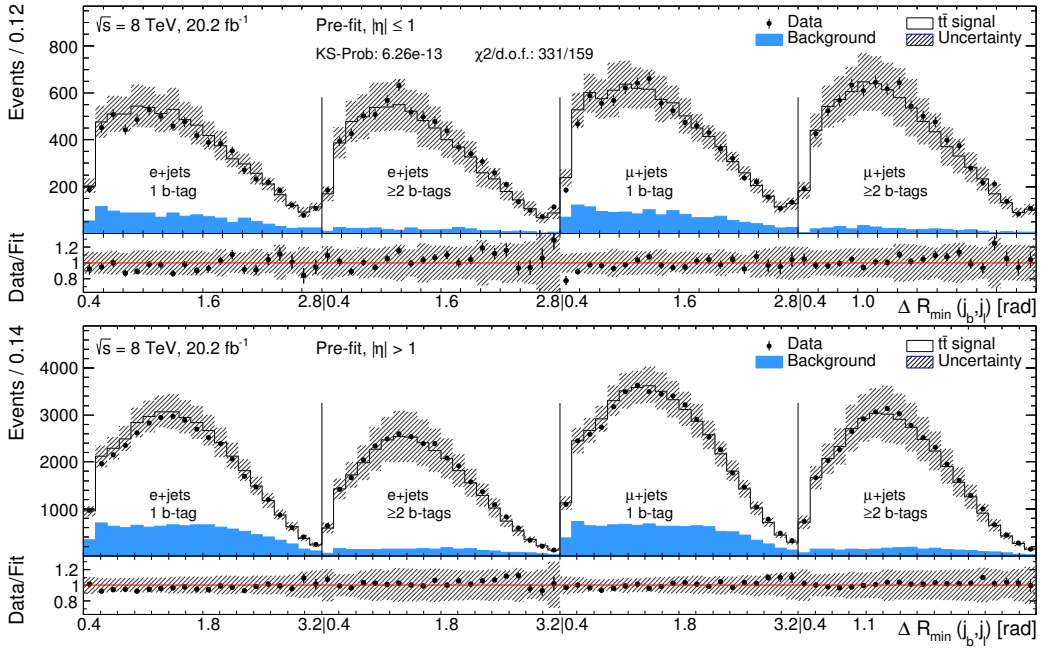

Figure G.1: Pre-fit distributions based on the nominal templates with $\Gamma_t = 1.33$ GeV for the observable $\Delta R_{\text{min}}(j_b, j_l)$ in all eight analysis regions corresponding to different lepton flavours, b-tag multiplicities and jet pseudorapidities. The lower panels show the ratio of data over the expected $t\bar{t}$ signal and background contributions, which are combined in the upper main panels. The vertical lines mark the boundaries between the binned observables in the lepton and b-tag regions. The hatched bands represent the total uncertainty. The systematic uncertainties are derived bin-by-bin based on the systematic variations by adding differences in quadrature. Finally, statistical and systematic uncertainties are added in quadrature to obtain the total uncertainty given in the bands. The results of χ^2 tests and Kolmogorov-Smirnov tests for the concatenated plots are given as well.

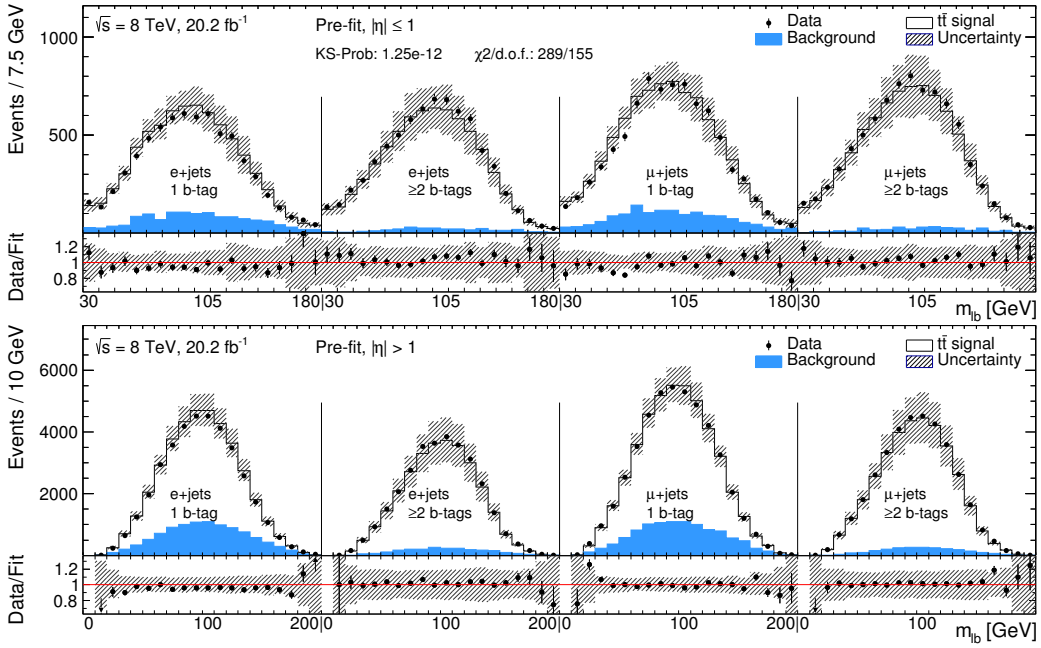

(a)

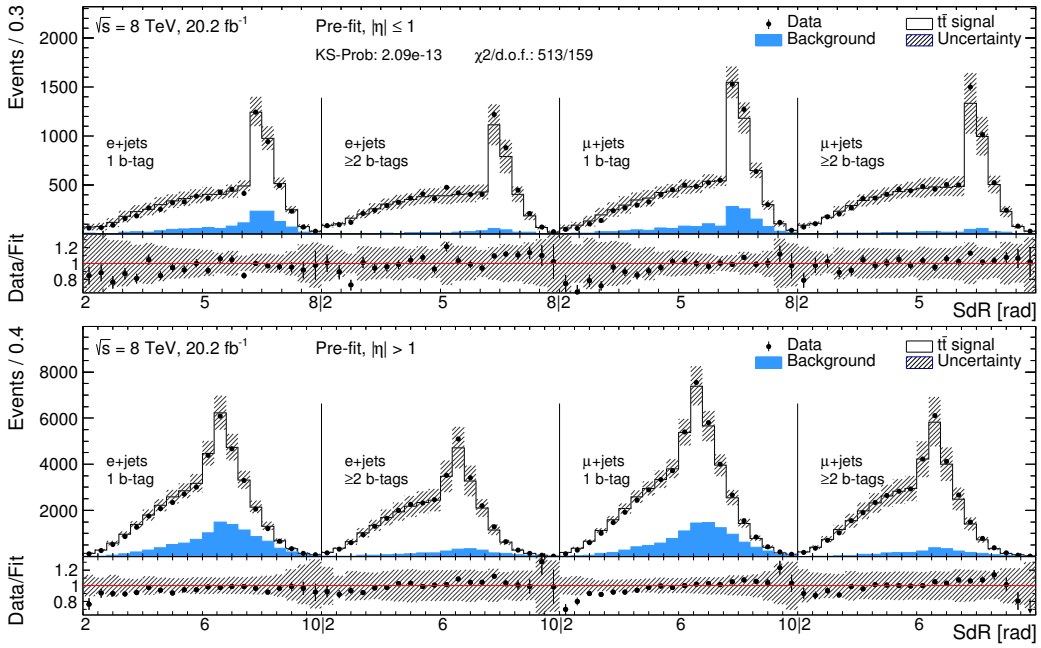

(b)

Figure G.2: Pre-fit distributions based on the nominal templates with $\Gamma_t = 1.33$ GeV for the observables (a) $m_{\ell b}$ and (b) SdR in all eight analysis regions corresponding to different lepton flavours, b-tag multiplicities and jet pseudorapidities. The lower panels show the ratio of data over the expected $t\bar{t}$ signal and background contributions, which are combined in the upper main panels. The vertical lines mark the boundaries between the binned observables in the lepton and b-tag regions. The hatched bands represent the total uncertainty. The systematic uncertainties are derived bin-by-bin based on the systematic variations by adding differences in quadrature. Finally, statistical and systematic uncertainties are added in quadrature to obtain the total uncertainty given in the bands. The results of χ^2 tests and Kolmogorov-Smirnov tests for the concatenated plots are given as well.

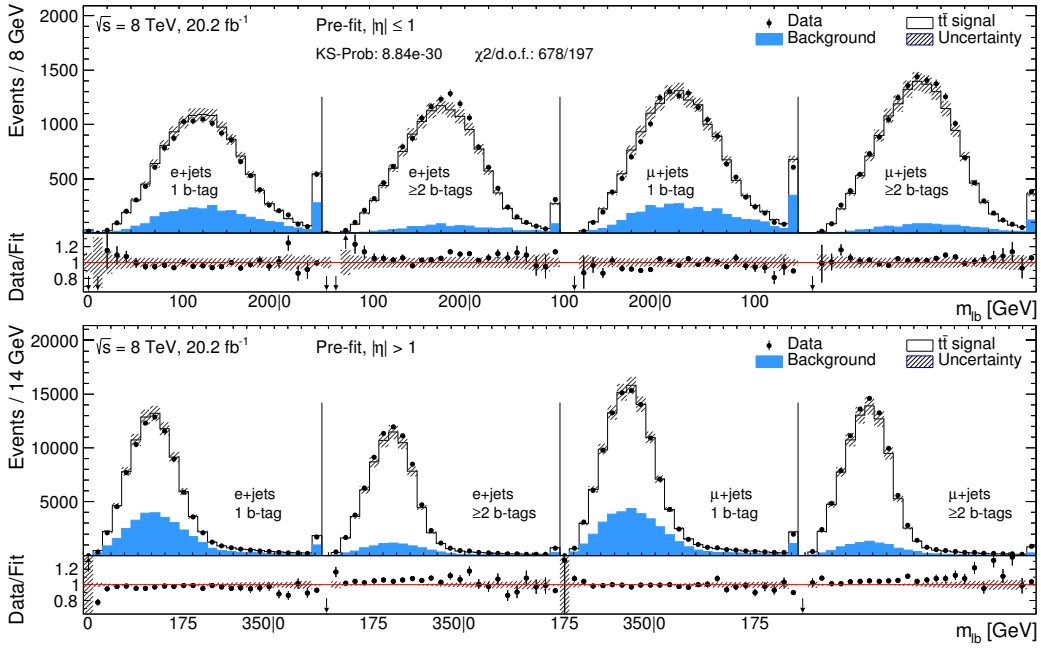

(a)

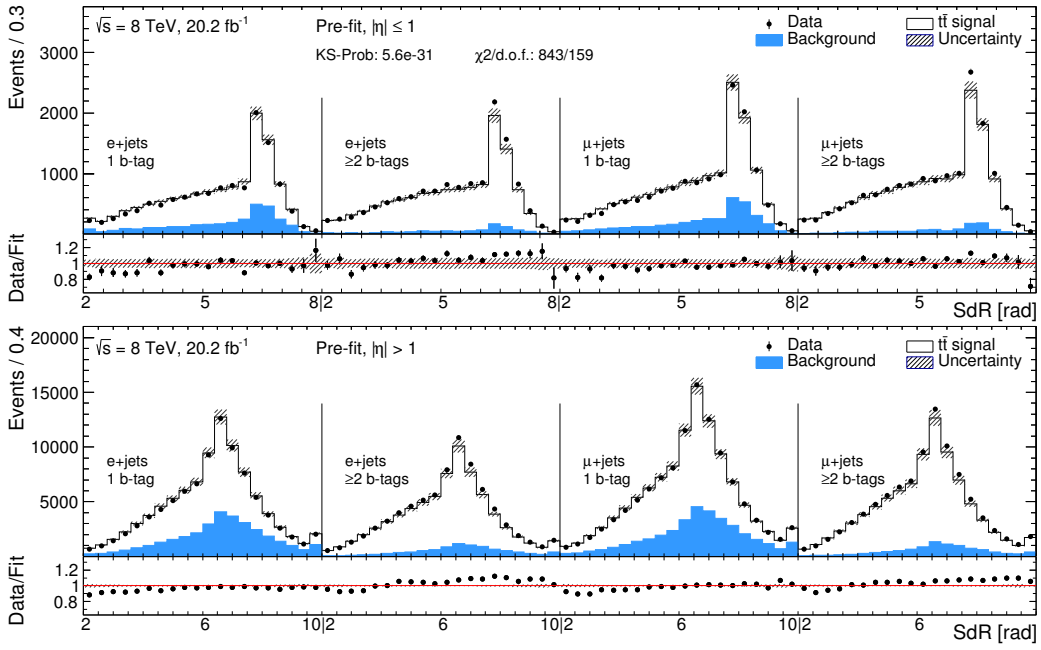

(b)

Figure G.3: Pre-fit distributions based on the nominal templates with $\Gamma_t = 1.33$ GeV for the observables (a) $m_{\ell b}$ and (b) SdR in all eight analysis regions corresponding to different lepton flavours, b-tag multiplicities and jet pseudorapidities. The cut on the logarithm of the KLFitter likelihood is not applied. The lower panels show the ratio of data over the expected $t\bar{t}$ signal and background contributions, which are combined in the upper main panels. The vertical lines mark the boundaries between the binned observables in the lepton and b-tag regions. The hatched bands represent the statistical uncertainty. The results of χ^2 tests and Kolmogorov-Smirnov tests for the concatenated plots are given as well.

H Post-Fit Plots in Individual Analysis Regions

The observable distributions based on the fit results obtained from the final fit to data with the best-fit templates ("post-fit") are presented in Fig. 10.2. In order to better visualise the fit results in the indiviudal analysis regions, these regions are plotted separately in Fig. H.1 for the observable $m_{\ell b}$ and in Fig. H.2 for the observable $\Delta R_{\mathrm{min}}(j_b, j_l)$.

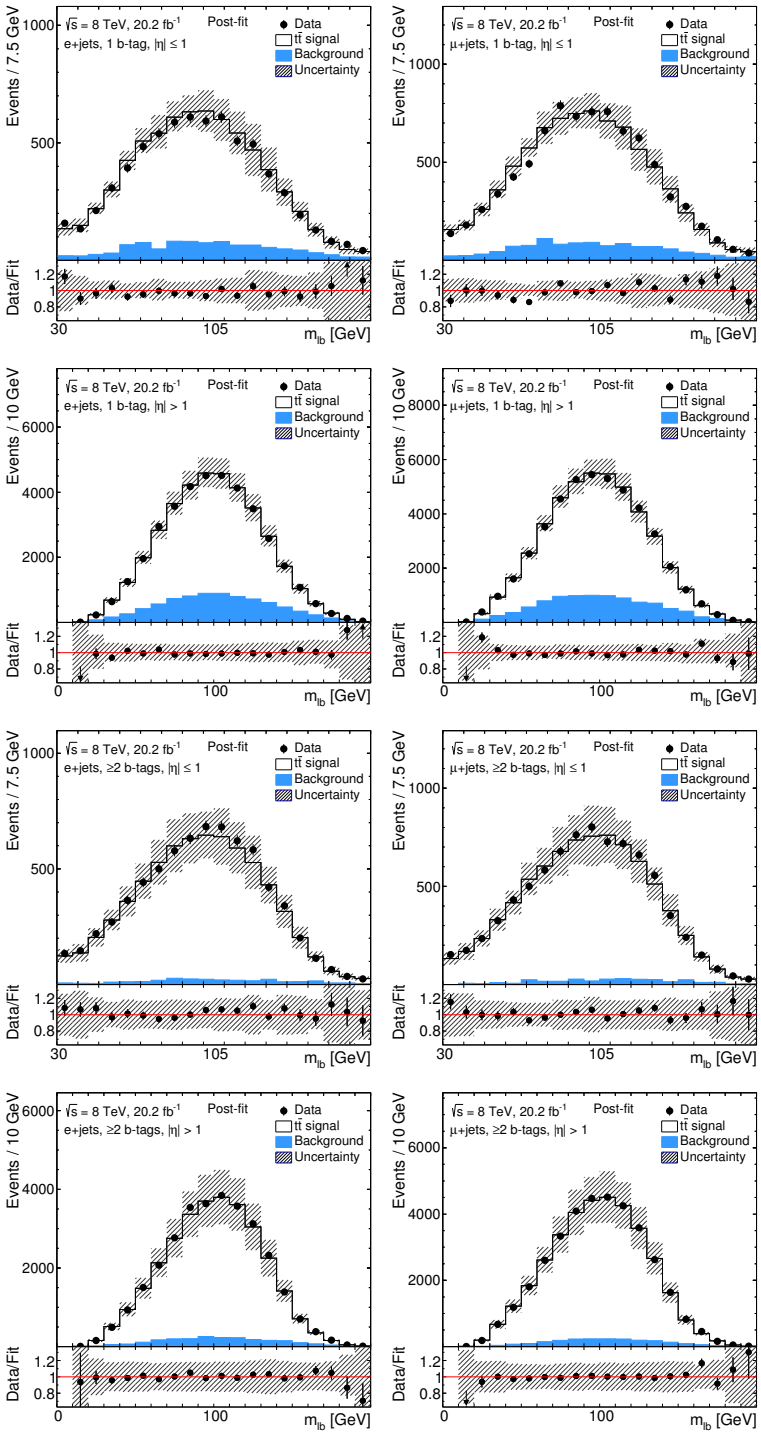

Figure H.1: Post-fit distributions of the eight analysis regions for $m_{\ell b}$ plotted separately using the best-fit templates. The background contributions are combined and the lower panels represent the ratio of data over post-fit $t\bar{t}$ signal and background. Systematic uncertainties are calculated bin-by-bin based on the different systematic variations by adding differences in quadrature. Then, statistical and systematic uncertainties are added in quadrature to obtain the quoted total uncertainty, visualised by the hatched bands.

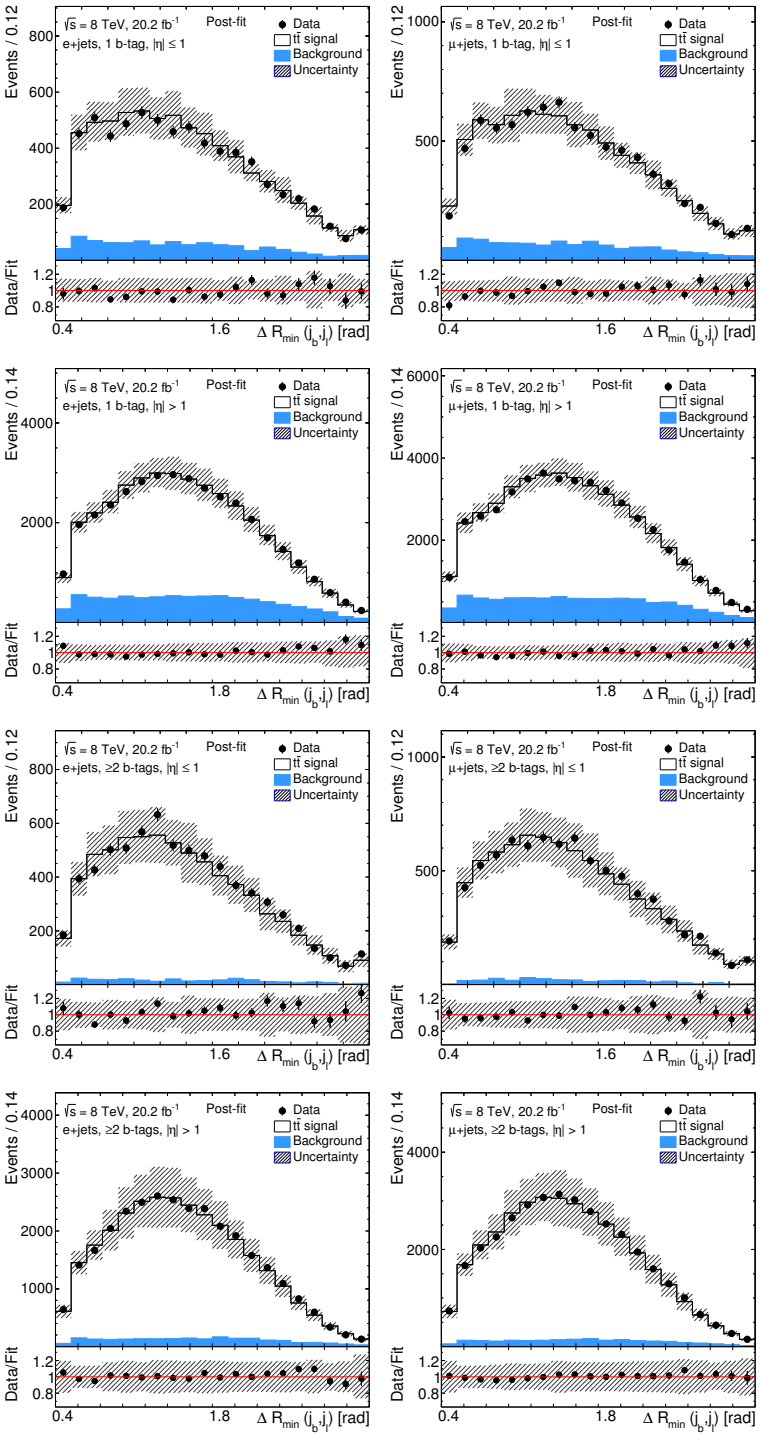

Figure H.2: Post-fit distributions of the eight analysis regions for $\Delta R_{\text{min}}(j_b, j_l)$ plotted separately using the best-fit templates. The background contributions are combined and the lower panels represent the ratio of data over post-fit $t\bar{t}$ signal and background. Systematic uncertainties are calculated bin-by-bin based on the different systematic variations by adding differences in quadrature. Then, statistical and systematic uncertainties are added in quadrature to obtain the quoted total uncertainty, visualised by the hatched bands.

I Two-Dimensional Template Fit

Initial studies with an older prescription for the estimate of the jet energy resolution uncertainty exhibited that the JER might be the largest single systematic effect with an uncertainty of more than 2 GeV. Consequently, a two-dimensional template fit was implemented and tested as a promising approach to constrain the JER uncertainty. A new prescription of the systematic uncertainty due to the JER was released in the course of this analysis which led to remarkably smaller JER uncertainties of the order of 0.25 GeV, close to the values obtained with the much more CPU-intensive two-dimensional template fits. Thus, a significantly faster one-dimensional fit was finally used for the direct decay width measurement.
This appendix serves to briefly describe the extensive studies performed with the fit setup of such a two-dimensional template fit as the corresponding ideas and techniques might be applicable to future analyses in the field of top quark physics.

The two-dimensional template fit, in contrast to the 1D approach, is based on two parameters of interest, Γ_t and a scale factor for the JER uncertainty, simply called "JER" in the following. This JER parameter has an expected value of 1σ. Mass distributions of the hadronically decaying W boson are used for different JER parameter values from 0σ-3σ since this mass, based on the reconstruction of two jets, depends on these differences between the JER parameters but not on Γ_t. Hence, the W boson mass is able to constrain the JER in the fit without affecting the extraction of Γ_t. As a consequence, the definition of the likelihood given in Eq. (7.2) needs to be extended by additional terms for the W boson mass distributions with additional Gaussian priors on the JER parameters. Fig. I.1 illustrates the result of such a two-dimensional fit based on a pseudo-data distribution with an input decay width of $\Gamma_t = 5.0$ GeV and a JER parameter value of 1.0σ.

The validation of this two-dimensional fit method, its stability and the determination of expected statistical uncertainties is done with ensemble tests following the description in Sec. 7.4. However, in addition to a value of Γ_t, also a certain JER parameter value needs to be chosen. For each combination of these two parameters of interest, 1,000 pseudo-data distributions were generated. The chosen decay width values lie in the range $0.5 \leq \Gamma_t \leq 5.0$ GeV using steps of $\Delta\Gamma_t = 0.5$ GeV, and for each of these values of Γ_t the JER parameter covers the values from 0.4σ to 1.6σ in steps of 0.2σ. The results obtained from the pseudo-experiments for all these parameter combinations were used to draw calibration curves, check pull values and calculate the expected statistical uncertainty. In contrast to the figures presented in Sec. 7.5, these two-dimensional fit approach results in calibration planes, planes for the pull values as well as planes for the expected statistical uncertainties.
Fig. I.2 contains such a calibration plane. As an example, the μ+jets channel is chosen for these

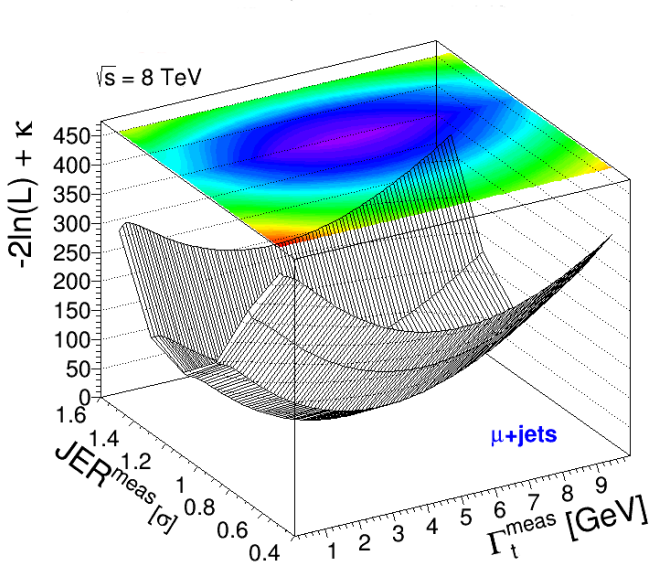

Figure I.1: Illustration of an example fit for the two dimensional fit implementation. The underlying pseudo-data distribution is based on an input decay width of $\Gamma_t = 5.0$ GeV and a JER parameter value of 1.0σ to visualise a comparatively broad parameter range in the plot.

initial test plots. A pseudorapidity split or a cut on the logarithm of the KLFitter likelihood is not applied. The underlying observable sensitive to the top quark decay width is D_{32}. The two-dimensional histogram on the right corresponds to the ratio plot given in Fig. 7.7, here with an additional dimension for JER. The results are in accordance with the findings in Sec. 7.5. The slope is still consistent with one within an uncertainty interval of two standard deviations around the measured slope of 0.995, but the intercept hints at an offset caused by the slightly shifted mean values of samples having small decay width values related to the edge of Γ_t values at 0 GeV. This behaviour due to the physical decay width edge is also reflected by pull distributions.

The expected statistical uncertainties derived from these sets of pseudo-experiments are illustrated in the two-dimensional plots in Fig. I.3, showing consistent results for the muon+jets and electron+jets channel.
Close to the region of expected values of $\Gamma_t = 1.33$ GeV and around a 1σ uncertainty of the jet energy resolution, the uncertainty values predict a single JER uncertainty of around 0.2-0.3 GeV (after separating the purely statistical and normalisation contributions). This uncertainty value is in the range of the quoted JER uncertainty from the actually chosen one-dimensional fit configuration after switching to the latest JER uncertainty prescription with eleven nuisance parameters.
Given the larger complexity of such a two-dimensional fit requiring additional stability tests and cross-checks of correlations (because the additional observable sensitive to JER like the hadronic W boson mass may be highly correlated with other width sensitive observables introducing a bias) and given the far larger CPU intensity of the 2D fit, the final fit to data relies on the one-dimensional

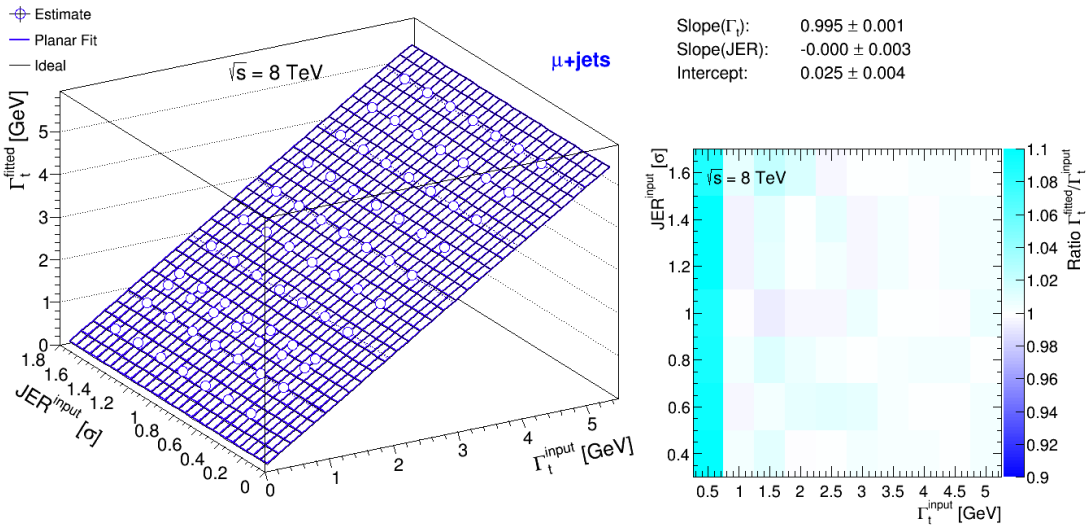

Figure I.2: Calibration plane for the two-dimensional fit implementation. The differences between the obtained fitted mean values and the underlying input parameter values are shown in the ratio plane on the right. The results of the fit are listed as well. The visible deviations from the theoretical expectation are well understood and explained in the text.

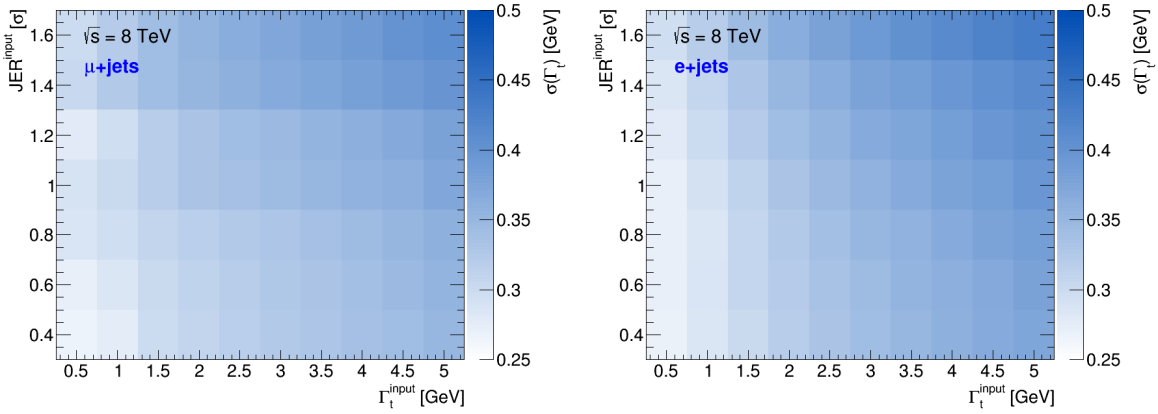

(a) **(b)**

Figure I.3: Mean expected statistical uncertainties for the two-dimensional fit implementation in the plane of tested Γ_t and JER parameter values, used in the underlying pseudo-experiments.

approach with Γ_t as the only parameter of interest. The chosen configuration with two observables and eight exclusive analysis regions constitutes a very good compromise with a still comparatively CPU-intensive fit but with an optimised set of observables, cuts and analysis regions to keep the systematic uncertainties at a low and very satisfying level.

List of Figures

2.1 Top quark pair production: Lowest order Feynman diagrams . . . 16
2.2 Cross-sections of physics processes at the Tevatron and the LHC . . . 17
2.3 Parton distribution functions . . . 19
2.4 $t\bar{t}$ production cross-sections . . . 19
2.5 Single top quark production: Lowest order Feynman diagrams . . . 20
2.6 $t\bar{t}$ pair decay in the lepton+jets channel . . . 24
2.7 W+1 jet production . . . 24
2.8 Top quark mass measurements . . . 25
2.9 Illustration of Γ_t within a mass distribution . . . 27
2.10 Top quark pair decay into a W boson and a b quark . . . 28
2.11 Templates used in a direct measurement of Γ_t performed by CDF . . . 32
2.12 Evolution of $CL_S(\Gamma_t)$ used for a direct measurement of Γ_t performed by CMS . . . 33
2.13 Illustration of $\Gamma(t \to H^+ b)$ including SM and SUSY corrections . . . 36
2.14 Total decay width and branching ratios for the fourth generation t' decay . . . 37

3.1 The LHC and the corresponding accelerator chain . . . 40
3.2 Integrated luminosity in pp collisions in 2012 . . . 41
3.3 ATLAS detector . . . 44
3.4 Inner detector . . . 46
3.5 Calorimeter system . . . 47
3.6 Muon system . . . 49
3.7 Magnet system . . . 51
3.8 Trigger/DAQ system . . . 52

4.1 Different object description levels . . . 54
4.2 Muon reconstruction efficiency . . . 56
4.3 Electron reconstruction efficiency . . . 58
4.4 Jet energy response . . . 61
4.5 Jet vertex fraction - definition and cut . . . 62
4.6 Performance of the MV1 b-tagging algorithm . . . 63
4.7 MV1 algorithm: b-tagging efficiencies and scale factors . . . 64

5.1 Simulated proton-proton collision . . . 68
5.2 Illustration of hadronisation models . . . 69

5.3 Extraction of correction factors for the W+jets background components 72

6.1 Summary of data-taking in 2012 77
6.2 Control plots of kinematic quantities (electron+jets, one b-tag) 81
6.3 Control plots of kinematic quantities (electron+jets, two b-tags) 82
6.4 Control plots of kinematic quantities (muon+jets, one b-tag) 83
6.5 Control plots of kinematic quantities (muon+jets, two b-tags) 84
6.6 Control plots of the observable $m_{\ell b}$ 85
6.7 Control plots of the observable $\Delta R_{\text{min}}(j_b, j_l)$ 86
6.8 Control plots of the lepton p_{T} with logarithmic scale 87
6.9 Comparison of matched/not matched events after KLFitter reconstruction 90
6.10 Control plots of $\ln(L)$ from KLFitter with correctly matched events 91
6.11 Control plots of $\ln(L)$ from KLFitter with correctly matched b-tagged jets 92
6.12 KLFitter reconstruction efficiencies for different configurations based on four or five jets in the reconstruction 97
6.13 KLFitter reconstruction efficiencies for different configurations based on four jets with or without cuts in the reconstruction 99
6.14 Distributions of $m_{\ell b}$ for KLFitter configurations with different Γ_t 100
6.15 Distributions of $\Delta R_{\text{min}}(j_b, j_l)$ for KLFitter configurations with different Γ_t 101

7.1 Template reweighting: MC weights as a function of m_t 106
7.2 Template reweighting: MC weights displayed as histograms 106
7.3 Templates for the observables D_{32}, $m_{\ell b}$ and $\Delta R_{\text{min}}(j_b, j_l)$ (region $|\eta| \leq 1$) 107
7.4 Templates for the observables D_{32}, $m_{\ell b}$ and $\Delta R_{\text{min}}(j_b, j_l)$ (region $|\eta| > 1$) 108
7.5 Closure test at parton level to validate the reweighting method 109
7.6 Closure test at reconstruction level to validate the reweighting method 111
7.7 Calibration curve for the final fit configuration 116
7.8 Pull values and mean expected stat. uncertainties for the final fit configuration . . . 117
7.9 Decay width distributions obtained from pseudo-experiments 118
7.10 Correlations between the two chosen observables $m_{\ell b}$ and $\Delta R_{\text{min}}(j_b, j_l)$ 120

8.1 Fraction of gluon-initiated jets and its uncertainty 128
8.2 Particle level comparison between radiation parameters 133
8.3 Particle level comparison between radiation tunes 134
8.4 PDF set systematic uncertainties as a function of nuisance parameters 137
8.5 Distributions of $m_{\ell b}$ for new NLO generator setups 139
8.6 Shape differences: NLO effects in comparison to known MC generator differences . 140
8.7 Correlation between parton and reconstruction level $m_{\ell b}$ distributions 141
8.8 Asymmetric response of Γ_t to m_t 144
8.9 Distributions of $m_{\ell b}$ for different m_t samples in all analysis regions 147
8.10 Distributions of $m_{\ell b}$ for different m_t samples and Γ_t templates 148

10.1 Concatenated pre-fit distributions for $m_{\ell b}$ and $\Delta R_{\mathrm{min}}(j_b, j_l)$ 164
10.2 Concatenated post-fit distributions for $m_{\ell b}$ and $\Delta R_{\mathrm{min}}(j_b, j_l)$ 165
10.3 Likelihood curves obtained from the fit to data 167
10.4 Measured p-values to extract statistical significances 172

C.1 Control plots without the KLFitter $\ln(L)$ cut (electron+jets, one b-tag) 186
C.2 Control plots without the KLFitter $\ln(L)$ cut (electron+jets, two b-tags) 187
C.3 Control plots without the KLFitter $\ln(L)$ cut (muon+jets, one b-tag) 188
C.4 Control plots without the KLFitter $\ln(L)$ cut (muon+jets, two b-tags) 189

D.1 Correlation between $m_{\ell b}$ and $\Delta R_{\mathrm{min}}(j_b, j_l)$ for signal based on $\Gamma_t = 1.33$ GeV 192
D.2 Correlation between $m_{\ell b}$ and $\Delta R_{\mathrm{min}}(j_b, j_l)$ for signal based on $\Gamma_t = 0.7$ GeV 193
D.3 Correlation between $m_{\ell b}$ and $\Delta R_{\mathrm{min}}(j_b, j_l)$ for signal based on $\Gamma_t = 3.0$ GeV 194
D.4 Correlation between $m_{\ell b}$ and $\Delta R_{\mathrm{min}}(j_b, j_l)$ for background contributions 195
D.5 Correlation between $m_{\ell b}$ and $\Delta R_{\mathrm{min}}(j_b, j_l)$ for a POWHEG+HERWIG generator . . . 196
D.6 Correlation between $m_{\ell b}$ and $\Delta R_{\mathrm{min}}(j_b, j_l)$ for an MC@NLO+HERWIG generator . 197

F.1 Distributions of $m_{\ell b}$ for different m_t samples with $\Gamma_t = 0.5$ GeV 204
F.2 Distributions of $m_{\ell b}$ for different m_t samples with $\Gamma_t = 2.0$ GeV 205
F.3 Distributions of $m_{\ell b}$ for different m_t samples and Γ_t templates ($|\eta| \leq 1$ region) . . . 206

G.1 Pre-fit distributions for $\Delta R_{\mathrm{min}}(j_b, j_l)$ with χ^2 tests 208
G.2 Pre-fit distributions for $m_{\ell b}$ and SdR with χ^2 tests 209
G.3 Pre-fit distributions for $m_{\ell b}$ and SdR with χ^2 tests w/o $\ln(L)$ cut 210

H.1 Post-fit distributions of the eight analysis regions for $m_{\ell b}$ 212
H.2 Post-fit distributions of the eight analysis regions for $\Delta R_{\mathrm{min}}(j_b, j_l)$ 213

I.1 Illustration of a two-dimensional example fit 216
I.2 Calibration plane for the two-dimensional fit implementation 217
I.3 Expected statistical uncertainties for the two-dimensional fit implementation 217

List of Tables

2.1 Particles and mediators in the SM . . . 7
2.2 Masses of fermions . . . 7
2.3 Fundamental forces and their properties . . . 13
2.4 Predictions for single top quark production cross-sections . . . 21
2.5 Measurements of single top quark production cross-sections . . . 21
2.6 Branching ratios $\mathscr{B}$ of the final states from W boson decays . . . 23
2.7 Γ_t at leading order and corrections for different masses m_t . . . 31

5.1 Fundamental generator settings . . . 74

6.1 Event yields in the eight analysis regions . . . 79
6.2 KLFitter reconstruction: Definition of bin labels . . . 98

7.1 List of studied observables . . . 104
7.2 Signal and background parameters with normalisation uncertainties . . . 113
7.3 Pre-fit yields in the eight channel combination . . . 114
7.4 Correlation factors for the two observables . . . 121

8.1 Systematic uncertainties considered in the analysis . . . 124
8.2 Impact of the JES flavour composition on Γ_t . . . 128
8.3 Impact of alternative simulation settings on Γ_t . . . 131
8.4 Mean values from PEs to estimate the impact of m_t . . . 143
8.5 Mean values from PEs to estimate the impact of m_t with various fit configurations . . . 145
8.6 Mean values from PEs to estimate the impact of m_t after template morphing . . . 146
8.7 Summary of systematic uncertainties considered for the Γ_t measurement . . . 151

9.1 One observable fit: Dominant syst. and exp. stat. uncertainties . . . 154
9.2 Two observable fit: Dominant syst. and exp. stat. uncertainties . . . 156
9.3 Comparison of uncert. for $m_{\ell b}$+SdR and $m_{\ell b}+\Delta R_{\mathrm{min}}(j_b, j_l)$, $|\eta|$ split . . . 157
9.4 Comparison of uncert. for $m_{\ell b}$+SdR and $m_{\ell b}+\Delta R_{\mathrm{min}}(j_b, j_l)$, energy split . . . 158
9.5 Comparison of uncert. for $m_{\ell b}$+SdR and $m_{\ell b}+\Delta R_{\mathrm{min}}(j_b, j_l)$, KLFitter options . . . 159
9.6 Comparison of uncert. for $m_{\ell b}+\Delta R_{\mathrm{min}}(j_b, j_l)$ in different b-tag regions . . . 162

10.1 Pre-fit and post-fit yields for $t\bar{t}$ signal and background contributions . . . 166
10.2 Pre-fit and post-fit yields for the multijet background in all analysis regions . . . 166

10.3 Pre-fit and post-fit yields for $t\bar{t}$ signal and background contributions after adding more fit parameters for the W+jets components 170
10.4 Post-fit yields and measured Γ_t values for different options to estimate the impact of the W+jets background 170

B.1 Event yields in the electron+jets channel before applying further analysis cuts . . . 183
B.2 Event yields in the muon+jets channel before applying further analysis cuts 184

D.1 Correlation factors for the two observables for different alternative settings 198

E.1 Considered systematic uncertainties with components treated as effective 200
E.2 Summary of considered systematic uncert. with components treated as effective . . 201

Bibliography

[1] ATLAS Collaboration, Observation of a new particle in the search for the Standard Model Higgs boson with the ATLAS detector at the LHC, *Phys. Lett. B*, 716:1, 2012.

[2] CMS Collaboration, Observation of a new boson at a mass of 125 GeV with the CMS experiment at the LHC, *Phys. Lett. B*, 716:30, 2012.

[3] ATLAS Collaboration, Evidence for the spin-0 nature of the Higgs boson using ATLAS data, *Phys. Lett. B*, 726:120, 2013.

[4] ATLAS Collaboration, Measurement of Higgs boson production in the diphoton decay channel in pp collisions at center-of-mass energies of 7 and 8 TeV with the ATLAS detector, *Phys. Rev. D*, 90:112015, 2014.

[5] ATLAS Collaboration, Measurement of Higgs boson production and couplings in the four-lepton channel in pp collisions at center-of-mass energies of 7 and 8 TeV with the ATLAS detector, *Phys. Rev. D*, 91:012006, 2015.

[6] ATLAS Collaboration, Observation and measurement of Higgs boson decays to WW^* with the ATLAS detector, *Phys. Rev. D*, 92:012006, 2015.

[7] ATLAS Collaboration, Search for the $b\bar{b}$ decay of the Standard Model Higgs boson in associated $(W/Z)H$ production with the ATLAS detector, *JHEP*, 01:069, 2015.

[8] ATLAS Collaboration, Evidence for the Higgs-boson Yukawa coupling to tau leptons with the ATLAS detector, *JHEP*, 04:117, 2015.

[9] ATLAS Collaboration, Search for the associated production of the Higgs boson with a top quark pair in multilepton final states with the ATLAS detector, *Phys. Lett. B*, 749:519–541, 2015.

[10] ATLAS and CMS Collaborations, Measurements of the Higgs boson production and decay rates and constraints on its couplings from a combined ATLAS and CMS analysis of the LHC pp collision data at $\sqrt{s} = 7$ and 8 TeV, *JHEP*, 08:045, 2016.

[11] ATLAS Collaboration, Combination of the searches for Higgs boson production in association with top quarks in the $\gamma\gamma$, multilepton, and $b\bar{b}$ decay channels at $\sqrt{s}$=13 TeV with the ATLAS Detector, *ATLAS-CONF-2016-068*, 2016.

[12] ATLAS Collaboration, Determination of spin and parity of the Higgs boson in the $WW^* \to e\nu\mu\nu$ decay channel with the ATLAS detector, *Eur. Phys. J. C*, 75:231, 2015.

[13] ATLAS Collaboration, Study of the spin and parity of the Higgs boson in diboson decays with the ATLAS detector, *Eur. Phys. J. C*, 75:476, 2015.

[14] CDF Collaboration, A Direct Measurement of the Total Decay Width of the Top Quark, *Phys. Rev. Lett.*, 111:202001, 2013.

[15] CMS Collaboration, Bounding the top quark width using final states with two charged leptons and two jets at $\sqrt{s} = 13$ TeV, *CMS-PAS-TOP-16-019*, 2016.

[16] Joshua Ellis, TikZ-Feynman: Feynman diagrams with TikZ, *arXiv:1601.05437 [hep-ph]*, 2016.

[17] S.L. Glashow, Partial Symmetries of Weak Interactions, *Nucl. Phys.*, 22:579, 1961.

[18] A. Salam and J. C. Ward, Electromagnetic and Weak Interactions, *Phys. Lett.*, 13:168, 1964.

[19] S. Weinberg, A Model of Leptons, *Phys. Rev. Lett.*, 19:1264, 1967.

[20] H. D. Politzer, Reliable Perturbative Results for Strong Interactions?, *Phys. Rev. Lett.*, 30:1346, 1973.

[21] D. J. Gross and F. Wilczek, Asymptotically Free Gauge Theories. I, *Phys. Rev. D*, 8:3633, 1973.

[22] H. D. Politzer, Asymptotic freedom: An approach to strong interactions, *Phys. Rept*, 14:129, 1974.

[23] P. W. Higgs, Broken Symmetries, Massless Particles and Gauge Fields, *Phys. Lett.*, 12:132-133, 1964.

[24] P. W. Higgs, Broken Symmetries and the Masses of Gauge Bosons, *Phys. Rev. Lett.*, 13:508-509, 1964.

[25] D. Griffiths, *Introduction to Elementary Particles*, WILEY-VCH, 2nd Edition, 2008.

[26] M. Thomson, *Modern Particle Physics*, Cambridge University Press, 2013.

[27] M. Kobayashi and T. Maskawa, CP-Violation in the Renormalizable Theory of Weak Interaction, *Prog. Theor. Phys.*, 49(2):652-657, 1973.

[28] C. Patrignani et al. (Particle Data Group), *Chin. Phys. C*, 40:100001, 2016 and 2017 update.

[29] C. Berger, *Elementarteilchenphysik: Von den Grundlagen zu den modernen Experimenten*, Springer, 2nd Edition, 2006.

[30] B. Pontecorvo, Mesonium and anti-mesonium, *Sov. Phys. JETP*, 6:429, 1957.

[31] Z. Maki, M. Nakagawa and S. Sakata, Remarks on the Unified Model of Elementary Particles, *Prog. Theor. Phys.*, 28:870, 1962.

[32] J. Thomson, Cathode rays, *Phil. Mag.*, 44:293–316, 1897.

[33] S. Neddermeyer and C. Anderson, Note on the Nature of Cosmic Ray Particles, *Phys. Rev.*, 51:884–886, 1937.

[34] M. L. Perl et al., Evidence for Anomalous Lepton Production in e^+e^- Annihilation, *Phys. Rev. Lett.*, 35:1489–1492, 1975.

[35] F. Reines and C. L. Cowan, Detection of the Free Neutrino, *Phys. Rev.*, 92:830, 1953.

[36] G. Danby et al., Observation of High-Energy Neutrino Reactions and the Existence of Two Kinds of Neutrinos, *Phys. Rev. Lett.*, 9:36–44, 1962.

[37] DONUT Collaboration, Observation of tau neutrino interactions, *Phys. Lett. B*, 504:218–224, 2001.

[38] E. D. Bloom et al., High-Energy Inelastic ep Scattering at 6-Degrees and 10-Degrees, *Phys. Rev. Lett.*, 23:930–934, 1969.

[39] M. Breidenbach et al., Observed Behavior of Highly Inelastic electron-Proton Scattering, *Phys. Rev. Lett.*, 23:935–939, 1969.

[40] SLAC-SP-017 Collaboration, Discovery of a Narrow Resonance in e^+e^- Annihilation, *Phys. Rev. Lett.*, 33:1406–1408, 1974.

[41] E598 Collaboration, Experimental Observation of a Heavy Particle J, *Phys. Rev. Lett.*, 33:1404–1406, 1974.

[42] CDF Collaboration, T. Aaltonen et al., Observation of Top Quark Production in $p\bar{p}$ Collisions, *Phys. Rev. Lett.*, 74:2626–2631, 1995.

[43] DØ Collaboration, Observation of the Top Quark, *Phys. Rev. Lett.*, 74:2632–2637, 1995.

[44] S. W. Herb et al., Observation of a Dimuon Resonance at 9.5 GeV in 400-GeV Proton-Nucleus Collisions, *Phys. Rev. Lett.*, 39:252, 1977.

[45] F. Halzen and A. D. Martin, *Quarks and Leptons: An Introductory Course in Modern Particle Physics*, John Wiley & Sons, 1984.

[46] TASSO Collaboration, Evidence for Planar Events in e^+e^- Annihilation at High-Energies, *Phys. Lett. B*, 86:243–249, 1979.

[47] PLUTO Collaboration, Evidence for Gluon Bremsstrahlung in e^+e^- Annihilations at High-Energies, *Phys. Lett. B*, 86:418–425, 1979.

[48] P. Villard, Sur la Reflexion et la Refraction des Rayons Cathodiques et des Rayons Deviables du Radium, *Compt. Ren.*, 130:1010, 1900.

[49] M. Planck, Über das Gesetz der Energieverteilung im Normalspectrum, *Ann. Phys.*, 309:553, 1900.

[50] UA1 Collaboration, Experimental Observation of Isolated Large Transverse Energy Electrons with Associated Missing Energy at $s^{1/2} = 540$ GeV, *Phys. Lett. B*, 122:103–116, 1983.

[51] UA2 Collaboration, Observation of Single Isolated Electrons of High Transverse Momentum in Events with Missing Transverse Energy at the CERN anti-pp Collider, *Phys. Lett. B*, 122:476–485, 1983.

[52] UA1 Collaboration, Experimental Observation of Lepton Pairs of Invariant Mass Around 95 GeV/c^2 at the CERN SPS Collider, *Phys. Lett. B*, 126:398–410, 1983.

[53] UA2 Collaboration, Evidence for $Z^0 \rightarrow e^+e^-$ at the CERN anti-pp Collider, *Phys. Lett. B*, 129:130–140, 1983.

[54] Super-Kamiokande Collaboration, Evidence for oscillation of atmospheric neutrinos, *Phys. Rev. Lett.*, 81:1562-1567, 1998.

[55] SNO Collaboration, Measurement of the rate of $\nu_e + d \rightarrow p + p + e^-$ interactions produced by ^8B solar neutrinos at the Sudbury Neutrino Observatory, *Phys. Rev. Lett.*, 87:071301, 2001.

[56] F. P. An et al., Observation of electron-antineutrino disappearance at Daya Bay, *Phys. Rev. Lett.*, 108:171803, 2012.

[57] J. H. Christenson, J. W. Cronin, V. L. Fitch, and R. Turlay, Evidence for the 2π Decay of the K_2^0 Meson, *Phys. Rev. Lett*, 13:138, 1964.

[58] DØ Collaboration, Observation of single top-quark production, *Phys. Rev. Lett.*, 103:092001, 2009.

[59] CDF Collaboration, First Observation of Electroweak Single Top Quark Production, *Phys. Rev. Lett.*, 103:092002, 2009.

[60] V. N. Gribov and L. N. Lipatov, Deep inelastic ep scattering in perturbation theory, *Sov. J. Nucl. Phys.*, 15:438, 1972.

[61] G. Altarelli and G. Parisi, Asymptotic freedom in parton language, *Nucl. Phys. B*, 126:298, 1977.

[62] Y. L. Dokshitzer, Calculation of the Structure Functions for Deep Inelastic Scattering and e^+e^- Annihilation by Perturbation Theory in Quantum Chromodynamics, *Sov. Phys. JETP*, 46:641, 1977.

[63] J. C. Collins, D. E. Soper and G. Sterman, Factorization of Hard Processes in QCD, *Adv. Ser. Direct. High Energy Phys.*, 5:1, 1988.

[64] M. Cacciari et al., Top-pair production at hadron colliders with next-to-next-to-leading logarithmic soft-gluon resummation, *Phys. Lett. B*, 710:612, 2012.

[65] P. Bärnreuther, M. Czakon and A. Mitov, Percent Level Precision Physics at the Tevatron: First Genuine NNLO QCD Corrections to $q\bar{q} \to t\bar{t} + X$, *Phys. Rev. Lett.*, 109:132001, 2012.

[66] M. Czakon and A. Mitov, NNLO corrections to top-pair production at hadron colliders: the all fermionic scattering channels, *JHEP*, 1212:054, 2012.

[67] M. Czakon and A. Mitov, NNLO corrections to top pair production at hadron colliders: the quark-gluon reaction, *JHEP*, 1301:080, 2013.

[68] M. Czakon, P. Fiedler and A. Mitov, The total top quark pair production cross-section at hadron colliders through $\mathcal{O}(\alpha_S^4)$, *Phys. Rev. Lett.*, 110:252004, 2013.

[69] A. D. Martin et al., Parton distributions for the LHC, *Eur. Phys. J. C*, 63:189, 2009.

[70] A. D. Martin et al., Uncertainties on α_S in global PDF analyses and implications for predicted hadronic cross-sections, *Eur. Phys. J. C*, 64:653, 2009.

[71] M. Czakon and A. Mitov, Top++: A Program for the Calculation of the Top-Pair Cross-Section at Hadron Colliders, *Comput. Phys. Commun.*, 185:2930, 2014.

[72] S. Catani, Aspects of QCD, from the Tevatron to the LHC, *arXiv:hep-ph/0005233v1*, 2000.

[73] J. Pumplin et al., New Generation of Parton Distributions with Uncertainties from Global QCD Analysis, *JHEP*, 0207:012, 2002.

[74] A. Quadt, Top quark physics at hadron colliders, *Eur. Phys. J. C*, 48:835–1000, 2006.

[75] M. Czakon, M. L. Mangano, A. Mitov and J. Rojo, Constraints on the gluon PDF from top quark pair production at hadron colliders, *JHEP*, 07:167, 2013.

[76] ATLAS Collaboration, Measurement of the $t\bar{t}$ production cross-section using $e\mu$ events with b-tagged jets in pp collisions at $\sqrt{s} = 7$ TeV and 8 TeV with the ATLAS detector, *Eur. Phys. J. C*, 74:3109, 2014.

[77] ATLAS Collaboration, Measurement of the top pair production cross-section in 8 TeV proton-proton collisions using kinematic information in the lepton+jets final state with ATLAS, *Phys. Rev. D*, 91:112013, 2015.

[78] ATLAS Collaboration, Measurement of the $t\bar{t}$ production cross-section in the τ+jets final state in pp collisions at $\sqrt{s} = 8$ TeV using the ATLAS detector, *Phys. Rev. D*, 95:072003, 2017.

[79] ATLAS and CMS Collaborations, Combination of ATLAS and CMS top quark pair cross-section measurements in the $e\mu$ final state using proton-proton collisions at $\sqrt{s} = 8$ TeV, *ATLAS-CONF-2014-054*, 2014.

[80] ATLAS Collaboration, Measurement of the $t\bar{t}$ production cross-section using $e\mu$ events with b-tagged jets in pp collisions at $\sqrt{s} = 13$ TeV with the ATLAS detector, *Phys. Lett. B*, 761:136, 2016.

[81] H.-L. Lai et al., New parton distributions for collider physics, *Phys. Rev. D*, 82:074024, 2010.

[82] The Durham HepData Project,
see: `http://hepdata.cedar.ac.uk/pdf/pdf3.html`, as of 10th March 2017.

[83] CDF and DØ Collaborations, Combination of measurements of the top-quark pair production cross section from the Tevatron Collider, *Phys. Rev. D*, 89:072001, 2014.

[84] CMS Collaboration, First measurement of the top quark pair production cross section in proton-proton collisions at $\sqrt{s} = 5.02$ TeV, *CMS-PAS-TOP-16-015*, 2016.

[85] CMS Collaboration, Measurement of the $t\bar{t}$ production cross section in the $e\mu$ channel in proton-proton collisions at $\sqrt{s} = 7$ and 8 TeV, *JHEP*, 08:029, 2016.

[86] CMS Collaboration, Measurement of the $t\bar{t}$ production cross section using events in the $e\mu$ final state in pp collisions at $\sqrt{s} = 13$ TeV, *Eur. Phys. J. C*, 77:172, 2017.

[87] ATLAS Collaboration, Measurements of the $t\bar{t}$ production cross-section in the dilepton and lepton-plus-jets channels and of the ratio of the $t\bar{t}$ and Z boson cross-sections in pp collisions at $\sqrt{s} = 13$ TeV with the ATLAS detector, *ATLAS-CONF-2015-049*, 2015.

[88] CMS Collaboration, Measurement of the $t\bar{t}$ production cross section using events with one lepton and at least one jet in pp collisions at $\sqrt{s} = 13$ TeV, *CMS-TOP-16-006*, 2016.

[89] CMS Collaboration, Measurement of the $t\bar{t}$ production cross section at 13 TeV in the all-jets final state, *CMS-PAS-TOP-16-013*, 2016.

[90] ATLAS Collaboration, Summary plots from the ATLAS Top physics group, see: `https://atlas.web.cern.ch/Atlas/GROUPS/PHYSICS/CombinedSummaryPlots/TOP/`, as of 17th September 2017.

[91] J. M. Campbell, R. Frederix, F. Maltoni and F. Tramontano, Next-to-leading order predictions for t-channel single-top production at hadron colliders, *Phys. Rev. Lett.*, 102:182003, 2009.

[92] N. Kidonakis, NNLL resummation for s-channel single top quark production, *Phys. Rev. D*, 81:054028, 2010.

[93] N. Kidonakis, Two-loop soft anomalous dimensions for single top quark associated production with a W^- or H^-, *Phys. Rev. D*, 82:054018, 2010.

[94] N. Kidonakis, Next-to-next-to-leading-order collinear and soft gluon corrections for t-channel single top quark production, *Phys. Rev. D*, 83:091503, 2011.

[95] P. Kant et al., HATHOR for single top-quark production: Updated predictions and uncertainty estimates for single top-quark production in hadronic collisions, *Comput. Phys. Commun.*, 191:74-89, 2015.

[96] N. Kidonakis, Theoretical results for electroweak-boson and single-top production, *arXiv:1506.04072 [hep-ph]*, 2015.

[97] DØ Collaboration, Model-independent measurement of t-channel single top quark production in $p\bar{p}$ collisions at $\sqrt{s} = 1.96$ TeV, *Phys. Lett. B*, 705:313-319, 2011.

[98] CDF Collaboration, Observation of Single Top Quark Production and Measurement of $|V_{tb}|$ with CDF, *Phys. Rev. D*, 82:112005, 2010.

[99] CDF and DØ Collaborations, Observation of s-channel production of single top quarks at the Tevatron, *Phys. Rev. Lett.*, 112:231803, 2014.

[100] ATLAS Collaboration, Evidence for the associated production of a W boson and a top quark in ATLAS at $\sqrt{s} = 7$ TeV, *Phys. Lett. B*, 716:142, 2012.

[101] CMS Collaboration, Evidence for associated production of a single top quark and W boson in pp collisions at $\sqrt{s} = 7$ TeV, *Phys. Rev. Lett.*, 110:022003, 2013.

[102] ATLAS Collaboration, Fiducial, total and differential cross-section measurements of t-channel single top-quark production in pp collisions at 8 TeV using data collected by the ATLAS detector, *Eur. Phys. J. C*, 77:531, 2017.

[103] ATLAS Collaboration, Measurement of the production cross-section of a single top quark in association with a W boson at 8 TeV with the ATLAS experiment, *JHEP*, 01:064, 2016.

[104] ATLAS Collaboration, Evidence for single top-quark production in the s-channel in proton-proton collisions at $\sqrt{s} = 8$ TeV with the ATLAS detector using the Matrix Element Method, *Phys. Lett. B*, 756:228, 2016.

[105] ATLAS and CMS Collaborations, Combination of single top-quark cross-section measurements in the t-channel at $\sqrt{s} = 8$ TeV with the ATLAS and CMS experiments, *ATLAS-CONF-2013-098*, 2013.

[106] ATLAS and CMS Collaborations, Combination of cross-section measurements for associated production of a single top-quark and a W boson at $\sqrt{s} = 8$ TeV with the ATLAS and CMS experiments, *ATLAS-CONF-2016-023*, 2016.

[107] ATLAS Collaboration, Measurement of the inclusive cross-sections of single top-quark and top-antiquark t-channel production in pp collisions at $\sqrt{s} = 13$ TeV with the ATLAS detector, *JHEP*, 04:086, 2017.

[108] ATLAS Collaboration, Measurement of the cross-section for producing a W boson in association with a single top quark in pp collisions at $\sqrt{s} = 13$ TeV with ATLAS, *CERN-EP-2016-238*, 2016.

[109] W. Bernreuther, Top quark physics at the LHC, *arXiv:0805.1333v1 [hep-ph]*, 2008.

[110] M. Baak et al., The global electroweak fit at NNLO and prospects for the LHC and ILC, *Eur. Phys. J. C*, 74:3046, 2014.

[111] ATLAS Collaboration, Measurement of the top quark mass in the $t\bar{t} \to$ dilepton channel from $\sqrt{s} = 8$ TeV ATLAS data, *Phys. Lett. B*, 761:350-371, 2016.

[112] ATLAS Collaboration, Measurement of the Top Quark Mass from $\sqrt{s} = 7$ TeV ATLAS Data using a 3-dimensional Template Fit, *ATLAS-CONF-2013-046*, 2013.

[113] ATLAS Collaboration, Measurement of the Top Quark Mass in Dileptonic Top Quark Pair Decays with $\sqrt{s} = 7$ TeV ATLAS Data, *ATLAS-CONF-2013-077*, 2013.

[114] CMS Collaboration, Measurement of the top-quark mass in $t\bar{t}$ events with lepton+jets final states in pp collisions at $\sqrt{s} = 7$ TeV, *JHEP*, 12:105, 2012.

[115] CMS Collaboration, Measurement of the top-quark mass in $t\bar{t}$ events with dilepton final states in pp collisions at $\sqrt{s} = 7$ TeV, *Eur. Phys. J. C*, 72:2202, 2012.

[116] CMS Collaboration, Measurement of the top-quark mass in all-jets $t\bar{t}$ events in pp collisions at $\sqrt{s} = 7$ TeV, *Eur. Phys. J. C*, 74:2758, 2014.

[117] ATLAS and CMS Collaborations, Combination of ATLAS and CMS results on the mass of the top-quark using up to 4.9 fb^{-1} of $\sqrt{s} = 7$ TeV LHC data, *ATLAS-CONF-2013-102*, 2013.

[118] ATLAS Collaboration, Measurement of the top quark mass in the $t\bar{t} \to$ lepton+jets and $t\bar{t} \to$ dilepton channels using $\sqrt{s} = 7$ TeV ATLAS data, *Eur. Phys. J. C*, 75:330, 2015.

[119] ATLAS Collaboration, Measurement of the top-quark mass in the fully hadronic decay channel from ATLAS data at $\sqrt{s} = 7$ TeV, *Eur. Phys. J. C*, 75:158, 2015.

[120] ATLAS Collaboration, Measurement of the top quark mass in topologies enhanced with single top-quarks produced in the t-channel in $\sqrt{s} = 8$ TeV ATLAS data, *ATLAS-CONF-2014-055*, 2014.

[121] ATLAS Collaboration, Top-quark mass measurement in the all-hadronic $t\bar{t}$ decay channel at $\sqrt{s} = 8$ TeV with the ATLAS detector, *CERN-EP-2016-264*, 2016.

[122] CMS Collaboration, Measurement of the top quark mass using single top quark events in proton-proton collisions at $\sqrt{s} = 8$ TeV, *Eur. Phys. J. C*, 77:354, 2017.

[123] CMS Collaboration, Measurement of the top quark mass using proton-proton data at $\sqrt{s} =$ 7 and 8 TeV, *Phys. Rev. D*, 93:072004, 2016.

[124] ATLAS, CDF, CMS and DØ Collaborations, First combination of Tevatron and LHC measurements of the top-quark mass, *ATLAS-CONF-2014-008*, 2014.

[125] ATLAS Collaboration, Measurement of the top quark charge in pp collisions at $\sqrt{s} = 7$ TeV with the ATLAS detector, *JHEP*, 11:031, 2013.

[126] CMS Collaboration, Constraints on the Top-Quark Charge from Top-Pair Events, *CMS-PAS-TOP-11-031*, 2011.

[127] DØ Collaboration, Experimental Discrimination between Charge $2e/3$ Top Quark and Charge $4e/3$ Exotic Quark Production Scenarios, *Physical Review Leters*, 98:041801, 2007.

[128] CDF Collaboration, Exclusion of exotic top-like quarks with -4/3 electric charge using jet-charge tagging in single-lepton $t\bar{t}$ events at CDF, *Phys. Rev. D*, 88:032003, 2013.

[129] ATLAS Collaboration, Observation of Spin Correlation in $t\bar{t}$ Events from pp Collisions at $\sqrt{s} = 7$ TeV Using the ATLAS Detector, *Phys. Rev. Lett.*, 108:212001, 2012.

[130] ATLAS Collaboration, Measurements of spin correlation in top-antitop quark events from proton-proton collisions at $\sqrt{s} = 7$ TeV using the ATLAS detector, *Phys. Rev. D*, 90:112016, 2014.

[131] ATLAS Collaboration, Measurement of Spin Correlation in Top-Antitop Quark Events and Search for Top Squark Pair Production in pp Collisions at $\sqrt{s} = 8$ TeV Using the ATLAS detector, *Phys. Rev. Lett.*, 114:142001, 2015.

[132] ATLAS Collaboration, Measurements of top quark spin observables in $t\bar{t}$ events using dilepton final states in $\sqrt{s} = 8$ TeV pp collisions with the ATLAS detector, *JHEP*, 03:113, 2017.

[133] CMS Collaboration, Measurements of $t\bar{t}$ spin correlations and top-quark polarization using dilepton final states in pp collisions at $\sqrt{s} = 7$ TeV, *Phys. Rev. Lett.*, 112:182001, 2014.

[134] CMS Collaboration, Measurements of spin correlations in $t\bar{t}$ production using the matrix element method in the muon+jets final state in pp collisions at $\sqrt{s} = 8$ TeV, *Phys. Lett. B*, 758:321, 2016.

[135] CMS Collaboration, Measurements of $t\bar{t}$ spin correlations and top quark polarization using dilepton final states in pp collisions at $\sqrt{s} = 8$ TeV, *Phys. Rev. D*, 93:052007, 2016.

[136] ATLAS Collaboration, Measurement of the W boson polarisation in top quark decays with the ATLAS detector, *JHEP*, 1206:88, 2012.

[137] ATLAS Collaboration, Measurement of the W boson polarisation in $t\bar{t}$ events from pp collisions at $\sqrt{s} = 8$ TeV in the lepton+jets channel with ATLAS, *Eur. Phys. J. C*, 77:264, 2017.

[138] CMS Collaboration, Measurement of the W-boson helicity in top-quark decays from $t\bar{t}$ production in lepton+jets events in pp collisions at $\sqrt{s} = 7$ TeV, *JHEP*, 10:167, 2013.

[139] CMS Collaboration, Measurement of the W boson helicity in events with a single reconstructed top quark in pp collisions at $\sqrt{s} = 8$ TeV, *JHEP*, 01:053, 2015.

[140] CMS Collaboration, Measurement of the W boson helicity fractions in the decays of top quark pairs to lepton+jets final states produced in pp collisions at $\sqrt{s} = 8$ TeV, *Phys. Lett. B*, 762:512, 2016.

[141] ATLAS Collaboration, Search for anomalous couplings in the Wtb vertex from the measurement of double differential angular decay rates of single top quarks produced in the t-channel with the ATLAS detector, *JHEP*, 04:023, 2016.

[142] ATLAS Collaboration, Probing the Wtb vertex structure in t-channel single-top-quark production and decay in pp collisions at $\sqrt{s} = 8$ TeV with the ATLAS detector, *JHEP*, 04:124, 2017.

[143] ATLAS Collaboration, Analysis of the Wtb vertex from the measurement of triple-differential angular decay rates of single top quarks produced in the t-channel at $\sqrt{s} = 8$ TeV with the ATLAS detector, *CERN-EP-2017-089*, 2017.

[144] CMS Collaboration, Search for anomalous Wtb couplings and flavour-changing neutral currents in t-channel single top quark production in pp collisions at $\sqrt{s} = 7$ and 8 TeV, *JHEP*, 02:028, 2017.

[145] DØ Collaboration, Measurement of the forward-backward asymmetry in top quark-antiquark production in $p\bar{p}$ collisions using the lepton+jets channel, *Phys. Rev. D*, 90:072011, 2014.

[146] DØ Collaboration, Measurement of the forward-backward asymmetry in the distribution of leptons in $t\bar{t}$ events in the lepton+jets channel, *Phys. Rev. D*, 90:072001, 2014.

[147] CDF Collaboration, Measurement of the top quark forward-backward production asymmetry and its dependence on event kinematic properties, *Phys. Rev. D*, 87:092002, 2013.

[148] CDF Collaboration, Measurement of the inclusive leptonic asymmetry in top-quark pairs that decay to two charged leptons at CDF, *Phys. Rev. Lett.*, 113:042001, 2014.

[149] ATLAS Collaboration, Measurement of the top quark pair production charge asymmetry in proton-proton collisions at 7 TeV using the ATLAS detector, *JHEP*, 02:107, 2014.

[150] ATLAS Collaboration, Measurement of the charge asymmetry in dileptonic decays of top quark pairs in pp collisions at $\sqrt{s} = 7$ TeV using the ATLAS detector, *JHEP*, 05:061, 2015.

[151] ATLAS Collaboration, Measurement of the charge asymmetry in top-quark pair production in the lepton-plus-jets final state in pp collision data at $\sqrt{s} = 8$ TeV with the ATLAS detector, *Eur. Phys. J. C*, 76:87, 2016.

[152] ATLAS Collaboration, Measurement of the charge asymmetry in highly boosted top-quark pair production in $\sqrt{s} = 8$ TeV pp collision data collected by the ATLAS experiment, *Phys. Lett. B*, 756:51-71, 2016.

[153] ATLAS Collaboration, Measurements of the charge asymmetry in top-quark pair production in the dilepton final state at $\sqrt{s} = 8$ TeV with the ATLAS detector, *Phys. Rev. D*, 94:032006, 2016.

[154] CMS Collaboration, Inclusive and differential measurements of the $t\bar{t}$ charge asymmetry in proton-proton collisions at $\sqrt{s} = 7$ TeV, *Phys. Lett. B*, 717:129-150, 2012.

[155] CMS Collaboration, Measurements of the $t\bar{t}$ charge asymmetry using the dilepton decay channel in pp collisions at $\sqrt{s} = 7$ TeV, *JHEP*, 04:191, 2014.

[156] CMS Collaboration, Inclusive and differential measurements of the $t\bar{t}$ charge asymmetry in pp collisions at $\sqrt{s} = 8$ TeV, *Phys. Lett. B*, 757:154, 2016.

[157] CMS Collaboration, Measurements of $t\bar{t}$ charge asymmetry using dilepton final states in pp collisions at $\sqrt{s} = 8$ TeV, *Phys. Lett. B*, 760:365, 2016.

[158] ATLAS Collaboration, Measurement of the $t\bar{t}W$ and $t\bar{t}Z$ production cross sections in pp collisions at $\sqrt{s} = 8$ TeV with the ATLAS detector, *JHEP*, 11:172, 2015.

[159] ATLAS Collaboration, Measurement of the $t\bar{t}W$ and $t\bar{t}Z$ production cross sections in multilepton final states using 3.2 fb^{-1} of pp collisions at $\sqrt{s} = 13$ TeV with the ATLAS detector, *Eur. Phys. J. C*, 77:40, 2017.

[160] CMS Collaboration, Measurement of associated production of vector bosons and $t\bar{t}$ at $\sqrt{s} =$ 7 TeV, *Phys. Rev. Lett.*, 110:172002, 2013.

[161] CMS Collaboration, Measurement of top quark-antiquark pair production in association with a W or Z boson in pp collisions at $\sqrt{s} = 8$ TeV, *Eur. Phys. J. C*, 74:3060, 2014.

[162] CMS Collaboration, Observation of top quark pairs produced in association with a vector boson in pp collisions at $\sqrt{s} = 8$ TeV, *JHEP*, 01:096, 2016.

[163] ATLAS Collaboration, Observation of top-quark pair production in association with a photon and measurement of the $t\bar{t}\gamma$ production cross section in pp collisions at $\sqrt{s} = 7$ TeV using the ATLAS detector, *Phys. Rev. D*, 91:072007, 2015.

[164] ATLAS Collaboration, Measurement of the $t\bar{t}\gamma$ production cross section in proton-proton collisions at $\sqrt{s} = 8$ TeV with the ATLAS detector, *CERN-EP-2017-086*, 2017.

[165] CMS Collaboration, Measurement of the inclusive top-quark pair + photon production cross section in the muon + jets channel in pp collisions at 8 TeV, *CMS-PAS-TOP-13-011*, 2013.

[166] CMS Collaboration, Measurement of the semileptonic $t\bar{t}\gamma$ production cross section in pp collisions at $\sqrt{s} = 8$ TeV, *CERN-EP-2017-112*, 2017.

[167] M. Jezabek and J. H. Kühn, QCD corrections to semileptonic decays of heavy quarks, *Nucl. Phys. B*, 314:1, 1989.

[168] I. I. Bigi et al., Production and Decay Properties of Ultraheavy Quarks, *Phys. Lett. B*, 181:157, 1986.

[169] A. Czarnecki and K. Melnikov, Two-loop QCD corrections to top quark width, *Nucl. Phys. B*, 554:520, 1999.

[170] K. G. Chetyrkin, R. Harlander, T. Seidensticker and M. Steinhauser, Second Order QCD Corrections to $\Gamma(t \to W b)$, *Phys. Rev. D*, 60:114015, 1999.

[171] A. Czarnecki, Two-loop Light Quark Corrections To The Top Width, *Act. Phys. Pol. B*, 26:845-849, 1995.

[172] J. Gao, Ch. Sh. Li and H. X. Zhu, Top-Quark Decay at Next-to-Next-to-Leading Order in QCD, *Phys. Rev. Lett.*, 110:042001, 2013.

[173] CMS Collaboration, Measurement of the ratio $\mathcal{B}(t \to W b)/\mathcal{B}(t \to W q)$ in pp collisions at $\sqrt{s} = 8$ TeV, *Phys. Lett. B*, 736:33, 2014.

[174] CMS Collaboration, Measurement of the single top t-channel cross section in pp collisions at $\sqrt{s} = 7$ TeV, *JHEP*, 12:035, 2012.

[175] DØ Collaboration, Improved determination of the width of the top quark, *Phys. Rev. D*, 85:091104, 2012.

[176] J. Guasch et al., Top-Quark Production and Decay in the MSSM, *arXiv:hep-ph/0003109*, 2000.

[177] D. P. Roy, Looking for the Charged Higgs Boson, *Mod. Phys. Lett. A*, 19:1813-1828, 2004.

[178] D. Garcia, W. Hollik, R. A. Jiméney and J. Solà, Electroweak Supersymmetric Quantum Corrections to the Top Quark Width, *Nucl. Phys. B*, 427:53-80, 1994.

[179] A. Dabelstein et al., Strong Supersymmetric Quantum Effects on the Top Quark Width, *Nucl. Phys. B*, 454:75-85, 1995.

[180] A. Czarnecki and S. Davidson, On the QCD corrections to the charged Higgs decay of a heavy quark, *Phys. Rev. D*, 47:3063-3064, 1993.

[181] A. Czarnecki and S. Davidson, QCD corrections to the charged Higgs decay of a heavy quark, *Phys. Rev. D*, 48:4183-4187, 1993.

[182] A. Coarasa, J. Guasch, W. Hollik and J. Solà, Top quark decay into charged Higgs boson in a general Two-Higgs-Doublet model: implications for the TEVATRON data, *Phys. Lett. B*, 442:326-334, 1998.

[183] A. Djouadi, W. Hollik and C. Junger, QCD Corrections to the Top Decay Mode $t \to \tilde{t}\chi^0$, *Phys. Rev. D*, 54:5629-5635, 1996.

[184] F. Larios, R. Martinez and M.A. Perez, New Physics effects in the flavor-changing neutral couplings of the top quark, *Int. J. Mod. Phys. A*, 21:3473-3494, 2006.

[185] G. Eilam, J. L. Hewett and A. Soni, Rare decays of the top quark in the standard and two-Higgs-doublet models, *Phys. Rev. D*, 59:039901, 1999.

[186] B. Mele, S. Petrarca and A. Soddu, A new evaluation of the $t \to cH$ decay width in the standard model, *Phys.Lett.B*, 435:401-406, 1998.

[187] J. A. Aguilar-Saavedra and B. M. Nobre, Rare top decays $t \to c\gamma$, $t \to cg$ and CKM unitarity, *Phys. Lett. B*, 553:251-260, 2003.

[188] J. A. Aguilar-Saavedra, Effects of mixing with quark singlets, *Phys. Rev. D*, 69:099901, 2004.

[189] J. A. Aguilar-Saavedra, Top flavour-changing neutral interactions: theoretical expectations and experimental detection, *Acta Phys. Polon. B*, 35:2695-2710, 2004.

[190] J. Alwall et al., Is $V_{tb} \simeq 1$?, *Eur. Phys. J. C*, 49:791-801, 2007.

[191] Y. Chao et al., Threshold Effects in the Decay of Heavy b' and t' Quarks, *Phys. Rev. D*, 84:014029, 2011.

[192] G. D. Kribs, T. Plehn, M. Spannowsky and T. M. P. Tait, Four Generations and Higgs Physics, *Phys. Rev. D*, 76:075016, 2007.

[193] B. Holdom et al., Four Statements about the Fourth Generation, *PMC Phys. A*, 3:4, 2009.

[194] F. J. Botella and L. L. Chau, Anticipating the higher generations of quarks from rephasing invariance of the mixing matrix, *Phys. Lett. B*, 168:96, 1986.

[195] O. Brüning et al., *LHC Design Report: Volume I, The LHC Main Ring*, CERN, 2004.

[196] O. Brüning et al., *LHC Design Report: Volume II, The LHC Infrastructure and General Services*, CERN, 2004.

[197] M. Benedikt, P. Collier, V. Mertens, J. Poole and K. Schindl, *LHC Design Report: Volume III, The LHC Injector Chain*, CERN, 2004.

[198] *LEP Design Report: Volume II, The LEP Main Ring*, CERN, 1984.

[199] ATLAS Collaboration, The ATLAS Experiment at the CERN Large Hadron Collider, *JINST*, 3:S08003, 2008.

[200] ATLAS Collaboration, *ATLAS Detector and Physics Performance, Technical Design Report: Volume I*, CERN, 1999.

[201] ATLAS Collaboration, *ATLAS Detector and Physics Performance, Technical Design Report: Volume II*, CERN, 1999.

[202] CMS Collaboration, The CMS experiment at the CERN LHC, *JINST*, 3:S08004, 2008.

[203] LHCb Collaboration, The LHCb Detector at the LHC, *JINST*, 3:S08005, 2008.

[204] ALICE Collaboration, The ALICE experiment at the CERN LHC, *JINST*, 3:S08002, 2008.

[205] TOTEM Collaboration, The TOTEM Experiment at the CERN Large Hadron Collider, *JINST* 3:S08007, 2008.

[206] LHCf Collaboration, The LHCf detector at the CERN Large Hadron Collider, *JINST* 3:S08006, 2008.

[207] MoEDAL Collaboration, Technical Design Report of the MoEDAL Experiment, *CERN-LHCC-2009-006*, 2009.

[208] CERN, The CERN accelerator complex, *OPEN-PHO-ACCEL-2016-009*, 2016.

[209] ATLAS Collaboration, Luminosity Public Results, see: `https://twiki.cern.ch/twiki/bin/view/AtlasPublic/LuminosityPublicResults`, as of 8th September 2017.

[210] ATLAS Collaboration, Luminosity determination in pp collisions at $\sqrt{s} = 8$ TeV using the ATLAS detector at the LHC, *Eur. Phys. J. C*, 76:653, 2016.

[211] ATLAS Collaboration, ATLAS Insertable B-Layer Technical Design Report, *CERN-LHCC-2010-013*, 2010.

[212] ATLAS Collaboration, The ATLAS Simulation Infrastructure, *Eur. Phys. J. C*, 70:823, 2010.

[213] T. Carli, K. Rabbertz and S. Schumann, Studies of Quantum Chromodynamics at the LHC, *arXiv:1506.03239 [hep-ex]*, 2015.

[214] ATLAS Collaboration, Performance of the ATLAS Silicon Pattern Recognition Algorithm in Data and Simulation at $\sqrt{s} = 7$ TeV, *ATLAS-CONF-2010-072*, 2010.

[215] ATLAS Collaboration, Performance of the ATLAS Inner Detector Track and Vertex Reconstruction in the High Pile-Up LHC Environment, *ATLAS-CONF-2012-042*, 2012.

[216] ATLAS Collaboration, Characterization of Interaction-Point Beam Parameters Using the pp Event-Vertex Distribution Reconstructed in the ATLAS Detector at the LHC, *ATLAS-CONF-2010-027*, 2010.

[217] K. Rehermann and B. Tweedie, Efficient Identification of Boosted Semileptonic Top Quarks at the LHC, *JHEP*, 03:059, 2011.

[218] ATLAS Collaboration, Measurement of the muon reconstruction performance of the ATLAS detector using 2011 and 2012 LHC proton-proton collision data, *Eur. Phys. J. C*, 74:3130, 2014.

[219] ATLAS Collaboration, Electron performance measurements with the ATLAS detector using the 2010 LHC proton-proton collision data, *Eur. Phys. J. C*, 72:1909, 2012.

[220] ATLAS Collaboration, Electron efficiency measurements with the ATLAS detector using the 2012 LHC proton-proton collision data, *ATLAS-CONF-2014-032*, 2014.

[221] ATLAS Collaboration, Electron and photon energy calibration with the ATLAS detector using LHC Run 1 data, *Eur. Phys. J. C*, 74:3071, 2014.

[222] G. P. Salam, Towards Jetography, *Eur. Phys. J. C*, 67:637-686, 2010.

[223] M. Cacciari, G. P. Salam and G. Soyez, The anti-k_t jet clustering algorithm, *JHEP*, 0804:063, 2008.

[224] M. Cacciari and G. P. Salam, Dispelling the N^3 myth for the k_t jet-finder, *Phys. Lett. B*, 641:57-61, 2006.

[225] M. Cacciari, G. P. Salam and G. Soyez, FastJet User Manual, *Eur. Phys. J. C*, 72:1896, 2012.

[226] ATLAS Collaboration, Topological cell clustering in the ATLAS calorimeters and its performance in LHC Run 1, *Eur. Phys. J. C*, 77:490, 2017.

[227] C. Cojocaru et al., Hadronic Calibration of the ATLAS Liquid Argon End-Cap Calorimeter in the Pseudorapidity Region $1.6 < |\eta| < 1.8$ in Beam Tests, *Nucl. Instrum. Meth. A*, 531:481-514, 2004.

[228] T. Barillari et al., Local Hadronic Calibration, *ATL-LARG-PUB-2009-001-2*, 2008.

[229] ATLAS Collaboration, Jet energy measurement with the ATLAS detector in proton-proton collisions at $\sqrt{s} = 7$ TeV, *Eur. Phys. J. C*, 73:2304, 2013.

[230] ATLAS Collaboration, Monte Carlo Calibration and Combination of In-situ Measurements of Jet Energy Scale, Jet Energy Resolution and Jet Mass in ATLAS, *ATLAS-CONF-2015-037*, 2015.

[231] ATLAS Collaboration, Determination of the jet energy scale and resolution at ATLAS using Z/γ-jet events in data at $\sqrt{s} = 8$ TeV, *ATLAS-CONF-2015-057*, 2015.

[232] M. Cacciari and G. P. Salam, The catchment area of jets, *JHEP* 04:005, 2008.

[233] ATLAS Collaboration, Performance of pile-up mitigation techniques for jets in pp collisions at $\sqrt{s} = 8$ TeV using the ATLAS detector, *Eur. Phys. J. C*, 76:581, 2016.

[234] ATLAS Collaboration, Performance of b-Jet Identification in the ATLAS Experiment, *JINST* 11:P04008, 2016.

[235] R. E. Kalman, A New Approach to Linear Filtering and Prediction Problems, *J. Basic Eng.*, 82:35, 1960.

[236] ATLAS Collaboration, Calibration of b-tagging using dileptonic top pair events in a combinatorial likelihood approach with the ATLAS experiment, *ATLAS-CONF-2014-004*, 2014.

[237] ATLAS Collaboration, Calibration of the performance of b-tagging for c and light-flavour jets in the 2012 ATLAS data, *ATLAS-CONF-2014-046*, 2014.

[238] ATLAS Collaboration, Performance of Missing Transverse Momentum Reconstruction in ATLAS studied in Proton-Proton Collisions recorded in 2012 at 8 TeV, *ATLAS-CONF-2013-082*, 2013.

[239] ATLAS Collaboration, Performance of algorithms that reconstruct missing transverse momentum in $\sqrt{s} = 8$ TeV proton-proton collisions in the ATLAS detector, *Eur. Phys. J. C*, 77:241, 2017.

[240] T. Gleisberg et al., Event generation with SHERPA 1.1, *JHEP*, 0902:007, 2009.

[241] B. Andersson, G. Gustafson, G. Ingelman and T. Sjostrand, Parton fragmentation and string dynamics, *Physics Reports*, 97:31, 1983.

[242] B. R. Webber, A QCD Model for Jet Fragmentation Including Soft Gluon Interference, *Nucl. Phys. B*, 238:492, 1984.

[243] R. Ellis, W. Stirling and B. R. Webber, *QCD and Collider Physics*, Cambridge Monographs, 2003.

[244] P. Nason, A new method for combining NLO QCD with shower Monte Carlo algorithms, *JHEP*, 0411:040, 2004.

[245] S. Frixione, P. Nason and C. Oleari, Matching NLO QCD computations with parton shower simulations: the POWHEG method, *JHEP*, 0711:070, 2007.

[246] S. Frixione and B. R. Webber, Matching NLO QCD computations and parton shower simulations, *JHEP*, 0206:029, 2002.

[247] S. Frixione, P. Nason and B. R. Webber, Matching NLO QCD and parton showers in heavy flavour production, *JHEP*, 0308:007, 2003.

[248] S. Alioli, P. Nason, C. Oleari and E. Re, A general framework for implementing NLO calculations in shower Monte Carlo programs: the POWHEG BOX, *JHEP*, 1006:040, 2010.

[249] T. Sjöstrand, S. Mrenna and P. Skands, Pythia 6.4 physics and manual, *JHEP*, 0605:026, 2006.

[250] G. Corcella et al., HERWIG 6.5: an event generator for Hadron Emission Reactions With Interfering Gluons (including supersymmetric processes), *JHEP*, 0101:010, 2001.

[251] J. M. Butterworth, J. R. Forshaw and M. H. Seymour, Multiparton Interactions in Photoproduction at HERA, *Z. Phys. C*, 72:637-646, 1996.

[252] M. L. Mangano et al., ALPGEN, a generator for hard multiparton processes in hadronic collisions, *JHEP*, 0307:001, 2003.

[253] M. L. Mangano, M. Moretti and R. Pittau, Multijet matrix elements and shower evolution in hadronic collisions: $W b\bar{b} + n$ jets as a case study, *Nucl. Phys. B*, 632:343-362, 2002.

[254] S. Catani, F. Krauss, R. Kuhn and B. R. Webber, QCD Matrix Elements + Parton Showers, *JHEP*, 0111:063, 2001.

[255] ATLAS Collaboration, The ATLAS Simulation Infrastructure, *Eur. Phys. J. C*, 70:823-874, 2010.

[256] GEANT4 Collaboration, GEANT4: A simulation toolkit, *Nucl. Instrum. Meth. A*, 506:250-303, 2003.

[257] J. Allison et al., GEANT4 developments and applications, *IEEE Trans. Nucl. Sci.*, 53:270, 2006.

[258] E. Richter-Was, D. Froidevaux and L. Poggioli, ATLFAST 2.0 a fast simulation package for ATLAS, *ATL-PHYS-98-131*, 1998.

[259] ATLAS Collaboration, Fast Simulation for ATLAS: Atlfast-II and ISF, *ATL-SOFT-PROC-2012-065*, 2012.

[260] S. Frixione, P. Nason and G. Ridolfi, A Positive-weight next-to-leading-order Monte Carlo for heavy flavour hadroproduction, *JHEP*, 0709:126, 2007.

[261] P. Z. Skands, Tuning Monte Carlo Generators: The Perugia Tunes, *Phys. Rev. D*, 82:074018, 2010.

[262] J. Pumplin et al., New generation of parton distributions with uncertainties from global QCD analysis, *JHEP*, 0207:012, 2002.

[263] M. Botje et al., The PDF4LHC Working Group Interim Recommendations, *arXiv:1101.0538*, 2011.

[264] J. Gao et al., CT10 next-to-next-to-leading order global analysis of QCD, *Phys. Rev. D*, 89.3:033009, 2014.

[265] R. D. Ball et al., Parton distributions with LHC data, *Nucl. Phys. B*, 867:244, 2013.

[266] S. Alioli, P. Nason, C. Oleari and E. Re, NLO single-top production matched with shower in POWHEG: s- and t-channel contributions, *JHEP*, 09:111, 2009 [Erratum: *JHEP*, 02:011, 2010].

[267] E. Re, Single-top Wt-channel production matched with parton showers using the POWHEG method, *Eur. Phys. J. C*, 71:1547, 2011.

[268] S. Frixione, E. Laenen, P. Motylinski and B. R. Webber, Single-top production in MC@NLO, *JHEP*, 0603:092, 2006.

[269] K. Melnikov and F. Petriello, Electroweak gauge boson production at hadron colliders through $\mathcal{O}(\alpha_S^2)$, *Phys. Rev. Lett.*, 74:114017, 2006.

[270] ATLAS Collaboration, Measurement of the charge asymmetry in top-quark pair production in the lepton-plus-jets final state in pp collision data at $\sqrt{s} = 8$ TeV with the ATLAS detector, *Eur. Phys. J. C*, 76:87, 2016.

[271] J. Campbell and R. Ellis, An update on vector boson pair production at hadron colliders, *Phys. Rev. Lett.*, 60:113006, 1999.

[272] DØ Collaboration, Measurement of the $t\bar{t}$ production cross section in $p\bar{p}$ collisions at $\sqrt{s} =$ 1.96 TeV using kinematic characteristics of lepton + jets events, *Phys. Rev. D*, 76:092007, 2007.

[273] ATLAS Collaboration, Estimation of non-prompt and fake lepton backgrounds in final states with top quarks produced in proton-proton collisions at $\sqrt{s} = 8$ TeV with the ATLAS detector, *ATLAS-CONF-2014-058*, 2014.

[274] A. Corso-Radu et al., Data quality monitoring framework for the ATLAS experiment: Performance achieved with colliding beams at the LHC, *J. Phys. Conf. Ser.*, 331:022027, 2011.

[275] ATLAS Collaboration, Luminosity determination in pp collisions at $\sqrt{s} = 8$ TeV using the ATLAS detector at the LHC, *Eur. Phys. J. C*, 76:653, 2016.

[276] ATLAS Collaboration, Luminosity for Physics, see: `https://twiki.cern.ch/twiki/bin/viewauth/Atlas/LuminosityForPhysics`, as of 13th July 2017.

[277] T. Sjöstrand, S. Mrenna and P. Z. Skands, A Brief Introduction to PYTHIA 8.1, *Comput. Phys. Commun.*, 178:852–867, 2008.

[278] ATLAS collaboration, Summary of ATLAS Pythia 8 tunes, *ATL-PHYS-PUB-2012-003*, 2012.

[279] The ROOT Team, *ROOT: User's Guide v5.34*, CERN, 2013.

[280] ATLAS Collaboration, Selection of jets produced in proton-proton collisions with the ATLAS detector using 2011 data, *ATLAS-CONF-2012-020*, 2012.

[281] J. Erdmann et al., A likelihood-based reconstruction algorithm for top-quark pairs and the KLFitter framework, *Nucl. Instrum. Meth. A*, 748:18-25, 2014.

[282] A. Caldwell, D. Kollar and K. Kröninger, BAT - The Bayesian Analysis Toolkit, *Comput. Phys. Commun.*, 180:2197, 2009.

[283] ATLAS Collaboration, Performance of missing transverse momentum reconstruction in proton-proton collisions at 7 TeV with ATLAS, *Eur. Phys. J. C*, 72:1844, 2012.

[284] M. Jezabek and J. H. Kühn, V-A tests through leptons from polarized top quarks, *Phys.Lett. B*, 329:317, 1994.

[285] I. M. Chakravarti, R. G. Laha and J. Roy, *Handbook of Methods of Applied Statistics, Volume I*, John Wiley and Sons, 1967.

[286] K. Pearson, On the Theory of Contingency and Its Relation to Association and Normal Correlation. *Drapers' Co. Memoirs, Biometric Series No. 1*, 1904.

[287] N. Gagunashvili, σ^2 test for comparison of weighted and unweighted histograms, *Statistical Problems in Particle Physics, Astrophysics and Cosmology, Proceedings of PHYSTAT05, Oxford, UK, 12-15 September 2005, Imperial College Press, London, 43-44*, 2006.

[288] N. Gagunashvili, Comparison of weighted and unweighted histograms, *arXiv:physics/0605123*, 2006.

[289] W. Verkerke and D. Kirkby, *RooFit Users Manual v2.91*, 2008.

[290] S. Frixione, E. Laenen, P. Motylinski, B. Webber and C. D. White, Single-top hadroproduction in association with a W boson, *JHEP*, 0807:029, 2008.

[291] T. Ježo, J. M. Lindert, P. Nason, C. Oleari and S. Pozzorini, An NLO+PS generator for $t\bar{t}$ and Wt production and decay including non-resonant and interference effects, *Eur. Phys. J. C*, 76.12:691, 2016.

[292] J. Campbell, R. K. Ellis, P. Nason and E. Re, Top-pair production and decay at NLO matched with parton showers, *JHEP*, 0415:114, 2015.

[293] T. Ježo and P. Nason, On the Treatment of Resonances in Next-to-Leading Order Calculations Matched to a Parton Shower. *JHEP*, 1215:065, 2015.

[294] T. Sjöstrand et al., An Introduction to PYTHIA 8.2, *Comput. Phys. Commun.*, 191:159, 2015.

Acknowledgements & Danksagung

In the first place, I would like to express my gratitude to Prof. Dr. Arnulf Quadt for being my doctorate supervisor during the last years and for enabling me to realise a very interesting and exciting measurement in the field of top quark physics. I would like to thank him for several business trips and stays at CERN in Geneva. It is definitely a fascinating and worthwhile experience to be so close to our particle physics experiments and meet and discuss with physicists from all over the world. I am very thankful to Prof. Dr. Ariane Frey, Prof. Dr. Arnulf Quadt and Prof. Dr. Kevin Kröninger for being the members of my thesis committee and to Prof. Dr. Arnulf Quadt and Prof. Dr. Stan Lai who consented to be the first and second referee of my PhD thesis. All of them always had a sympathetic ear in case important physics- or non-physics-related questions arose. In this context, I would also like to refer to their instructive and interesting lectures I attended over the past years and their dedicated and often entertaining way of teaching. Thank you very much!
I would like to thank Prof. Dr. Arnulf Quadt, Prof. Dr. Stan Lai, Prof. Dr. Ariane Frey, Prof. Dr. Wolfram Kollatschny, Prof. Dr. Ulrich Parlitz and Jun.-Prof. Dr. Steffen Schumann who agreed to be the members of my examining board.

I am much obliged to Dr. Elisaveta Shabalina and Dr. Boris Lemmer for supervising my daily work in a very committed manner, for answering a lot of questions concerning the top quark decay width measurement and for discussing the obtained results and all emerged problems associated with this analysis in detail. And, not forgetting, many thanks for your extensive proof-reading! I would like to give thanks to Tomas Dado for his contribution to this measurement and for thoroughly discussing issues associated with the research project, also including technical details of the various implementations or test setups.
Genuine thanks to all colleagues and friends working at the II. Institute of Physics - your contagious enthusiasm for particle physics constitutes a substantial reason for staying in Göttingen for such a long time (more than seven years in this institute by now!!!). Thank you ever so much!

Weiterhin möchte ich mich bei der Studienstiftung des deutschen Volkes bedanken, die mich nicht nur fünf Jahre lang während des Physikstudiums gefördert hat, sondern auch noch mein Promotionsvorhaben drei weitere Jahre ideell wie auch finanziell unterstützte. Die Veranstaltungen der Studienstiftung vor Ort in Göttingen wie aber auch Sommerakademien haben meine Studienzeit sehr bereichert und sind ein Grund für mein heutiges Engagement in der lokalen Regionalgruppe des Alumnivereins beziehungsweise in der Auswahlkommission der Studienstiftung.

Ebenso danken möchte ich allen, die mich fachlich für die Physik begeistern konnten und dafür

verantwortlich waren, dass ich zunächst Physik studiert und nun auch noch in diesem Fach promoviert habe. Dies umfasst bereits meine Physiklehrer ab der Mittelstufe, weswegen ich schon in der 9. Klasse ernsthaft vorhatte, Physik zu studieren, aber logischerweise auch viele Professoren an der Universität in Göttingen bis hin zu meinem Doktorvater. Sie alle haben mich rückblickend sehr geprägt und motiviert!

In dieser Auflistung niemals fehlen dürfen meine Familie, meine Freunde und natürlich meine Frau. Vielen Dank an meine Eltern - danke, dass ihr immer für mich da gewesen seid und mich in allen meinen Plänen unterstützt habt, auch in schwierigen und vor allem arbeitsintensiven Phasen! Danke an alle meine Freunde in und um Göttingen - es war und ist schön mit euch, gemeinsam in Göttingen Physik zu studieren, gesellige Abende zu verbringen und euch immer noch wöchentlich in unserer “Nordmensa”-Runde zu sehen!
Johanna, ich bin sehr glücklich, dass ich dich kennengelernt habe und über alles dankbar, dass ich mein Leben mit dir teilen darf!